

Statistical Mechanics and Dynamics Of Surfaces and Membranes

by

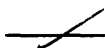
Terence Tai-Li Hwa

B.S. in Physics, Biology, and Electrical Engineering
Stanford University
(June 1986)

SUBMITTED TO THE DEPARTMENT OF
PHYSICS
IN PARTIAL FULFILLMENT OF THE
REQUIREMENTS FOR THE
DEGREE OF
DOCTOR OF PHILOSOPHY IN PHYSICS
at the
MASSACHUSETTS INSTITUTE OF TECHNOLOGY
June 1990


© 1990 Massachusetts Institute of Technology

Signature of Author:




Department of Physics
May 4, 1990

Certified by:




Mehran Kardar
Assistant Professor, Department of Physics
Thesis Supervisor

Certified by:



Toyochi Tanaka
Professor, Department of Physics
Thesis Co-Supervisor

Accepted by:



George F. Koster, Chairman
Departmental Graduate Committee

MASSACHUSETTS INSTITUTE
OF TECHNOLOGY

JUN 28 1990

Acknowledgements

I must first thank Professor Daniel Kleppner who hosted my pre-graduate school visit. Professor Kleppner showed genuine care for students and was a major factor in my decision to come to MIT. The four years at MIT has since been very enjoyable and fruitful thanks to the help and encouragement of many faculty members and fellow students. I am very grateful to Professor Toyochi Tanaka for accepting me to join the lab and for believing in my abilities; a good portion of the works reported in this thesis would not have been possible without Professor Tanaka's support, or the academic freedom he grants to his students. I am very fortunate to have Professor A. Nihat Berker as the instructor of the graduate course in statistical mechanics. It is Professor Berker's dedication and enthusiasm in the course that enlightened my interest in the subject matter pursued in this thesis. I am also grateful to Professor Berker for introducing me to Professor Mehran Kardar with whom many fruitful works resulted. I have benefitted tremendously from Professor Kardar's breadth of knowledge and his depth of understanding of physics, from his almost unlimited availability, and from his attentiveness to details. Professor Kardar has provided me with invaluable help in guiding my research and career, and has been a mentor in almost every category of my life at MIT.

I have learned a great deal from frequent exchange of ideas with Ernesto Medina, John Marko, Maya Paczuski, Sid Gorti, Yong Li, Yong-Ching Zhang, Eriko Sato Matsuo, as well as from many other fellow students of the theory group and the lab. And the friendship of Anthony Yen, Thomas Luke, Kin S. Cheung, Joseph Kung, Albert Young, and Yao-Ching Ku have certainly made life outside of school a lot more exciting. I especially thank Carson Chow for sharing many thoughts and ideas, and for broadening my knowledge in many subjects. I am also grateful to the constant support and care of Zheng-Rong Wang, Maria Yang, the Serdy family, and the Stadler family, whose steadfast friendships have greatly enriched my life in Boston. Lastly, I attribute all of my achievements to the self-less love and encouragements from my mother, who has taught me a responsible, persistent, and relentless working attitude which has been a powerful weapon I have in "attacking" many problems.

I am indebted to Carson Chow, Joseph Kung, Thomas Luke, Ernesto Medina, Poon Tze, Zheng-Rong Wang, Kevin Wasserman, Anthony Yen and Albert Young for their help in the preparation of this manuscript. I have also enjoyed collaborations with a number of colleagues whom I will acknowledge at the end of Chapter 1.

Contents

| | | |
|----------|---|-----------|
| 1 | General Introduction | 1 |
| 2 | The Theory of Self-Avoiding Tethered Membranes | 8 |
| 2.1 | Introduction | 9 |
| 2.1.1 | The Model | 9 |
| 2.1.2 | Scaling Properties | 13 |
| 2.2 | Perturbative Analysis | 17 |
| 2.2.1 | The Two-Point Correlation Function | 20 |
| 2.2.2 | The Second Virial Coefficient | 29 |
| 2.3 | Interpretation of the Generalized ϵ -Expansion | 34 |
| 2.4 | The Renormalization-Group Formalism | 46 |
| 2.5 | Conclusion | 53 |
| 3 | Experimental Studies of the Graphite Oxide Membranes | 55 |
| 3.1 | Introduction | 56 |
| 3.2 | Sample Preparation | 59 |

| | | |
|----------|--|------------|
| 3.2.1 | Survey of Different Approaches | 59 |
| 3.2.2 | Synthesis of Graphite Oxide | 61 |
| 3.2.3 | Suspension of Graphite Oxide | 64 |
| 3.3 | Light-Scattering From GO Membranes | 68 |
| 3.3.1 | Light-Scattering Theory | 68 |
| 3.3.2 | Light-Scattering Set-Ups | 78 |
| 3.3.3 | Experiments and Results | 83 |
| 3.4 | Discussion | 93 |
| 4 | Interface Dynamics | 95 |
| 4.1 | Evolution of Surface Patterns on Swelling Gels | 97 |
| 4.1.1 | The Phenomenon | 97 |
| 4.1.2 | The Model and Hamiltonian | 101 |
| 4.1.3 | Dynamics | 104 |
| 4.2 | Stochastic Dynamics of Interfaces | 116 |
| 4.2.1 | Symmetry in Dynamics | 116 |
| 4.2.2 | Stochasticity in Dynamics | 124 |
| 5 | Stochastic Growth of Interfaces | 132 |
| 5.1 | Introduction | 133 |
| 5.2 | The KPZ Equation and Dynamical RG | 137 |
| 5.3 | Spatial Correlations | 149 |
| 5.4 | Temporal Correlations | 153 |

| | |
|--|------------|
| Appendix: Galilean Invariance | 163 |
| 6 Self-Organized Critical Phenomena | 165 |
| 6.1 Introduction | 166 |
| 6.2 The Sandpile Model | 170 |
| 6.2.1 The Automaton | 171 |
| 6.2.2 The Discrete Model | 176 |
| 6.2.3 The Continuum Model | 192 |
| 6.3 Field Theory of Dissipative Transport | 203 |
| 6.3.1 The Driven Diffusion Equation | 203 |
| 6.3.2 Dynamical Renormalization Group Analysis | 209 |
| 6.3.3 Spatial and Temporal Fluctuations | 219 |
| 6.3.4 Universality Classes and Other Models | 225 |
| 6.4 Conclusion | 231 |
| Appendix: Propagator Renormalization | 232 |
| 7 Conclusions and Future Outlooks | 234 |
| Bibliography | 243 |
| About the Author | 249 |

Chapter 1

General Introduction

One of the first things physics students learn in college is to solve for the motion of two particles interacting via a central force. Soon after that we learn that problems involving three body interactions are in general much more complicated. It then seems that the understanding of worldly objects (which involve 10^{23} particles) would be totally intractable. This is certainly true if by understanding we mean obtaining knowledge for the exact motion of each constituent particle. But this is hardly ever the case – even if we are given the information for each of the particles, we would not know what to do with it. Instead, with a large number of particles, we are usually interested in a small number of “gross” properties of the system. These could be pressure, temperature and density for a gas. It is the role of statistical physics to link the details of microscopic constituents to the observable macroscopic properties.

It turns out that many interesting macroscopic properties are not too sensitive to the microscopic details. For example the phenomena of melting and vaporization are qualitatively similar for all materials. And at some special points, say the critical point of a liquid-vapor system, a vast range of materials exhibit quantitatively identical behaviors. These behaviors are quite often in the form of scaling laws and are summarized by a few scaling exponents[1][2]. Discovery of the existence of such universal behaviors has led to the development of a new branch of statistical physics (critical phenomena)[3] which thrives on characterizing classes of systems by their scaling behaviors (e.g. exponents). These classifications are based on a few fundamental microscopic properties such as the connectivity of the system and certain

underlying symmetries.

Thanks to the advances made in the study of critical phenomena in the past two decades[3], we have by now a fairly good understanding of the equilibrium properties of interacting particles for a wide range of condensed matter systems. The focus of fundamental study has since shifted to more complex systems such as interacting lines and surfaces[4], non-equilibrium/stochastic processes (growth, aggregation)[5], and disordered/frustrated systems (spin glasses, neural networks)[6]. The works presented in this thesis are a collection of endeavors towards some understanding of the universal macroscopic properties of examples of these more complex systems.

In Chapter 2, I explore a simple theoretical model for a polymerized membrane[7]. I first perform a straightforward but tedious calculation through which I introduce the concept of ϵ -expansions and obtain the scaling properties of the membrane's equilibrium conformation. Also explicitly demonstrated is the idea of universality: how macroscopic observables become independent of microscopic parameters. These calculations are followed by the presentation of a renormalization-group (RG) method which enables us to short-cut the tedious calculation. However, because these calculations are perturbative in nature, the exact conformation of the membrane in 3-dimensional space is not obtained using this theory.

Recent large-scale numerical simulations[8] indicate that the membranes may be macroscopically flat at any finite temperature, in contradiction with some earlier theoretical findings. To resolve the actual membrane conformation, I resort to exper-

imental methods. In Chapter 3, I first survey various methods one can use to fabricate/synthesize membranes. The most promising material is thin foils of a graphite derivative known as Graphite Oxide (GO). I describe in detail the method of synthesis of GO. Then I report static light-scattering experiments on a GO suspension. Preliminary results indicate quite strongly that the membranes are indeed crumpled. More thorough studies involving the characterization of membrane dynamics is currently underway.

The dynamics of non-equilibrium fluctuations of interfaces is examined in chapters 4 and 5. First I consider the evolution of patterns on surfaces of expanding gels[47]. It turns out that a model Hamiltonian can be constructed to mimic the process. From the Hamiltonian, dynamics of evolution can be quite straightforwardly derived. Results obtained are in qualitative agreement with experimental observations.

Next I consider the growth of a surface resulting from random deposition[10]. Here, no Hamiltonian can be constructed. However, a good deal can be learned by examining the presence/absence of various symmetries[11] – the relevant equation of motion can be guessed based on such symmetry principles. I present the general method of treating nonlinear, stochastic equations, borrowing and extending the RG method sketched in Chapter 2. The method is applied to growth in the presence of spatially and temporally correlated noise. A translational invariance of the growing surface gives rise to scale-invariance of the surface morphology. Due to additional simplifications, scaling laws in 1+1 dimension can be obtained exactly (even in the

presence of long-range spatially correlated noise). In higher dimensions, an exact exponent identity can be established. These predictions have been verified by recent large scale computer simulations.

Scale-invariant structures occur quite often in nature. Spatial organizations of mountain ranges, river networks are described by fractal geometry[12]. On the other hand, self-similar temporal patterns are also abundant, as reflected by the ubiquity of “noise” with $1/f$ -like power-spectra[13]. These phenomena are much like what happens in the vicinity of a second order phase-transition in conventional critical phenomena, except that in nature the criticality is achieved not by external tuning of some parameter (e.g., pressure or temperature). Rather, the systems spontaneously find a way to the critical state, i.e., they are self-organized. Some key features of Self-Organized-Criticality (SOC) are thought to be dissipation and transport in an open and extended environment. Recently, a toy sandpile model has been proposed to demonstrate these points[14]. In Chapter 6, I first present and analyze the results of numerical simulations of a “running” one-dimensional sandpile. Three different scaling regions consisting of (i) independent avalanches at small time scales, (ii) interacting avalanches at intermediate time scales, and (iii) system-wide discharges (great events) at large time scales have been observed. The behaviors at small scale are known mostly through numerical work and have been addressed by other authors. Interesting broad-band noise spectra occur in the intermediate scale and is studied by the method of continuum field theory. Existence of correlated great events in

the long-time region is attributed to the threshold nature of the dynamics, and the scaling properties are also characterized. The results reported here are not peculiar to 1-d systems as similar behaviors are obtained in simulations of 2-d automata. These results also agree qualitatively with observed sand flow from recent experiments, dispelling the notion that the “sandpile model” does not describe the flow of real sand.

Finally, I apply the formalism described in Chapter 4 to the sandpile model by considering the fluctuation of a sandpile surface in the intermediate hydrodynamic region. Again, by recognizing the presence/absence of various symmetries, combined with conservation laws of local dynamics, a simple equation of motion is constructed. Scale-invariance is established as a consequence of the conservation law. I describe the extension of traditional dynamical RG to anisotropic systems such as the sandpile, and show how scaling exponents for its surface can be calculated. I then establish the connections between these exponents and the exponents ϕ of the $1/f^\phi$ noise-spectra for various transport quantities. A discussion of various universality classes of SOC is given at the end.

In order not to break the continuity of the main text, I would like to acknowledge in the following paragraph some of the many helps I have received during the course of this work:

The calculations described in Chapter 2 resulted from collaborations with B. Duplantier (Saclay, France) and M. Kardar. Some of the results have already been

published and can be found in references [15] and [16]. The experiments reported in Chapter 3 are done with E. Kokufuta (Tsukuba University, Japan) and T. Tanaka. I am fortunate to have M. Dresselhaus and J. Steck providing me with the initial guidance into the world of graphite. I would like to thank M. Frongillo of the MIT Electron Microscopy Facilities for assistances in carrying out the electron-microscopy analysis. I am grateful to S. Gorti and Y. Li for trouble-shooting the equipment problems, and to M. Kardar for many helpful discussions. The study of pattern evolution on expanding gels was done with M. Kardar and has been published in reference [17]. I appreciate many encouragements and comments from S. Gorti, E. Sato and T. Tanaka. The work on surface growth (Chapter 5) is done in collaboration with E. Medina, M. Kardar, and Y.-C. Zhang; most of the results have been published in reference [18]. I am grateful to P. Bak for initiating my interests in Self-Organized Criticality. Some preliminary work on SOC has been published in reference [19]. I thank the MIT VAX Resource Center for providing some of the computing times, and E. Medina for trouble-shooting many computer-related problems. I have also benefitted from a number of conversations with J. Carlson, P. Littlewood, S. Nagel, S. Obukhov, J. Sethna and C. Tang during the course of the work on SOC. Finally, I would like to acknowledge the support of a MIT-Industry Forum Fellowship, an IBM pre-doctoral fellowship, and the National Science Foundation through the MIT Center for Material Science Grants No. DMR-84-18718 and DMR-86-20386, without which the work reported here would not have been possible.

Chapter 2

The Theory of Self-Avoiding

Tethered Membranes

2.1 Introduction

One of the major challenges in theoretical physics today is to understand the properties and behaviors of surface and membranes[4]. There are considerable interests and applications of this new branch of physics in fields ranging from cell membrane interactions in biology[20] to world-sheet dynamics in string theory[21]. Progress in studies of these surfaces has been limited, however, due to enormous mathematical complexities. To gain more insight and knowledge, we investigate the macroscopic properties of membranes in thermodynamic equilibrium. As is often the case in statistical physics, membranes can be categorized by a number of “universality classes”[4]. For instance, cell membranes (lipid bilayers) belong to the class of liquid membranes, while polymerized membranes belong to the class of solid (or tethered) membranes[22]. In this chapter, we will discuss some theoretical aspects of the macroscopic conformation of polymerized membranes; and in Chapter 3, we will present results of experimental studies on thin graphite oxide films, a realization of polymerized membranes.

2.1.1 The Model

A simple theoretical model for interacting polymerized membranes is the Self-Avoiding Tethered Membrane (SATM)[7][22][23][24]. As depicted in Figure 2.1, this model consists of point-particles connected together in a regular 2-dimensional lattice of fixed length. Under thermal excitations, these particles execute random motion as long as they respect their fixed connectivity and the constraint that they don't pass

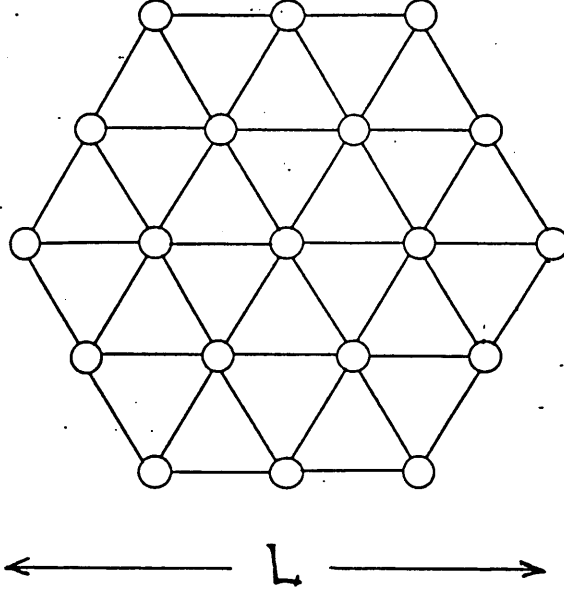


Figure 2.1: A tethered membrane of linear size L .

through each other. The latter constraint is called “self-avoidance”.

To formulate a theory for SATM, let us take a step back and ask what if the connectivity is 1-dimensional? In this case the resulting object has a linear structure (chain) and is a simple model for self-avoiding polymers. Let us further take away the self-avoidance constraint, then the configuration of this “polymer chain” becomes that of an ideal random walk[25]. For a chain of n units each with length Δ_0 , embedded in d -dimensional space, the probability $P(\vec{r})$ that the last unit is at a position \vec{r} away from the first unit (end-to-end distance) is given by the binomial distribution. However, for $n \geq 10$, it can be well approximated by a Gaussian, $P(\vec{r}) \sim \exp(-\frac{d}{2n\Delta_0^2}r^2)$. We next join N such segments together, forming a long chain. Using $\vec{r}(x)$ to denote

the position of the last unit of x^{th} segment, then

$$P\{\vec{r}(x)\} \sim \exp\left(-\frac{d}{2n\Delta_0^2} \sum_{x=1}^N [\vec{r}(x+1) - \vec{r}(x)]^2\right).$$

In the absence of interactions, the free energy is $F = -TS$, where the total entropy for this system is $S = k \log(\int \mathcal{D}\vec{r}(x) P\{\vec{r}(x)\})$. Thus the partition function is

$$Z = \exp(-F/kT) = \int \mathcal{D}\vec{r}(x) \exp\left(-\frac{d}{2n\Delta_0^2} \sum_{x=1}^N [\vec{r}(x+1) - \vec{r}(x)]^2\right).$$

From the form of the partition function, we can identify an effective Hamiltonian

$$\beta\mathcal{H} = \frac{d}{2n\Delta_0^2} \sum_{x=1}^N [\vec{r}(x+1) - \vec{r}(x)]^2.$$

We are always interested in the macroscopic properties of the system, for which $N \gg 1$. In this limit, we can coarse-grain and express \mathcal{H} in the continuum form

$$\beta\mathcal{H} = \frac{K}{2} \int_0^L dx \left(\frac{d\vec{r}}{dx}\right)^2, \quad (2.1)$$

where $K = dn/\Delta$ is the effective linear elasticity of the chain, $\Delta = n\Delta_0$ is the “internal” length of the unit segment, and $L = N\Delta$ is the “internal” size of the chain. For a polymer, L is proportional to the molecular weight. Eqn. (2.1) is the Hamiltonian describing a free polymer chain. The entropic origin of the effective elastic energy is clear from the derivation. It is important to observe that the parameters

K , Δ , and L depend on the definition of the microscopic parameters n , Δ_0 . Any universal observables calculated/measured should not depend on the values of these parameters.

In the polymer case, self-avoidance can be incorporated by ruling out configurations which have two different units occupying the same position in space. Mathematically, this can be achieved by making the following modification to (2.1)

$$\beta\mathcal{H} = \frac{K}{2} \int_0^L dx \left(\frac{d\vec{r}}{dx} \right)^2 + \frac{v}{2} \int_{|x-x'| > \Delta}^L dx dx' \delta^d[\vec{r}(x) - \vec{r}(x')]. \quad (2.2)$$

Eqn. (2.2) is the well-known Edwards Hamiltonian[26] which is very successful in describing self-avoiding polymers in a good solvent. Here v is a parameter which characterizes the strength of the excluded-volume interaction. The microscopic cutoff $|x - x'| > \Delta$ is needed so that the interaction term does not become divergent.

Back to the Self-Avoiding Membrane problem at hand, it is very tempting to generalize Eqn. (2.2) to 2-dimensional internal connectivity. If we use a position vector $\vec{r}(\mathbf{x}) \in \mathcal{E}^d$ to denote the location of particle \mathbf{x} , then the generalized Edwards Hamiltonian is simply

$$\beta\mathcal{H} = \frac{K}{2} \int^L d^2\mathbf{x} [\nabla\vec{r}(\mathbf{x})]^2 + \frac{v}{2} \int_{|\mathbf{x}-\mathbf{x}'| > \Delta}^L d^2\mathbf{x} d^2\mathbf{x}' \delta^d[\vec{r}(\mathbf{x}) - \vec{r}(\mathbf{x}')], \quad (2.3)$$

where Δ and L are again the microscopic and macroscopic cutoff lengths, and K and v are respectively the elasticity coefficient and the excluded-volume interaction

parameter as in the polymer case.

The linear elasticity term has the same entropic origin, and has been checked by Kantor through Monte Carlo simulations[27]. In a hard-sphere-and-string model in which the microscopic interaction potential for nearest neighbor particles in the membrane has the form

$$V(\vec{r}) = \begin{cases} 0 & \text{for } \Delta_0 < r < \Delta_1 \\ \infty & \text{otherwise,} \end{cases}$$

the distribution of the end-to-end distance for a $n \times n$ parallelogram is again well approximated by a Gaussian for $n > 16$. It is assumed that the form of the elastic energy will be valid for any short-ranged central force interaction between nearest-neighbor particles of the membrane.

2.1.2 Scaling Properties

One of the most important macroscopic observables for polymers and membranes is the radius of gyration R_g , in particular the dependence of R_g on molecular weight, or alternatively, on the intrinsic linear dimension L of the system. Such dependence gives information on the macroscopic conformation of the membrane: If $R_g \sim L^{1/d}$, then the network is compressed (compact); if $R_g \sim L$ then the network is stretched; and if R_g lies in between the two limits the network is loosely folded, or crumpled. In the absence of self-avoidance (i.e. $v = 0$), it is easy to show from (2.2) and (2.3) that $R_g^2 \sim$

L for polymers (loosely folded) and $R_g^2 \sim \log L$ for membranes (extremely compact). The theory becomes much more complicated when self-avoidance is included.

In the polymer case, it is established experimentally that $R_g \sim L^\nu$ where ν is called the radius-of-gyration exponent. The exponent ν can also be calculated theoretically. The simplest method is Flory's mean-field estimate[25]. A polymer chain of length L and radius of gyration R_g has an average concentration $\langle c \rangle \sim L/R_g^d$. From (2.2) the average elastic energy scales as $\langle c \rangle (R_g/L)^2$, while the average repulsion energy scales as $\langle c \rangle^2$. Balancing of the two terms immediately leads to

$$\nu_F = \frac{3}{d+2}, \quad (2.4)$$

the celebrated Flory exponents for semi-dilute polymers in good solvent.

Of course the mean-field approximation made in Flory's estimate is not controlled. A much more elaborate calculation is needed if we are to take into account the effect of correlations. In the polymer case, the Edwards Hamiltonian in (2.2) can be mapped to a ϕ^4 -field theory through a Laplace-de-Gennes Transform[28]; and essentially all the machinery developed for the ϕ^4 -theory can be directly transferred to the polymer problem[29]. It is found that above an upper critical dimension $d_c = 4$, the polymer behaves as if it is ideal ($v = 0$) with $\nu_0 = 1/2$. Below 4-dimensions self-avoidance becomes increasingly more important, and the exponent ν smoothly increases from $1/2$. This allows a perturbative expansion of ν in powers of $\epsilon = 4 - d$. The values of ν obtained from detailed calculations are in very good agreement with the Flory results

though the origin of such agreement is not understood. A more detailed discussion of ϵ -expansion results and the Flory exponent is given in section 2.3.

For self-avoiding membranes, we can also do a Flory-type estimate. Realizing that the average concentration is $\langle c \rangle \sim L^2/R_g^d$ for membranes, we balance the elastic energy against the repulsive excluded-volume interaction and obtain

$$\nu_F = \frac{4}{3+d} \quad \text{for membranes.} \quad (2.5)$$

This suggests that the membranes are macroscopically “crumpled” in 3-dimension since $2/3 < \nu_F(d=3) = 0.8 < 1$. Systematic calculation using the membrane theory (2.3) is much more difficult. Firstly, there is no known mapping to any field theory; in fact, the membrane theory looks more like a “string-type” theory than conventional field theories for point particles. Secondly, the corresponding upper critical dimension for membranes is at $d_c = \infty$, making it difficult to carry out a conventional ϵ -expansion.

The second difficulty can be overcome by generalizing the connectivity of the network to D -dimensions[7]. Since we know that the $D=1$ case (polymer theory) is well under control, there is hope that the solution to the membrane problem can be obtained by analytically continuing D from 1 to 2. In the next section, we present a perturbative analysis for this D -dimensional self-avoiding manifold[15]. Through the analysis, we will discover that there emerges an upper critical dimension above which the manifold is “free”, with $\nu_0 = (2-D)/2$, and below which ν smoothly increases,

just as in the case of self-avoiding polymers.

2.2 Perturbative Analysis

In section 2.1 we showed that a simple model describing the polymerized membrane is the self-avoiding tethered membrane. The equilibrium properties can be calculated within this theory by generalizing the Edwards Hamiltonian of (2.3) to D -dimensional manifolds[7]:

$$\beta\mathcal{H} = \frac{K}{2} \int^L d^D \mathbf{x} [\nabla \vec{r}(\mathbf{x})]^2 + \frac{v}{2} \int_{|\mathbf{x}-\mathbf{x}'|>\Delta}^L d^D \mathbf{x} d^D \mathbf{x}' \delta^d [\vec{r}(\mathbf{x}) - \vec{r}(\mathbf{x}')], \quad (2.6)$$

where $\mathbf{x} \in \mathcal{E}^D$ is the internal coordinate label for the manifold, $\vec{r}(\mathbf{x}) \in \mathcal{E}^d$ is the position vector of \mathbf{x} , and the parameters K , v , L , and Δ are as defined for (2.3). Of course, the Hamiltonian for a real membrane contains additional terms such as $(\nabla^2 \vec{r})^2$ (bending energy), $[\nabla \vec{r}]^4$ (anharmonic stretching energy), etc. But for a crumpled membrane, i.e. $r \sim x^\nu$ with $\nu < 1$, these terms are small in the thermodynamic limit $x \rightarrow \infty$ and are therefore not included in (2.6).

In this section, we will use (2.6) to compute several macroscopic observables. We will first calculate the two-point correlation function $R(\mathbf{x}_0 - \mathbf{x}'_0) = \langle [|\vec{r}(\mathbf{x})_0 - \vec{r}(\mathbf{x}'_0)|^2] \rangle$ from which the scaling properties of the radius of gyration (and hence the exponent ν) may be obtained. This will be followed by a calculation of the dimensionless second virial coefficient g which characterizes the strength of the excluded-volume interaction. The calculations themselves are rather tedious; interested readers can find some details in sections 2.2.1 and 2.2.2. In the following, we will outline the

calculations and state the results.

The two-point correlation function $R(\mathbf{x}_0 - \mathbf{x}'_0)$ can be obtained from the characteristic function

$$\langle \exp \{ i \vec{q}_0 \cdot [\vec{r}(\mathbf{x})_0 - \vec{r}(\mathbf{x}'_0)] \} \rangle$$

which can be calculated perturbatively in powers of v using (2.6). In the absence of self-avoidance, the two-point function is simply given by $R_0^2(\mathbf{x} = \mathbf{x}_0 - \mathbf{x}'_0) = 2dC(\mathbf{x})$, where $C(\mathbf{x}) \sim |\mathbf{x}|^{2-D}$ is the D -dimensional Coulomb potential. The effect of excluded volume interaction is to “swell” the manifold, and the two-point function becomes

$$R^2(\mathbf{x}) = R_0^2(\mathbf{x}) \cdot \mathcal{X}(\mathbf{x}), \quad (2.7)$$

where \mathcal{X} is a swelling factor and has the form

$$\mathcal{X}(\mathbf{x}) = 1 + f_1(\mathbf{x})v + f_2(\mathbf{x})v^2 + \dots$$

from the perturbation expansion. The interaction parameter has a dimension

$$v \sim K^{-d/2} |\mathbf{x}|^{-2D+(2-D)d/2}.$$

It is convenient to define a dimensionless interaction parameter $\tilde{z}(\mathbf{x}) \sim v K^{d/2} |\mathbf{x}|^{\epsilon/2}$ with $\epsilon \equiv 4D - (2 - D)d$. Since \mathcal{X} is itself a dimensionless factor, its dependence on

v must be through the dimensionless parameter $\bar{z}(\mathbf{x})$, i.e.

$$\mathcal{X}(\mathbf{x}) = \sum_{n=0}^{\infty} A_n [\bar{z}(\mathbf{x})]^n,$$

where the coefficients A_n are now dimensionless (they can only depend on d and D in the thermodynamic limit $|\mathbf{x}|/\Delta \rightarrow \infty$). It turns out that in the limit $\epsilon \rightarrow 0$, the coefficients A have a simple structure, and the perturbation series may be summed:

$$\mathcal{X}(\mathbf{x}) = (1 + B_1 \bar{z}(\mathbf{x}))^{A_1/B_1}.$$

Inserting the above expression in Eqn. (2.7), we find the two-point correlation function to have the simple scaling form

$$R^2(\mathbf{x}) \sim |\mathbf{x}|^{2-D+\frac{\epsilon}{2}\frac{A_1}{B_1}}$$

to $O(\epsilon)$ in the limit $\mathbf{x} \rightarrow \infty$.

The dimensionless second virial-coefficient g is defined from the virial expansion

$$\Pi\beta = C \left[1 + \frac{1}{2}g \left(\frac{2\pi}{d} R^2(L) \right)^{d/2} C \right], \quad (2.8)$$

where C is the concentration of manifolds in solution, Π is the osmotic pressure, and $R^2(L)$ is the physical size of the manifold (or the end-to-end distance) as calculated from (2.7). The factor g is calculated from the *two-manifold* partition function. It

has a perturbative expansion much like the swelling factor \mathcal{X} (they are both dimensionless). The perturbation series for g can also be summed, and in the limit of small ϵ :

$$g(L) = \frac{\bar{z}(L)}{1 + B_1 \bar{z}(L)}.$$

This expression again takes on a very simple form in the thermodynamic limit, i.e. $g \rightarrow 1/B_1$ as $L \rightarrow \infty$.

Interpretation of the scaling forms and a discussion of the generalized ϵ -expansion is given in section 2.3. A more convenient way of obtaining the scaling properties using the method of Renormalization-Group(RG) is described in section 2.4; we will demonstrate how the RG method works in light of the exact results (for $\epsilon \ll 1$) of the perturbation analysis.

2.2.1 The Two-Point Correlation Function

The two-point correlation function can be obtained from the characteristic function which has the following series when expanded in powers of v from (2.6)

$$\begin{aligned} \langle \exp\{i\vec{q}_0 \cdot [\vec{r}(\mathbf{x}_0) - \vec{r}(\mathbf{x}'_0)]\} \rangle &= \sum_n \frac{1}{n!} \left(-\frac{v}{2}\right)^n \int \dots \\ &\left\langle \exp \left\{ i \sum_{m=0}^n \vec{q}_m \cdot [\vec{r}(\mathbf{x}_m) - \vec{r}(\mathbf{x}'_m)] \right\} \right\rangle_0 / Z. \end{aligned} \quad (2.9)$$

Here, the integration is performed over all internal variables $\mathbf{x}_1, \mathbf{x}'_1, \dots, \mathbf{x}_n, \mathbf{x}'_n$, and momenta $\vec{q}_1, \dots, \vec{q}_n$; and $\langle \dots \rangle_0$ is the expectation value for the ideal Gaussian manifold

(i.e. with $v = 0$). The expansion for the partition function $Z = \int \mathcal{D}\vec{r}\{\mathbf{x}\} \exp\{-\beta\mathcal{H}\}$ in the denominator is similar to the numerator, but with $\vec{q}_0 = \vec{0}$. One shows[7][23] that $\left\langle \exp\left\{i \sum_{m=0}^n \vec{q}_m \cdot [\vec{r}(\mathbf{x}_m) - \vec{r}(\mathbf{x}'_m)]\right\} \right\rangle_0 = \exp\left\{-\sum_{l,m=0}^n \vec{q}_l \cdot \vec{q}_m \mathcal{A}_{lm}\right\}$, where

$$\mathcal{A}_{lm} = \frac{1}{2} [C(\mathbf{x}_l - \mathbf{x}'_m) + C(\mathbf{x}'_l - \mathbf{x}_m) - C(\mathbf{x}_l - \mathbf{x}_m) - C(\mathbf{x}'_l - \mathbf{x}'_m)],$$

and $C(\mathbf{x}) = |\mathbf{x}|^{2-D}/S_D(2-D)$ is the Coulomb potential in D -dimensions (S_D is the area of a unit sphere). \mathcal{A}_{lm} is the dipole interaction between pairs l and m , and $\mathcal{A}_{ll} = C(\mathbf{x}'_l - \mathbf{x}_l)$. After integrating over internal momenta, the n^{th} term in (2.9) becomes:

$$S_n = \frac{1}{n!} \left(-\frac{v}{2}\right)^n \left(\frac{4\pi}{K}\right)^{-nd/2} \int d(1) \cdots d(n) A_n^{-d/2}(\mathbf{x}_1, \mathbf{x}'_1, \cdots, \mathbf{x}_n, \mathbf{x}'_n) \times \exp\left\{-\frac{q_0^2}{K} \frac{A_{n+1}^{(0)}(\mathbf{x}_0, \mathbf{x}'_0, \mathbf{x}_1, \mathbf{x}'_1, \cdots, \mathbf{x}_n, \mathbf{x}'_n)}{A_n(\mathbf{x}_1, \mathbf{x}'_1, \cdots, \mathbf{x}_n, \mathbf{x}'_n)}\right\},$$

where A_n is the determinant of an $n \times n$ matrix of elements \mathcal{A}_{lm} , while in $A_{n+1}^{(0)}$ the pair $(\mathbf{x}_0, \mathbf{x}'_0)$ is also present. We have also used the notation $d(m) = d^D \mathbf{x}_m d^D \mathbf{x}'_m$.

Expanding Eq. (2.9) in powers of q_0 yields

$$\left\langle [\vec{r}(\mathbf{x}_0) - \vec{r}(\mathbf{x}'_0)]^2 \right\rangle = 2dC(\mathbf{x}_0 - \mathbf{x}'_0) Z^{(0)}(\mathbf{x}_0 - \mathbf{x}'_0, L) / Z(L). \quad (2.10)$$

To rid ourselves of cumbersome numerical factors, we normalize the Coulomb potential such that $C(\mathbf{x}) = |\mathbf{x}|^{2-D}$, and introduce an interaction parameter $z = [(2 -$

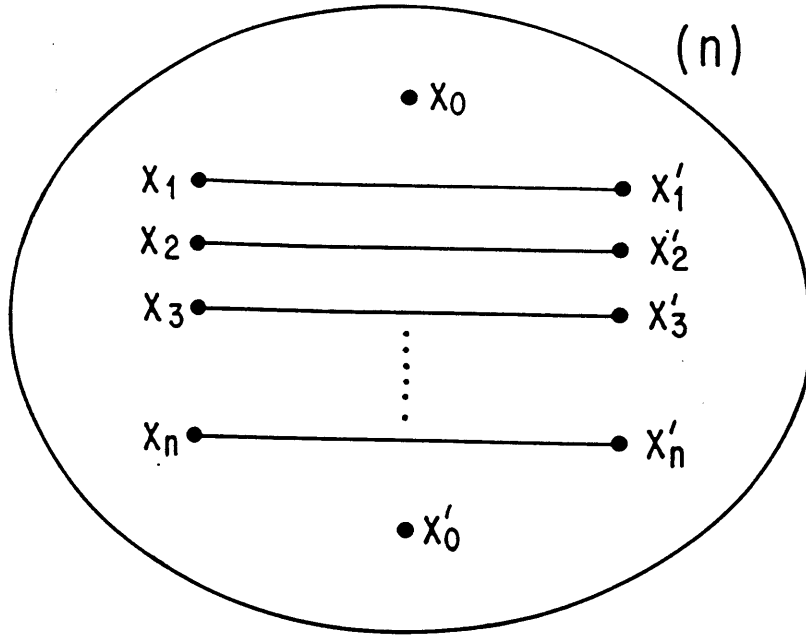


Figure 2.2: Diagrammatical representation of the n^{th} order term, S_n in the perturbation expansion. The manifold has n “handles” at order n .

$D) S_D K/4\pi]^{d/2} v$. The expansion for the partition function now reads $Z = \sum_{n=0}^{\infty} (-z/2)^n X_n(L)/n!$, with a similar expansion for $Z^{(0)}$ in terms of $X_n^{(0)}$, where

$$X_n = \int d(1) \cdots d(n) A_n^{-d/2}, \quad (2.11)$$

$$X_n^{(0)} = \int d(1) \cdots d(n) A_n^{-1-d/2} A_{n+1}^{(0)}/A_1^{(0)}. \quad (2.12)$$

The terms in the perturbation series are shown diagrammatically in Figure 2.2. Each line connecting two internal points can be thought of as a “handle” on the manifold. Thus the order of a diagram may be classified by the number of handles.

We see that there is only one diagram at each order in the perturbation, which is reminiscent of string models[21]. Although this appears as a simplification, various combinatorial rules for assembling Feynman diagrams (such as one-line reducibility) cannot be applied to reorganize this perturbation series. Recently, Duplantier[30] proposed a method of direct resummation of leading order “divergent” terms in the perturbation series for a “half-model” of excluded volume interactions between a flat and a crumpled manifold. Here we sketch the outline of a similar direct resummation for the full SATM problem.

Much information about the perturbation series can be gained by examining the first term in the expansion of the partition function, i.e. $X_1 = \int d(1)y_1^{-d(2-D)/2}$, where $y_1 = |\mathbf{x}_1 - \mathbf{x}'_1|$. Clearly, this integral has a leading analytical behavior proportional to the manifold volume $(L/\Delta)^D$, where L and Δ are the macroscopic and microscopic cutoff lengths as described earlier. Subleading terms proportional to lower powers of L/Δ may also appear. As discussed in references [7] [23] and [24], there can be an additional *singular contribution* which becomes divergent for $\epsilon \equiv 4D - d(2 - D) \geq 0$. Therefore X_1 can be decomposed as $X_1^{(\text{regular})}(L/\Delta) - 2a_1(L^{\epsilon/2} - \Delta^{\epsilon/2})/\epsilon$.¹ In fact such decompositions occur for all terms in the perturbation series. By analogy to polymers we expect the cutoff dependent terms in Z (as well as $Z^{(0)}$) to re-exponentiate and yield the extensive free energy of the manifold, i.e. $Z = Z^{\text{reg}}(L/\Delta) \times Z^{\text{sing}}$. This factorization (which is the essence of dimensional regularization) is well established for

¹Here $a_1(D)$ is crucially dependent on the shape of the manifold[24][7]. But it will not be present in the final expression for the two-point function as we will soon see.

polymers[31]; its validity for manifolds, an assumption at this point, will be discussed elsewhere. In $\mathcal{Z}^{\text{sing.}}$, on which we focus henceforth, the leading divergence of an n^{th} -order graph is proportional to $(L^{n\epsilon/2} - \Delta^{n\epsilon/2})/\epsilon^n$. This can be used to develop a systematic resummation procedure, for \mathcal{Z} and \mathcal{Z}^0 , valid for $\epsilon \rightarrow 0$. To avoid a dependence on different length scales we initially take $|\mathbf{x}_0 - \mathbf{x}'_0| \sim L$ (but away from the boundary) and $\Delta \rightarrow 0$.

A careful inspection of A_n , $A_{n+1}^{(0)}$ indicates that singularities in X_n , $X_n^{(0)}$ come from either self-contraction of handles (Figure 2.3a) or fusion of two handles (Figure 2.3b). More complicated situations such as the one shown in Figure 2.3c contain only sub-leading divergences which contribute to corrections higher order in ϵ . We first consider the case (b) of handle fusion: let $\mathbf{x}_1 - \mathbf{x}_l = \mathbf{u}$, $\mathbf{x}'_1 - \mathbf{x}'_l = \mathbf{u}'$, and suppose $\mathbf{u} \rightarrow 0$, $\mathbf{u}' \rightarrow 0$ are the smallest pairwise distances of the $2n$ internal points in S_n . Then simple manipulations yield the crucial factorization $A_n = [C(\mathbf{u}) + C(\mathbf{u}')]A_{n-1}$, to leading order for $0 < D < 2$, where A_{n-1} is the reduced $n - 1 \times n - 1$ determinant after pair (1) has been dropped from A_n . Integrating in X_n or $X_n^{(0)}$ in the sector $|\mathbf{u}|, |\mathbf{u}'| \leq y$, where y is the next smallest pairwise distance, gives to leading order for $\epsilon \rightarrow 0$

$$\int d^D u d^D u' [C(\mathbf{u}) + C(\mathbf{u}')]^{-d/2} = \frac{2}{\epsilon} a_2 y^{\epsilon/2},$$

where

$$a_2 = \frac{S_B^2}{2 - D} \frac{\Gamma^2[D/(2 - D)]}{\Gamma(d/2)}. \quad (2.13)$$

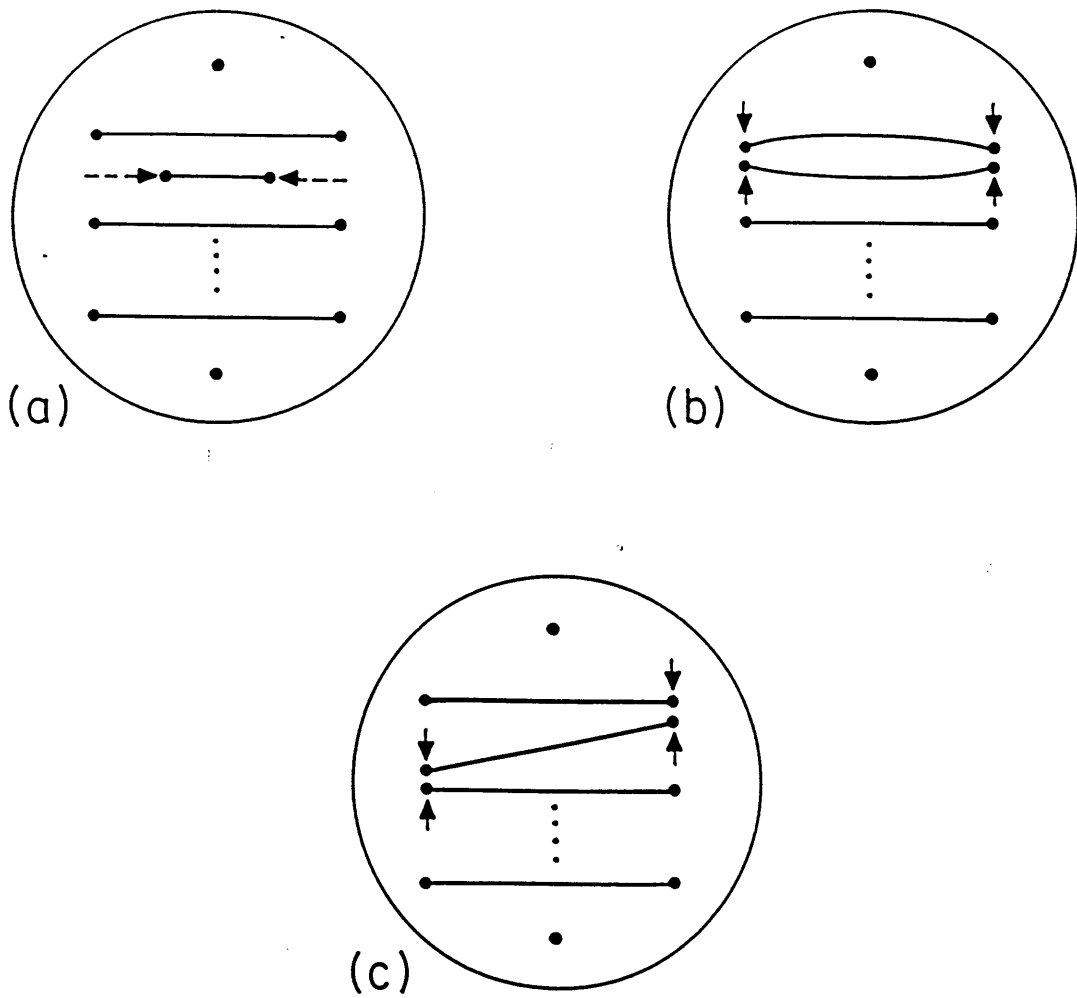


Figure 2.3: Leading divergences come from (a) self-contraction of a handle, and (b) fusion of two handles; a configuration such as (c) contributes to sub-leading divergences.

Hence in X_n (and $X_n^{(0)}$), the *fusion sector* (b) ($1 \rightarrow l$) gives a contribution

$$X_n|_{(b)} = \frac{2a_2}{\epsilon} \int \dots y^{\epsilon/2} A_{n-1}^{-d/2}, \quad (2.14)$$

with integrals now performed over $n - 1$ pairs. The case (a) of self-contraction of a handle (Figure 2.3a) is more complicated. Here $|\mathbf{x}_1 - \mathbf{x}'_1| = y_1$ is the smallest of all pairwise distances. In this sector of the integration space, one expands determinants $A_n, A_{n+1}^{(0)}$ with respect to the first row \mathcal{A}_{1l} , i.e.

$$A_n^{-d/2} = A_{n-1}^{-d/2} \mathcal{A}_{11}^{-d/2} \left\{ 1 - \frac{d}{2} \sum_{l \geq 2} \frac{\mathcal{A}_{1l} \Delta_{1l}}{\mathcal{A}_{11} A_{n-1}} + \dots \right\},$$

where $\mathcal{A}_{11} = y_1^{2-D}$, and where Δ_{1l} is the cofactor ($(-1)^{1+l} \times$ codeterminant) of element \mathcal{A}_{1l} in A_n . A similar expansion holds for $A_{n+1}^{(0)}$. Note that Δ_{1l} contains always a factor \mathcal{A}_{1m} , $m \geq 2$. Then we need the basic integration formulae in the sector $y_1 \leq y$

$$\int d(1) \mathcal{A}_{11}^{-d/2} = -\frac{2a_1}{\epsilon} y^{\epsilon/2}, \quad \int d(1) \frac{\mathcal{A}_{1l} \mathcal{A}_{1m}}{\mathcal{A}_{11}^{1+d/2}} = \frac{2a_0}{\epsilon} y^{\epsilon/2} \mathcal{A}_{lm},$$

the latter implying

$$\int d(1) \frac{\mathcal{A}_{1l} \Delta_{1l}}{\mathcal{A}_{11}^{1+d/2}} = -\frac{2a_0}{\epsilon} y^{\epsilon/2} A_{n-1}.$$

The integral a_0 is easily evaluated[7][23][24] to be

$$a_0 = S_D^2 (2 - D) / 2D. \quad (2.15)$$

The other integral $a_1(D)$ is manifold-shape dependent in this sector due to the center of mass integration in $d(1)$ near the boundary. It can also be calculated given the manifold shape; but we will not need the form of a_1 because it will not affect the two-point correlation function as we will soon show. We therefore have in sector (a) the recursion

$$X_n|_{(a)} = \frac{-2}{\epsilon} \left[a_1 - (n-1)a_0 \frac{d}{2} \right] \int \cdots y^{\epsilon/2} A_{n-1}^{-d/2}, \quad (2.16)$$

and a similar one for $X_n^{(0)}$ with a_1 in (2.16) *simply replaced by* $a_1 + a_0$. We now take care of the combinatorics of fusions (2.14) and self-contractions of the handles (2.16). At level n there are $2 \times n(n-1)/2$ ways of fusing two out of n handles, which multiplies (2.14). There are independently n choices for self-contracting any of the handles, multiplying (2.16). Hence we find $X_n = n X_n|_{(a)} + n(n-1) X_n|_{(b)}$. Iterating the recursions (2.14) and (2.16) gives

$$X_n = (-2L^{\epsilon/2}/\epsilon)^n \prod_{p=1}^n [a_1 - (p-1)a], \quad (2.17)$$

where $a \equiv a_0(d/2) + a_2$. Note that an overall factor of $1/n!$ in X_n comes from *nested* integrations over successive pairwise distances y [30]. $X_n^{(0)}$ is also given by (2.17) with a_1 replaced by $a_1 + a_0$. Now \mathcal{Z} , and $\mathcal{Z}^{(0)}$ are exactly summable as

$$\mathcal{Z} = \left(1 + \frac{a}{\epsilon} z L^{\epsilon/2} \right)^{a_1/a}, \quad \mathcal{Z}^{(0)} = \left(1 + \frac{a}{\epsilon} z L^{\epsilon/2} \right)^{(a_1+a_0)/a}. \quad (2.18)$$

The two-point swelling factor (2.10) is

$$\mathcal{X} = \mathcal{Z}^{(0)}/\mathcal{Z} = \left(1 + \frac{a}{\epsilon} z L^{\epsilon/2}\right)^{a_0/a}. \quad (2.19)$$

Notice that the boundary dependent term a_1 which dominates \mathcal{Z} , has dropped out of the swelling factor \mathcal{X} .² For $\epsilon > 0$, we get the asymptotic behavior for the end-to-end distance $R^2(L) = \langle [\vec{r}(L) - \vec{r}(0)]^2 \rangle \sim L^{2\nu}$ with $\nu = \frac{2-D}{2} + \frac{\epsilon a_0}{2a}$, and a_0 and a_2 given by (2.15) and (2.13) respectively; these results are in agreement with previous calculations[7][23][24]. But they put previous calculations on a more rigorous footing as will be shown in section 2.4. An interpretative discussion of this ϵ -expansion is given in section 2.3.

We have thus established scaling forms in (2.18), (2.19) as functions of the overall size L , subject to the validity of dimensional regularization. We can also directly derive the scaling form for the two point distance in Eq. (2.10), without this assumption, for $\Delta \ll y_0 = |\mathbf{x}_0 - \mathbf{x}'_0| \ll L$. The singularities in $X_n^{(0)}(y_0, L)$ can be traced to regions where various pairwise distances are small (fusions or annihilations of handles). The presence of an intermediate external distance y_0 breaks up such integrations into intervals where the separations are smaller, or larger than y_0 . In particular, we can divide the overall integration to segments with m distances less than y_0 , and write

$$X_n^{(0)}(y_0, L) = \sum_{m=0}^n \frac{n!}{m!(n-m)!} \mathcal{Y}_m^{(o)}(y_0) X_{n-m}(L). \quad (2.20)$$

²On physical grounds, we do not expect the *external* shape of a manifold to affect the two-point function which characterizes the *internal* correlations of the manifold.

The coefficients $\mathcal{Y}_m^{(o)}(y_0)$ correspond to the singularities obtained with an upper cutoff of y_0 rather than L . They can thus be calculated from $X_m^{(0)}(L)$, by replacing L with y_0 , and setting $a_1 = 0$. The latter is required since all the singularities proportional to a_1 come from integrations over the whole manifold and as such contribute to $X_{n-m}(L)$. In fact Eq. (2.20) is analogous to decomposition by the cluster expansion. The full partition function Z now simply factors out of $Z^{(0)} = \sum_n (-z/2)^n X_n^{(0)}(y_0, L)/n!$, and we obtain

$$\langle [\vec{r}(\mathbf{x}_0) - \vec{r}(\mathbf{x}'_0)]^2 \rangle = \frac{2d|\mathbf{x}_0 - \mathbf{x}'_0|^{2-D}}{S_D(2-D)} \left(1 + \frac{a}{\epsilon} z |\mathbf{x}_0 - \mathbf{x}'_0|^{\epsilon/2} \right)^{a_0/a},$$

which depends on $|\mathbf{x}_0 - \mathbf{x}'_0|$ only. This result yields right away the radius of gyration R_g :

$$R_g^2(L) = \frac{1}{L^{2D}} \int d^D \mathbf{x} d^D \mathbf{x}' \langle [\vec{r}(\mathbf{x}_0) - \vec{r}(\mathbf{x}'_0)]^2 \rangle \sim L^{2\nu}.$$

2.2.2 The Second Virial Coefficient

In this section we calculate the physical interaction constant. One place the excluded-volume interaction of the tethered membrane manifests itself is in the second virial coefficient. For a dilute solution of N membranes (manifolds), the osmotic pressure is given by

$$\beta\Pi = \frac{\langle N \rangle}{V} + B_2 \frac{\langle N \rangle^2}{V^2}, \quad (2.21)$$

where the second virial coefficient B_2 can be calculated from the grand partition function $\mathbf{Z} = \sum_N e^{\mu N} Z_N / N!$. Since $\beta\Pi V = \log \mathbf{Z}$ and $\langle N \rangle = (\partial/\partial\mu) \log \mathbf{Z}$, we have

$$B_2 = \frac{1}{2} \left[1 - \frac{Z_2}{Z_1^2} \right]. \quad (2.22)$$

Here Z is the one-manifold partition function encountered in section 2.2.1, and Z_2 is the *two*-manifold partition function:

$$Z_2 = \int \mathcal{D}\vec{r}_a \mathcal{D}\vec{r}_b \exp \left\{ -\frac{1}{2} \int d^D \mathbf{x} [(\nabla \vec{r}_a)^2 + (\nabla \vec{r}_b)^2] - \frac{v}{2} \sum_{i=a,b} \sum_{j=a,b} \int d^D \mathbf{x} d^D \mathbf{x}' \delta^d[\vec{r}_i(\mathbf{x}) - \vec{r}_j(\mathbf{x}')] \right\}.$$

Again we expand (2.22) in powers of v . After performing the multiple gaussian integrals over the variables \vec{r} , the perturbation series for B_2 takes on the following form:

$$B_2 = -\frac{1}{2} \sum_{\mu,\nu,m=0}^{\infty} \left(-\frac{z}{2}\right)^{\mu} \left(-\frac{z}{2}\right)^{\nu} (-z)^{m+1} \frac{1}{\mu! \nu! (m+1)!} X_{\mu,\nu,m+1} / Z_1^2. \quad (2.23)$$

The diagrammatic representation of $X_{\mu,\nu,m}$ is shown in Figure 2.4. Each term in the sum represents μ handles on manifold a , ν handles on manifold b , and $m+1$ “inter-manifold” handles, with

$$X_{\mu,\nu,m+1} = \int d(x)d(y)d(s) [A_{\mu}(x)A_{\nu}(y)D_m^{\mu,\nu}(x,y,s)]^{-d/2}.$$

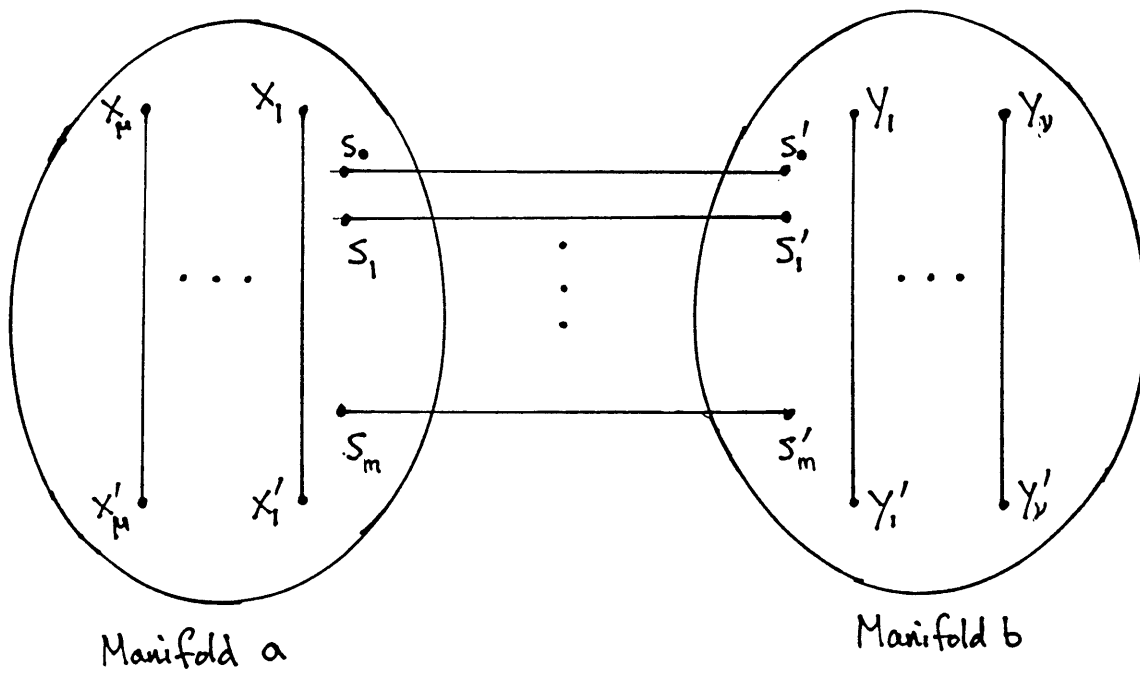


Figure 2.4: The diagrammatic representation of a term $X_{\mu, \nu, m}$ involved in perturbation expansion of the two-manifold partition function Z_2 . Each handle represents a pair-wise excluded volume interaction. There are μ handles for manifold a , ν handles for manifold b , and $m + 1$ intra-manifold handles shown in this diagram.

The integrations are performed over all internal points $d(x) \equiv dx_1 dx'_1 \cdots dx_\mu dx'_\mu$, $d(y) \equiv dy_1 dy'_1 \cdots dy_\nu dy'_\nu$, and $d(s) \equiv ds_1 ds'_1 \cdots ds_m ds'_m$. A_n is the $n \times n$ matrix describing the n -handle *intra*-manifold interactions introduced in section 2.2.1, and $D_m^{\mu,\nu}$ is the determinant of a $m \times m$ matrix whose elements are themselves determinant of matrices involving the interactions of the *inter*-manifold handles with each of the *intra*-manifold handles.

Needless to say, the calculation of the above expression is even more tedious than the one for the two-point function in section 2.2.1. However, the principle in both calculations is the same: We again identify the leading order divergences of (2.23) as originating from (i) self-contraction of *intra*-manifold handles, (ii) fusion of *intra*-manifold handle pairs, and (iii) fusion of *inter*-manifold handle pairs. Again to leading order in ϵ , only three integrals a_0 , a_1 , and a_2 are involved, and the boundary dependent a_1 terms do not enter the final expression for B_2 . (The contributions of the a_1 term to Z_2 and Z_1 cancel as in the case of the two-point function.)

After going through the combinatorics similar to section 2.2.1, we can sum the series (2.23):

$$B_2 = -\frac{z}{2} L^{2D} \left[1 + \frac{a}{\epsilon} z L^{\epsilon/2} \right]^{-a_0/a}.$$

This expression can be further simplified when expressed in terms of the physical size (ene-to-end distance) $R^2(L) = 2dC(L)\mathcal{X}(L)$ where the swelling factor \mathcal{X} is given by Eqn. (2.19):

$$B_2 = \frac{1}{2} \frac{z L^{\epsilon/2}}{1 + \frac{a}{\epsilon} z L^{\epsilon/2}} \left[\frac{2\pi}{d} R^2(L) \right]^{d/2}. \quad (2.24)$$

Comparing Eqs. (2.21) and (2.24) with the definition of the *dimensionless* second virial coefficient g given by Eqn. (2.8), we immediately read off

$$g(L) = \frac{zL^{\epsilon/2}}{1 + \frac{a}{\epsilon}zL^{\epsilon/2}}.$$

2.3 Interpretation of the Generalized ϵ -Expansion

In section 2.2, we calculated the two-point correlation function $R^2(x)$ and the dimensionless second-virial coefficient g of the D -dimensional manifold by directly summing the perturbation series in powers of the effective interaction parameter $z = v[S_D(2 - D)K/4\pi]^{d/2}$, where S_D is the area of a D -dimensional unit sphere, and K and v are the parameters in the Hamiltonian (2.6). The results to first-order in

$$\epsilon(d, D) = 4D - d(2 - D) \quad (2.25)$$

are restated below

$$R^2(L) = \frac{2d}{S_D(2 - D)K} L^{2-D} \left[1 + \frac{a}{\epsilon} z L^{\epsilon/2} \right]^{a_0/a}, \quad (2.26)$$

$$g(L) = \frac{z L^{\epsilon/2}}{1 + \frac{a}{\epsilon} z L^{\epsilon/2}}, \quad (2.27)$$

where L is the intrinsic linear-size of the manifold, a_0 and $a = (d/2)a_0 + a_2$ are integration constants given in Eqs. (2.13) and (2.15).

In the thermodynamic limit of $L \rightarrow \infty$, we see that the second virial coefficient g is zero for $\epsilon < 0$. But it goes to a fixed value of $g^* = \epsilon(d, D)/a(d, D) > 0$ for $\epsilon > 0$. The function $\epsilon(d, D) = 0$ thus forms a line of “critical dimensions” in the (d, D) plane (see Figure 2.5). As far as macroscopic behavior is concerned, the excluded-volume interaction is irrelevant to the right of the critical line ($\epsilon < 0$); there the manifold behaves as if it is free. But to the left of the line where $\epsilon > 0$, the

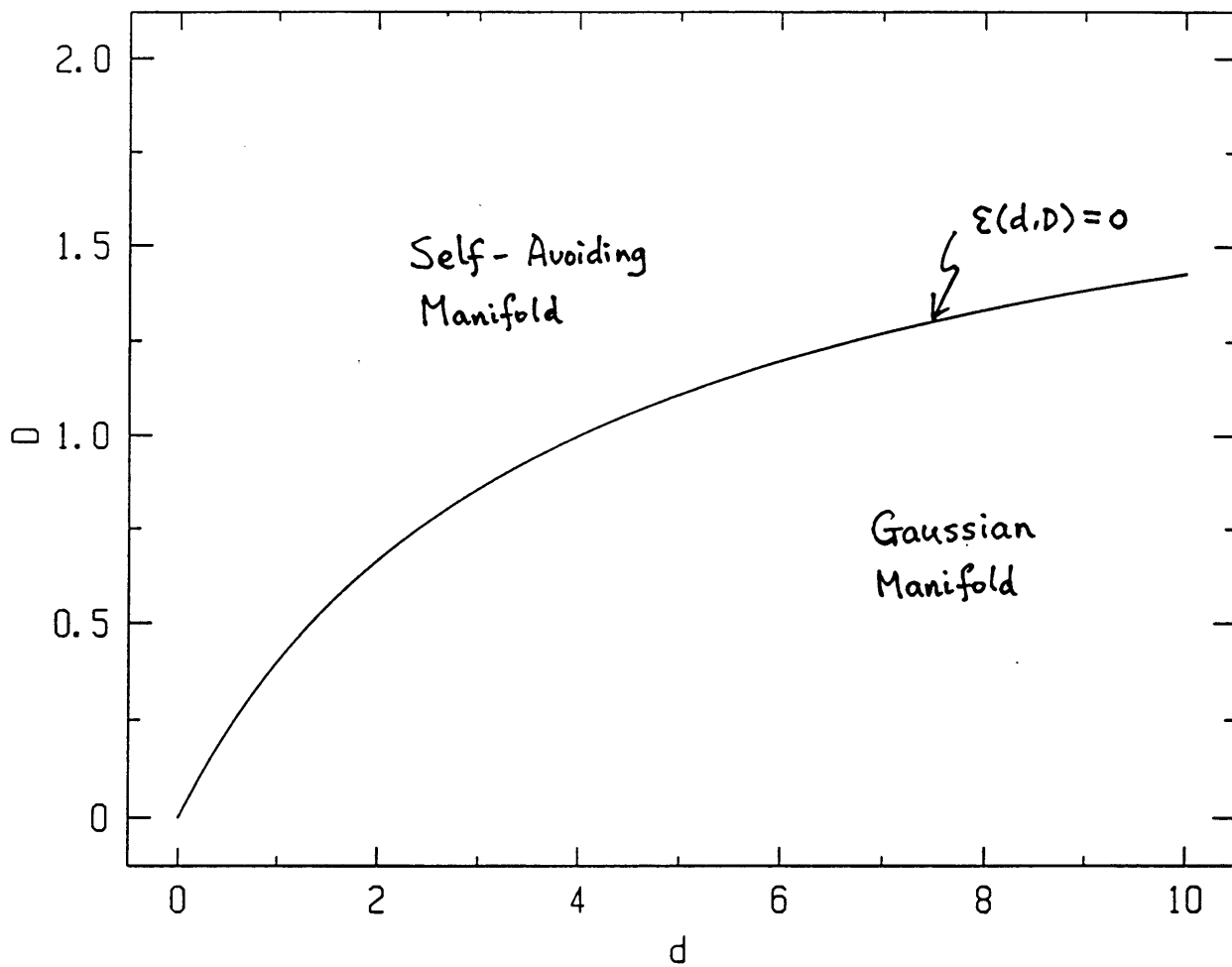


Figure 2.5: The line of critical dimension $\epsilon(d, D) = 4D - d(2 - D) = 0$ in the (d, D) plane. The upper critical dimension for polymers ($D = 1$) is 4-dimension, but is infinite for membranes because the critical line only approaches $D = 2$ asymptotically as $d \rightarrow \infty$. The manifold is “free” (i.e. Gaussian) in the region $\epsilon < 0$; but for $\epsilon > 0$, self-avoidance is relevant.

excluded-volume interaction becomes relevant as manifested by a finite and positive second virial coefficient in this region.³

In the thermodynamic limit, we also have $R \sim L^\nu$. The radius-of-gyration exponent ν takes on the ideal value (for free manifold) of $\nu_0 = (2 - D)/2$ for $\epsilon < 0$. But in physically relevant cases where $\epsilon > 0$, the manifold swells, with

$$\nu(d, D) = \frac{2 - D}{2} + \frac{1}{2} \frac{a_0(d, D)}{a(d, D)} \epsilon(d, D). \quad (2.28)$$

As claimed in section 2.1, the values of ν and g^* are *universal* in that they do not depend on the values of microscopic parameters such as K , v , L , and Δ .

If our interest lies only in the numerical values of the exponent ν for membranes, then we can simply use the Flory exponent (2.5) which agrees quite well with the most recent experimental result (see Chapter 3). However, the Flory expression cannot be extended to study other universal quantities; nor can it be used to calculate scaling functions, determine relevances of other interactions, etc., which can be studied systematically using the ϵ -expansion. In this section, we use the exponent ν as a case study to explore the ϵ -expansion properties of all universal quantities. We then use the Flory exponent as a guide against which we check results of the ϵ -expansion.

It is important to recognize that, as in all renormalizable theories, an expression

³The expression (2.25) for the critical dimension can be understood by the following intuitive argument[7]: a manifold of exponent ν has a fractal dimension of $D_f = D/\nu$ (see Chapter 3). Two D_f -dimensional objects do not intersect in general if the embedding spatial dimension is $d > 2D_f$. Using the exponent for free membranes $\nu_0 = (2 - D)/2$, we immediately see that there is no intersection for $d > d_c = 4D/(2 - D)$. Hence self-avoidance is irrelevant until $d \leq d_c$.

such as the correlation function (2.26) is merely a *re-organization* of the perturbation series. The small parameter ϵ , which emerged naturally from perturbative calculations, is nothing more than a mathematical convenience which is exploited to organize the expansion. Normally ϵ is a linear function of the spatial dimension d only, for instance, $\epsilon = 4 - d$ in the theory of polymers. Expansion in powers of ϵ is therefore conceptually very simple. In the present case, however, we find that by generalizing the manifold dimension to D , we are left with an ϵ which is a *non-linear* function of d and D . Since a universal quantity such as the exponent ν is an arbitrary function of d and D , it usually cannot be written in terms of $\epsilon(d, D)$ alone. If we still want to take advantage of the expansion parameter ϵ , we need to make a transformation of variables from d, D to $\epsilon = \epsilon(d, D), \delta = \delta(d, D)$, such that $\nu(d, D) = \tilde{\nu}_\delta(\epsilon(d, D), \delta(d, D))$. The subscript δ is a reminder that the function $\tilde{\nu}$ will depend on the form of $\delta(d, D)$ used. In this way, ν can be written as a double expansion in ϵ and δ .

While the form of $\epsilon(d, D)$ is given by (2.25), we have at our disposal an infinite number of invertible transformations $\delta(d, D)$, all of which will lead to the same value of the exponent $\nu(d, D)$. This freedom in choosing $\delta(d, D)$ was a cause of concern in previous studies[7], and the ϵ -expansion was thought to be ambiguous at least to first order since different forms of $\delta(d, D)$ would lead to different values of ν at $\mathcal{O}(\epsilon)$. We will show in the followings that it is exactly this freedom that provides us with a guide to resolve the apparent ambiguities.

We would like to choose a transformation $\delta(d, D)$ that is either physically mean-

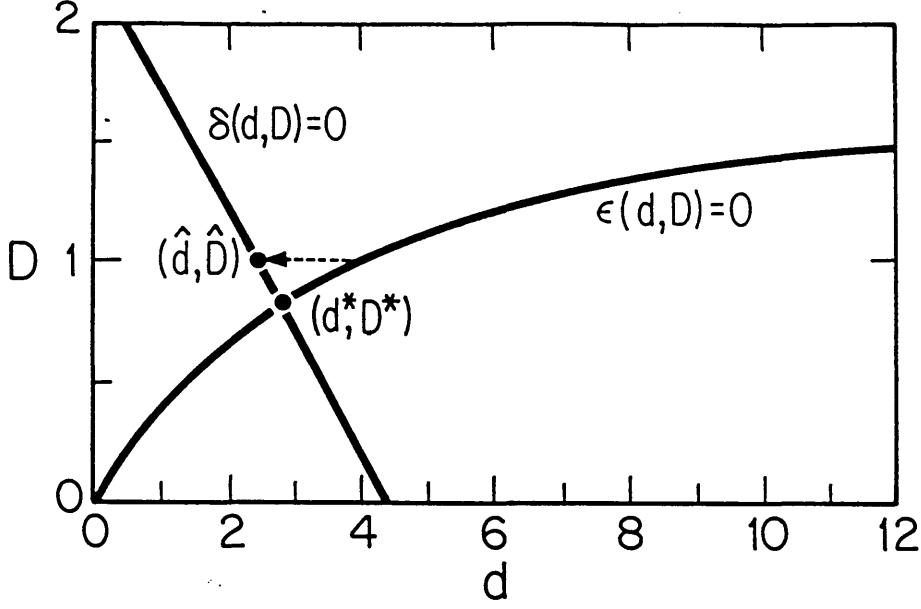


Figure 2.6: The lines $\epsilon(d, D) = 0$ and $\delta(d, D) = 0$ in the (d, D) plane. The path of the traditional ϵ -expansion is marked by the arrow.

ingful or mathematically convenient. One very simple choice is to have the point of interest, say (\hat{d}, \hat{D}) , be on the line $\delta(d, D) = 0$. In this case $\bar{\nu}_\delta(\epsilon, \delta)$ becomes a single power series in ϵ . We limit our discussion to $\delta(d, D)$'s such that $\delta = 0$ are straight lines in the (d, D) plane. (We will soon see that a straight line is all we need for $\mathcal{O}(\epsilon)$ calculations.) Suppose the straight line $\delta(d, D) = 0$ intersects the curve $\epsilon(d, D) = 0$ at (d^*, D^*) as shown in Figure 2.6, then the transformation $\delta(d, D)$ is completely specified by the point (d^*, D^*) for a given (\hat{d}, \hat{D}) , i.e.,

$$\delta(d, D) = D(d^* - \hat{d}) - d(D^* - \hat{D}) + D^*\hat{d} - \hat{D}d^*, \quad (2.29)$$

with $4D^* = d^*(2 - D^*)$. The point (d^*, D^*) is called the expansion point. Since d^* (or D^*) serves as a parameter in $\delta(d, D)$, we write $\nu(\hat{d}, \hat{D}) = \bar{\nu}_{d^*}(\epsilon(\hat{d}, \hat{D}), \delta(\hat{d}, \hat{D}) = 0)$.

Note that the case $d^* = 4\hat{D}/(2 - \hat{D})$ (or $D^* = \hat{D}$, see dashed line in Figure 2.6) corresponds to the traditional ϵ -expansion.

Eqs. (2.25) and (2.29) can then be inverted, with

$$D(\epsilon, \delta = 0) = D^* + \epsilon \frac{D^*(D^* - \hat{D})}{(D^*)^2(d^* - \hat{d}) + 2(D^*\hat{d} - d^*\hat{D})} + \mathcal{O}(\epsilon^2), \quad (2.30)$$

and a similar expression for d : $d(\epsilon, \delta = 0) = d^*(1 + \mathcal{O}(\epsilon))$. Substituting these expressions for d and D into (2.28) and keeping everything to $\mathcal{O}(\epsilon)$, we can compute the value of the exponent $\nu(\hat{d}, \hat{D}) = \tilde{\nu}_{d^*}(\epsilon, \delta = 0)$ as a function of the parameter d^* . The results for $(\hat{d}, \hat{D}) = (3, 2)$, $(3, 1)$, and $(2, 1)$ are plotted in Figures 2.7 (a)-(c). As is clear from these figures, ν is not a monotonically decreasing function of d^* , in contradiction to a finding in reference[7]. There, $D(\epsilon, \delta) = \hat{D}$ was inadvertently used (instead of Eq. (2.30)) in evaluating ν . Due to the nonlinear form of $\epsilon(d, D)$, it is easy to see that in general $D(\epsilon, \delta) \neq \hat{D}$ to $\mathcal{O}(\epsilon)$, except in the special cases when $d^* = \hat{d}$ or $d^* = 4\hat{D}/(2 - \hat{D})$.

There is now an apparent ambiguity in the values of ν due to the dependency on d^* . To find the “optimal” ν to $\mathcal{O}(\epsilon)$, we recall that $\nu(\hat{d}, \hat{D})$ is independent of the choice of $\delta(d, D)$. Therefore $\partial\nu(\hat{d}, \hat{D})/\partial d^* = 0$. It follows that

$$\nu_{\text{optimal}} = \tilde{\nu}_{\hat{d}} \quad \text{where} \quad \left. \frac{\partial \tilde{\nu}_{d^*}}{\partial d^*} \right|_{d^*=\hat{d}} = 0.$$

We see that ambiguity in ν may be removed to a large degree by choosing the ex-

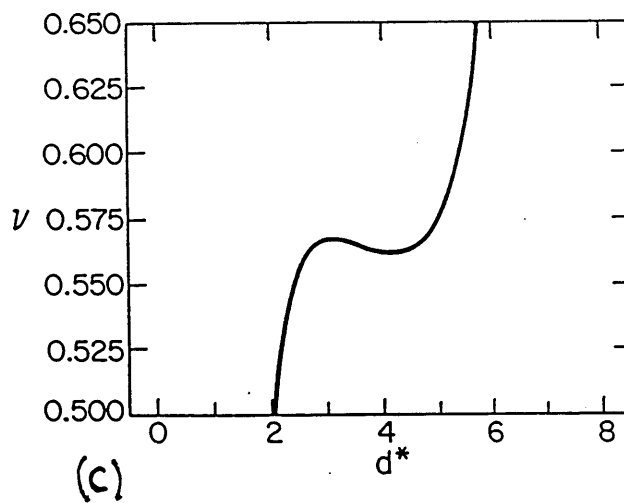
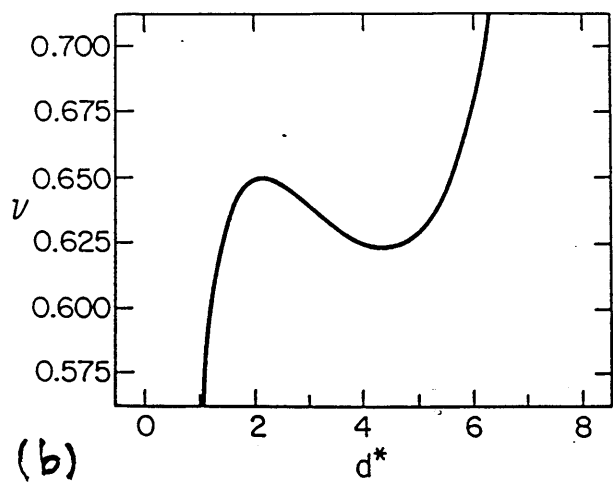
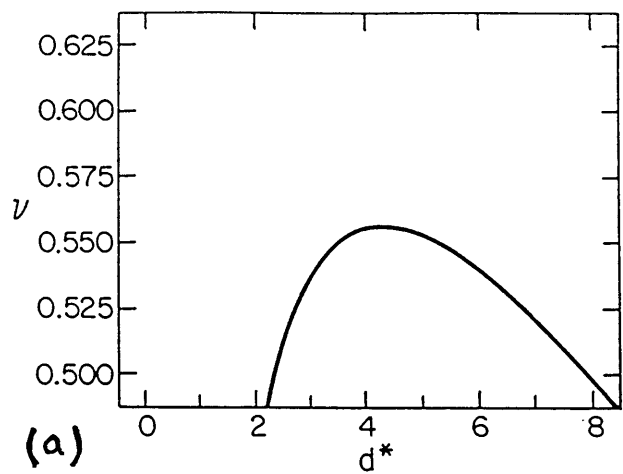


Figure 2.7: Numerical results of $\tilde{\nu}_d$ for (a) membranes in 3-dimension, (b) polymers in 3-dimension, and (c) polymers in 2-dimension.

tremum value of $\bar{\nu}_{d^*}$. This is readily applied to higher orders in ϵ and more complicated curves $\delta(d, D) = 0$. In the latter case, if the curve is specified by n parameters p_1, \dots, p_n , there will be n conditions, $\partial\bar{\nu}/\partial p_i = 0$ to fix every parameter. However to $\mathcal{O}(\epsilon)$, the dependence of $\bar{\nu}$ on p_i 's comes only from its dependence on $D(\epsilon, \delta)$ in (2.28). Suppose $D = D^* + f_1(d^*, p_i)\epsilon + \mathcal{O}(\epsilon^2)$, then $\partial\bar{\nu}/\partial p_i = 0$ implies that $\partial D/\partial p_i = 0$, or $f_1(d^*, p_i) = f(d^*)$. Hence, the straight line (2.29) is the only family of curves needed to be searched for the optimized value of ν to $\mathcal{O}(\epsilon)$.

Applying our optimization scheme to the exponent values plotted in Figures 2.7, we find the $\mathcal{O}(\epsilon)$ estimate for tethered membranes in 3-dimensions to be $\nu(\hat{d} = 3, \hat{D} = 2) = 0.556$; the optimal expansion point (the maximum in Figure 2.7(a)) is at $\bar{d} \approx 4.3$. The exponents for membranes in higher embedding spatial dimensions are also obtained by this method. Their values are listed in Table 2.1. The corresponding exponent values as calculated from the Flory expression (2.4) and (2.5) are also listed for ease of comparison.

For polymers in 3- and 2- dimensions (Figures 2.7(b),(c)), two extrema are present. We choose the maximum values since the exponent values are under-estimated in both cases⁴; these results are again listed in Table 2.1. Since $\bar{d} \neq 4$, we discover that the traditional $\epsilon = 4 - d$ expansion for polymers is not the “optimal” expansion; our

⁴This choice seems to be rather arbitrary; however, there is another justification: Of the two extrema, the maximum is close to \hat{d} while the minimum is close to $4\hat{D}/(2 - \hat{D})$ in both cases. Using (2.25) and (2.30), we see that $d(\epsilon, \delta = 0) = \hat{d}$, and $D(\epsilon, \delta = 0) = D^* + \epsilon D^*/2d^* = \hat{D}$ when $d^* = \hat{d}$. There is no term higher than $\mathcal{O}(\epsilon)$ generated from expansion of $d(\epsilon, \delta)$ and $D(\epsilon, \delta)$ in (2.28). So we expect the extremum close to \hat{d} (maximum in both cases) to be closer to the exact value of the exponent.

| (\hat{d}, \hat{D}) | \bar{d} | $\nu^{(a)}$ | $\nu_F^{(b)}$ | $\nu^{(c)}$ | $\nu^{(d)}$ |
|-----------------------------------|-----------|-------------|---------------|-------------|-------------|
| (3,2) | 4.3 | 0.556 | 0.800 | 0.83±0.03 | ... |
| (4,2) | 5.3 | 0.517 | 0.667 | ... | ... |
| (5,2) | 6.2 | 0.484 | 0.571 | ... | ... |
| (6,2) | 6.9 | 0.454 | 0.500 | ... | ... |
| (7,2) | 7.7 | 0.426 | 0.444 | ... | ... |
| (8,2) | 8.4 | 0.401 | 0.400 | ... | ... |
| $(\hat{d} \rightarrow \infty, 2)$ | \hat{d} | $4/\hat{d}$ | $4/\hat{d}$ | ... | ... |
| (3,1) | 3.2 | 0.567 | 0.600 | 0.591 | 0.562 |
| (2,1) | 2.2 | 0.650 | 0.750 | 0.750 | 0.625 |

Table 2.1: Values of the exponent ν obtained from (a) the optimization method described in text to $\mathcal{O}(\epsilon)$ (\bar{d} is the optimal expansion point), (b) the Flory expression (2.4) and (2.5), (c) best estimates: [The exponent value for polymers in 2-dimension is exact (conformal field theory) and that in 3-dimension is from higher order ϵ -expansion. The value for membrane in 3-dimension is taken from the experimental results described in Chapter 3.] and (d) the traditional ϵ -expansion for polymers to $\mathcal{O}(\epsilon)$.

scheme is thus an improvement over the traditional method.

There is clearly a trend in Table 2.1: Estimates of the exponent values for manifolds in high dimensional embedding space ($\hat{d} \gg \hat{D}$) are in good agreement with the Flory result (which is in turn in good agreement with best estimates); but it starts to deviate from the Flory results as embedding spatial dimension \hat{d} is reduced. Unfortunately the physically relevant situation of membranes in 3-dimensions is the worst case. It should be noted that this trend is not related to the value of ϵ . For 2-dimensional membranes, we have $\epsilon = 8$ in any \hat{d} , yet $\mathcal{O}(\epsilon)$ estimate of ν is very sensitive to \hat{d} . In fact, it is easy to see (at $d^* = \hat{d}$) that ν of (2.28) and ν_F of (2.5) have the same limit $4/\hat{d}$ for membranes embedded in very high dimensional space, i.e., for $\hat{d} \rightarrow \infty$. (With a little algebra, we can show that ν_{opt} also goes to the limit

4/ \hat{d} .)

For manifolds embedded in low dimensional space, can the situation be improved if we are able to compute and include terms higher order in ϵ ? To answer this question, we go to the extreme situation where $\hat{d} \approx \hat{D}$. On physical ground we expect the manifold to be “stretched”, i.e., $\nu = 1$, for $\hat{d} = \hat{D}$. Therefore if we do a double expansion in $\epsilon(d, D)$ and $\delta(d, D) = d - D$, we expect to have $\nu(\epsilon, \delta)$ be independent of ϵ at small δ . In particular, we must have $\nu(\epsilon, \delta = 0) = 1$ for all ϵ .⁵

In the vicinity of $\epsilon \approx 0$ and $\delta \approx 0$, we have to the lowest order: $D = \delta + \epsilon/2$ and $d = 2\delta + \epsilon/2$. The integrals (2.15) and (2.13) are in this limit[16] $a_0 = S_D^2/\delta$ and $a_2 = 2S_D^2/\delta$, yielding

$$\begin{aligned} \nu &= \frac{2-D}{2} + \frac{\epsilon}{4} \frac{a_0}{a_2 + \frac{d}{2}a_0} \\ &= 1 - \frac{\delta}{2} - \frac{\epsilon}{8} + \mathcal{O}(\delta\epsilon, \epsilon^2, \delta^2). \end{aligned}$$

The above expression clearly shows that $\nu \neq 1$ at $\delta = 0$ for any non-zero ϵ , underestimating the exact result $\nu = 1$. The dependence of $\nu(\epsilon, \delta = 0)$ on ϵ will persist even if higher-order ϵ terms are included (except for isolated values of ϵ). We thus have to conclude that the Hamiltonian (2.6), from which we obtained the correlation function (2.26) and the above expression for ν , does not fully describe the self-avoiding manifold in the region $\delta \approx 0$ and small ϵ . A moment of reflection suggests that as the

⁵The limit of small ϵ and small δ is similar to the limit $d, D \rightarrow 0$. The latter case has also been considered by R.C. Ball (private communication), who obtained a result different from ours.

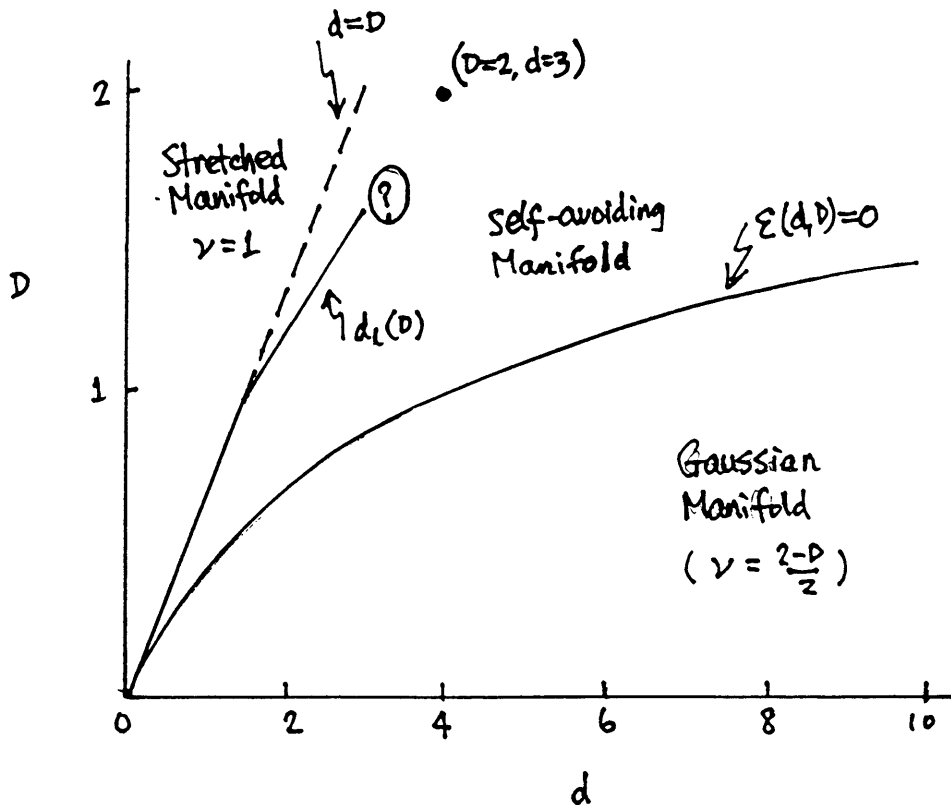


Figure 2.8: A possible phase diagram with the indicated lower critical dimensions. It is not known whether the physical case for the membranes ($d = 3, D = 2$) belongs to the “stretched” phase.

dimension of the embedding space approaches that of the manifold dimension, the manifold is “squeezed” and n -body excluded volume interactions of the form

$$\frac{v_n}{n!} \int d^D \mathbf{x}_1 \cdots d^D \mathbf{x}_n \delta^d [\vec{r}(\mathbf{x}_1) - \vec{r}(\mathbf{x}_2)] \cdots [\vec{r}(\mathbf{x}_{n-1}) - \vec{r}(\mathbf{x}_n)]$$

become increasingly important. These terms might be needed in (2.6) as $\delta \rightarrow 0$ (at least for small ϵ). They will tend to “stretch” the network and increase ν . This problem is however not believed to be present for polymers. (Higher-order ϵ -expansion of the polymer theory seems to indicate that $\nu \approx 1$ for $d \rightarrow 1$.) It is possible that $\nu > 1$ when higher order ϵ terms are included for $D > 1$. If this is the case, then the lower critical dimension for the theory (2.6) can be $d_l > D$ for $D > 1$, suggesting a line of *lower critical dimension* as shown in Figure 2.8. The Hamiltonian in (2.6)

will not be valid for $d < d_l$ as its construction is based on an expansion in powers of $\nabla \vec{r}$ which is small only if $\nu < 1$.

$\nu = 1$ signals that the network is “stretched” (or flat for membranes). Since the lower critical dimension cannot be accessed through the perturbative studies, it leaves open the possibility that membranes in 3-dimensions may not be crumpled if the line of lower critical dimension passes to the right of the point ($D = 2, d = 3$) (see Figure 2.8). Recent numerical simulations[8] seem to indicate that the membranes are flat in 3-dimensions. But we shall see in Chapter 3 that light-scattering experiments on real membranes strongly suggest that the membranes are crumpled, with $\nu = 0.83 \pm 0.03$, close to the Flory estimate.

2.4 The Renormalization-Group Formalism

The expressions for $R(L)$ and $g(L)$ calculated in section 2.2 are in fact quite simple and are governed by only two integration constants (a and a_0) in the macroscopic limit. We now describe the method of renormalization-group (RG) analysis which allows us to extract the universal numbers (the radius-of-gyration exponent ν and the fixed value of the dimensionless second-virial coefficient g^*) with much less work.

Eqn. (2.26) can be rewritten as

$$R^2(L) = \frac{2D}{S_D(2-D)K^R} L^{2-D}, \quad (2.31)$$

where

$$K^R(L) = K \left[1 + \frac{a}{\epsilon} z L^{\epsilon/2} \right]^{-a_0/a} \quad (2.32)$$

is identified as the *renormalized* elasticity coefficient due to the excluded-volume interaction. Similarly, we have

$$g(L) = z^R L^{\epsilon/2}, \quad (2.33)$$

where

$$z^R = z \left[1 + \frac{a}{\epsilon} z L^{\epsilon/2} \right]^{-1}. \quad (2.34)$$

In the thermodynamic limit ($L \rightarrow \infty$), $R(L) \rightarrow L^\nu$ and $g(L) \rightarrow g^* = \text{constant}$. If we define

$$\tilde{K}^R = K^R L^{2\nu-D+2}, \quad (2.35)$$

and

$$\tilde{z}^R = z^R L^{\epsilon/2}, \quad (2.36)$$

then according to (2.31) and (2.33), \tilde{K}^R and \tilde{z}^R should be dimensionless in the limit $L \rightarrow \infty$. Using (2.32) and (2.34), we obtain the scaling properties of \tilde{K}^R and \tilde{z}^R by applying the rescaling operator $L(\partial/\partial L)$:

$$L \frac{\partial}{\partial L} \tilde{K}^R = \tilde{K}^R(L) \left[(2\nu + D - 2) - \frac{a_0}{2} \tilde{z}^R(L) \right], \quad (2.37)$$

$$L \frac{\partial}{\partial L} \tilde{z}^R = \tilde{z}^R(L) \left[\frac{\epsilon}{2} - \frac{a}{2} \tilde{z}^R(L) \right]. \quad (2.38)$$

Eqs. (2.37) and (2.38) are called the renormalization-group flow equations, or the recursion relations. Since $\tilde{K}^R(L)$ and \tilde{z}^R are dimensionless in the $L \rightarrow \infty$ limit, then $L(\partial\tilde{K}^R/\partial L) = 0$ and $L(\partial\tilde{z}^R/\partial L) = 0$ as $L \rightarrow \infty$ (the infra-red limit). The exponent ν and the universal second virial coefficient g can be solved at the “infra-red fixed point” of the recursion relations.

But of course these recursion relations are *equivalent* to the direct solutions (2.26) and (2.27) since the former are obtained from simple manipulations of the solution. Major simplification occurs when we make the following observation: From the leading order terms in the expansions (2.32) and (2.34),

$$K^R(L) \approx K - K \frac{a_0}{\epsilon} z L^{\epsilon/2},$$

$$z^R(L) \approx z - \frac{a}{\epsilon} z^2 L^{\epsilon/2},$$

we find that the application of the scaling operator yields

$$L \frac{\partial}{\partial L} \tilde{K}^R = K L^{2\nu+D-2} \left[(2\nu + D - 2) - \frac{a_0}{2} z L^{\epsilon/2} \right], \quad (2.39)$$

$$L \frac{\partial}{\partial L} \tilde{z}^R = z L^{\epsilon/2} \left[\frac{\epsilon}{2} - \frac{a}{2} z L^{\epsilon/2} \right]. \quad (2.40)$$

These equations appear to be very similar to the flow equations (2.37) and (2.38), except that the parameters K and z appearing on the right-hand side of Eqs. (2.39) and (2.40) are not the renormalized ones. Thus for this problem, it suffices just to calculate the *first-order* correction to the linear elasticity and interaction parameters. The recursion relations obtained from the first-order perturbation result are equivalent to the *full* solution (for $\epsilon \ll 1$) if we simply replace the parameters K and z by K^R and z^R . The first estimate of the exponent ν for the manifold was done this way by Kardar and Nelson[7]. The fact that the full solution can be obtained from simple manipulations of the first-order results (without going through the messy combinatorics as was done in section 2) seems to be miraculous. But this actually works for a wide range of systems.

The insistence on distinguishing between the variables K , z and their renormalized counterparts K^R and z^R seems pedantic so far; and in practice the first-order recursion relations have been traditionally calculated without explicitly using the renormalized variables. However, this is an accidental simplification because $K^R = K$ and $z^R = z$ only to first order in ϵ . If one wants to extend the RG calculations to higher orders in ϵ , it becomes absolutely essential to use the renormalized variables in the recursion

relations. Since this point has not always been appreciated, we will demonstrate its importance by doing a second-order calculation in a symbolic form.

Let us suppose that we have calculated the excluded-volume corrections to the two-point function $R^2(L)$ and the interaction parameter v to second-order in v and second-order in ϵ with the results

$$\mathcal{X}(L) = 1 + \frac{\alpha_1}{\epsilon} zL^{\epsilon/2} + \frac{\alpha_2}{\epsilon^2} (zL^{\epsilon/2})^2, \quad (2.41)$$

$$v^R = v \left[1 + \frac{\beta_1}{\epsilon} zL^{\epsilon/2} + \frac{\beta_2}{\epsilon^2} (zL^{\epsilon/2})^2 \right]. \quad (2.42)$$

Eqn. (2.41) also implies

$$K^R = K \left[1 - \frac{\alpha_1}{\epsilon} zL^{\epsilon/2} + \frac{\alpha_1^2 - \alpha_2}{\epsilon^2} (zL^{\epsilon/2})^2 \right] \quad (2.43)$$

since $K^R = K \cdot \mathcal{X}^{-1}(L)$. Operating the $L\partial/\partial L$ on (2.42) and (2.43) gives

$$L \frac{\partial}{\partial L} K^R = K \left[-\frac{\alpha_1}{2} zL^{\epsilon/2} + \frac{\alpha_1^2 - \alpha_2}{\epsilon} (zL^{\epsilon/2})^2 \right], \quad (2.44)$$

$$L \frac{\partial}{\partial L} v^R = v \left[\frac{\beta_1}{2} zL^{\epsilon/2} + \frac{\beta_2}{\epsilon} (zL^{\epsilon/2})^2 \right]. \quad (2.45)$$

The recursion relations for the dimensionless renormalized parameters $\tilde{z}^R = v^R [S_D(2-D)K^R/4\pi]^{d/2} L^{\epsilon/2}$ and $\tilde{K}^R = K^R L^{2\nu+D-2}$ are:

$$L \frac{\partial}{\partial L} \tilde{K}^R = \tilde{K}^R \left[(2\nu + D - 2) + \frac{1}{K^R} \left(L \frac{\partial}{\partial L} K^R \right) \right],$$

$$L \frac{\partial}{\partial L} \tilde{z}^R = \tilde{z}^R \left[\frac{\epsilon}{2} + \frac{1}{v^R} \left(L \frac{\partial}{\partial L} v^R \right) + \frac{d}{2} \frac{1}{K^R} \left(L \frac{\partial}{\partial L} K^R \right) \right].$$

Using (2.42) through (2.45), the above become

$$L \frac{\partial}{\partial L} \tilde{K}^R = \tilde{K}^R \left[(2\nu + D - 2) - \frac{\alpha_1}{2} \tilde{z} + \frac{\alpha_1^2 - 2\alpha_2}{2\epsilon} \tilde{z}^2 \right], \quad (2.46)$$

$$L \frac{\partial}{\partial L} \tilde{z}^R = \tilde{z}^R \left[\frac{\epsilon}{2} + \frac{\beta_1}{2} \tilde{z} - \frac{\beta_1^2 - 2\beta_2}{2\epsilon} \tilde{z}^2 - \frac{d}{2} \left(\frac{\alpha_1}{2} \tilde{z} - \frac{\alpha_1^2 - 2\alpha_2}{2\epsilon} \tilde{z}^2 \right) \right], \quad (2.47)$$

where we defined $\tilde{z} = zL^{\epsilon/2}$ to be the *bare* dimensionless interaction parameter.

At this point, one may naively expect that the exponent and fixed point can be solved by setting the left-hand sides of Eqs. (2.46) and (2.47) to zero, as was done before. However this procedure will not lead to any solution as we will soon see. The correct procedure is instead to express the right-hand sides of the recursion relations also in terms of the renormalized variable \tilde{z}^R . From (2.42) and (2.43), we have

$$\tilde{z}^R = \tilde{z} \left[1 + \frac{\beta_1 - \frac{d}{2}\alpha_1}{\epsilon} \tilde{z} + O(\tilde{z}^2) \right],$$

which can be inverted to give

$$\tilde{z} = \tilde{z}^R \left[1 + \frac{\frac{d}{2}\alpha_1 - \beta_1}{\epsilon} \tilde{z}^R + O((\tilde{z}^R)^2) \right].$$

We can now substitute $\tilde{z}(\tilde{z}^R)$ into the recursion relations (2.46) and (2.47). Let $\alpha_n = \alpha_n^{(1)} + \epsilon\alpha_n^{(2)}$ and $\beta_n = \beta_n^{(1)} + \epsilon\beta_n^{(2)}$ be the results of perturbative calculation to n^{th} order

in z and first sub-leading order in ϵ , then the recursion relations are

$$\begin{aligned}
L \frac{\partial}{\partial L} \tilde{K}^R = & \tilde{K}^R \left\{ (2\nu + D - 2) - \frac{\alpha_1^{(1)}}{2} \tilde{z}^R - \frac{\alpha_1^{(2)}}{2} \tilde{z}^R \epsilon \right. \\
& - \left[\left(\frac{d}{2} - 1 \right) \alpha_1^{(1)} \alpha_1^{(2)} - \frac{1}{2} \left(\alpha_1^{(1)} \beta_1^{(2)} + \alpha_1^{(2)} \beta_1^{(1)} \right) + \alpha_2^{(2)} \right] (\tilde{z}^R)^2 \\
& \left. - \left[\left(\frac{d}{2} - 1 \right) \frac{(\alpha_1^{(1)})^2}{2} - \frac{1}{2} \alpha_1^{(1)} \beta_1^{(1)} + \alpha_2^{(1)} \right] \frac{(\tilde{z}^R)^2}{\epsilon} \right\}, \quad (2.48)
\end{aligned}$$

and,

$$\begin{aligned}
L \frac{\partial}{\partial L} \tilde{z}^R = & \tilde{z}^R \left\{ \frac{\epsilon}{2} - \frac{1}{2} \left(\frac{d}{2} \alpha_1^{(1)} - \beta_1^{(1)} \right) \tilde{z}^R - \frac{1}{2} \left(\frac{d}{2} \alpha_1^{(1)} - \beta_1^{(1)} \right) \tilde{z}^R \epsilon \right. \\
& - \left[\frac{d}{2} \left(\frac{d}{2} - 1 \right) \alpha_1^{(1)} \alpha_1^{(2)} + 2\beta_1^{(1)} \beta_1^{(2)} - \frac{d}{2} \left(\alpha_1^{(1)} \beta_1^{(2)} + \alpha_1^{(2)} \beta_1^{(1)} \right) + \left(\frac{d}{2} \alpha_2^{(2)} - \beta_2^{(2)} \right) \right] (\tilde{z}^R)^2 \\
& \left. - \left[\frac{d}{2} \left(\frac{d}{2} - 1 \right) \frac{(\alpha_1^{(1)})^2}{2} + (\beta_1^{(1)})^2 - \frac{d}{2} \alpha_1^{(1)} \beta_1^{(1)} + \left(\frac{d}{2} \alpha_2^{(2)} - \beta_2^{(2)} \right) \right] \frac{(\tilde{z}^R)^2}{\epsilon} \right\}. \quad (2.49)
\end{aligned}$$

The infra-red fixed point of flow equations (2.48) and (2.49) can now be used to evaluate the fixed value $\tilde{z}^* = \tilde{z}^R(L \rightarrow \infty)$ and ν . The first-order result is $z^* = \epsilon / (\frac{d}{2} \alpha_1^{(1)} - \beta_1^{(1)})$ which is what was found before.⁶ Using the first-order result in (2.49), we find however that there is an additional contribution to z^* at order ϵ , coming from the term $(\tilde{z}^R)^2 / \epsilon$. Such a term will of course nullify the order ϵ result and render the entire ϵ -expansion scheme useless. It is only when a theory is summable to forms like (2.26) and (2.27) that the coefficients of the $(\tilde{z}^R)^2 / \epsilon$ terms vanish.⁷ Without the

⁶In terms of the original integrals (2.15) and (2.13), $\alpha_1^{(1)} = a_0$ and $\beta_1^{(1)} = -a_2$, so $z^* = \epsilon / a$, where $a = (d/2)a_0 + a_2$ as before.

⁷Expanding (2.26) we see that $\alpha_2^{(1)} = a_0(a_0 - a) = a_0^2(1 - d/2) - a_0 a_2$. So the coefficient of the

problematic $(\tilde{z}^R)^2/\epsilon$ terms, the recursion relations (2.48) and (2.49) can then be solved systematically in powers of ϵ . The exponent ν and the fixed value z^* are computed to second-order in ϵ once the sub-leading integrals are calculated. Note that such cancellations would not have occurred had we used the bare interaction parameter \tilde{z} in (2.46) and (2.47). This is the reason why the renormalized expression \tilde{z}^R must be used in the recursion relations.

Theories which sum to forms such as (2.26) and (2.27) can be described by RG flow equations and are called “renormalizable” theories. The renormalizability of the self-avoiding polymer theory as well as many other field theories have been proven to arbitrary order in ϵ . For the self-avoiding manifolds, there exist no general proof of the renormalizability other than this work. Sections 2.2.1 and 2.2.2 serve as a proof of the renormalizability of this theory to first order in ϵ . In analogy with field theory, this is sometime called one-loop renormalizability.⁸

In chapters 5 and 6, we will extend the renormalization-group method described here to non-equilibrium and anisotropic systems. A detailed account of using the RG procedure can be found in these chapters.

$(\tilde{z}^R)^2/\epsilon$ term in (2.48) vanishes. Similarly by expanding (2.27), we obtain $\beta_2^{(1)} = (\beta_1^{(1)})^2$ so that the corresponding coefficient of (2.49) also vanishes.

⁸For surfaces, a more appropriate name is “one-handle” renormalizability.

2.5 Conclusion

In this chapter, we presented calculations for self-avoiding membranes in the framework of the generalized Edwards model. The radius-of-gyration exponent ν and the dimensionless second virial coefficient g are calculated to first order in ϵ from a direct summation of the perturbation series. RG formalism is then introduced to shortcut the summation procedure. We demonstrated a systematic way of constructing recursion relations to higher orders in ϵ . We also presented a scheme to interpret the generalized ϵ -expansion encountered. This scheme resolves ambiguities and gives “optimal” numerical results to a given order in ϵ . The $\mathcal{O}(\epsilon)$ estimate of ν for polymers is an improvement over the traditional $\epsilon = 4 - d$ expansion. The estimates obtained for membranes are good in high dimensional embedding spaces; but become less good as the embedding spatial dimension is reduced. However, the actual conformation of membranes in 3D is not resolved in the ϵ -expansion scheme because $\epsilon = 8$.

The field of self-avoiding membranes is still very young with many studies left to be done. Among them, a direct calculation of the partition function (which would validate the dimensional regularization method used) seems to be within reach. For the theory to be of any practical use (e.g., in evaluating exponents), we need to extend the RG calculations to higher orders in ϵ .⁹ But before that, we first need to understand

⁹The need to understand higher order behavior goes beyond mere “utility”. The sub-leading integrals $\alpha_n^{(2)}$ and $\beta_n^{(2)}$ in the recursion relations (2.48) and (2.49) are boundary dependent. On the otherhand, we do not expect the exponent ν to be boundary dependent as it only describes the *internal* density correlations of the membranes. Hence we expect cancellation of all of the boundary dependent terms. In the polymer case, the boundary dependent terms can be calculated explicitly, and one then shows their cancellation. However explicit calculation of the boundary dependent sub-

the contribution of sub-leading divergences to the contact exponents (see reference [24]). Knowledge of the subleading divergences is also needed for understanding the leading order scaling behavior of a manifold at its θ -point. Finally, it would be interesting to investigate the possibility of applying the optimization scheme for the generalized ϵ -expansion to other problems that are presently treated by the traditional approach.

leading integrals is much more difficult to do for the membranes. One must understand the general structure of the sub-leading terms in order to calculate the exponent ν to higher orders.

Chapter 3

Experimental Studies of the Graphite Oxide Membranes

3.1 Introduction

In Chapter 2 we learned that the conformation of a 2-dimensional tethered membrane may be described by the radius of gyration exponent ν . In the crumpled state, the radius of gyration of a membrane R_g scales with its intrinsic linear size L (square root of membrane's weight) as $R_g \sim L^\nu$, with $\nu < 1$. The Flory estimate of the radius-of-gyration exponent is $\nu_F = 4/5$. Renormalization Group calculations have been carried out via a generalized ϵ -expansion to first order in ϵ , with the result $\nu_1 = 0.556 + O(\epsilon^2)$. However, $\epsilon = 8$ in this case makes the RG result not very meaningful. In fact the first-order estimate is not even in the physical region since the most compact folding of a 2-dimensional membrane in 3-dimensions leads to an exponent of $\nu = 2/3 > \nu_1$. As pointed out in section 2.3, there exists a line of lower critical dimensions d_l . Membranes embedded in spatial dimensions $d \leq d_l$ have $\nu = 1$ and are no longer crumpled. (They become stretched, or flat.)

Unfortunately, the value of d_l is not known analytically (other than an obvious lower bound of $d_l \geq 2$). If $d_l > 3$, then the membranes can only be flat. Instead if $d_l < 3$, then we can expect to have crumpled membranes with $2/3 < \nu < 1$. Even then, recent studies predict[32] that at sufficiently low temperature, where the bending energies are important, the membranes can undergo a phase transition from the crumpled phase to the flat phase.

Recently, there have been a number of large scale numerical studies of this problem[8][33]. The results of these studies seem to indicate that the membranes are anisotropic as

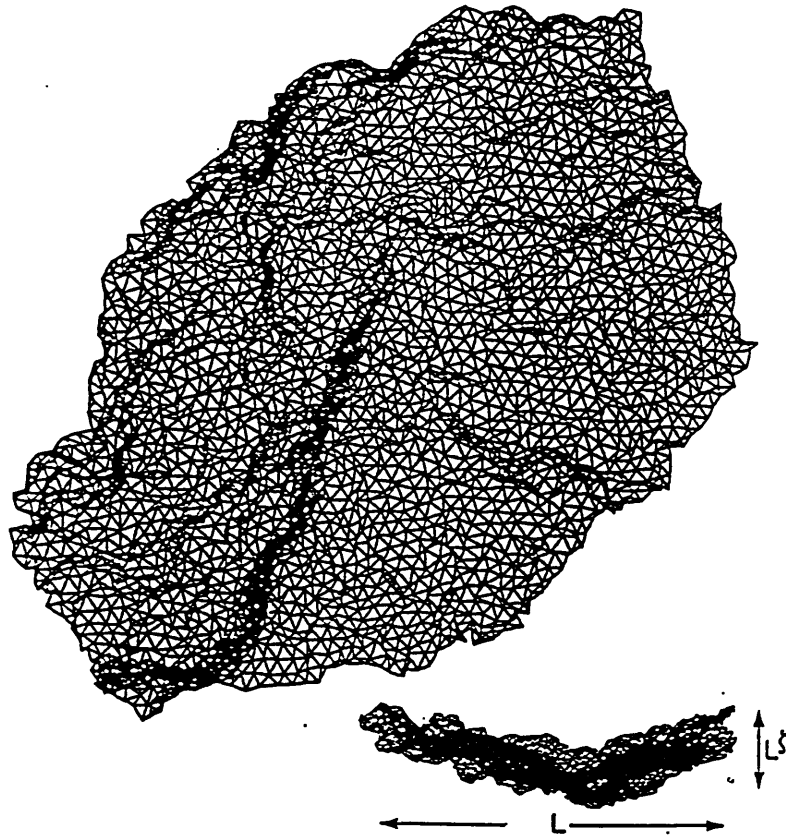


Figure 3.1: A “flat” membrane found by Molecular Dynamics simulation. (Reproduced from reference [33].)

shown in Figure 3.1. The effective width (w) of the membrane scales with the linear size L as $w \sim L^\zeta$ where the roughness exponent is determined to be $\zeta \approx 0.65$. However, this does not conclusively answer the question “can the membranes be crumpled in 3-d” because at least three different scenarios can produce the observed flat phase: (a) the membranes are always flat (i.e. $d_t > 3$), (b) the membranes are below the crumpling transition temperature, and (c) the membranes are crumpled, but the simulations performed are not at length scales large compared to the intrinsic persistence length and are therefore limited by finite size effects. A definitive answer is not possible at this stage unless crumpled membranes are directly observed. It is therefore the

purpose of this experiment to look for possible phases of *real* membranes in solution. In an experiment, the finite-size effect can be overcome by synthesizing very thin membranes, and the possible crumpling transition may be investigated by varying solvent composition and temperature. Light scattering methods can then be used to probe the conformations of the membranes as well as their dynamics. Our results indicate that the membranes indeed have a crumpled isotropic phase; the radius-of-gyration exponent found is $\nu = 0.83 \pm 0.03$ in agreement with the Flory exponent. We are currently investigating the dynamical aspects of fluctuating membranes in order to address the question of membrane equilibration.

3.2 Sample Preparation

3.2.1 Survey of Different Approaches

It is not difficult to obtain quasi-two-dimensional membranes. A normal piece of paper easily has an aspect ratio of 1:5000; and this ratio can be indefinitely enlarged by going to bigger and thinner paper. However, it is also true that a large object takes a long time to get to equilibrium. From an experimental point of view, we are limited to a relaxation time of at most a few tenths of seconds. This translates to a membrane size of not more than $10\mu m$. If we still want to keep an aspect ratio of approximately 1000, we find that a membrane thickness of $\leq 100\text{\AA}$ is needed. Fabricating $10\mu m \times 10\mu m \times 100\text{\AA}$ objects is no longer an easy task!

There are a variety of possible fabrication methods. One approach is based on making a thin layer of polymer solution which can later be cross-linked. In one of our earlier trials, we spin-coated thin layers of poly-acrylamide (PAM) solution and a UV sensitive cross-linker DAS on silicon wafers pre-coated with silicon dioxide (SiO_2). After drying, the wafer is exposed to UV light which initiates cross-linking of PAM by DAS. The exposed wafer is then immersed in a solution of hydrofluoric acid (HF) which diffuses through the cross-linked membrane, etches away the underlying SiO_2 layer, thereby setting free the membranes. By inserting metal masks during the UV exposure, we can produce membranes of controlled size and shape. These

membranes are good for visualization, but they are too thick¹ ($\sim 1000\text{\AA}$ when dried) for quantitative characterization. A similar approach based on suspension of PAM solution between liquid crystal films has been investigated by Nelson and Meyer[34].

A different approach is to take from nature something that is already close to a tethered membrane. One candidate being recently looked at is the anchoring protein of a red blood cell membrane known as spectrin[35]. Spectrin is constructed by tying together linear protein segments. The internal connectivity of spectrin looks just like the tethered membrane shown in Figure 2.1. It has a linear dimension of $\sim 10\mu m$, but it also has an intrinsic curvature as it is after all a closed shell. The intrinsic curvature at $10\mu m$ length scale makes it difficult to characterize a possible flat phase. However, it does have the advantage of approximate mono-dispersity; it also has a low mass-fraction which is believed to encourage crumpling. These factors make the spectrin molecule a worthwhile system to study, though the intrinsic curvature may place it in a different universality class.

Our present approach also takes advantage of existing quasi-2-dimensional structures: Graphitized carbon consists of two-dimensional covalently bonded carbon films loosely stacked together by van der Waals forces. By selectively severing the vertical inter-layer bonds using oxidation reaction, we can break graphite into individual layers. The product is called graphite oxide (GO). Upon suitable solvent conditions,

¹The thickness of the membrane is limited by wetting properties between the polymer solution and the SiO_2 substrate. It is conceivable that better polymer/substrate selection can decrease the film thickness somewhat, but it is not expected to be much below individual polymer size ($\sim 500\text{\AA}$) as sufficient polymer density is needed for cross-linking.

the GO layers may be separated. Free GO films can form a stable suspension in an alkaline solution. The conformation of GO in suspension can consequently be probed.

3.2.2 Synthesis of Graphite Oxide

Graphite Oxide (GO), also known as graphitic acid, has been known for over a century[36]. There exists a number of ways of synthesizing GO; all involve treating graphite with strong oxidizing agents such as potassium chlorate[37] or potassium permanganate[38]. Although the reaction is itself simple, great care must be taken in controlling the rate of reaction (and observing temperature limitations). Otherwise, explosion may result as the reaction is very close to the synthesis of “gun-powder”. The synthesis method used for this experiment is based on reference [38], though the optimal reaction condition is found by trial and error as is usual in any chemical reaction. Here we will describe the key features of the reaction.

100 mg of powder graphite is obtained from Union Carbide as a starting material. It is stirred into 5 ml of concentrated sulphuric acid (H_2SO_4) resulting in a very viscous solution. 50 mg of sodium nitrate ($NaNO_3$) is added to the graphite-acid mixture. The mixture is placed in a large test tube kept in an ice bath. A glass stirrer, inserted from the top of the test tube, provides uniform mixing of the solution. Also inserted into the test tube are a thermometer and a plastic tube for the injection of water needed later. The set-up is sketched in Figure 3.2. It is important to note that the steadiness of the stirrer and careful control of temperature are crucial for the

safety of the reaction.

To start the reaction, 300 mg of potassium permanganate ($KMnO_4$) is *slowly* added to the graphite-acid mixture which is being stirred constantly. The temperature of the solution is kept under $20^\circ C$ during the addition. Afterwards, the water bath is changed to $35^\circ C$, and the solution is maintained for 30 minutes under steady stirring. The reactant solution becomes very thick and brown/grey in color at the end of 30 minutes.

To dilute the reactant mixture, 5 ml of water is *very slowly* injected into the test tube through the plastic tube. This causes violent effervescence (and can lead to explosion if water addition is too fast). The temperature of the solution must be kept under $100^\circ C$, and stirring must be kept steady for safety. After 15 minutes, another 10 ml of warm water is added to dilute the solution further. Enough 3% hydrogen peroxide (H_2O_2) is then added to reduce the residual oxidizing agent and stop the oxidation reaction. The solution turns bright yellow in color at this point.

The suspension is filtered while warm to remove side-products of the reaction. After washing and filtering three times (with warm water), the product is treated with resinous anion and cation exchanger three times each (overnight each time) to remove salt impurities such as Na^+ , K^+ , Cl^- etc. Finally the purified product is collected by lyophyztion (freeze-drying in liquid-nitrogen bath).

The graphite oxide product obtained is brownish yellow in color. Its chemical properties have been investigated in reference [39]. GO consists of layers of carbon

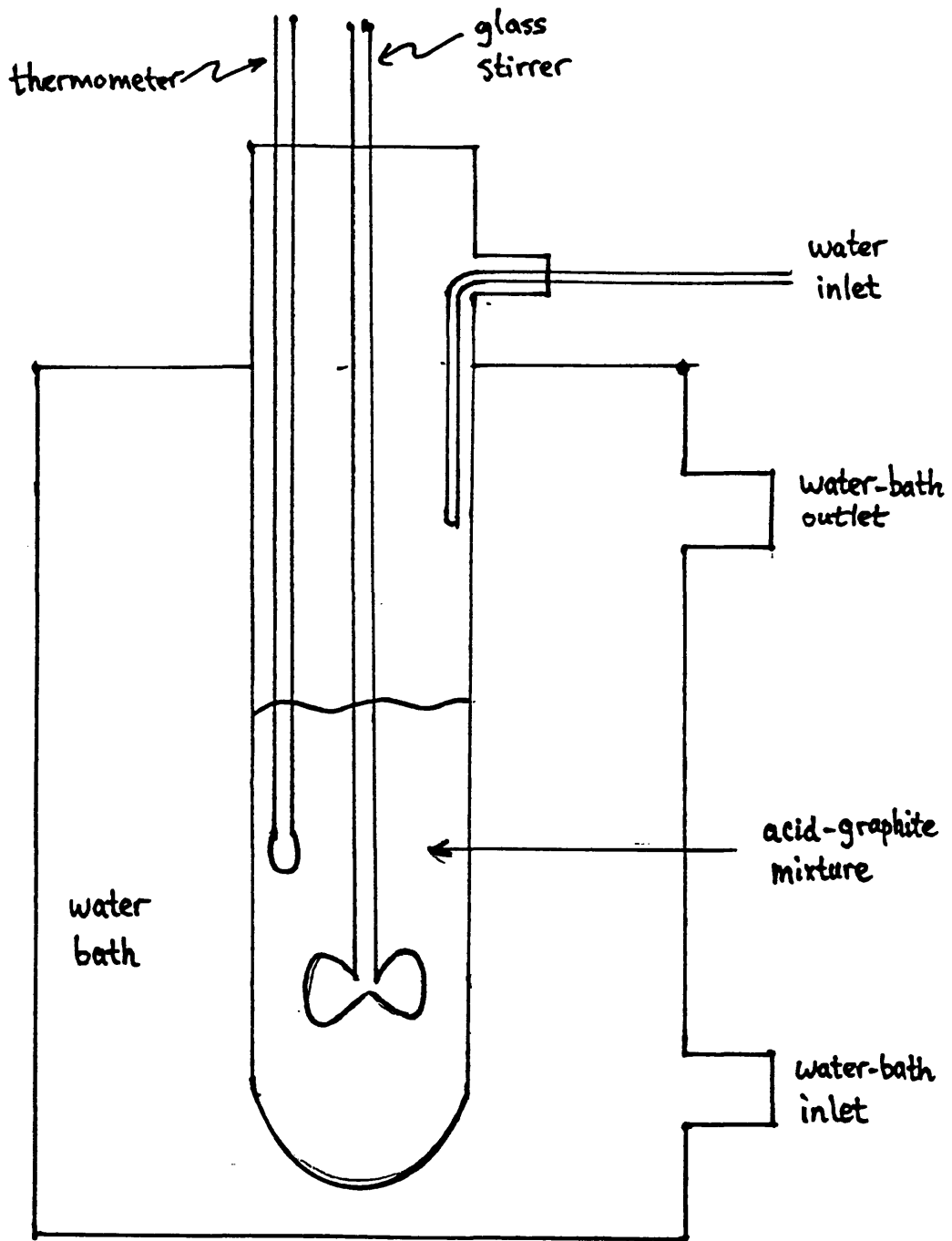


Figure 3.2: Set-up for the oxidation reaction of powder-graphite.

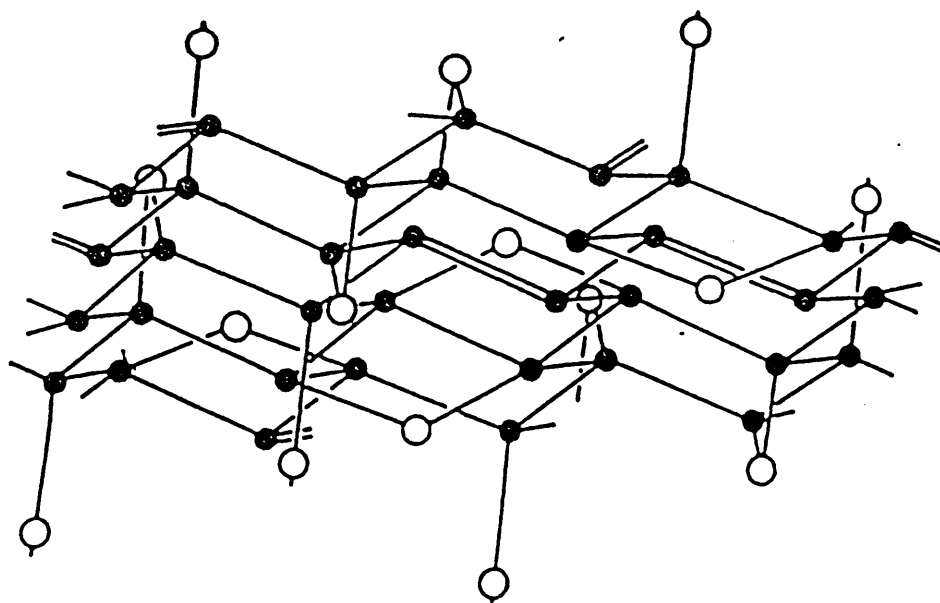


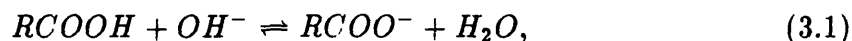
Figure 3.3: A proposed structure for graphite oxide. The filled/open circles represent carbon and oxygen atoms respectively. (Reproduced from reference [39].

network loosely attached via association with oxygen. On average, one oxygen atom is added for every two carbon atoms. Figure 3.3 is a proposed structure of GO reproduced from reference [39].

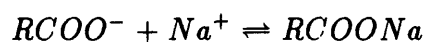
3.2.3 Suspension of Graphite Oxide

Graphite oxide does not suspend well in pure water; but the solubility is much improved in alkaline solution. We tested GO solubility in $NaOH$ solution with pH value ranging from 7 to 14 and found that maximum solubility is obtained at $pH = 11 \sim 12$. The dependence of solubility on ionic strength (pH) of the solution is a consequence of the carboxylic acid ($COOH$) group in GO. (The acid group of course comes from the oxidation of graphite.) Solvent with a high $[OH^-]$ (high pH) causes dissociation

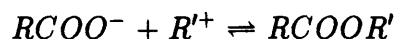
of the acid



and therefore increases the solubility of GO. However, addition of OH^- is accompanied by equal addition of the cation (Na^+ in this case). At very high pH values, the competing reaction



dominates. As a result, we obtain GO-salt precipitate, and the solubility is decreased. It so happens that a window of reasonable solubility exists ($pH = 11 \sim 12$) for GO using $NaOH$ solution. It is possible that with an organic base R'^+OH^- , the competing reaction



will be much less likely to take place. In such cases, the solubility of GO can be further enhanced.

For the experiment reported here, we use $NaOH$ solution. 1 mg of purified GO is dispersed in 10 ml (0.01N) $NaOH$ solution. The suspension is vigorously agitated (by manual shaking or by ultrasonicator). It is left standing for several days. Afterwards the suspension is centrifuged for 20 minutes, and the precipitate is discarded. The remaining suspension contains 0.1% to 1% (weight percent) of GO.² The suspension is homogeneous in appearance and brown in color. Inspection in op-

²The exact percentage of GO in suspension depends on the length of time left in the alkaline solution, the pH value of solution used, and the quality of GO, etc.

tical microscope reveals micron-sized particles executing Brownian walks as well as tumbling and spinning. For typical concentrations, interparticle distance is $\leq 10\times$ the particle size. Particle-particle adhesion has not been observed over observations lasting 30 minutes. Macroscopically, the suspension has been stable for roughly half a year, i.e., no precipitation has been observed for the GO suspension.

The physical structure of GO particles can first be examined by electron-microscopy. A drop of GO suspension is left on a sample holder made of thin (200\AA) carbon or silicon film. The suspension is dried in air and the remaining GO particles are examined using a transmission electron microscope (TEM). A typical picture is shown in Figure 3.4. We see slightly wrinkled, irregularly shaped thin films. The typical thickness of these films is estimated to be between 50\AA and 100\AA by comparing the transmitted electron intensity with the background intensity (200\AA carbon film). The connectivity of the GO thin films are probed by diffracting electrons. Figure 3.5 shows a resulting diffraction pattern. The inter-particle spacing is estimated to be close to that of the graphitized carbon ($\sim 2.5\text{\AA}$). Also, the 6-fold orientational order of the starting graphite is maintained in GO to some extent.

But of course, TEM can only give us information on the “dry” state of the films. We next describe the use of light scattering methods to probe the conformations of these films in suspension.

1 μm



Figure 3.4: A TEM picture of "dried" graphite oxide films.

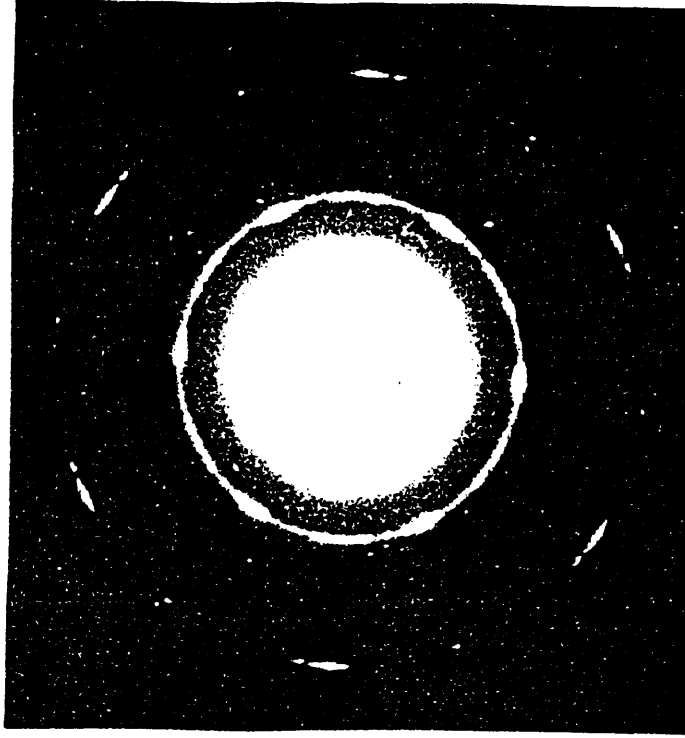


Figure 3.5: An Electron diffraction pattern of the GO thin films.

3.3 Light-Scattering of Graphite Oxide Membranes

3.3.1 Light-Scattering Theory

Homodyne light-scattering is the tool we used to study the conformation of the GO membranes. As the light-scattering method used here is quite standard, we will only briefly review some salient features of the theory; the details can be found in reference [40].

Figure 3.6 illustrates a typical situation: An incident beam of light with field $\vec{E}_i = E_i e^{i(\vec{k}_i \cdot \vec{r} - \Omega t)} \hat{z}$ impinges upon a scattering medium of dielectric constant $\epsilon(\vec{r}, t)$.

We start with the familiar solution to Maxwell's Equation

$$\vec{E}_s(\vec{R}, t) = \frac{e^{i\vec{k}_s \cdot \vec{R}}}{4\pi R \epsilon_0} \vec{k}_s \times \left[\vec{k}_s \times \int_V d^3\vec{r} \delta\epsilon(\vec{r}, t) \vec{E}_i(\vec{r}, t) e^{i\vec{k}_s \cdot \vec{r}} \right],$$

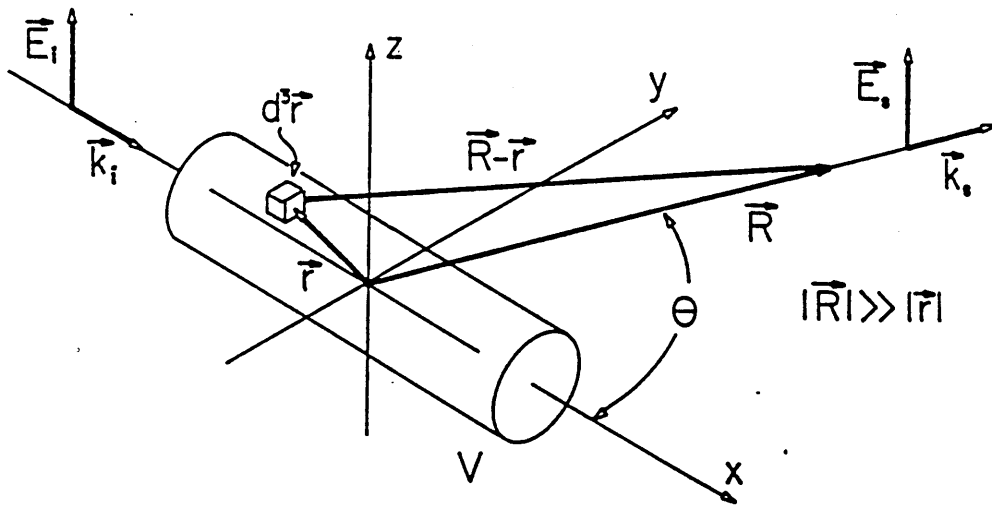


Figure 3.6: Scattered Field Geometry: The incident field consists of plane waves polarized in the $+\hat{z}$ direction. The scattered field is detected in the direction θ at a point \vec{R} that is much farther from the origin than the dimensions of the scattering volume V .

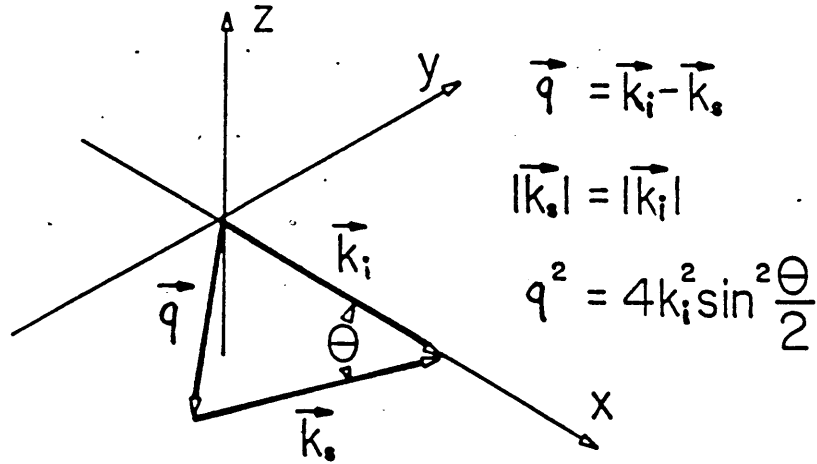


Figure 3.7: Scattered wave vector $\vec{q} = \vec{k}_s - \vec{k}_i$.

where V is the scattering volume, and we have assumed that the medium is isotropic (the dielectric constant is in general a tensor), and that fluctuations in the medium are small, i.e. $\epsilon(\vec{r}, t) = \epsilon_0 + \delta\epsilon(\vec{r}, t)$, with $\delta\epsilon \ll \epsilon_0$.

Introducing the scattered-wave vector $\vec{q} = \vec{k}_s - \vec{k}_i$, (see Figure 3.7), we can write the scattered field amplitude as

$$E_s(\vec{R}, t) = \frac{E_0 k_s^2 e^{i(k_i R - \Omega t)}}{4\pi R \epsilon_0} \int_V d^3\vec{r} \delta\epsilon(\vec{r}, t) e^{i\vec{q}\cdot\vec{r}}, \quad (3.2)$$

that is, the scattered field is the spatial Fourier transform of the fluctuations in the medium probed.

Experimentally what is observed is the scattered light intensity $I_s = E_s^* E_s$. Typ-

ically, $|\vec{R}|$ is kept fixed and the scattering angle $\theta(\hat{R})$ is varied, and

$$I_s = I_s(\vec{q}, t) = E_s^*(\vec{q}, t)E_s(\vec{q}, t). \quad (3.3)$$

In static light scattering, the time dependence is averaged out, i.e. $\bar{I}_s(\vec{q}) = \frac{1}{T} \int_0^T dt I_s(\vec{q}, t)$. Using (3.2) we have

$$\bar{I}_s(\vec{q}) = I_0 \int d^3\vec{r} d^3\vec{r}' \overline{\delta\epsilon(\vec{r})\delta\epsilon(\vec{r}')e^{i\vec{q}(\vec{r}-\vec{r}')}},$$

where $\overline{\delta\epsilon\delta\epsilon}$ is the time averaged spatial correlation of the fluctuations in the scattering medium. We make a reasonable assumption that the fluctuations are due to density fluctuations, i.e, $\delta\epsilon \propto \delta\rho(\vec{r}, t)$. We also assume ergodicity of the system studied. Thus $\bar{I}_s(\vec{q}) = I_0 S(\vec{q})$, with

$$S(\vec{q}) = \int d^3\vec{r} \langle \delta\rho(\vec{r})\delta\rho(\vec{0}) \rangle \quad (3.4)$$

being the static structure factor, and $\langle \dots \rangle$ indicating the ensemble average of density correlations which can be computed in equilibrium for a given Hamiltonian. Let us see what this quantity is for membranes described by the generalized Edwards Hamiltonian (2.6).

The density $\delta\rho(\vec{r})$ is obtained by counting the number of particles in a volume dV

about \vec{r} . In the continuum limit, this is simply

$$\delta\rho(\vec{r}) = \sum_n \int d^2\mathbf{x} \delta^3[\vec{r} - \vec{r}_n(\mathbf{x})], \quad (3.5)$$

where $\vec{r}_n(\mathbf{x})$ is the position vector of the n^{th} membrane with internal label \mathbf{x} . Using (3.5), the structure factor (3.4) becomes

$$S(\vec{q}) = \sum_n \int d^2\mathbf{x} \langle e^{i\vec{q}\cdot[\vec{r}_n(\mathbf{x}) - \vec{r}(\mathbf{0})]} \rangle. \quad (3.6)$$

The integrand is called the characteristic function and can be calculated from the Hamiltonian as in section 2.2. In the present case, the membrane suspension is sufficiently dilute that the inter-membrane contribution in (3.6) can be neglected. For a single membrane (of linear size L) that scales as $R_g \sim L^\nu$ we must have

$$\langle e^{i\vec{q}\cdot[\vec{r}_n(\mathbf{x}) - \vec{r}(\mathbf{0})]} \rangle = F(q|\mathbf{x}|^\nu),$$

where $F(y)$ is a dimensionless function. Inserting the above expression into (3.6), we get

$$S(\vec{q}) = q^{-2/\nu} G(qL^\nu), \quad (3.7)$$

with $G(\xi)$ being a cutoff function due to the finite size of each membrane.

The amplitude of the scattered wave vector \vec{q} gives the length scale being probed ($\sim q^{-1}$). For $q^{-1} \ll L^\nu$, we are probing at a length scale much smaller than the

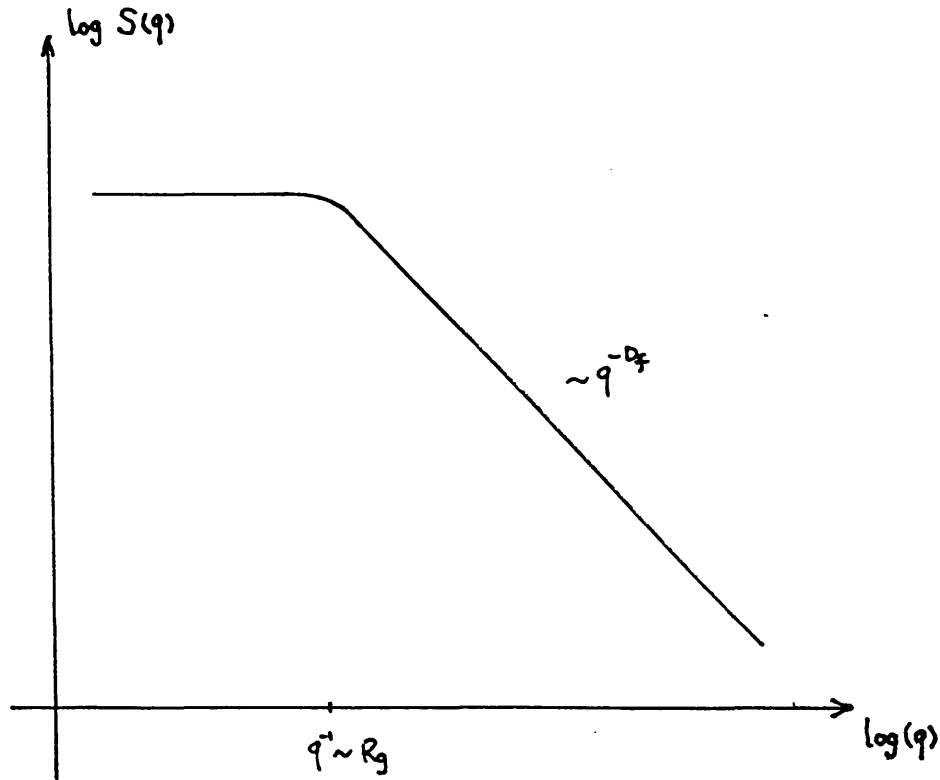


Figure 3.8: The generic behavior of the static structure factor $S(q)$.

membrane size. Since the *internal* density correlations are not expected to depend on the membrane size, we have $S(q) \sim q^{-2/\nu}$ in this region. In the region $q^{-1} \gg R_g = L^\nu$ however, we are probing at a length scale large compared to the membrane size. The membranes appear as point scatterers to the incident beam, and we expect the scattered field to be spherically symmetric, i.e., $S(q) = 1$. Hence, the scattered intensity $S(q)$ is expected to have the generic form sketched in Figure 3.8. In general, for a fractal object of fractal dimension D_f , the q -dependent part of the scattered intensity is $S(\vec{q}) \sim q^{-D_f}$. In this way, the static structure (or equilibrium conformation) can be probed by determining the large- q dependence of $S(\vec{q})$.

We can check the above argument against the structure factor of simple known

objects. For a sphere of radius R , we have

$$S(\vec{q}) = \frac{3}{(qR)^3} [\sin(qR) - qR \cos(qR)]. \quad (3.8)$$

It is easy to see from the above expression that $S(q^{-1} \rightarrow \infty) \rightarrow 1$ and $S(q^{-1} \rightarrow 0) \sim q^{-3}$. Hence we conclude that the “fractal dimension” for a solid sphere is 3 as expected.

The scaling behavior above assumes isotropic scatterers. In our study, the membranes encountered may be flat (and therefore anisotropic), as found in some simulations[8][33]. However the qualitative arguments leading to (3.7) also apply to the anisotropic phase, as the arguments are based solely on dimensional analysis. In a light scattering experiment, the measured scattered intensity is a spherical average of the anisotropic structure factor. For a simple geometry such as a rod of length L , the spherically averaged form factor can again be straight-forwardly calculated,³ with

$$S(q) = \frac{2}{qL} \int_0^{qL} dz \frac{\sin z}{z} - \left[\frac{2}{qL} \sin \left(\frac{2}{qL} \right) \right]^2,$$

giving $D_f = 1$ for $q^{-1} \ll L$.

The membrane of Figure 3.1 is complicated by the presence of a second length scale, $w \sim L^\zeta$. However it is not difficult to see that at a length scale $q^{-1} \gg L$, the membrane still looks like a point object and $S(q) \rightarrow 1$. At intermediate scales

³From here on $S(q)$ represents the spherically averaged structure factor.

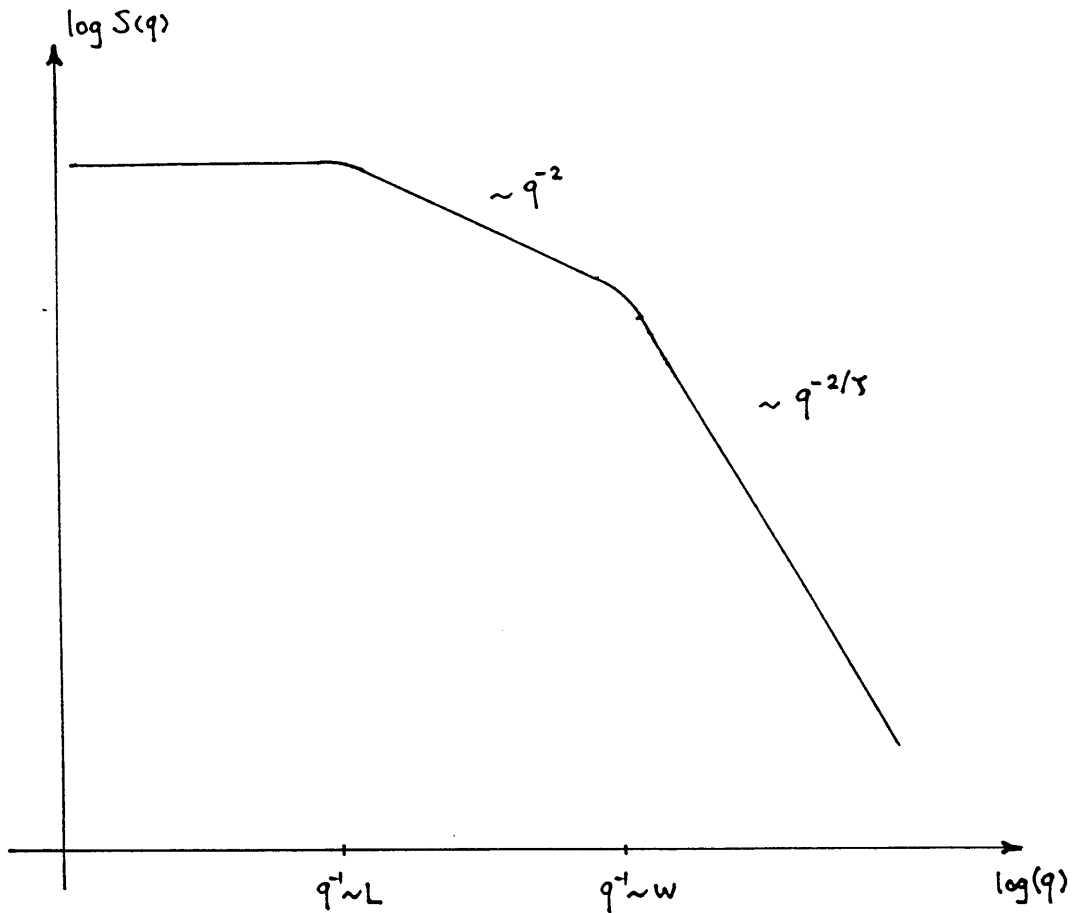


Figure 3.9: The expected q -dependence of the structure factor for the flat membrane shown in Figure 3.1. There is an additional length scale due to the effective width of the membrane.

$w \ll q^{-1} \ll L$, the object is essentially a 2-dimensional disc, so that $S(q) \sim q^{-2}$ in this region; and at $q^{-1} \ll w$, some effective fractal dimension will be seen. A detailed calculation[33] shows that $S(q^{-1} \rightarrow 0) \sim q^{-2/\zeta}$; for $\zeta \approx 0.65$ found in simulations, the exponent is ~ 3.1 . The expected q -dependence of the structure factor for a flat membrane is depicted in Figure 3.9. Note that Figures 3.8 and 3.9 are sufficiently different that an accurate measurement of $S(q)$ can resolve the crumpled phase from the flat phases of the membranes, as well as determining the scaling exponents.

The dynamical relaxation of the membranes can also be probed by examining the temporal fluctuations of $I_s(q, t)$. The auto-correlation function of the scattered

intensity is by (3.3)

$$\begin{aligned}\bar{G}(\vec{q}, \tau) &\equiv \frac{1}{T} \int_0^T dt I_s(\vec{q}, t) I_s(\vec{q}, t + \tau) \\ &= \langle |E_s(\vec{q}, 0)|^2 |E_s(\vec{q}, \tau)|^2 \rangle,\end{aligned}$$

where we have again used the assumption of ergodicity.

Here the scattered field E_s is the superposition of contributions from individual scatterers $E_s^{(n)}$, i.e. $E_s = \sum_{n=1}^N E_s^{(n)}$, with $N \gg 1$ being the total number of scatterers in the scattering volume. Again for a dilute solution of scatterers, the fluctuations of different scatterers are *uncorrelated*. Hence the scattered field E_s is a sum of uncorrelated random variables; it is described by a Gaussian distribution in the limit of large N (central-limit theorem). Ignoring the fluctuations in N , the scattered intensity auto-correlation is easily simplified using properties of the Gaussian distribution:

$$\bar{G}(\vec{q}, \tau) = \langle E_s^*(\vec{q}, 0) E_s(\vec{q}, 0) \rangle^2 + \langle E_s^*(\vec{q}, 0) E_s(\vec{q}, \tau) \rangle^2,$$

or in terms of density fluctuations,

$$\bar{G}(\vec{q}, \tau) = \bar{I}_s^2(\vec{q}) + I_0^2 \left[\int d^3\vec{r} \langle \delta\rho(\vec{r}, \tau) \delta\rho(\vec{0}, 0) \rangle e^{i\vec{q}\cdot\vec{r}} \right]^2.$$

It is convenient to separate the motion of a complex object into its center-of-mass motion and internal motion. Using (3.5) for $\delta\rho$, with $\vec{r}(\mathbf{x}, t) = \vec{R}_{\text{cm}}(t) + \delta\vec{r}(\mathbf{x}, t)$, the

auto-correlation function becomes:

$$\bar{G}(\vec{q}, \tau) = \bar{I}_s^2(\vec{q}) + I_0^2 \left[\left\langle e^{i\vec{q} \cdot (\vec{R}_{\text{cm}}(t) - \vec{R}_{\text{cm}}(0))} \right\rangle \int \frac{d\omega}{2\pi} e^{-i\omega\tau} S(\vec{q}, \omega) \right]^2,$$

where

$$S(\vec{q}, \omega) = \int d^2\mathbf{x} d\tau e^{-i\omega\tau} \left\langle e^{i\vec{q} \cdot [\delta\vec{r}(\mathbf{x}, t) - \delta\vec{r}(\mathbf{0}, 0)]} \right\rangle$$

is the dynamic structure factor for an individual scatterer. The center-of-mass simply executes a Brownian motion, i.e.

$$\left\langle e^{i\vec{q} \cdot (\vec{R}_{\text{cm}}(t) - \vec{R}_{\text{cm}}(0))} \right\rangle = e^{-Dq^2\tau}.$$

The diffusion constant D is related to the frictional coefficient f (arising from the center-of-mass motion with respect to the solvent) by the Einstein relation $D = kT/f$. For a macroscopically spherical object, Stoke's law gives $f = 6\pi\eta R_H$ where η is the solvent viscosity and R_H is the hydrodynamic radius of the object. This gives an independent way of probing the sizes of the scatterers.

Finally we mention that in a real experimental situation, the size L of the membranes being probed is not uniform. They are instead polydispersed, according to a distribution $\mathcal{D}(L)$ which depends on the way the membrane suspension is prepared. Polydispersity will change the behavior of the observed correlation function $\bar{G}(\vec{q}, \tau)$. Fortunately, the observed correlation function is simply a weighted sum of correlation

functions of mono-dispersed samples,⁴ i.e.

$$\bar{G}(\vec{q}, \tau) = \int_0^\infty dL \mathcal{D}(L) \bar{G}_L(\vec{q}, \tau), \quad (3.9)$$

where

$$\bar{G}_L(\vec{q}, \tau) = \bar{I}_s^2(\vec{q}, L) + I_0^2 e^{-2D(L)q^2\tau} \left[\int \frac{d\omega}{2\pi} e^{-i\omega\tau} S_L(\vec{q}, \omega) \right]^2. \quad (3.10)$$

In the next section, we will see that by appropriately manipulating the distribution $\mathcal{D}(L)$, we can recover the desired structure factor $\bar{G}_L(\vec{q}, \tau)$.

3.3.2 Light-Scattering Set-Ups

The light-scattering set-up used for this experiment is quite standard. Here we provide a brief account of the key components; a detailed description of the apparatus can be found in reference [41].

The GO suspension is filtered and collected in a cylindrical optical-grade quartz cell, which is firmly placed in a cell holder. An incident beam of laser light is brought to a focus within the sample by a lens. Scattered light is selected by two apertures which limit the scattering angle and volume, and is detected by a photo-multiplier tube (PMT). The apertures and PMT are mounted on a rotating arm whose position specifies the angle θ of collected scattered-light. A sketch of the experimental layout and the relevant dimensions for the collection optics are shown in Figure 3.10 and

⁴This is a consequence of uncorrelated scatterers which is only true in a dilute suspension.

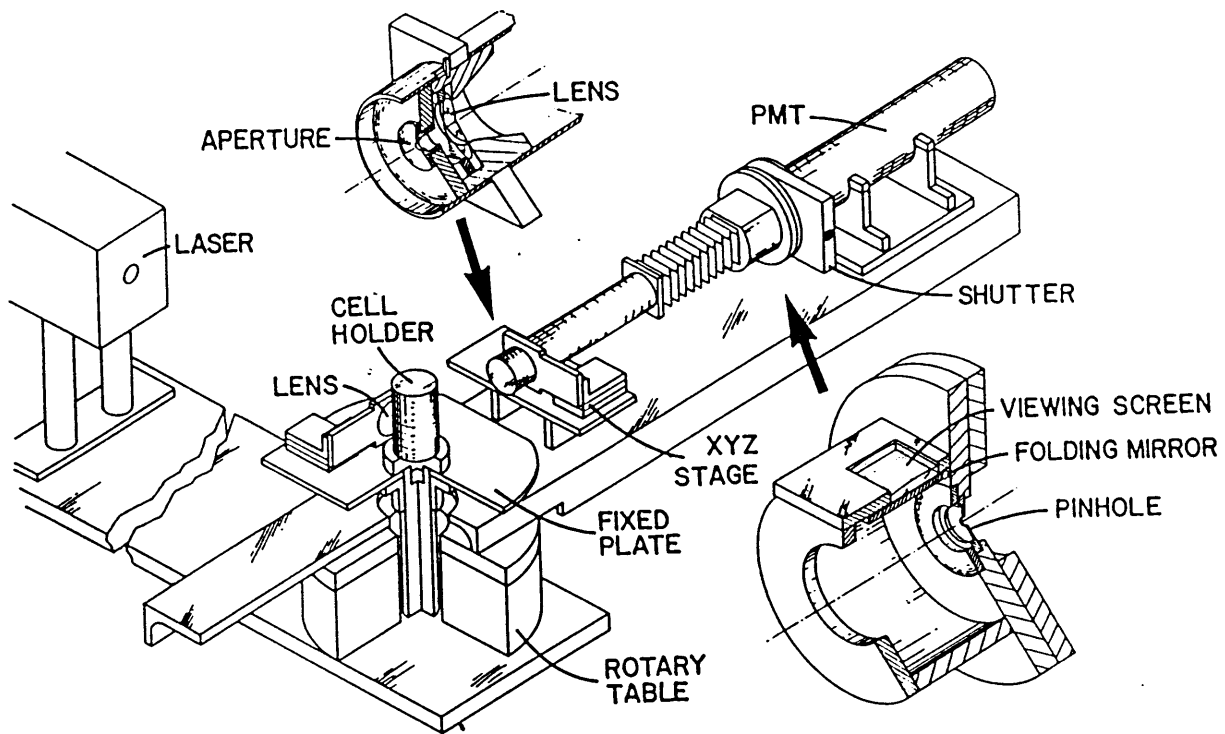


Figure 3.10: Light-scattering set-up. (Reproduced from reference [41].)

3.11.

The scattering volume (V) is a disc of diameter ϕ (diameter of focused laser beam, $\phi \approx 0.1\text{mm}$) and of length b . This length is selected by the diameter d of the pinhole P2 and the scattering angle θ . For the set-up shown in Figure 3.11, $b = (s_i/s_o)d/\sin\theta$. Using the dimensions in Figure 3.11, we get a scattering volume of $V = \phi\pi(b/2)^2 \sim (100\mu\text{m})^3/\sin\theta$. Given the mean membrane separation of a few microns for a typical concentration, this scattering volume contains a minimum of $\sim 10^4$ particles (at $\theta = 90^\circ$). Typical resolution of the scattering angle θ is controlled by the diameter D of pinhole P1. With maximum $D = 1.5\text{mm}$, the uncertainty in scattering angle is about 0.5° .

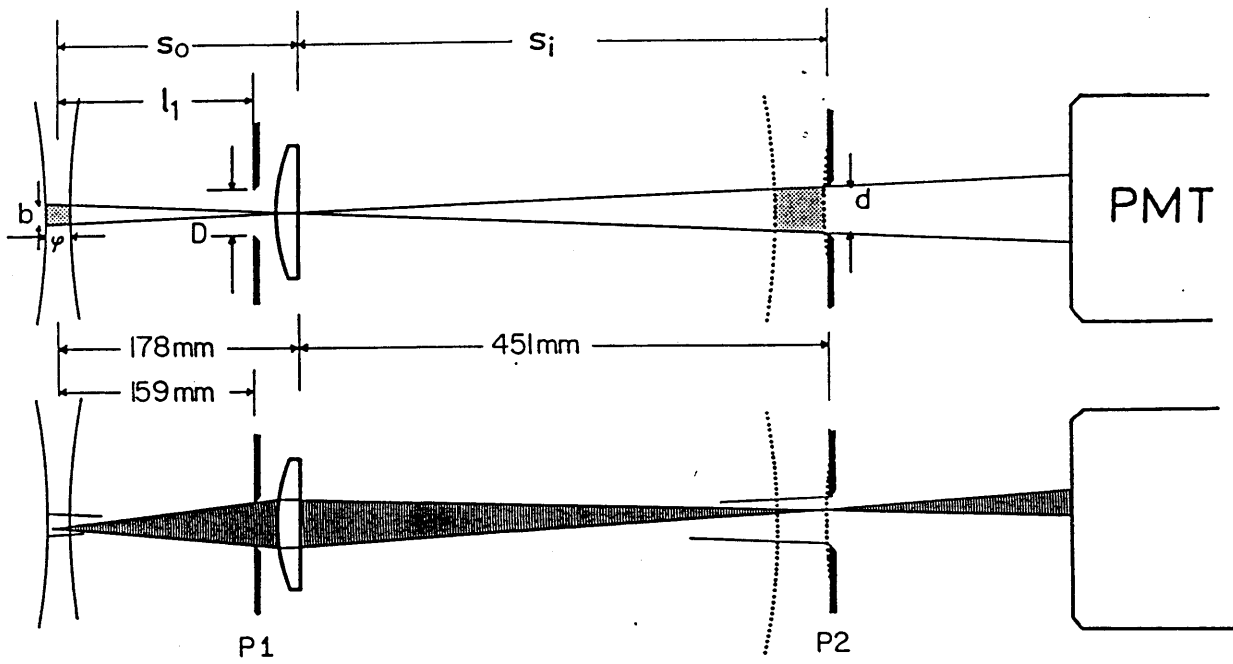


Figure 3.11: Schematics of collection optics. (Reproduced from reference [41].)

| θ (deg) | q^{-1} (Å) | θ (deg) | q^{-1} (Å) |
|----------------|--------------|----------------|--------------|
| 5 | 7057 | 40 | 900 |
| 10 | 3532 | 50 | 728 |
| 15 | 2358 | 60 | 616 |
| 20 | 1773 | 70 | 537 |
| 25 | 1422 | 80 | 479 |
| 30 | 1189 | 90 | 435 |

Table 3.1: A list of length scales probed (q^{-1}) for various scattering angles θ .

A Spectra-Physics model 164 Argon-ion laser is used to generate the incident beam. Typical power used is 100 – 150mW. (Too high a power would heat the sample and initiate convection within the cell). The green line at $\lambda = 5145\text{Å}$ was chosen for the experiment. The length scales probed at different scattering angle θ is given by the inverse of the scattered wave vector $q = (4\pi n/\lambda) \sin(\theta/2)$, where $n = 1.33$ is the refractive index of the scattering medium (water). Table 3.1 gives a list of the magnitudes of inverse scattering vector q^{-1} for a series of scattering angles at this wavelength. We see that the length scales being probed are roughly from 500Å to 5000Å.

The scattered light collected is converted to electric pulses by a photomultiplier tube. The photomultiplier housing contains an integrated pre-amplifier and discriminator. The discriminator output is buffered to provide replicas of the signal for the digital correlator and a count-rate meter. The meter is then read by a computer once every second. Typically, count rate ranges from $\sim 100\text{Hz}$ near 90° to $\sim 100\text{kHz}$ at low scattering angles. For static light-scattering, scattered light intensity is collected for a duration of several minutes at each scattering angle. A typical run from $\theta = 10^\circ$

to $\theta = 90^\circ$ at 5° intervals takes ~ 30 minutes.

For dynamic light scattering, the measured scattered light intensity is fed into a digital correlator (Brookhaven Instrument BI2030, with 136 channels). The correlator has built in routines to analyze the correlation functions. The decay time (τ) of the auto-correlation function $R(t)$ is extracted from the second cumulant of the correlation function.

We are currently making an improved set-up to expedite the data collection process and to automatize the analysis of q -dependence of the entire auto-correlation function $G_q(\tau)$.

3.3.3 Experiments and Results

To calibrate the experimental set-ups, we first do light-scattering of simple objects of known geometry. Poly-styrene (PS) latex spheres (obtained from Duke Scientific) are chosen for this purpose. Samples of 0.1% solution PS spheres of 270\AA radius are prepared. They are carefully filtered through filters of $1\mu\text{m}$ pore-size to remove dust within the solution and then injected into the cylindrical optical cells. Scattered light intensities are accumulated for scattering angles ranging from $\theta = 10^\circ$ to $\theta = 90^\circ$. (3 minute accumulation for measurement at each angle). The measured intensities are normalized by the θ -dependent scattering volume (recall $V \sim 1/\sin\theta$), and the resulting structure factor is plotted against $q = (4\pi n/\lambda)\sin(\theta/2)$ in Figure 3.12. As the size of the PS sphere is very small, the structure factor is expected to be flat over the range of q probed. Using (3.8), we expect the drop in $S(q)$ to be at most $\sim 30\%$ (at 90°). The flat behavior is verified as shown in Figure 3.12, though larger fluctuations in the scattered-intensities are encountered at lower angles. In fact, doing light-scattering measurement at such low angles is quite tricky; the presence of dust (i.e. large particles) tend to increase the observed scattered-intensities at low angles. Extreme care in filtering the sample solutions and washing the sample cells is needed to get good data down to a scattering angle of 10° .

We next repeat the above light-scattering experiment for the graphite oxide suspension. When we plot the result on a log-log scale (Figure 3.13), we see that the structure factor is not quite a straight line (i.e. a power law) as expected for fractal

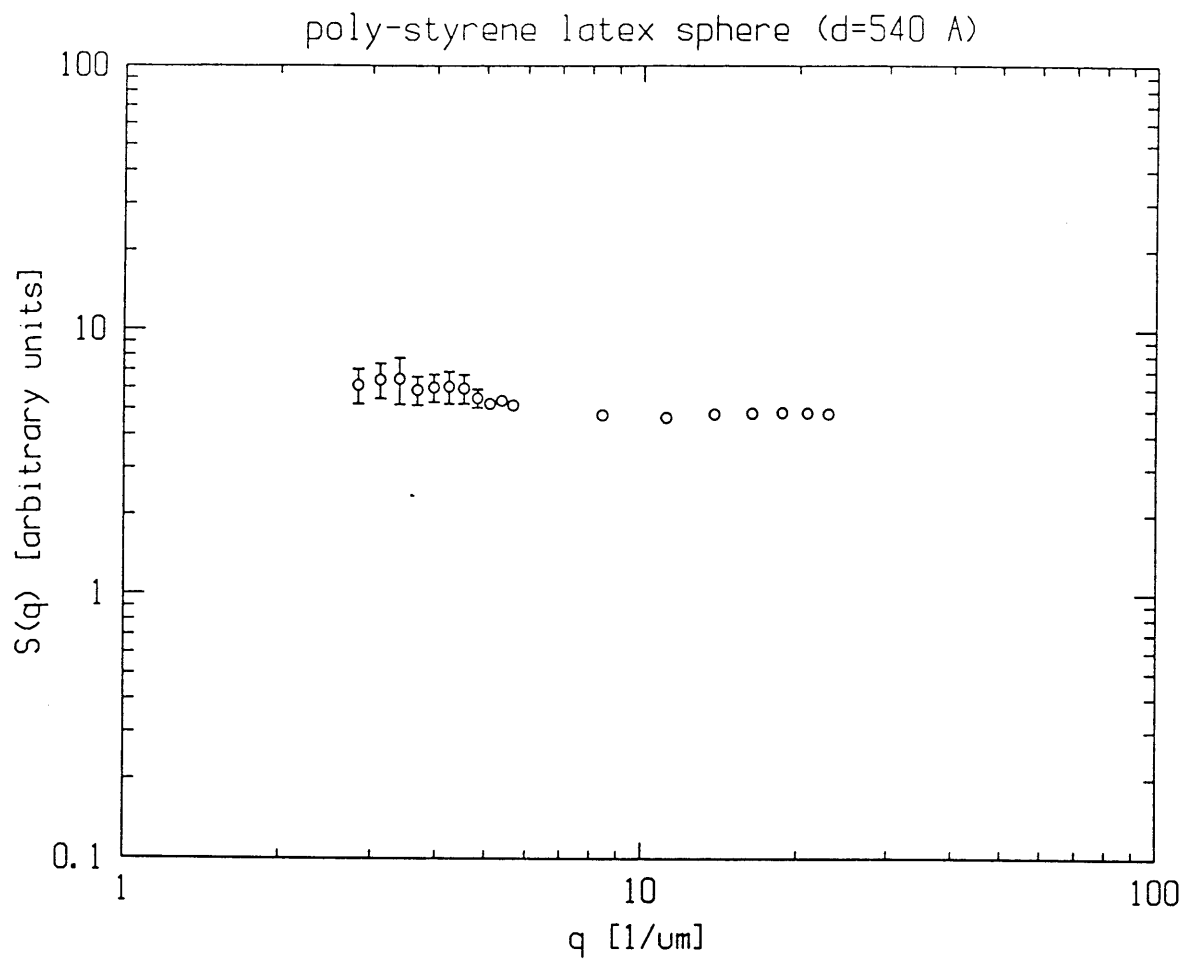


Figure 3.12: Measured structure factor $S(q)$ for poly-styrene latex spheres of $R = 270\text{\AA}$. (1° interval for $\theta = 10^\circ$ to 20° ; and 10° interval for $\theta = 20^\circ$ to 90° . The structure factor is largely flat for the range of q probed as is expected from Eqn. (3.8).

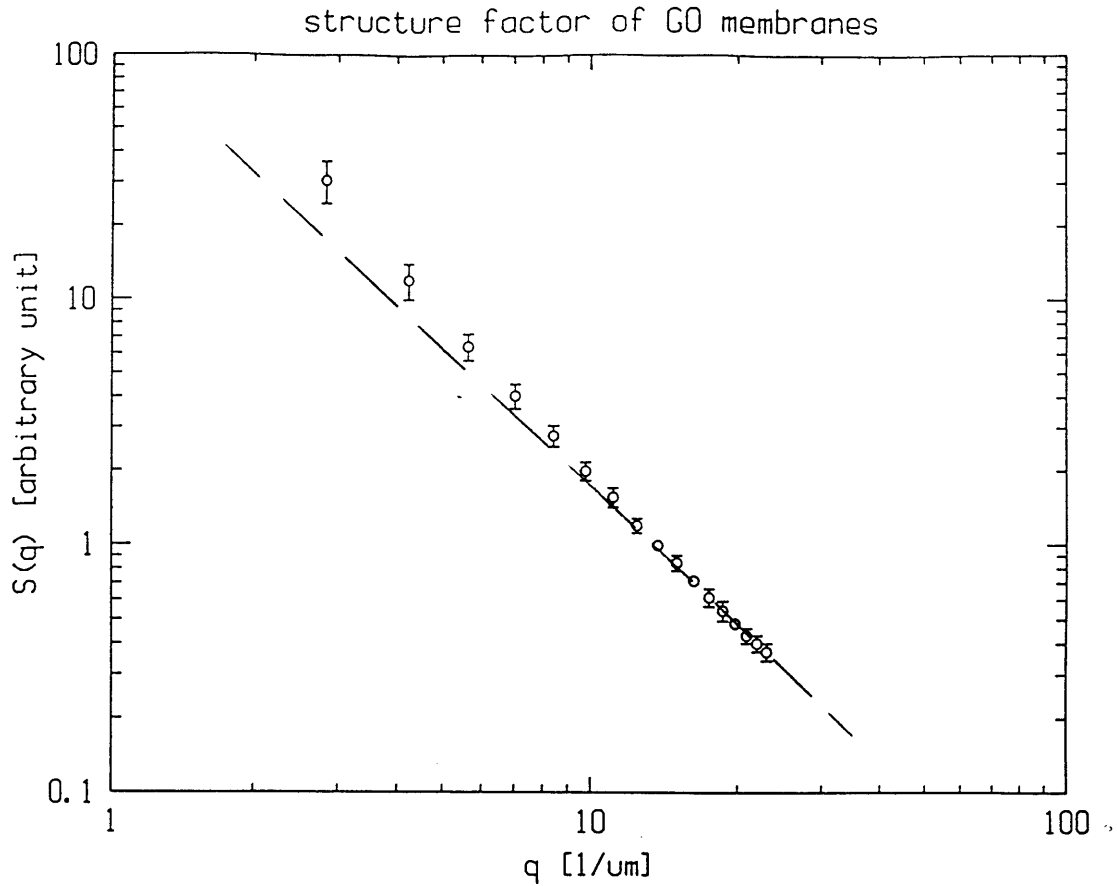


Figure 3.13: Structure factor for a poly-dispersed GO suspension.

objects. This result is attributed to the poly-dispersity of the GO in suspension: Since the membranes in the suspension have a range of sizes, the actual observed structure factor is averaged over the distribution of membrane sizes as in Eq. (3.9); it may have an arbitrary q -dependence depending on the distribution function $\mathcal{D}(L)$.

To make this effect more clear, we consider a simple system consisting of two particle sizes R_1 and R_2 with scattering strength⁵ c_1 and c_2 respectively. If the structure factor for each species is $S_i(q) = 1/[1 + (qR_i)^D]$, then the effective (observed) structure factor is $S(q) = c_1/[1 + (qR_1)^D] + c_2/[1 + (qR_2)^D]$. Figure 3.14 gives the q -dependence of $S_1(q)$, $S_2(q)$ and the weighted sum $S(q)$ for $D = 3$, $R_1 = 10 \times R_2$,

⁵The scattering strength is a function of the concentration of the particles as well as their sizes.

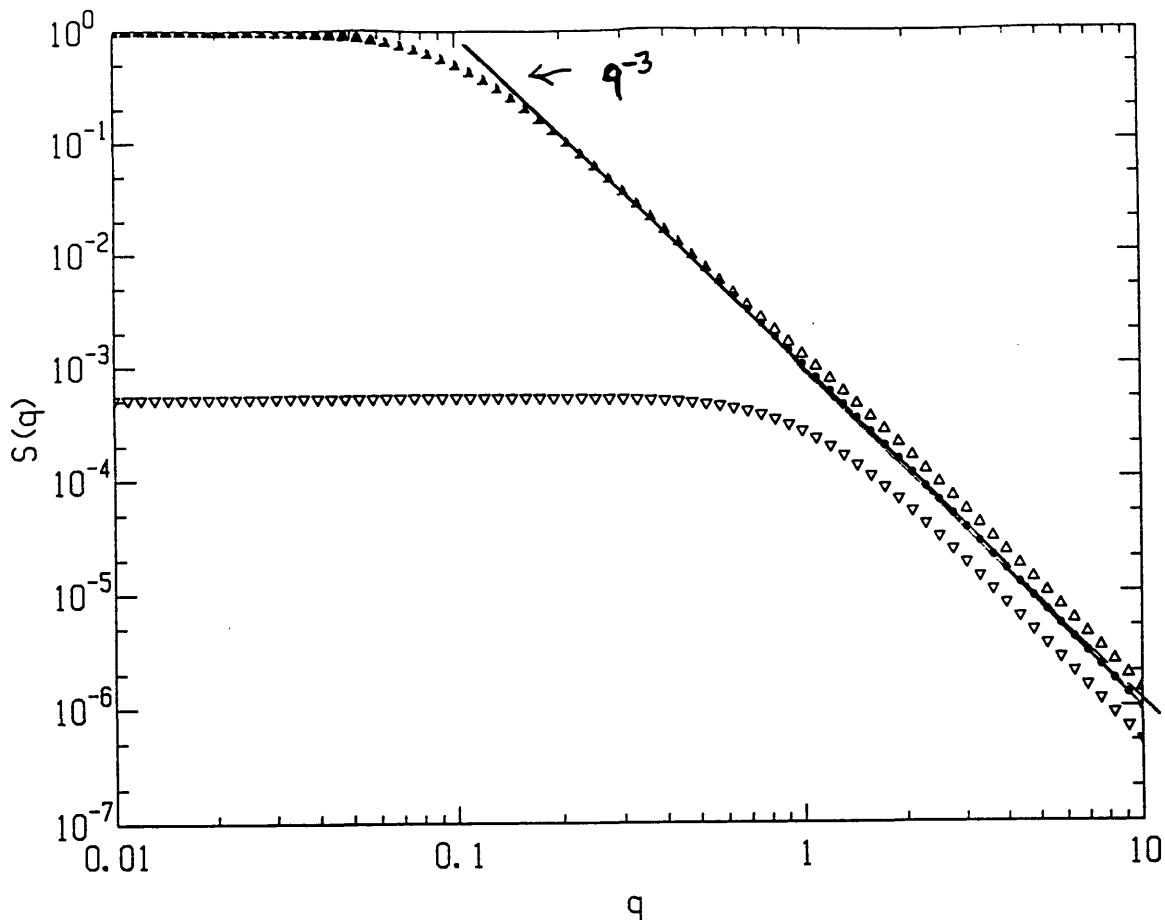


Figure 3.14: The structure factors for a simple system composed of two different sphere sizes: \bullet represent the structure factor of the large particles ($S_1(q)$, with $R_1 = 10$), and ∇ represents that of the small particles ($S_2(q)$, with $R_2 = 1$). The effective structure factor of the two-component system is indicated by Δ .

and $c_1 = 20000 \times c_2$. It is clear that the small particles (∇) do not contribute at low angles (small q) but they shift the structure factor at high q , producing an effective $S(q)$ (Δ) that is not describable by a simple power law.

Of course, this problem is simply solved if we can pre-select the membrane sizes. Size selection of GO membranes can in principle be done by processes such as gel-electrophoresis, but the selection of solvent is very tricky in this case due to possible aggregation of the membranes. The next point to note is that, for the purpose of *static* light-scattering, we actually do not need a completely mono-dispersed sample.

As long as we are probing at a length scale smaller than the smallest membrane size, we are only probing the *internal* density correlations of the membrane; and the result in this limit will be insensitive to the membrane size. Since the length scale of our probe is at most $\sim 5000\text{\AA}$ (see Table 3.1) it appears that we can recover the “true” structure factor if we only remove all particles under 5000\AA in size from the suspension.

Removing small particles from a sample is a much easier job than selecting a monodispersed sample, but it is still a nontrivial task. The problematic gel-electrophoresis method is still needed if one is to do this properly. A different approach is to remove directly the contribution to scattered light intensity by small particles. We can first measure the structure factor $S(q)$ for a sample containing all membrane sizes, then remove the *large* membranes from the sample (this is easily done by filtration) and obtain $S_2(q)$ for the remaining small membranes. Taking the difference between $S(q)$ and $S_2(q)$ yields the desired structure factor for the large membranes. This process is illustrated in Figure 3.15.

We have used the above method in our experiment. Two samples are prepared from the same GO suspension. One sample is filtered by a syringe filter with $0.5\ \mu\text{m}$ pore size to obtain small particle’s contribution to $S(q)$. The other sample is filtered by a $5\ \mu\text{m}$ syringe filter to remove dirt in the sample. The structure factors obtained from the two samples are shown in Figure 3.16 by \triangle and ∇ . The solid \bullet depicts the difference of these two sets of data. It represents the contribution to the scattered light

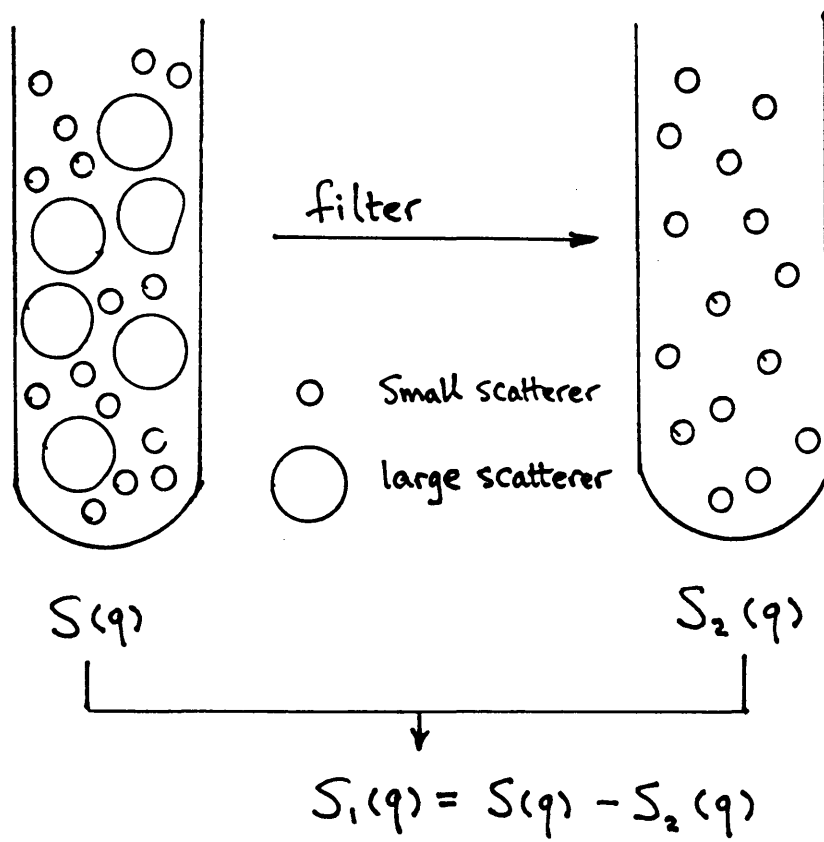


Figure 3.15: Obtaining the structure factor $S_1(q)$ of large membranes by the subtraction method discussed in the text.

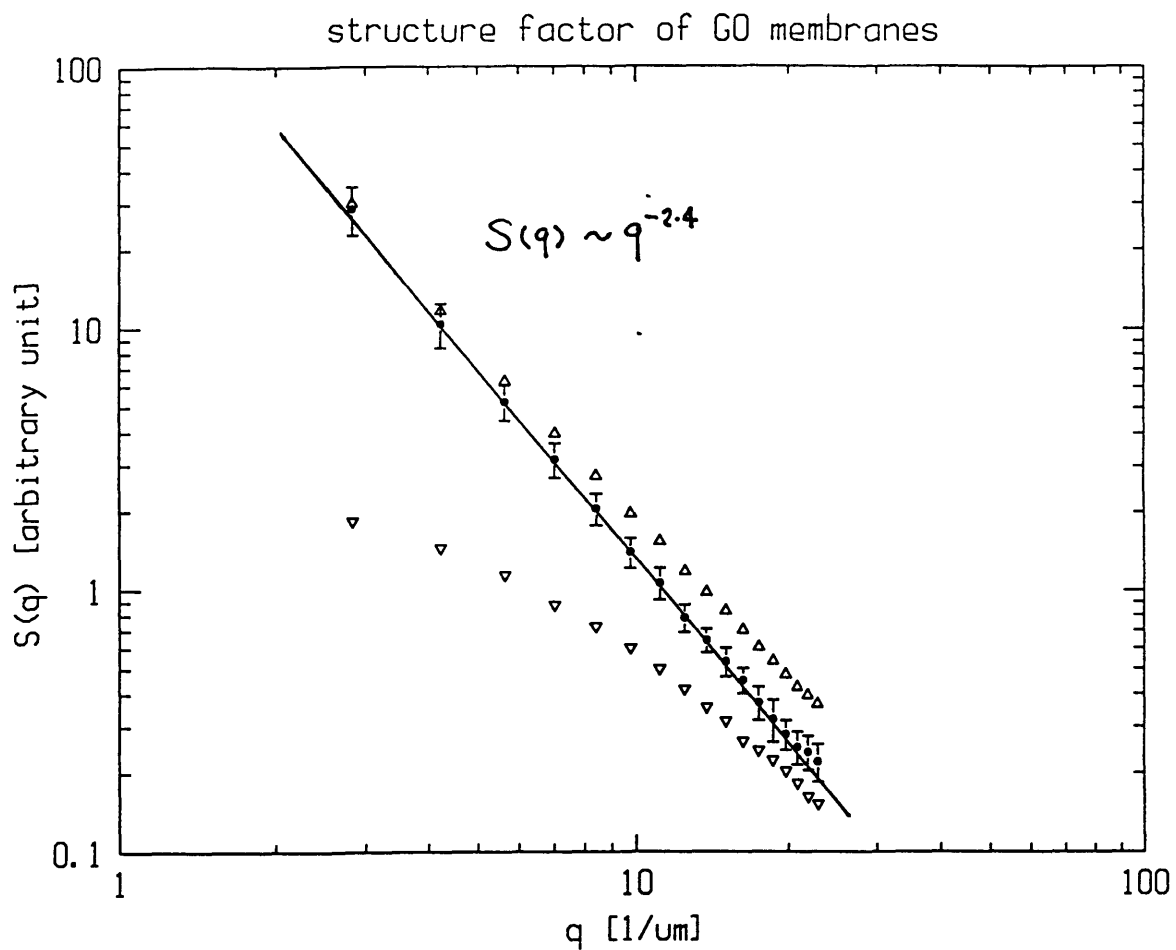


Figure 3.16: The structure factor of GO membranes in alkaline solution. Δ is the result from the entire poly-dispersed suspension. ∇ denotes the contribution from small ($< 0.5\mu m$) particles. And the difference (indicated by \bullet) is the contribution from particles larger than $0.5\mu m$.

intensity from the membranes ranging from $0.5\mu m$ to $5\mu m$ in sizes.⁶ Since the length of the probe is under $0.5\mu m$, the structure factor obtained for these large membranes reflects the *internal* density correlations of the membranes. The data is nicely fitted to a straight line on a log-log scale for the probe interval of $500\text{\AA} \sim 5000\text{\AA}$, indicating that membranes are self-similar over this range of length scales. The fractal dimension of the membranes may be obtained from the slope of the straight line (see Eq. (3.7)), yielding $D_f = 2.4 \pm 0.1$.

Since $D_f < 3$, we know that the membranes are not compact. Also, the data (solid \bullet in Figure 3.16) is clearly incompatible with the structure factor for a flat membrane, shown in Figure 3.9. Though the break-point of the $S(q)$ curve in Figure 3.9 would be smeared for a poly-dispersed sample, the structure factor should still show a tendency to level down at low q if the membranes were flat. Such tendency has never been observed for membranes in good suspension. Hence we conclude that the conformation of the probed membrane is not flat, nor compact, but loosely crumpled. From the measured fractal dimensions, we estimate the radius of gyration exponent to be $\nu = 2/D_f \approx 0.83 \pm 0.03$, which is rather close to the Flory estimate of $4/5$ (see section 2.1).

We have also measured the structure factors for GO membranes dispersed in water. As mentioned previously, the concentration of GO suspended in H_2O is much lower than that in an alkaline solution. Nevertheless, if we repeat the light-scattering

⁶This is the actual sizes, i.e. the radius of gyration R_g , not the intrinsic size L .

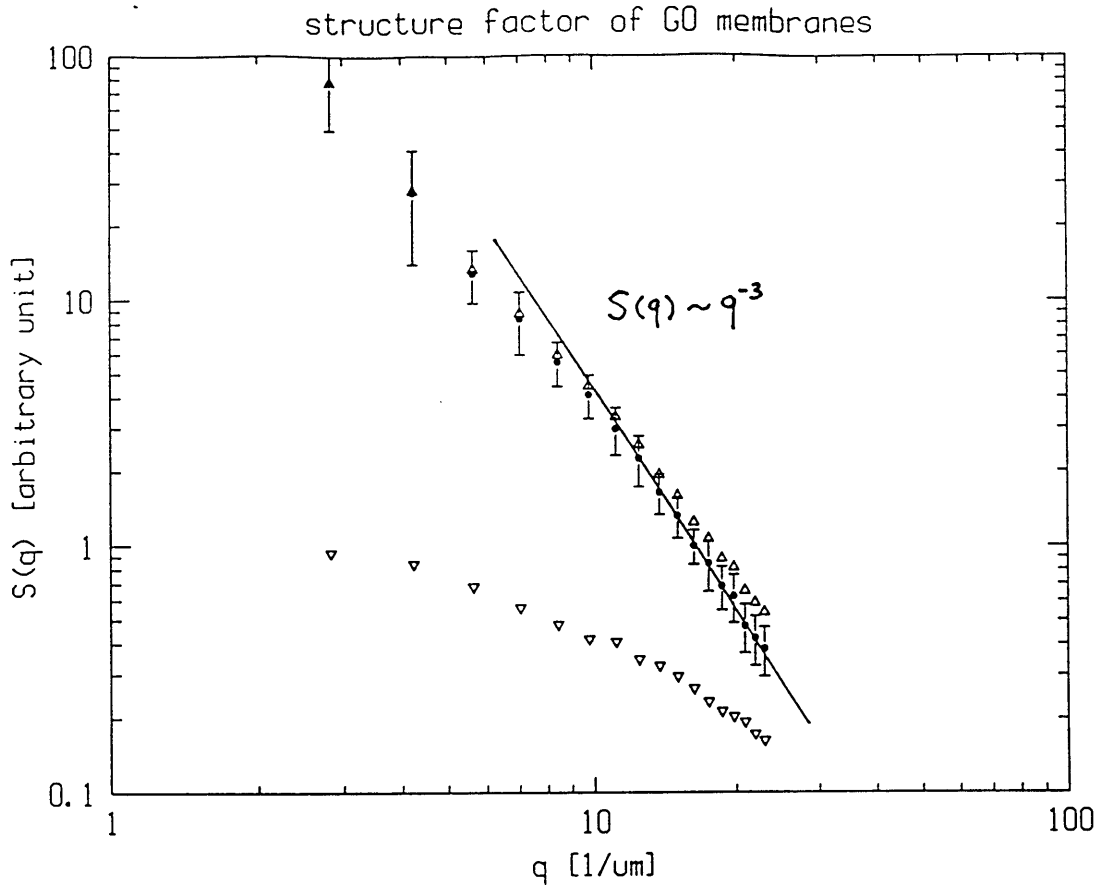


Figure 3.17: The structure factor of GO suspended in water.

experiment for the GO membranes suspended in water, we obtain the structure factor shown in Figure 3.17. There is clearly a q^{-3} dependence at large q , and there is a downward bend of the structure factor at lower q values. The origin of this form of $S(q)$ is unclear: one scenario is that the membranes never got separated in H_2O . Another possibility is that the water is such a poor solvent that the membrane collapsed, i.e. became compact. A third possibility is that the membrane in water is below its crumpling transition point and therefore flat.⁷ Obviously, more careful experimentation is needed to elucidate the nature of this phase.

We have also started to examine the dynamical behavior of the crumpled mem-

⁷Recall that in the region $q^{-1} > w$ in Figure 3.9, $S(q) \sim q^{-2/\zeta} \sim q^{-3.1}$ for $\zeta \approx 0.65$, making it indistinguishable from the compact phase.

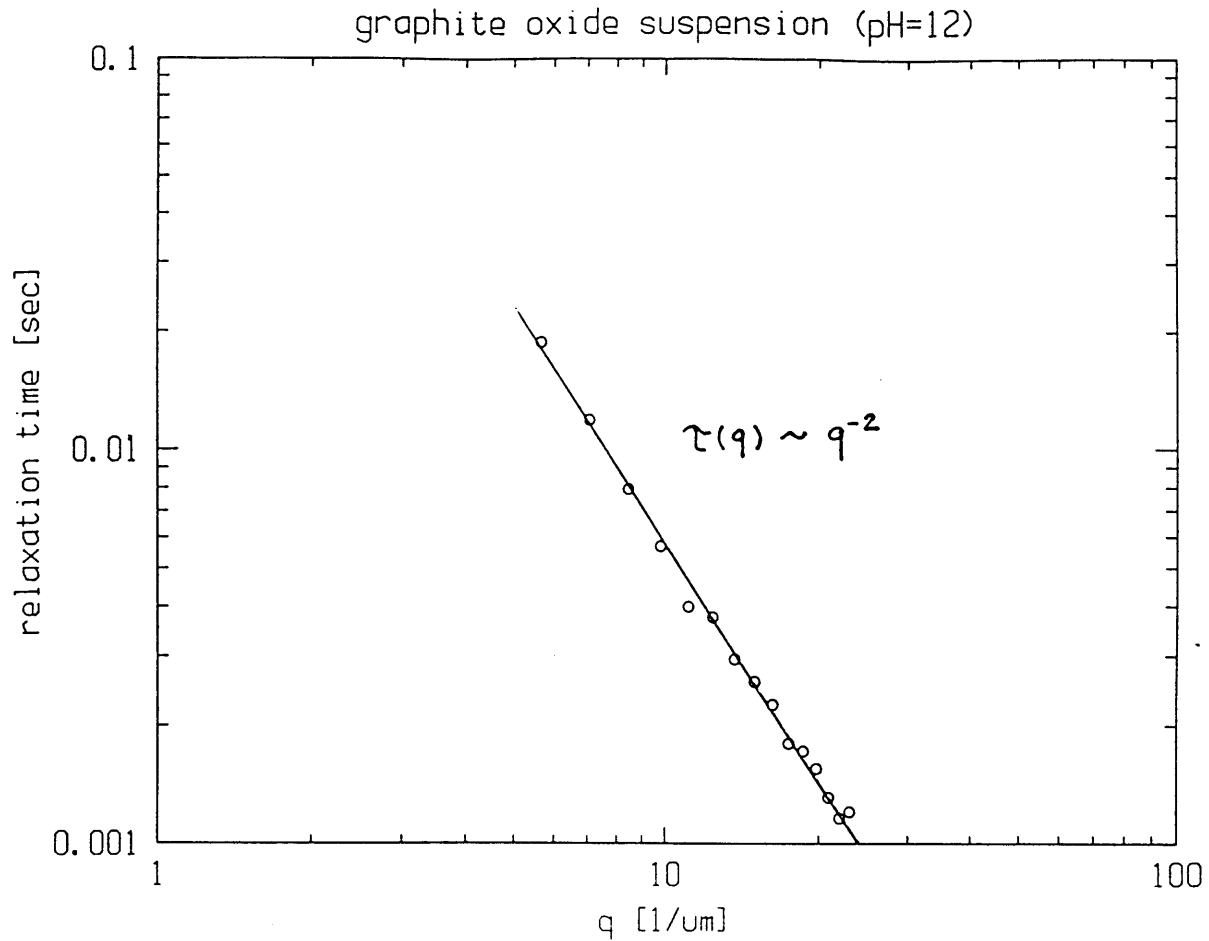


Figure 3.18: The q -dependence of the relaxation time of the scattered-intensity auto-correlation.

branes. As is expected from Eqs. (3.9) and (3.10), the auto-correlation function will be dominated by the Brownian motion of the center-of-mass. This is indeed seen experimentally. Figure 3.18 shows the q -dependence of the decay-time τ of the auto-correlation function for the poly-dispersed GO suspension. Here τ is obtained from the second-cumulant of the correlation function. We obtain $\tau(q) = [2D_{\text{eff}}q^2]^{-1}$ where $D_{\text{eff}} \sim 10^{-8} \text{ cm}^2/\text{sec}$ is the size-averaged diffusion constant. From D_{eff} we obtain a mean membrane-size of $0.25 \mu\text{m}$ in radius (where the small-sized membrane are much more heavily weighted (see Eqs. (3.9) and (3.10)). We are currently working to obtain the internal-motion part of the auto-correlation function.

3.4 Discussion

In this chapter, we have reported the synthesis of the graphite oxide membranes, and the measurement of the membranes conformations using light scattering methods. The membranes are found to be “crumpled” when suspended in an alkaline solution. The radius-of-gyration exponent obtained is $\nu = 0.83 \pm 0.03$ in agreement with the Flory estimate for the membranes. However, we add a cautionary note that this result does not completely answer the original question which addresses the conformation of the membranes in a “good” solvent: Intra-membrane attractions can also give rise to a crumpled state. If the quality of solvent is not good enough, then van der Waal attraction will overwhelm the short-distance repulsion effects. In such situations, the solution will phase-separate into a condensed phase (precipitate of the membrane particles) and a dilute phase which consists of mostly solvent with a few collapsed membranes. The structure of the collapsed phase is *compact* for polymers (i.e. $R \sim L^{1/3}$). But the nature of the collapsed phase of membranes is not clear. It is thought to be difficult to obtain the compact phase for 2- d sheets. If we manually crumple pieces of paper (press until they cannot get any smaller), we obtain $R \sim L^{0.8}$ [42]. In fact, one needs to fold a piece of paper in a very specific way to obtain a compact structure[43]. However, recent Molecular Dynamics simulations indicate that the membranes indeed settle down to a compact phase ($\nu = 2/3$) in the presence of (short-ranged) attractive potentials; though the relaxation time for this phase is somewhat long.

Does the suspensin of GO used in our experiment correspond to the membranes

in a “good” solvent? Are the membranes well equilibrated over the duration of the measurements? The answer to the first question is positive as up to a few percent of the membranes may be suspended in alkaline solutions ($pH = 11 \sim 12$), and aggregations have not been observed for over half of a year. The second question can only be answered with information on the *internal* motions of the membranes using dynamic light-scattering. Such information is very difficult to extract; and attempts are currently underway. The study reported here represents just the beginning of a systematic investigation of the rich phases and structures of the polymerized membranes.

Chapter 4

Interface Dynamics

In Chapters 2 and 3, we described some equilibrium properties of the membranes. In the next three chapters, we proceed to investigate problems associated with dynamics. However, we will not pursue the dynamics of membranes as they are needlessly complicated by the presence of *non-local* hydrodynamic and self-avoidance interactions. Instead we will examine several dynamical processes that involve only simple local interactions; they are exemplified by the non-equilibrium fluctuation of interfaces. It has been recognized that complex physical and biological patterns can evolve from simple underlying dynamics. Linear instabilities, interaction of different modes through non-linearities are some of the ingredients in the formulation of complex patterns. Through the exploration of interface dynamics in these chapters, we hope to bring to light some unique features of non-equilibrium dynamics; and along the way, present some theoretical tools useful in such studies.

We first investigate the dynamics of pattern evolution on the surface of a swelling gel. Here we can construct a model Hamiltonian from which the dynamics are rather easily derived. Next, we consider the growth of a surface in a deposition process for which no Hamiltonian exists. We resort to using symmetry principles to construct simple dynamical equations. We then analyze these equations using the method of dynamical renormalization-group (DRG).

4.1 Evolution of Surface Patterns on Swelling Gels

As a first example in the studies of dynamics, let us consider the formation and evolution of surface patterns on swelling gels[44]. This is a problem whose statics has already been understood, first on a heuristic basis by Tanaka *et al*[9], and later through detailed elasticity calculations by Onuki[45], and Sekimoto and Kawasaki[46]. In this study we will address the dynamics of pattern evolution after a brief description of the phenomenon.

4.1.1 The Phenomenon

The phenomena of phase transition and pattern formation of polymer gels are described in great detail in reference [47]. Here we summarize some key observations. A polymer gel consists of cross-linked polymer network immersed in liquids. If the liquid is a good solvent for the polymer, then the polymers are expanded due to entropy (described by the Self-Avoiding Manifold Theory of Chapter 2), causing the gel network to swell. However, if the liquid is a poor solvent, then it is energetically more favorable for the polymer to be surrounded by other polymers. In such a case, liquid is expelled from gel, and the network is collapsed. By changing the composition of the solvent[48] (or by changing the temperature[49], pH[50] etc) one can force the gel network to go from the collapsed phase to the swollen phase (swelling) or from swollen to the collapsed phase (shrinking). The volume phase transition of polymer gel can be either continuous or discontinuous much like the liquid-gas transition. Figure 4.1

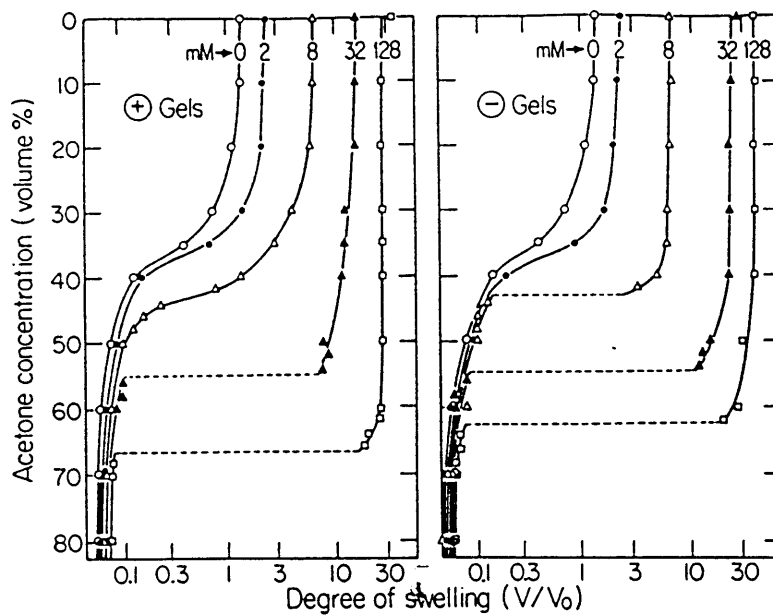


Figure 4.1: Equilibrium swelling ratio (V/V_0) of ionizable poly-acrylamide gels plotted against the solvent composition (% of acetone). The different curves are for gels with different degrees of ionization. (Reproduced from Reference [51].)

gives a typical phase-diagram. The nature of this phase transition has been investigated in great detail for a variety of gels but is not the subject of this study. For the purpose of the pattern formation study, we restrict ourselves near a first order transition point. As shown in Figure 4.1, a slight change in acetone concentration near a discontinuous transition (the dashed lines) can result in as much as a thousand-fold increase in gel volume. Similar swelling can be initiated from a small change in the ambient temperature.

However due to very large friction arising from the relative motion between polymer network and the liquid it is immersed in, the expansion process is heavily damped and is found to be diffusive in nature[52]. When we monitor the gel network during the swelling process, we find that swelling is initiated by the relaxation of outer layers

of the gels. In Figure 4.2, we look at the cross-section of a cylindrical poly-acrylamide gel at various stages of expansion. The polymer is marked by a fluorescent dye so that the intensity of light observed at each position gives a measure of local polymer density. Clearly we see that the outer layer swells first (low intensity), with the swollen region gradually moving towards the inner core of the network. At any given moment, the transition from the swollen to collapsed region is rather abrupt. A closer examination of the cross-sectional view of the swollen region reveals intricate patterns on the surface of the swollen network. These patterns are initially very fine, but they coalesce and become coarser as swelling proceeds. Experimentally, the typical sizes of the patterns are found to scale with the thickness of the swollen layer. Finer details of the patterns can be observed in later stages of swelling – the patterns consist of smooth arcs (buckles) that come together to form cusps into the gel. These cusps are not due to gel breaking, nor are they the unswollen portion of the gel.¹ They are like folding lines resulting from bending of homogeneous swollen gels. Figure 4.3 shows the top view of patterns formed on the surface of a swelling spherical gel. The planar organization of protruding buckles is randomly packed.

One final important observation is that the patterns are formed only when swelling is extensive (say at least a factor of 2 in linear expansion). If the swelling is small, the surface of the gel remains smooth throughout the entire process.

¹When the surface is sliced off in a thin layer, the patterns disappear instantly, and the layer is found to be homogeneous. If the cusps are due to local shrinking of gels they will take a long time to disappear due to the slow diffusion process involved.

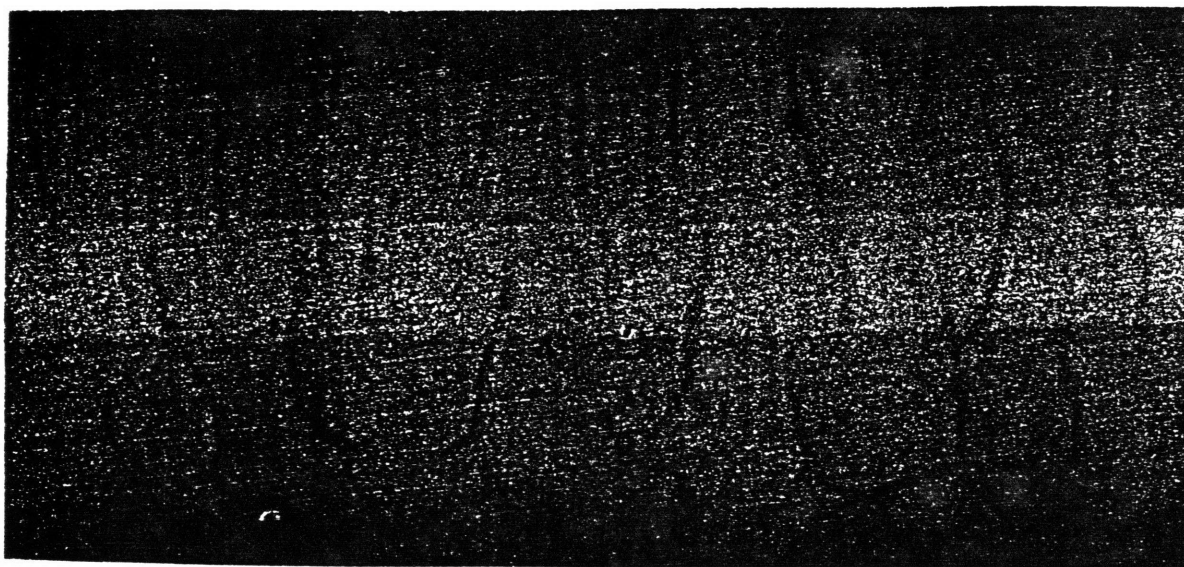
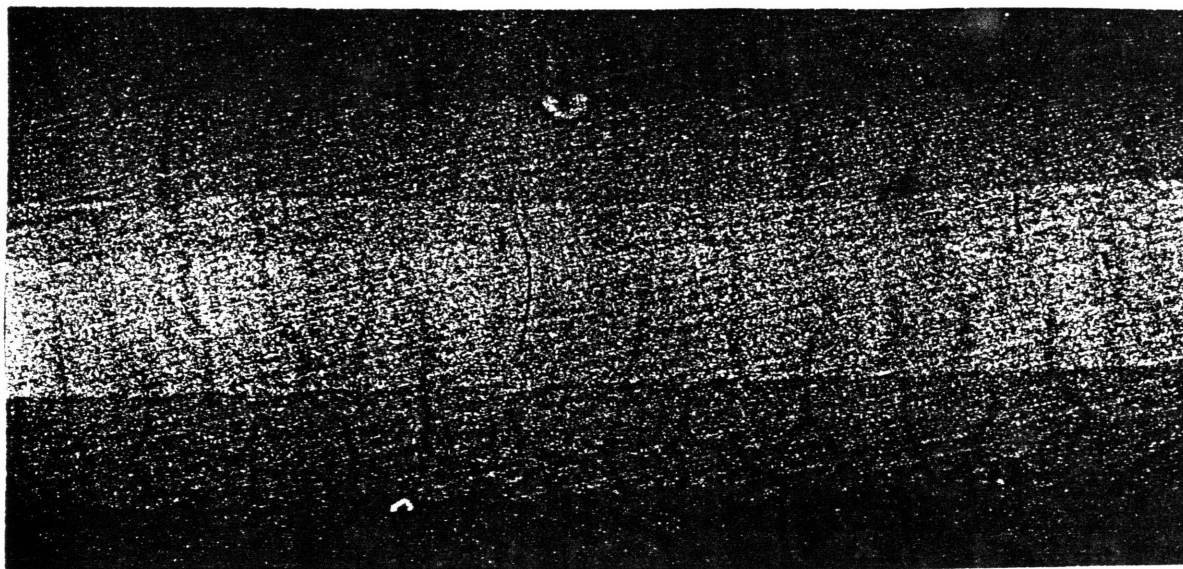


Figure 4.2: Cross-section of a cylindrical gel at (a) an early and (b) later stage of the expansion process. The bright cores seen in the middle of the gel are the unswollen portion of the network.

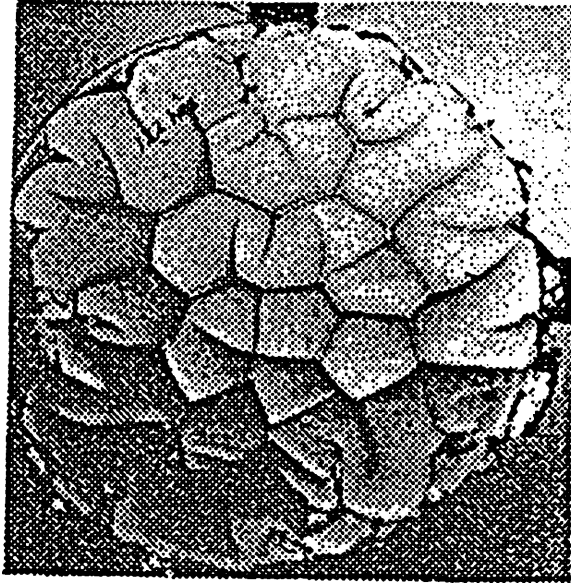


Figure 4.3: Top view of patterns of a swelling spherical gel. (Reproduced from reference [9].)

4.1.2 The Model and Hamiltonian

We introduce a very simple model[17], a network of springs expanding against friction in 1+1 dimensions, for the gel and construct a Hamiltonian for this model. We show that the equation of motion derived from this Hamiltonian can account for all key observed phenomena concerning the patterns. After making some reasonable assumptions regarding the strains and the taming of instabilities by interactions, we can actually follow the evolution of patterns on a computer. The basic results in 1+1 dimensions are: a swollen layer of thickness $l(t)$ (measured from the surface of the gel) growing diffusively with time; for large enough expansion, a band of unstable modes develop for transverse fluctuations over a range of wavelengths proportional to $l(t)$; formation of cusps as a result of instabilities and lateral motion of the particles; and the hierarchy of cusp evolution. Simple extension of the model can also account

for patterns in 2+1 dimensions.

We model a rectangular slab of gel in 1 + 1 dimensions by a square lattice of beads connected by harmonic springs of spring constant K and equilibrium length a . In this model, the beads are caricatures of cross-links of polymer units, and the springs are used to mimick the entropy-generated elasticity of the polymer network. The equilibrium spring length a is related to the end-to-end distance of the polymer connecting two cross-links. To incorporate the viscous motion of polymer units with respect to the solvent, we let the beads in our model to move against a frictional force with friction coefficient f .

Swelling implies an increase in the equilibrium spring length a . If the average number of monomers between two cross-links is N , then in the collapsed phase, $a \sim N^{1/3}$, while in the swollen phase, $a \sim N^{1/2}$; if the gel is ionic, electrostatic repulsion makes $a \sim N$. In an experiment this change can be brought about by a very small change in temperature or solvent composition as described in the previous section, and the equilibration time following this change is very short (order of seconds) compared to the relaxation time of the network (minutes to hours depending on size). In our model, we initiate swelling by changing the equilibrium spring constant a from 1 to E abruptly at $t = 0$. The linear expansion coefficient E can be as large as a factor of 10 for ionic gels.

Let $\mathbf{x} = (x_0, x_1)$ be the internal label of a bead in the spring network. The actual position of this bead is specified by the vector $\vec{r}(\mathbf{x}, t) = r_0(\mathbf{x}, t)\vec{e}_0 + r_1(\mathbf{x}, t)\vec{e}_1$ as shown

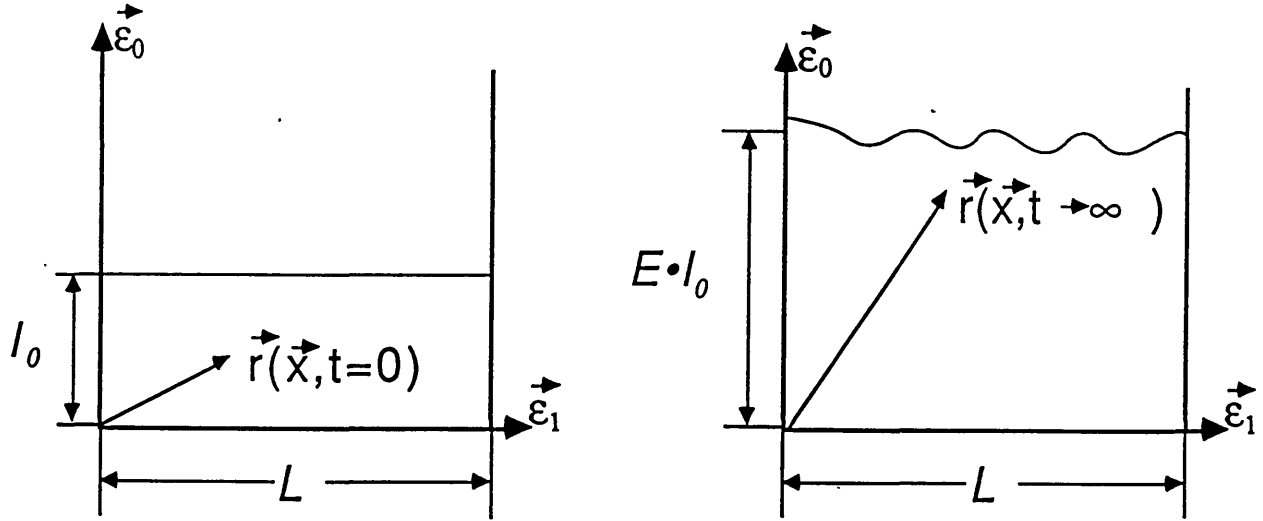


Figure 4.4: A slab of gel of thickness l_0 expands uniaxially in the \vec{e}_0 direction; $\vec{r}(\mathbf{x}, t)$ is the position vector of gel element \mathbf{x} .

in Figure 4.4. (\vec{e}_0 and \vec{e}_1 are unit vectors.) The total potential energy stored in the springs during swelling is given in the continuum limit by

$$\mathcal{H} = \frac{K}{2} \int d^2 \mathbf{x} \{ (|\partial_0 \vec{r}| - E)^2 + (|\partial_1 \vec{r}| - E)^2 \}, \quad (4.1)$$

where $|\partial_i \vec{r}| \equiv \sqrt{(\partial_i r_0)^2 + (\partial_i r_1)^2}$ is the spring length in the \vec{e}_i direction.

For a uniaxially expanding slab, the bottom surface ($x_0 = 0$) is fixed and hence undeformed (i.e., $\vec{r}(x_0 = 0, x_1, t) = x_1 \vec{e}_1$); while the top surface ($x_0 = l_0$) is free and does not support any normal or shear forces. The latter condition implies^[53]²

²The absence of normal stress implies $(1 - \sigma) \cdot (\partial_0 r_0 - E) + \sigma(\partial_1 r_1 - E) = 0$, where σ is the

$$\partial_0 r_0(x_0 = l_0, x_1, t) = E, \quad (4.2)$$

$$\partial_0 r_1(x_0 = l_0, x_1, t) + \partial_1 r_0(x_0 = l_0, x_1, t) = 0. \quad (4.3)$$

As will be shown below, this zero-stress condition for the free surface provides the necessary short-wavelength stability and accounts for cusp formation. The effect of this condition is heuristically included by Tanaka *et al*[9] in the form of a bending energy, and is anticipated by Sekimoto & Kawasaki[46] from stability considerations. The remaining boundary conditions, necessary to specify the problem completely, are that the network starts off in a compact form, i.e., $\vec{r}(\mathbf{x}, t \leq 0) = x_0 \vec{e}_0 + x_1 \vec{e}_1$, and periodic boundary conditions parallel to the slab of width L , i.e., $\vec{r}(x_0, 0, t) = \vec{r}(x_0, L, t)$, (and similar constraints on $\partial_i \vec{r}$) are chosen for convenience.

4.1.3 Dynamics

In a highly viscous medium, inertial effects and kinetic energy terms can be ignored. The elastic forces are then balanced against the frictional forces, and the full motion of the beads is governed by the coupled differential equations

$$-f \partial_t r_i = \frac{\delta \mathcal{H}}{\delta r_i} \{r_0, r_1, \partial_j r_0, \partial_j r_1, \dots\}.$$

Poisson ratio. However for our model (4.1), $\sigma = 0$; and (4.2) is used instead.

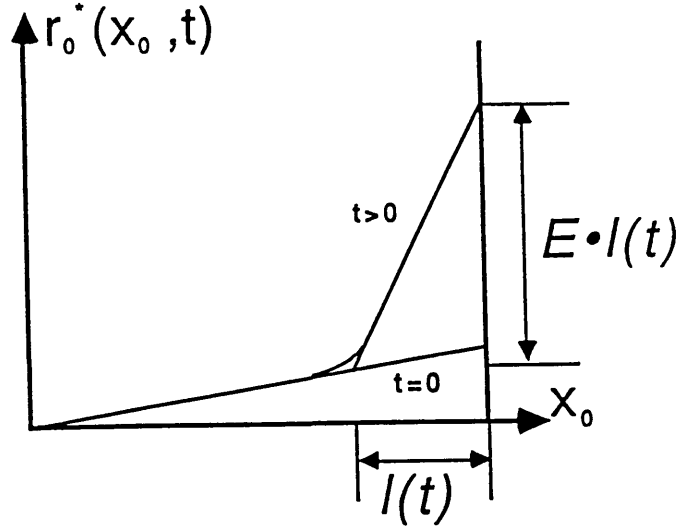


Figure 4.5: Solution of the diffusion equation at time t , and its approximation by two linear segments; $E \cdot l(t)$ is the thickness of the layer as measured from the surface of the gel.

These equations admit a uniformly expanding solution $r_0(\mathbf{x}, t) = r_0^*(x_0, t)$, and $r_1(\mathbf{x}, t) = x_1$. The expansion factor $r_0^*(x_0, t)$ satisfies a simple diffusion equation $\partial_t r_0^* = (K/f) \partial_0^2 r_0^*$, and its behavior subject to the boundary conditions specified before is depicted in Figure 4.5.

Qualitatively, the solution consists of a swollen layer of thickness $E \cdot l(t)$ on top of an unswollen inner core, much like the cross-sectional view of the cylindrical gel in Figure 4.2. Since the transition region (between swollen and collapsed parts) is rather sharp, we approximate the solution r_0^* by two linear segments: a swollen layer of thickness $E \cdot l(t)$ on top, and an undeformed gel at the bottom, i.e.,

$$r_0^*(x_0, t) = x_0 + (E - 1)[x_0 - (l_0 - l(t))] \quad \text{for } x_0 > l_0 - l(t),$$

and

$$r_0^*(x_0, t) = x_0 \quad \text{for } x_0 < l_0 - l(t).$$

The thickness of the swollen layer grows diffusively since $l(t) \sim \sqrt{Dt}$, with $D \equiv K/f$.

The full set of coupled differential equations are too complicated to be studied analytically or numerically, and approximations must be made. We assume that any fluctuations on the surface layer are affinely followed by the layers below, but with reduced amplitude. We further assume that these fluctuations only exist in the swollen region, i.e., their amplitude goes to zero as $x_0 \rightarrow l_0 - l(t)$. The simplest form of $\vec{r}(\mathbf{x}, t)$ subject to these restrictions is

$$r_0(x_0, x_1, t) = r_0^*(x_0, t) + (r_0^*(x_0, t) - x_0)h(x_1, t), \quad (4.4)$$

$$r_1(x_0, x_1, t) = x_1 + (r_0^*(x_0, t) - x_0)w(x_1, t). \quad (4.5)$$

This is a mean-field type approximation as fluctuations in different vertical layers are coordinated. Note that we explicitly allow fluctuations in the lateral ($\vec{\epsilon}_1$) direction; this is a key difference between this theory and reference [9], and it leads to an account of the formation of cusps as will shortly become apparent.

Using the linear approximate form for r_0^* and applying boundary condition (4.2) and (4.3), we obtain a relation between h and w ,

$$w(x_1, t) = -l(t)\partial_1 h(x_1, t). \quad (4.6)$$

Using Eqs. (4.4), (4.5), and (4.6) we can express \mathcal{H} as a functional of $h(x_1, t)$ only,

i.e.,

$$\mathcal{H} = \frac{\kappa}{2} \int d^2\mathbf{x} \left\{ \left[\sqrt{(r_0^* - x_0)^2 (\partial_1 h)^2 + (1 - (r_0^* - x_0) l^2 \partial_1^2 h)^2} - E \right]^2 + \left[\sqrt{(\partial_0 r_0^* + h \partial_0 r_0^* - h)^2 + (\partial_0 r_0^* - 1)^2 l^2 (\partial_1 h)^2} - E \right]^2 \right\}.$$

After averaging over the x_0 variable, the above Hamiltonian is , to leading orders in

h

$$\mathcal{H}\{h(x_1)\} = \frac{\kappa}{2} (E - 1)^2 \int dx_1 \left[h^2 - \frac{E - 1}{3} (\partial_1 h)^2 + \frac{(\partial_1^2 h)^2}{3} + \frac{E - 1}{E} h (\partial_1 h)^2 + \mathcal{O}(h^4, (\partial_1 h)^4, (\partial_1^2 h)^4, \dots) \right] \quad (4.7)$$

It is worth re-emphasizing that Eqs. (4.4), (4.5), and (4.6) are only approximations, and the restricted form is not exactly preserved under the full dynamic equations for $\partial_t r_i$. However, we believe that the form itself is reasonable and that the evolution of $h(x_1, t)$ can now be obtained by varying (4.7) with respect to h . To leading orders in h , we get

$$\begin{aligned} \frac{l^2(t)}{D} \partial_t h(x_1, t) &= -h - \frac{E - 1}{3} l^2(t) \partial_1^2 h - \frac{1}{3} l^4(t) \partial_1^4 h \\ &+ \frac{E - 1}{E} l^2(t) (\partial_1 h)^2 + 2 \frac{E - 1}{E} l^2(t) h \partial_1^2 h \end{aligned} \quad (4.8)$$

valid for $l^2(t) \gg 1$.

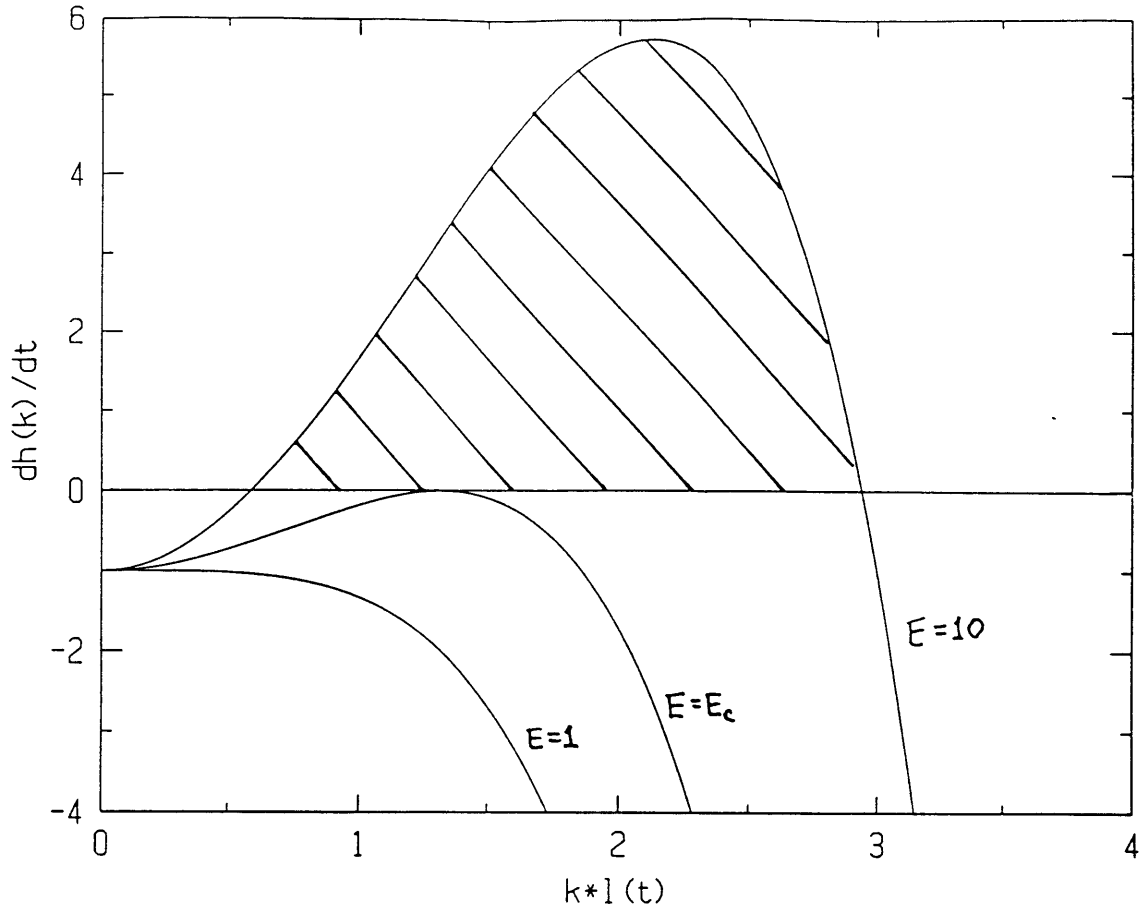


Figure 4.6: Linear stability of Eqn. (4.8) for $E = 1$, $E = E_c = 4.464$, and $E = 10$. The shaded region is the band of unstable modes for $E = 10$.

The linear stability of (4.8) is plotted for several values of the expansion factor E in Figure 4.6. When the expansion factor is small, Eqn. (4.8) is stable and no patterns appear. But for E larger than $E_c = 1 + 2\sqrt{3} \approx 4.464$, there is a band of unstable modes for $3 - (E - 1)(lk)^2 + (lk)^4 < 0$. The instability comes from the linear stretching elasticity ($-\partial_1 h^2$ term) and is a manifestation of gel's tendency to expand. The stability in the short-wavelength limit is provided by the $\partial_1^4 h$ term which is a consequence of the condition of a free top surface (4.3), and resembles the bending energy that was heuristically included in reference [9]. It is also clear that the unstable wavelengths (and hence the dominant wavelengths of the observed

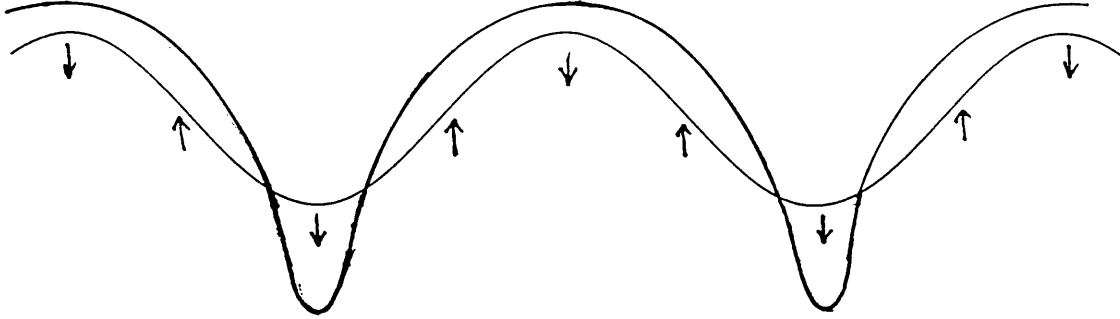


Figure 4.7: The evolution of surface profile $h(x_1, t)$. The effect of nonlinearity is marked by the arrows: Near the top of the buckles, the nonlinear term in (4.7) retards the growth rate, while it enhances the growth rate near the troughs.

patterns) scale with the swollen layer thickness as $\lambda^*(t) \sim l(t) \sim \sqrt{Dt}$.

Nonlinearities obtained from the variation of $\mathcal{H}\{h\}$ are then partly responsible for preventing the exponential growth of these instabilities. As can be seen from (4.7) and (4.8), one effect of the nonlinearity is to reduce the coefficient of the linearly unstable stretching energy term for $h > 0$ (the convex part of h). The instability at the top of the buckles are thus tamed. However, the instability at trough (concave part of h) cannot be controlled by the non-linear term as illustrated in Figure 4.7. To understand what is happening near the troughs, we observe that $h(x_1, t)$ is *not* the actual surface profile, which must also include the transverse motions of the surface described by w in Eq (4.5), and required by the stress-free condition of the top surface. The actual loci of surface points is the curve $\tilde{h}(\xi)$ obtained with $x_0 = l_0$ in Eqs. (4.4),

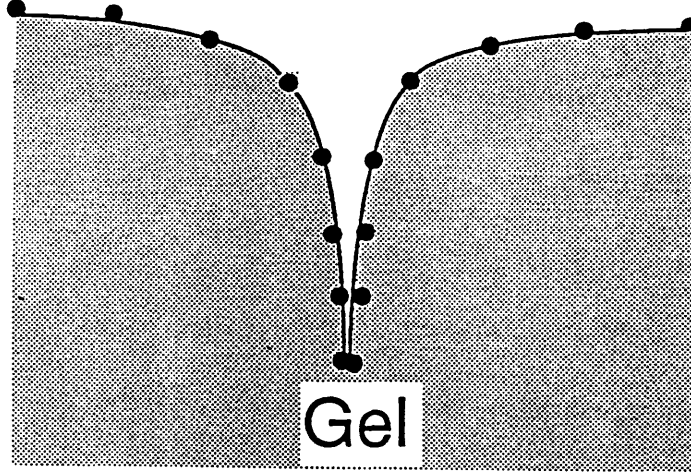


Figure 4.8: Cusps are formed when beads from the surfaces of neighboring arcs run into each other.

(4.5), and (4.6):

$$\begin{aligned}\tilde{h}(x_1, t) &= l_0 + (E - 1)l(t)[1 + h(x_1, t)], \\ \xi(x_1, t) &= x_1 - (E - 1)l^2(t)\partial_1 h(x_1, t).\end{aligned}\tag{4.9}$$

We examine the tangents at the surface,

$$\frac{\partial \tilde{h}}{\partial \xi} = \frac{\partial \tilde{h}}{\partial x_1} \cdot \frac{\partial x_1}{\partial \xi} = \frac{(E - 1)l(t)\partial_1 h(x_1, t)}{1 - (E - 1)l^2(t)\partial_1^2 h},$$

and note that the curve $\tilde{h}(\xi)$ develops singularities as the curvature $\partial_1^2 h$ approaches $1/(E - 1)l^2(t)$. This singularity occurs when the horizontal components of neighboring beads coincide, i.e. the surface becomes folded, and signals cusp formation as illustrated in Figure 4.8.

Once this happens, further evolution according to the original equations would

have the beads go past each other, which is clearly unphysical. In fact the folded regions of the cusp are no longer part of the free surface, and evolve under a different dynamical rule. When a bead falls within the folded region, it is free to expand vertically, i.e., $\partial_1 r_0(x_0 = l_0, x_1) \rightarrow E$, for $x_1 \in$ folded regions. Since such motion is much faster than the vertical motion of neighboring beads outside of the folded region, then as soon as a bead gets caught in the folded region, it is pushed out by the vertical expansion. It is therefore believed that the cusp regions are “barely folded”.

We are now ready to follow the evolution of patterns on a computer. We numerically evolve the non-linear equation of motion (4.8) for all beads outside of the folded region. Then we make sure that if a region does become folded, it is only “barely folded”. This is implemented numerically by evolving the beads in the folded region in such a way that the curvature $\partial_1^2 h$ does not increase further. Figure 4.9 (solid lines) depicts the result of such a simulation.

The necessity of the gel surface to fold was first suggested by Onuki[45]. He assumed that *in equilibrium* there is a *finite width* over which the surface particles are in contact (i.e., folded), and calculated the final shape of buckling with this width as an unknown parameter. The equilibrium shape of the buckle can also be calculated in the present approach by minimizing (4.7) with appropriate boundary conditions. Our “barely folded” assumption corresponds to setting this width to be very small during the pattern evolution.

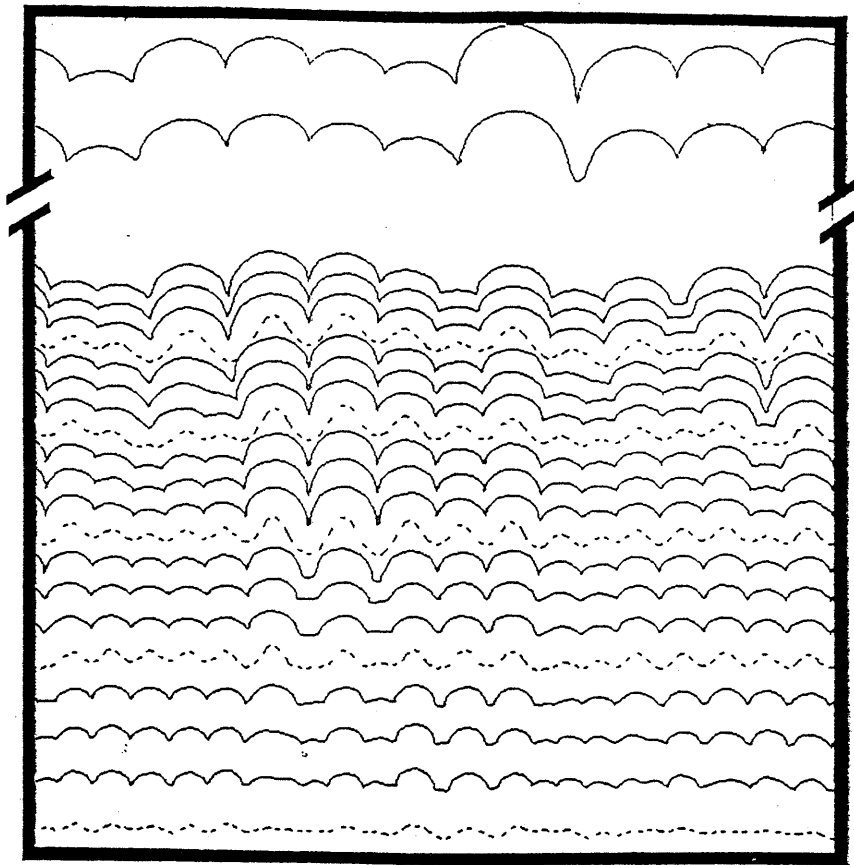


Figure 4.9: The nonlinear equation of motion (4.8) for $h(x_1, t)$ is solved numerically (for $E = 10$) at various stages of the evolution: The dashed lines, $h(x_1, t)$, are profiles obtained when no horizontal displacement is allowed; the solid lines, $\bar{h}(\xi, t)$, are the surface profiles when the horizontal motion is included.

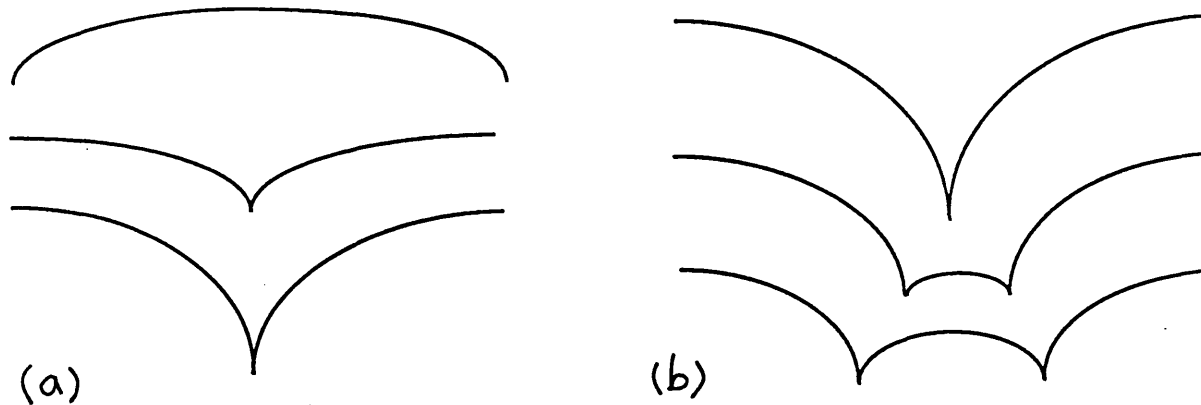


Figure 4.10: (a) and (b) are the two mechanisms for the merging of cusps, as found from computer simulations.

This completes the description for following the patterns on the gel surface. Our model is completely specified by two parameters D and E which are simply related to the elastic moduli, viscosity, and the osmotic pressure of the gel. The resulting patterns in Figure 4.9 (corresponding to $E = 10$) reproduce various features such as scaling forms and cusps obtained in the experiments. The origin of the cusps is the following: mechanical instabilities of the swollen layer of the gel lead to height fluctuations on the surface. The height fluctuations are accompanied by transverse expansions of the surface particles which brings them in contact. At this point the particles are no longer part of the free surface and fold in cusps. Further evolution of cusps shows that these singularities can be removed by two mechanisms as indicated in Figure 4.10. Either a cusp is pushed out by neighboring regions (Figure 4.10a), or two neighboring cusps merge to form a single one (Figure 4.10b). The equilibrium

profiles obtained are in qualitative agreement with observations. Both mechanisms for cusp annihilation have also been observed in experiments.

A real gel is actually highly cross-linked in random; a more realistic model would have (weaker) springs connecting the diagonals of the square lattice, thus requiring two independent elastic moduli as is expected by symmetry considerations alone. The addition complicates boundary condition (4.2), and the uniformly expanding solution will have an E_{eff} which is a function of E and the ratio of the two elastic constants. The new Hamiltonian also results in changes in the coefficients of the $\partial_1^2 h$ and $\partial_1^4 h$ terms in (4.8), but should not change the characteristic behaviours of the solution. The reason is that in 1+1 dimensions, upon reducing the problem to that of a free string, the additional shear energy can only add to the string's stretching and bending energies which are already present in (4.1); only one elastic constant is needed to describe a string.

Finally, we can extend our model to 2 + 1 dimensions by generalizing the Hamiltonian in (4.1) to include an additional transverse direction \vec{e}_2 . However in this case, the diagonal springs do become necessary, because when we try to reduce the 3-d problem down to that of a membrane, two elastic constants are now needed to describe its dynamics, even though the diagonal springs in planes perpendicular to the surface still add nothing new. Despite this difference, we believe that the characteristics of the cross-section profiles found in 1+1 dimensions are preserved; and indeed a simulation of the 2-dimensional version of the *linear* part of the growth equation (4.8) resulted

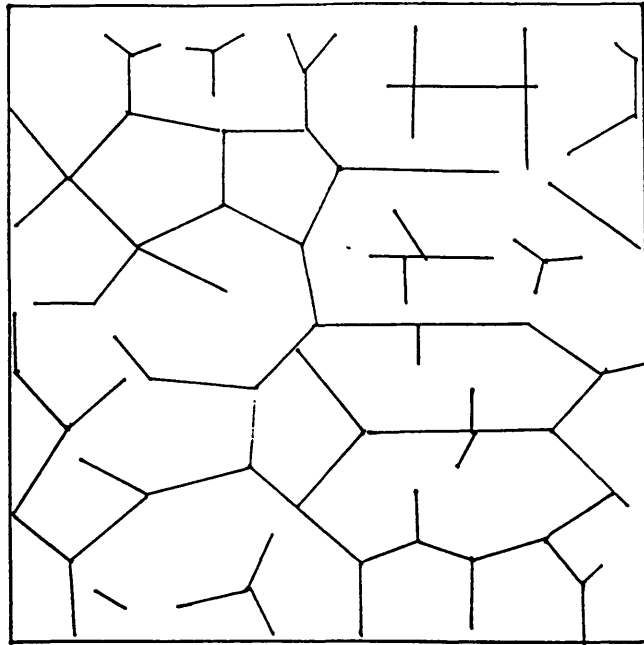


Figure 4.11: Two-dimensional patterns generated using a generalization of the equation of motion (4.8), starting from a random initial condition. The lines in the figure are the folding lines.

in formation of randomly packed buckles as shown in Figure 4.11, reminiscent of the surface patterns seen on the spherical gels (Figure 4.3).

4.2 Stochastic Dynamics of Interfaces

In the previous section we saw that for processes governed by an underlying Hamiltonian (or processes that can be mimicked by a Hamiltonian), the dynamics can be rather straightforwardly derived by a variation of that Hamiltonian. However, systems in nature are often quite more complicated; Hamiltonians are not always available, or are sometimes difficult to construct. In particular, dynamics away from equilibrium usually need not be described by a Hamiltonian. As in the static case, we can make some quantitative characterization of the dynamics if we look at the collective, macroscopic behavior. For dynamics, this is the limit of long time and large distances, also known as the hydrodynamic limit.

We will first present a way of constructing equations of motion based on symmetry considerations, and demonstrate the important role of stochasticity. This will be followed by an analysis of the linear stochastic diffusion equation, through which we introduce the important scaling ideas for dynamical processes.

4.2.1 Symmetry in Dynamics

Our construction of equations of motion is similar in spirit to Landau's construction of field theory for equilibrium systems[54]. The basic principle is that the equation of motion for a system is the simplest one consistent with various symmetries the system possesses. This principle, along with our interest in the *macroscopic* properties of systems in question, usually gives quite a good guide in obtaining the relevant

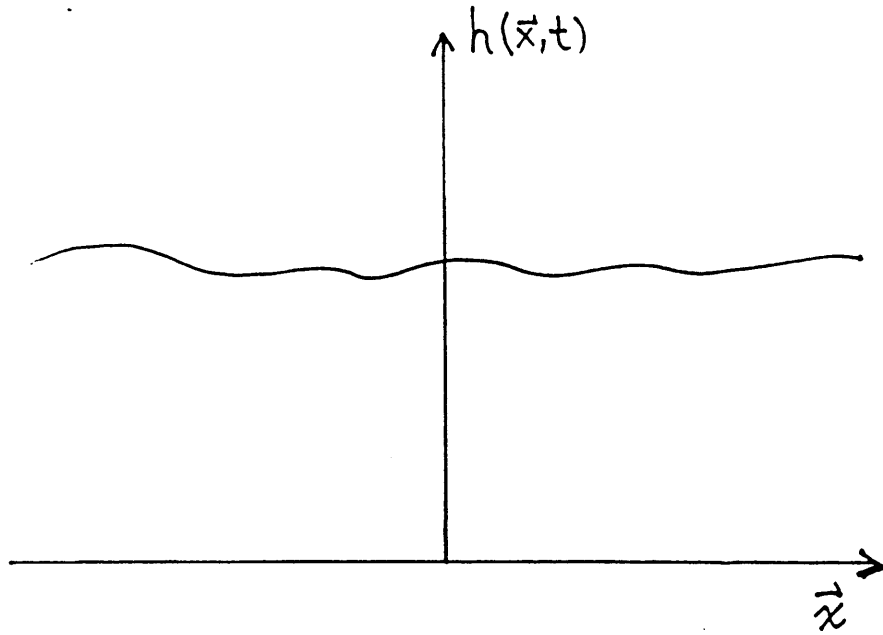


Figure 4.12: A “free” surface described by a scalar height function $h(\vec{x}, t)$ where \vec{x} is vector in a d -dimensional substrate.

equation of motion. Several examples should make this clear.

Let us first examine the simplest interface system. Consider an interface separating a liquid and gas mixture, or a domain wall separating the up and down phase of an Ising ferromagnet. Upon coarse-graining, the surface is represented by a scalar height function³ $h(\vec{x}, t)$ as shown in Figure 4.12. For generality, we consider the substrate to be d -dimensional, i.e., $\vec{x} \in \mathcal{E}^d$, so that the surface is embedded in $d + 1$

³Of course this is not always possible. What is described here cannot be applied to surfaces whose overhangs cannot be ignored, such as the crumpled membranes of Chapter 2.

dimensions. The equation of motion for the interface has the form

$$\frac{\partial h}{\partial t} = F(h(\vec{x}, t), \vec{x}, t).$$

Again, the inertial term $\partial^2 h / \partial t^2$ has been ignored since we are interested in the long-time (hydrodynamic) properties of dissipative systems. We assume that the surface normal is pre-selected (by boundary conditions, lattice orientation, etc) and list the symmetries present for such a surface:

1. translational symmetry along surface normal: certainly the physics of this problem does not depend on where we define $h(\vec{x}, t) = 0$. So the equation of motion must be constructed from $\vec{\nabla}h$, $\nabla^2 h$, etc.
2. translational symmetry parallel to the surface: rules out explicit \vec{x} dependence in F .
3. time translational invariance: rules out explicit t dependence in F .
4. $\mathcal{O}(d)$ rotational symmetry about the surface normal: cannot have vectors such as $\vec{\nabla}h$, $\vec{\nabla}h(\vec{\nabla}h)^2$, $\vec{\nabla}(\nabla^2 h)$ present in F .
5. up-down symmetry in h : The parity invariance condition requires F to be odd in h , this rules out terms such as $(\vec{\nabla}h)^2$, $(\nabla^2 h)^2$, etc.

There are of course many other symmetries for the free surface, but we will not try to enumerate them all. Just from the symmetries listed above, we see that the equation

of motion is already quite restricted:

$$\frac{\partial h}{\partial t} = a_1(\nabla^2 h) + a_2(\nabla^2 h)(\vec{\nabla} h)^2 + a_3(\nabla^4 h) + \text{higher order terms.}$$

Of the three terms written above, the $(\nabla^4 h)$ term is small compared to $(\nabla^2 h)$ term in the hydrodynamic limit and is ignored. For reasonably smooth surfaces whose overhangs are not important, $(\vec{\nabla} h)^2 \ll 1$ in the hydrodynamic limit, and the a_2 term is also small. (This will be made more quantitative in section 4.2.2.) We are then left with the leading order term

$$\frac{\partial h}{\partial t} = \nu(\nabla^2 h), \tag{4.10}$$

where ν can be interpreted as the surface tension for this interface. The diffusion equation (4.10) is the equation of motion describing the free surface. In the above derivation, we have looked for the simplest possible form of the equation of motion. We do not consider the possibility of nonanalytic terms such as $|\vec{\nabla} h|$ which would certainly make things more complicated.

To appreciate the effect of various symmetries, it is useful to study situations in which some of these symmetries are absent. Suppose we introduce gravity into the liquid-gas interface problem. Then the liquid phase will tend to settle down to the bottom of the box, and translational symmetry along the surface normal is broken: Given the amount of liquid (fixed by chemical potential etc) and the size of the box, the interface is fixed at a preferred height. Lack of translational symmetry allows us

to construct an equation of motion with the field h itself, giving

$$\frac{\partial h}{\partial t} = -\frac{h}{\tau} + \nu(\nabla^2 h). \quad (4.11)$$

The additional term $-h/\tau$ introduces a time scale, and associated with it a length scale (this is the length scale beyond which interface dose not fluctuate).⁴

The dynamics of (4.10) and (4.11) can also be derived from a Hamiltonian. For example, the interface under gravity is described by a Hamiltonian

$$\beta\mathcal{H} = \int d^d x \left[\frac{1}{2\tau} h^2 + \nu(\vec{\nabla} h)^2 \right].$$

where the first term is the potential energy cost of a column of height h . The dynamics is then derived by the variation of \mathcal{H} . For non-conservative dynamics,

$$\frac{\partial h}{\partial t} \sim \frac{\delta \mathcal{H}}{\delta h}$$

as in the previous section for gels, giving (4.11). However, if the dynamics is conservative, i.e.,

$$\frac{\partial}{\partial t} \int d^d x h(\vec{x}, t) = 0,$$

⁴The term $-h/\tau$ is like the energy “gap” in solid-state physics, or the “mass” term in field theory.

then the correct prescription is instead

$$\frac{\partial h}{\partial t} \sim \nabla^2 \frac{\delta \mathcal{H}}{\delta h}$$

and the mass term in (4.11) is removed. Although we will be restricting our attentions to non-conservative dynamics in what follows, we will return to conservative dynamics in Chapter 6.

We next examine the phenomena of growth. We consider particles raining straight down from the top of a box, piling up at the bottom, causing the interface to move up. If the deposition rate per area is F , then the mean height $\langle h \rangle$ increases as $\langle h \rangle = Ft$. But what are the fluctuations about $\langle h \rangle$?

To construct the equation of motion for a growing interface, we realize that out of the five symmetries listed, the only one broken is the up-down reflection symmetry, as we have picked a growth direction. Since parity no longer needs to be respected, terms even in h are now allowed in the equation of motion. Including the leading order term, we get

$$\frac{\partial h}{\partial t} = \nu(\nabla^2 h) + \frac{\lambda}{2}(\vec{\nabla} h)^2 + F. \quad (4.12)$$

Note that the mass term is again not allowed in the above equation due to a translational symmetry along the surface normal. To see how the non-linear term in (4.12) originates, consider growth by addition of discrete spherical particles of diameter d to a surface as shown in Figure 4.13. It is clear that the growth direction is always

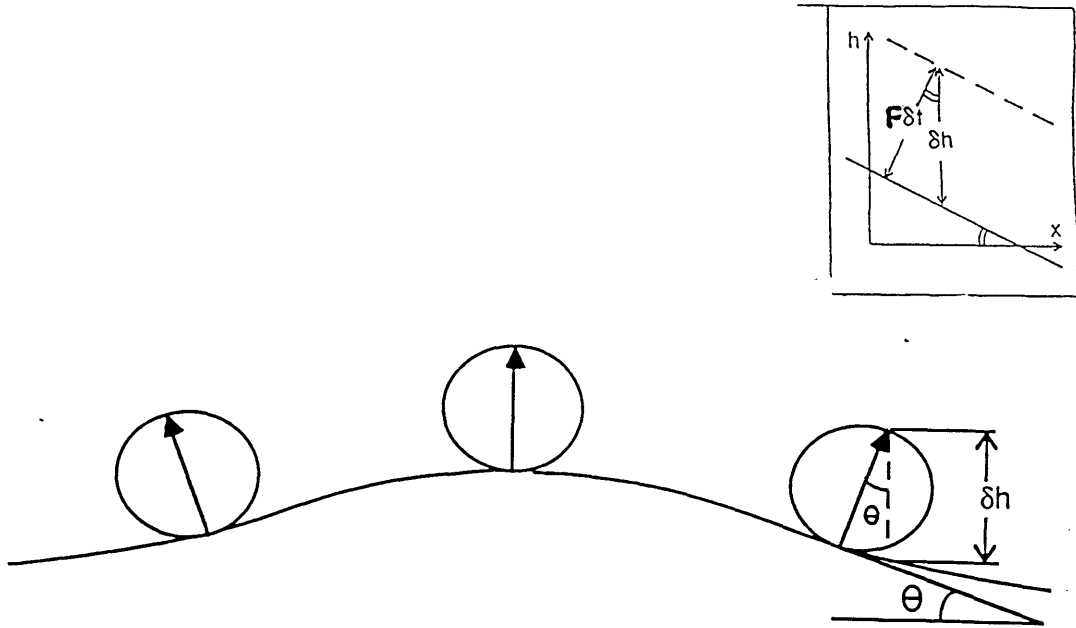


Figure 4.13: Growth by addition of spherical particles. It can be seen that growth occurs always normal to the interface so that the local tangent vector is parallel transported.

locally normal to the surface. Consequently, as Figure 4.13 demonstrates, the change in height (δh) in a time δt is given by $\delta h = F\delta t / \cos \theta = F\delta t[1 + (\vec{\nabla}h)^2]^{1/2}$. The local slope $\vec{\nabla}h$ therefore appears in the growth equation in a nonlinear and non-symmetric form. Also it is clear that the parameter λ in (4.12) has to be proportional to the average growth velocity F ; i.e., the nonlinearity is dynamically generated.

Eqn. (4.12) is a very interesting equation[10] whose properties will be explored in detail in the next chapter. Here we mention that the nonlinear term $(\vec{\nabla}h)^2$ cannot be generated from variations of any Hamiltonian that satisfies translational symmetry in h and is therefore unique to non-equilibrium processes.

The growth problem is made more complicated if the particles added have tendency to form layers. The layering order, say with period a in the growth direction,

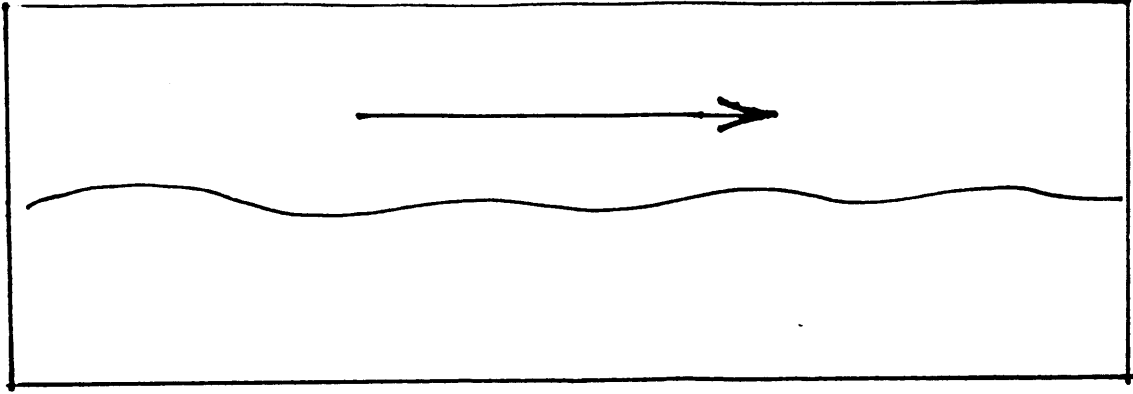


Figure 4.14: Surface with an applied driving force perpendicular to the normal.

destroys the infinitesimal translational invariance in h . What remains is the symmetry $h \rightarrow h + na, n = \text{integer}$. A simple equation consistent with this symmetry is

$$\frac{\partial h}{\partial t} = \nu(\nabla^2 h) + \frac{\lambda}{2}(\vec{\nabla}h)^2 - y \sin\left(\frac{2\pi}{a}h\right) + F. \quad (4.13)$$

This equation gives a more realistic description of deposition processes such as molecular-beam epitaxy, and therefore may have some technological importance. However, the analysis of (4.13) is rather involved and will not be presented here[55].

Instead of breaking the up-down symmetry, we can also consider systems in which one of the in-plane directions is singled out, say by applying a field parallel to the surface as shown in Figure 4.14. The presence of a driving force introduces a transport direction \hat{T} , allowing term such as $\vec{\nabla}h$ to remain in the equation of motion. If translational and up-down symmetries in h are not broken, then a simple equation of motion is

$$\frac{\partial h}{\partial t} = \nu(\nabla^2 h) + v\hat{T} \cdot \vec{\nabla}h + g\hat{T} \cdot \vec{\nabla}h(\vec{\nabla}h)^2, \quad (4.14)$$

where the linear streaming term can be transformed away by going to a moving coordinate system $\vec{x}' \cdot \hat{T} = \vec{x} \cdot \hat{T} - vt$. Alternatively, the driving force can be coupled to the field in such a way that a flip of the interface ($h \rightarrow -h$) causes a reversal in the transport direction. The simplest equation associated with such dynamics is

$$\frac{\partial h}{\partial t} = \nu(\nabla^2 h) + g\hat{T} \cdot \vec{\nabla} h(\nabla^2 h). \quad (4.15)$$

Transport phenomena will be discussed in detail in Chapter 6.

4.2.2 Stochasticity in Dynamics

Another important ingredient in determining the qualitative behavior of non-equilibrium dynamics is stochasticity. Quite often, dynamics we encounter is stochastic in nature. Stochasticity can come from thermal fluctuations, random driving forces, disorder in the environment, or it can be a manifestation of chaotic microscopic degrees of freedom. Stochasticity may or may not change the dynamics generated from the deterministic equation of motion. In the gel case considered in section 4.1, addition of a small amount of randomness during growth is not expected to qualitatively change the pattern formation and evolution. This is due to the presence of a “mass” term in the equation of motion (4.8). However, we shall soon see that the introduction of randomness does change the qualitative picture of the deposited surface.

The deterministic growth equation (4.12) can be turned into a diffusion equation upon the transformation $W = \exp\left[\frac{\lambda}{2\nu}(h - Ft)\right]$. The equation is thereby solved

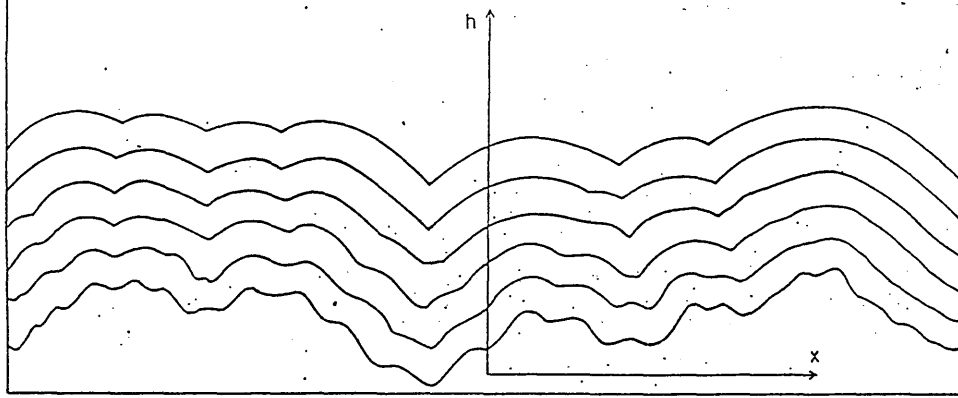


Figure 4.15: Successive layers of an interface relaxing to a flat configuration by a deterministic growth mechanism described by Eqn. (4.12). The relaxation occurs via paraboloid segments joined together at cusps.

analytically[10]

$$h(\vec{x}, t) = Ft + \frac{2\nu}{\lambda} \log \left\{ \int_{-\infty}^{\infty} \frac{d^d \xi}{(4\pi\nu t)^{d/2}} \exp \left[-\frac{(x - \xi)^2}{4\nu t} + \frac{\lambda}{2\nu} h_0(\xi) \right] \right\}.$$

where $h_0(\vec{x}) = h(\vec{x}, t = 0)$ is a random initial condition. The inside integral can be evaluated by the saddle point method for small surface tensions, i.e. $\nu \rightarrow 0$. After maximizing the integrand and taking a logarithm, the solution is found to be composed of paraboloid segments $h_n = A_n - (x - \xi_n)^2/2\lambda t$ joined together by discontinuities in (∇h) . For a finite ν the discontinuity is somewhat smoothed out. A typical one dimensional growth pattern is sketched in Figure 4.15. These patterns are reminiscent of patterns on surface of swelling gels in Figure 4.9: In fact the underlying physics is similar: In both processes the surface has a tendency to grow

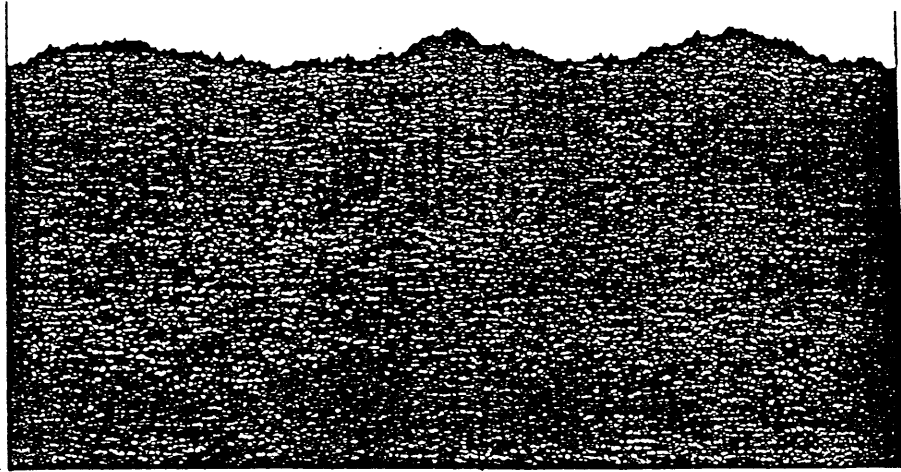
normal to itself; such normal growth usually leads to cusp formation. Similar patterns are commonly encountered in nature in geological stratifications, and successive layers of snow-drifts, etc.

However, when we include stochastic fluctuation into the driving force (random deposition), the picture obtained (Figure 4.16a) is qualitatively different[56]. Instead of smooth paraboli, we obtain a rough “landscape” that has a rich structure. Furthermore, if the noise in the deposition process is strongly correlated spatially, we obtain yet different patterns as seen in Figure 4.16b. These examples clearly demonstrate the relevance of stochasticity in determining surface patterns in this growth problem. To see how the effect of stochasticity can be followed analytically and systematically, we first analyze the stochastic version of the free surface equation (4.10).

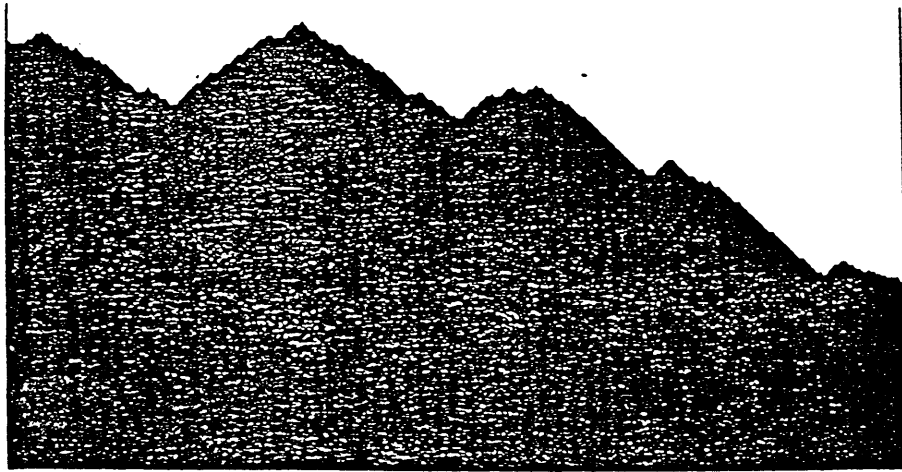
Stochasticity may be included in the dynamics by adding a noise term $\eta(\vec{x}, t)$ to Eqn. (4.10). The noise has zero mean, and is uncorrelated in the simplest case. The stochastic equation therefore reads

$$\begin{aligned}\frac{\partial h}{\partial t} &= \nu(\nabla^2 h) + \eta(\vec{x}, t), \\ \langle \eta(\vec{x}, t) \rangle &= 0, \\ \langle \eta(\vec{x}, t) \eta(\vec{x}', t') \rangle &= 2D\delta^d(\vec{x} - \vec{x}')\delta(t - t').\end{aligned}\tag{4.16}$$

This is the well-known model Edwards and Wilkinson used to describe the stochastic dynamics of a free surface[57]. The parameter D is the magnitude of noise auto-



(a)



(b)

Figure 4.16: Growth profiles obtained from “ballistic deposition” processes. (Reproduced from reference [56].) (a) deposition is random, (b) deposition is spatially correlated.

correlation; it is a measure of the strength of noise.

Eqn. (4.16) is a linear equation and is readily solved in Fourier space:

$$h(\vec{k}, \omega) = \frac{\eta(\vec{k}, \omega)}{\nu k^2 - i\omega},$$

with $\langle \eta(\vec{k}, \omega) \rangle = 0$ and

$$\langle \eta(\vec{k}, \omega) \eta(\vec{k}', \omega') \rangle = 2D \delta^d(\vec{k} + \vec{k}') \delta(\omega + \omega').$$

In stochastic processes, it is often more meaningful to study the correlation functions averaged over randomness. In this case, the average correlation function is

$$\langle h(\vec{k}, \omega) h(\vec{k}', \omega') \rangle = \frac{\langle \eta(\vec{k}, \omega) \eta(\vec{k}', \omega') \rangle}{\nu^2 k^4 + \omega^2}.$$

Using the form of noise-correlation, and inverse transforming back to real-space, we obtain

$$\langle h(\vec{x}, t) h(\vec{x}', t') \rangle = \frac{D}{\nu} |\vec{x} - \vec{x}'|^{2-d} G\left(\frac{\nu|t - t'|}{|\vec{x} - \vec{x}'|^2}\right). \quad (4.17)$$

The scaling function $G(y)$ has the property $G(y \rightarrow 0) \rightarrow \text{constant}$, and $G(y \rightarrow \infty) \rightarrow y^{(2-d)/2}$; its detailed form is otherwise not important for our discussions.

We will find in Chapter 6 that the effect of including nonlinear interactions is to modify the parameters D and ν to $D^R = D(1 + a_1 |\vec{x} - \vec{x}'|^\epsilon)^{b_1}$ and $\nu^R = \nu(1 + a_2 |\vec{x} - \vec{x}'|^\epsilon)^{b_2}$ where $\epsilon = d_c - d$, d_c being the upper-critical dimension for the nonlinear

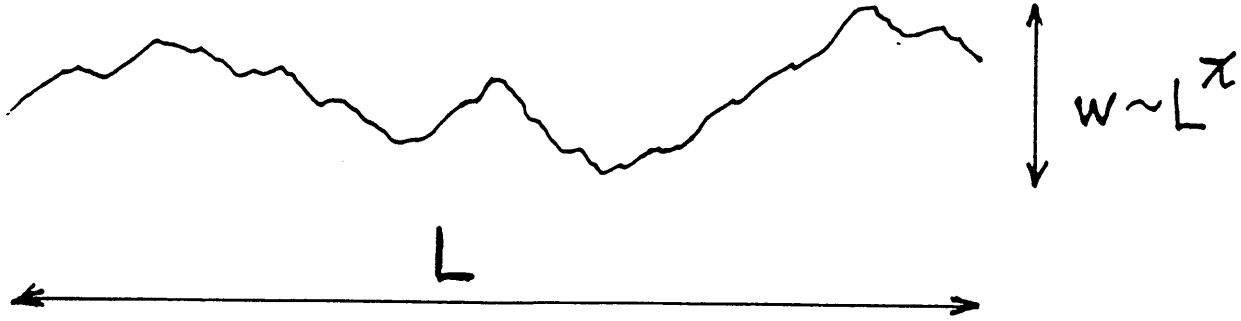


Figure 4.17: The scaling of the width w of an interface with its length L is described by the roughness exponent χ .

interaction, similar to what was encountered in Chapter 2. Substituting D^R and ν^R for D and ν in (4.17), we see that in the limit $|\vec{x} - \vec{x}'| \rightarrow \infty$, the form of the correlation function is preserved, but with altered values of exponents. In general

$$\langle h(\vec{x}, t) h(\vec{x}', t') \rangle = \frac{D}{\nu} |\vec{x} - \vec{x}'|^{2\chi} G \left(\frac{\nu |t - t'|}{|\vec{x} - \vec{x}'|^z} \right). \quad (4.18)$$

The exponent χ in (4.18) is called the roughness exponent. It describes the roughness or wandering of the interface. As shown in Figure 4.17 typical width w of the interface scales with its length L as $w \sim L^\chi$. If $\chi < 0$, then the width goes to zero asymptotically, and the interface is “flat” in the hydrodynamic limit ($L \rightarrow \infty$). If $1 > \chi > 0$, then the interface is “rough”, but $\nabla h \sim w/L \sim L^{\chi-1}$ is small, and expansion in powers of (∇h) is still valid. However, for $\chi > 1$, the interface wanders off too much and becomes “fractal”-like. Overhangs are no longer ignorable and the description of the interface based on a scalar height function breaks down in this limit. For the free surface, comparison of (4.17) and (4.18) gives $\chi = (2 - d)/2$. We see that

the interface is macroscopically smooth above $2 + 1$ dimension and becomes rough below that. But $\chi < 1$ for all $d > 0$, justifying the procedures of coarse-graining and ignoring overhangs carried out in the section 4.2.1.

From the scaling form (4.18), we can also obtain information in the dynamics of surface fluctuation from the dynamic exponent z . $z = 2$ corresponds to ideal diffusion and $z = 1$ is simple streaming or ballistic motion. We shall find in the next two chapters that anomalous diffusion ($1 < z < 2$) can be generated with the inclusion of nonlinear interactions.

Before closing this section, let us investigate the effect of a correlated noise. Correlation in noise can arise if the noise is itself the result of removing “faster” degrees of freedom. If $\eta(\vec{x}, t)$ is related to uncorrelated (white) noise $R(\vec{x}, t)$ through

$$\eta(\vec{x}, t) = \int_{-\infty}^t dt' \int_{-\infty}^{\infty} d^d \vec{x}' K(\vec{x} - \vec{x}', t - t') R(\vec{x}', t'),$$

then a long range power law decay of the kernel K results in algebraic correlations in η . For example if asymptotically $K(\vec{x}, t) \sim 1/(|\vec{x}|^{d-\rho} |t|^{1-\theta})$, then

$$\langle \eta(\vec{x}, t) \eta(\vec{x}', t') \rangle \sim |\vec{x} - \vec{x}'|^{2\rho-d} |t - t'|^{2\theta-1}, \quad (4.19)$$

and in Fourier space as $(\vec{k}, \omega) \rightarrow 0$,

$$\langle \eta(\vec{k}, \omega) \eta(\vec{k}', \omega') \rangle = 2D k^{-2\rho} \omega^{-2\theta} \delta^d(\vec{k} + \vec{k}') \delta(\omega + \omega'). \quad (4.20)$$

If we use the above noise spectrum for the free surface, the noise averaged height-height correlation function becomes

$$\langle h(\vec{x}, t)h(\vec{x}', t') \rangle = \frac{D}{\nu} |\vec{x} - \vec{x}'|^{2-d+2\rho+4\theta} G\left(\frac{\nu|t-t'|}{|\vec{x} - \vec{x}'|^2}\right) \quad \text{for } \theta < \frac{1}{2}. \quad (4.21)$$

Clearly, the effect of spatial-temporal correlation is to increase the roughness of the surface. In fact a $2 + 1$ -dimensional surface becomes too “ragged” to be described by a height function for $\chi = \rho + 2\theta > 1$.

The restriction $\theta < 1/2$ in (4.21) is necessary for the inverse Fourier Transform to make sense. For $\theta \geq 1/2$, there is too much power contained in the $\omega \rightarrow 0$ limit; and the long-time correlation in noise eventually “destroys” the smoothness of the surface. The behavior for $\theta \geq 1/2$ is very interesting to study in its own right, but it will not be pursued here. When we study temporal correlation in the next chapter, we will restrict ourselves to the range $\theta < 1/2$.

Chapter 5

Stochastic Growth of Interfaces

5.1 Introduction

We showed in the last chapter that the simplest equation describing the hydrodynamic behavior of non-equilibrium surface growth resulting from deposition is Eqn. (4.12).

We go to the moving frame $h \rightarrow h + Ft$ and consider the fluctuations of the interface in the presence of stochasticity. The relevant equation of motion is[10]

$$\frac{\partial h}{\partial t} = \nu \nabla^2 h + \frac{\lambda}{2} (\nabla h)^2 + \eta(\vec{x}, t), \quad (5.1)$$

where ν is the surface tension, λ is the coefficient of the dynamically generated nonlinearity and is proportional to the deposition rate F . $\eta(\vec{x}, t)$ is a stochasticity term mimicking the random deposition process. The noise term has zero mean, i.e., $\langle \eta(\vec{x}, t) \rangle = 0$, and may or may not be correlated (see section 4.2.2)

$$\langle \eta(\vec{k}, \omega) \eta(\vec{k}', \omega') \rangle = 2D(k, \omega) \delta^{d-1}(\vec{k} + \vec{k}') \delta(\omega + \omega'). \quad (5.2)$$

The general form of the noise spectrum is

$$D(\vec{k}, \omega) = D k^{-2\rho} \omega^{-2\theta}, \quad (5.3)$$

as in (4.20). The noise is uncorrelated if $\theta = \rho = 0$. The correlation becomes strong if ρ and θ increase as discussed at the end of section 4.2.2.

Before delving into a detailed analysis of Eqn. (5.1) we would like to point out

that this equation in disguise actually shows up in a great variety of problems in physics. In fluid mechanics, one of the simplest archetypes of nonlinear evolution is the Burgers' equation for a vorticity-free, compressible fluid[58]. In the presence of a random stirring force $f(\vec{x}, t)$, the velocity field of the Burgers' equation evolves as

$$\frac{\partial \vec{v}}{\partial t} + \lambda \vec{v} \cdot \nabla \vec{v} = \nu \nabla^2 \vec{v} + \vec{f}(\vec{x}, t), \quad (5.4)$$

where ν is the viscosity of the fluid and λ is a coefficient introduced for convenience. Forster, Nelson and Stephen[59] studied the above equation with several forms of stochastic noises f , by dynamical renormalization group (DRG) techniques and demonstrated that it exhibits non-trivial scaling behavior below two-dimensions. For a vorticity free fluid, we can of course write the velocity field as $\vec{v} = -\nabla h$, and (5.4) can be obtained by applying $\vec{\nabla}$ to both sides of Eqn. (5.1). The random stirring force is identified in this way as $\vec{f} = -\vec{\nabla} \eta$. It is the difference in noise spectrum that makes the analysis in this section different from that of FNS.

Another variant of Eqn. (5.1) is obtained by the nonlinear transformation $W = \exp(\frac{\lambda}{2\nu} h)$. W satisfies

$$\frac{\partial W}{\partial t} = \nu \nabla^2 W + \frac{\eta(\vec{x}, t)}{\lambda} W,$$

which is a diffusion equation with random sources and sinks. It is in general related to directed polymers in random media[60], and in the special case of two dimensions describes roughening of an interface by impurities[61].

Two other related problems are worth mentioning. One is the density fluctuations h in a driven diffusive system which satisfy[62]

$$\frac{\partial h}{\partial t} = D\nabla^2 h - \vec{w} \cdot \nabla h^2.$$

The nonlinear term expresses the fact that the velocity at which a density fluctuation travels depends on its magnitude[62]. Although this is not identical to Burgers' equation, it is equivalent to it in one dimension. This equation will be discussed in great detail in Chapter 6. Finally the Sivashinski equation[63] applied to the evolution of flame fronts takes the form

$$\frac{\partial h}{\partial t} = -\nu\nabla^2 h + \frac{\lambda}{2}(\nabla h)^2 - \nu'\nabla^4 h.$$

This is a deterministic equation with a band of linearly unstable modes at short wavelengths. It is believed[63] that the chaotic behavior generated by these modes can be described by a stochastic noise acting on the long wavelength modes, so that the long time, large distance behavior of this equation is identical to Eqn. (5.1).

We now return to the stochastic growth process. Eqn (5.1) with uncorrelated noise has been studied by Kardar, Parisi and Zhang (KPZ) using the method of dynamical renormalization group (DRG) and ϵ -expansions[10]. In section 5.2, we will introduce the perturbative calculation, illustrate the DRG method, and recapitulate the KPZ results; then we will show the emergence of a strong coupling fixed point and the

failure of the conventional ϵ -expansions. As a remedy we propose an expansion about a lower critical dimension $d = 0$. In section 5.3 we discuss the effect of including spatial correlations in the noise spectrum, and in section 5.4 we include temporally correlated noise.

5.2 The KPZ Equation and Dynamical RG

We start by doing a naive dimensional analysis of Eqs. (5.1) and (5.2). We generalize the renormalization-group procedure of section 2.4 to dynamics by making the following scaling hypothesis:

$$\langle h(\vec{x}, t)h(\vec{0}, 0) \rangle = |\vec{x}|^{2\chi}G(t/|\vec{x}|^z). \quad (5.5)$$

If (5.5) is to hold, then in the hydrodynamic limit, a change of scale $\vec{x} \rightarrow b\vec{x}$, accompanied by $t \rightarrow b^z t$ and $h \rightarrow b^\chi h$ turns Eqn. (5.1) into

$$b^{\chi-z} \frac{\partial h}{\partial t} = \nu b^{\chi-2} \nabla^2 h + \frac{\lambda}{2} b^{2\chi-2} (\nabla h)^2 + b^{\rho-d/2+(2\theta-1/2)z} \eta,$$

where Eqs. (5.2) and (5.3) have been used to determine the scaling of the noise η .

Thus under this transformation the parameters change to

$$\begin{aligned} \nu &\rightarrow b^{z-2} \nu, \\ D &\rightarrow b^{2\rho-d-2\chi+(2\theta+1)z} D, \\ \lambda &\rightarrow b^{\chi+z-2} \lambda. \end{aligned}$$

The exponents of b are the *naive* dimensions for the respective parameters. To get the general picture of what is going on, let us examine the simplest case of uncorrelated noise ($\theta = \rho = 0$). In the absence of the nonlinear term, (i.e. $\lambda = 0$), the equation is

made scale invariant upon the choice of

$$z = z_0 = 2,$$

$$\chi = \chi_0 = \frac{(2-d)}{2}.$$

The nonlinearity added to this scale invariant equation has a dimension $y_\lambda^0 = z_0 + \chi_0 - 2 = (2-d)/2$. For $d > d_c = 2$ a small nonlinearity scales to zero and is *irrelevant*, while for $d < d_c$ the nonlinearity is *relevant* and grows under rescaling. Nontrivial exponents are expected for $d < d_c$ in the presence of nonlinearities.

Let us now go to Fourier space

$$h(\vec{x}, t) = \int \int \frac{d\omega}{2\pi} \frac{d^d k}{(2\pi)^d} h(\vec{k}, \omega) e^{i(\vec{k} \cdot \vec{x} - \omega t)},$$

whereupon Eqn. (5.1) becomes

$$h(\vec{k}, \omega) = G_0(\vec{k}, \omega) \eta(\vec{k}, \omega) - \frac{\lambda}{2} G_0(\vec{k}, \omega) \int \int \frac{d\mu}{2\pi} \frac{d^d q}{(2\pi)^d} \vec{q} \cdot (\vec{k} - \vec{q}) h(\vec{q}, \mu) h(\vec{k} - \vec{q}, \omega - \mu),$$
(5.6)

with a bare propagator

$$G_0(\vec{k}, \omega) = \frac{1}{\nu k^2 - i\omega}.$$
(5.7)

Eqn. (5.6) is a convenient starting point for a perturbative calculation of $h(\vec{k}, \omega)$ in powers of λ as indicated diagrammatically in Figure 5.1. The graphic expansion is quite standard[59] with \longrightarrow indicating the propagator G_0 , and \times depicting the noise

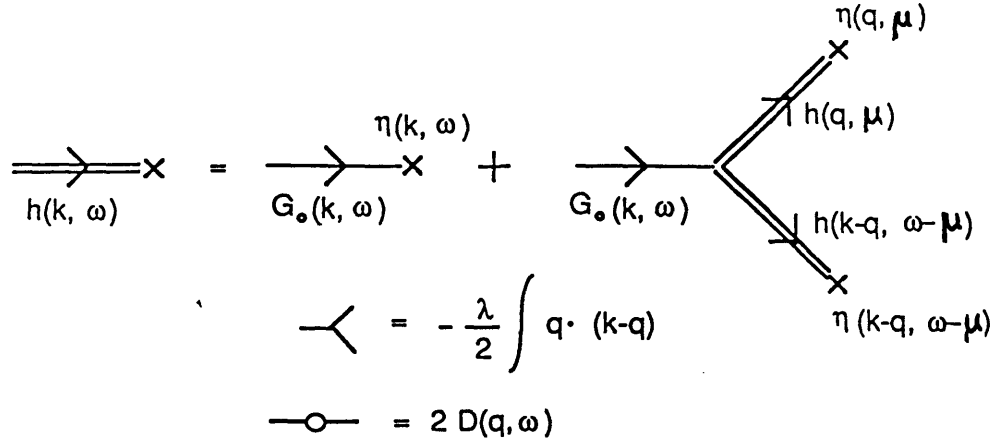


Figure 5.1: Diagrammatic representation of the nonlinear integral equation (5.6), and the perturbation series that results from it.

$\eta(\vec{k}, \omega)$. The averaging over stochastic noise is performed using Eqn. (5.2), and the renormalized response function $G^R(\vec{k}, \omega)$ (defined by $h(\vec{k}, \omega) \equiv G^R(\vec{k}, \omega)\eta(\vec{k}, \omega)$) is given perturbatively in Figure 5.2a. The lowest order (one-loop) correction is

$$\begin{aligned}
G^R(\vec{k}, \omega) &= G_0(\vec{k}, \omega) + 4 \left(\frac{-\lambda}{2} \right)^2 G_0(\vec{k}, \omega)^2 \int \frac{d\mu}{2\pi} \frac{d^d q}{(2\pi)^d} [\vec{q} \cdot (\vec{k} - \vec{q})] [\vec{q} \cdot \vec{k}] \\
&\quad G_0(\vec{k} - \vec{q}, \omega - \mu) G_0(\vec{q}, \mu) G_0(-\vec{q}, -\mu) 2D(\vec{q}, \mu) + O(\lambda^4),
\end{aligned}$$

where the combinatorial factor of four represents possible noise contractions leading to Figure 5.2a. Calculating the integrals is reasonably complicated and not particularly instructive. Details of the calculations can be found in reference [18]. After performing the frequency integrals and letting $\omega \rightarrow 0$, we obtain in the case of uncorrelated noise

$$(D(k, \omega) = D_0)$$

$$G^R(\vec{k}, 0) = G_0(\vec{k}, 0) - \left(\frac{\lambda^2 D_0}{\nu^2} \right) G_0(\vec{k}, \omega)^2 \left(\frac{2-d}{4d} \right) k^2 \int_k \frac{d^d q}{(2\pi)^d} q^{-2}, \quad (5.8)$$

where $k \rightarrow 0$ is used as the lower cutoff of the q -integral, and only terms of the order k^2 have been kept. Since $G_0(k, 0) = 1/(\nu k^2)$, this allows us to determine a renormalized surface tension $\nu^R(k)$ from $G^R(k, 0) \equiv 1/(\nu^R(k)k^2)$. From the above integral, the first order correction of surface tension from nonlinearity takes the form

$$\nu^R(k) = \nu \left[1 + K_d \frac{\lambda^2 D_0}{\nu^3} \frac{2-d}{4d} \frac{k^{d-2}}{2-d} \right], \quad (5.9)$$

where $K_d = S_d/(2\pi)^d$, and S_d is the surface area of a unit d -dimensional sphere. We are now ready to apply the RG procedure of section 2.4. Let a be a microscopic length (e.g., lattice constant), we can define a dimensionless renormalized surface tension $\tilde{\nu}^R(b) \equiv (ba)^{z-2} \nu^R(k^{-1} = ba)$, and a dimensionless interaction parameter $\tilde{u}_0(b) = K_d (ba)^{2-d} \lambda^2 D_0 / \nu^3$. The recursion relation for $\tilde{\nu}^R(b)$ is found by applying the rescaling operator $b(\partial/\partial b)$

$$b \frac{\partial}{\partial b} \tilde{\nu}^R = \nu (ba)^{z-2} \left[z - 2 + \tilde{u}_0(b) \frac{2-d}{4d} \right],$$

where the first order result (5.9) is used. Assuming the renormalizability of the KPZ equation, we may replace ν by ν^R and $\tilde{u}_0(b)$ by $\tilde{u}_0^R(b) \equiv K_d (ba)^{2-d} [(\lambda^R)^2 D_0^R / (\nu^R)^3]$

(see section 2.4). Expressing in terms of $l = \log b$, we obtain

$$\frac{d\tilde{\nu}^R}{dl} = \tilde{\nu}^R \left[z - 2 + \tilde{u}_0^R \frac{2-d}{4d} \right] \quad (5.10)$$

to one loop order.

A renormalized spectral function $D^R(k, \omega)$ can be defined from

$$\langle h^*(\vec{k}, \omega) h(\vec{k}, \omega) \rangle = 2G^R(\vec{k}, \omega) G^R(-\vec{k}, -\omega) D^R(\vec{k}, \omega).$$

This quantity is calculated perturbatively by the series shown in Figure 5.2b. The first correction term gives

$$\begin{aligned} 2D^R(\vec{k}, \omega) &= 2D(\vec{k}, \omega) + 2 \left(\frac{-\lambda}{2} \right)^2 \int \frac{d\mu}{2\pi} \frac{d^d q}{(2\pi)^d} [\vec{q} \cdot (\vec{k} - \vec{q})]^2 \\ &\quad G_0(\vec{q}, \mu) G_0(-\vec{q}, -\mu) G_0(\vec{k} - \vec{q}, \omega - \mu) G_0(-\vec{k} + \vec{q}, -\omega + \mu) \\ &\quad 2D(\vec{q}, \mu) 2D(\vec{k} - \vec{q}, \omega - \mu) + \mathcal{O}(\lambda^4). \end{aligned} \quad (5.11)$$

In the case of uncorrelated noise, the above integral easily simplifies to

$$D_0^R(k) = D_0 \left[1 + \frac{\lambda^2 D_0}{\nu^3} \frac{1}{4} \int_k \frac{d^d q}{(2\pi)^d} q^{-2} \right]$$

in the limit $k \rightarrow 0$, yielding the recursion relation

$$\frac{d\tilde{D}_0^R}{dl} = \tilde{D}_0^R \left[z - d - 2\chi + \frac{\tilde{u}_0^R}{4} \right], \quad (5.12)$$

where $\tilde{D}_0^R = D_0^R (ae^l)^{z-d-2\chi}$ is the dimensionless noise parameter.

The third parameter to consider is the nonlinearity coefficient λ which has contributions coming from the graphs in Figure 5.2c. The integrations give a null result for the uncorrelated noise. This is a consequence of a Galilean invariance that is preserved under renormalization. (See the appendix for a discussion.) In fact $\lambda^R = \lambda$ to all loop orders. Non-renormalization of λ immediately gives us a third recursion relation for the dimensionless parameter $\tilde{\lambda}^R = \lambda^R (ae^l)^{\chi+z-2}$

$$\frac{d\tilde{\lambda}^R}{dl} = \tilde{\lambda}^R [\chi + z - 2], \quad (5.13)$$

which is exact to all loop orders.

Eqs. (5.10), (5.12) and (5.13) are the recursion relations (also known as the RG flow equations) for the parameters of the KPZ equation in the presence of uncorrelated noise, calculated to the one-loop order. If the scaling hypothesis (5.5) is to hold, then the parameters $\tilde{\nu}^R$, \tilde{D}^R , and $\tilde{\lambda}^R$ are dimensionless (in the hydrodynamic limit), and

$$\left. \frac{d\tilde{\nu}^R}{dl} \right|_{l \rightarrow \infty} = \left. \frac{d\tilde{D}^R}{dl} \right|_{l \rightarrow \infty} = \left. \frac{d\tilde{\lambda}^R}{dl} \right|_{l \rightarrow \infty} = 0.$$

$$\overline{\overline{\longrightarrow}}_{k, \omega} = \overline{\longrightarrow}_{k, \omega} + 4 \overline{\longrightarrow}_{k, \omega} \overbrace{\text{loop}}^{q, \mu \quad -q, -\mu} \overline{\longrightarrow}_{k, \omega} + O(\lambda^4)$$

(a)

$$\overline{\circlearrowleft}_{k, \omega} = \overline{\circlearrowleft}_{k, \omega} + 2 \overline{\circlearrowleft}_{k, \omega} \overbrace{\text{loop}}^{q, \mu \quad -q, -\mu} \overline{\circlearrowleft}_{k, \omega} + O(\lambda^4)$$

(b)

$$\overline{\bullet} = \overline{\bullet} + 4 \overline{\text{triangle}} + 4 \overline{\text{triangle}} + 4 \overline{\text{triangle}} + \text{h.o.t}$$

$\Gamma = \Gamma_0 + \Gamma_a + \Gamma_b + \Gamma_c + \text{h.o.t}$

Figure 5.2: After averaging over the noise, the perturbation series of (5.6) can be reorganized to describe (a) a renormalized propagator, (b) a renormalized noise spectrum, and (c) and a renormalized vertex function (or interaction constant).

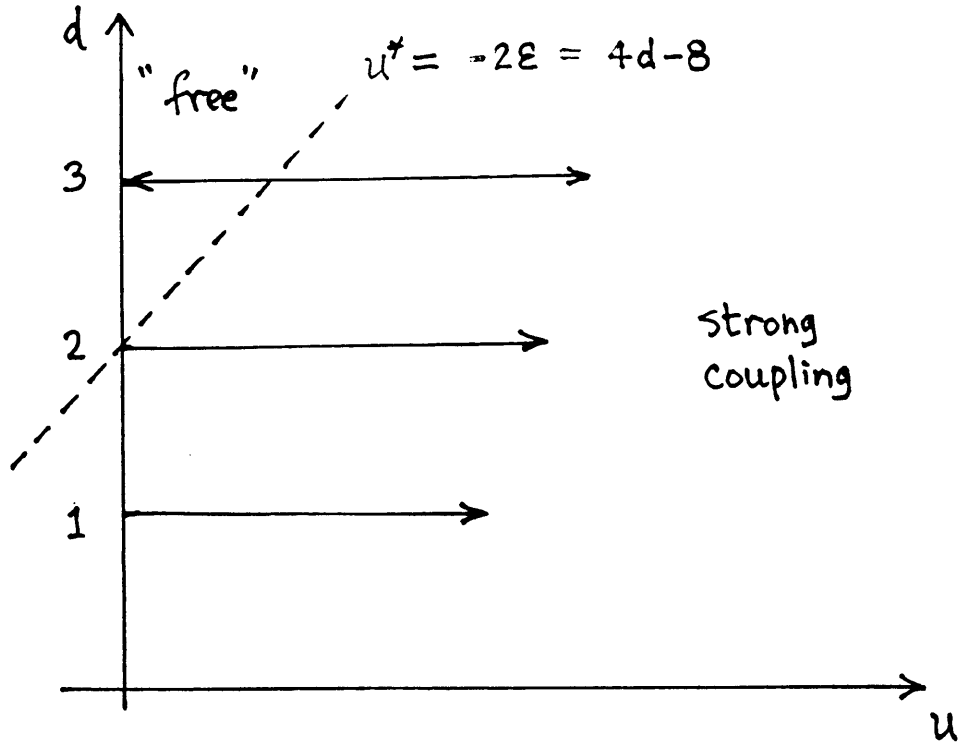


Figure 5.3: Flow diagram of the KPZ equation to first order in ϵ . The dashed line indicates the position of the fixed point u^* to order ϵ .

The hydrodynamic properties of the system can then be solved at the infra-red fixed point $\bar{u}^* = \bar{u}^R(l \rightarrow \infty)$ of the flow equations. Combining the three recursion relations, we obtain the RG flow equation for the effective coupling constant \bar{u}_0^R

$$\frac{d\bar{u}_0^R}{dl} = \bar{u}_0^R \left[(2 - d) + \bar{u}_0^R \frac{2d - 3}{2d} \right]. \quad (5.14)$$

The flow (upon rescaling) is shown in Figure 5.3 for various dimensions. Note that the non-trivial fixed point $\bar{u}_0^* = 2d(2 - d)/(3 - 2d)$ is unstable *above* the upper critical dimension $d_c = 2$. This is a signal for a phase transition in $d > 2$: small non-linearity (driving force) is irrelevant, but larger ones flow to strong coupling. Below

$d = 2$, no fixed point is found to $O(\epsilon = 2 - d)$; and \bar{u}_0 always flows to a strong coupling point, and we see that conventional ϵ -expansion fails to give us a controlled expansion. Consequently, the exponents χ and z cannot be calculated in the normal way. Nevertheless through the KPZ analysis we obtain the predictions of a phase transition for $d > 2$, and an exponent identity $\chi + z = 2$ which should be obeyed for all d .

The exponents χ and z can actually be obtained exactly in the special dimensions $d = 0$ and $d = 1$. For $d = 0$ we look at the height fluctuation of a single column. Formally we have from (5.5)

$$\langle h(x, t)h(0, 0) \rangle = t^{\chi/z} f(t/x^z) \sim t^{\chi/z}.$$

Since the addition of particles to the column is random (uncorrelated noise) this process is just a random walk (i.e. $h(t) = \int^t \eta(t') dt'$), giving immediately $\chi/z = 1/2$. This result, coupled with the exponent identity $\chi + z = 2$ yields $\chi = 2/3$ and $z = 4/3$ as $d \rightarrow 0$.

Special simplifications also happen in $d=1$. From (5.10), (5.12) and (5.13) we see that the flow equations for $\bar{\nu}^R$ and \bar{D}^R are the same to one loop order in $d = 1$. In fact, due to a fluctuation-dissipation theorem that holds in $d = 1$ only[59], ν^R and D^R are required to scale the same way to any loop-order. From this requirement we

deduce

$$\frac{d}{dl} \left(\frac{\tilde{D}^R}{\tilde{\nu}^R} \right) = \left(\frac{\tilde{D}^R}{\tilde{\nu}^R} \right) [2 - d - 2\chi] \quad \text{for } d = 1,$$

giving the exact result $\chi = 1/2$ in $d = 1$. The exponent identity then gives the dynamic exponent $z = 3/2$. Note that in this case the exact exponents are obtained even though we do not even have a perturbative knowledge of the fixed point \tilde{u}_0^* .

The prediction of exponents $\chi = 1/2$, $z = 3/2$ in $d = 1$ has since been confirmed by numerous numerical studies[64][65][66][67]. More recently, large scale simulations have been performed in $2 + 1$ and $3 + 1$ dimensions. For $d = 2$, exponent values of $\chi = 0.4$, $z = 1.6$ are found[68][69][70][75], and in $3 + 1$ dimension references [71]–[75] find a phase transition between the ideal flat phase ($\chi = 0$, $z = 2$) and a rough phase described by $\chi = 0.34$ and $z = 1.67$. Clearly the exponents found are all consistent with the identity $\chi + z = 2$, and the phase transition for $d > 2$ is seen as predicted by the theory. Based on the known values of exponents in $d = 1, 2, 3$, Kim and Kosterlitz (KK) conjecture that $\chi = 2/(3 + d)$ for all d [68]. An alternative conjecture by Wulff and Kertesz (WK) is $\chi = 1/(1 + d)$ [67], which however does not give the correct exponent at $d = 0$. Present simulation results are in favor of the KK conjecture, though the results are not precise enough to rule out the WK conjecture.

Before moving onwards to the case of correlated noise, we make one interesting observation: Let us expand the flow equation (5.14) in the vicinity of $d = 0$. The motivation is that the nonlinear interaction which comes in the form of $(\nabla h)^2$ must vanish at $d = 0$ as d is the number of components of $\vec{\nabla} h$. Around $d = 0$, we obtain a

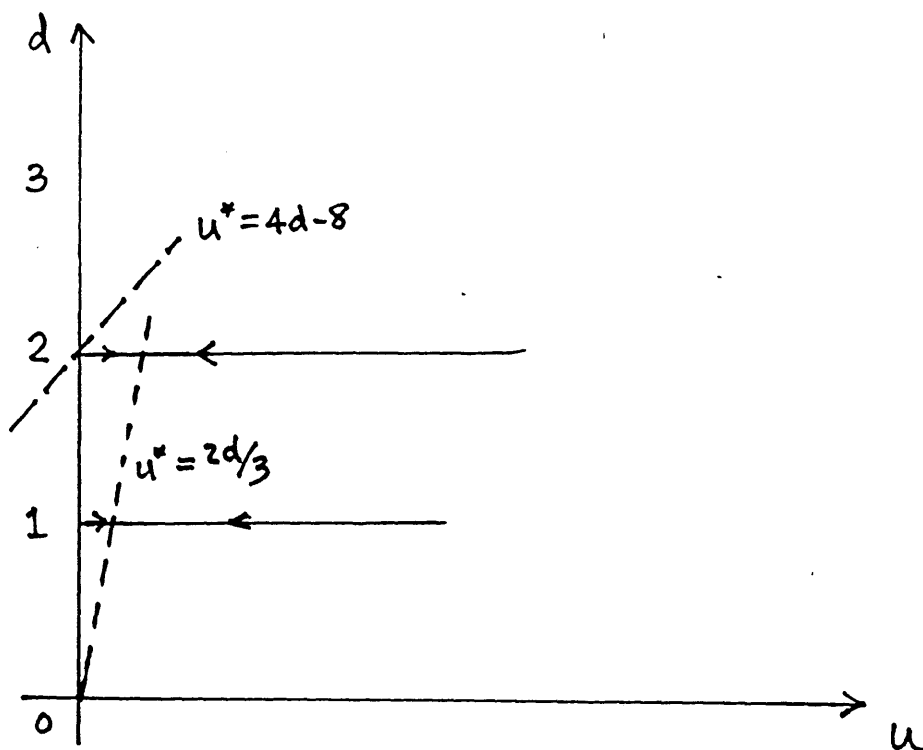


Figure 5.4: A possible RG flow diagram obtained by combining the small d -expansion and the ϵ -expansion.

stable non-trivial fixed point $\tilde{u}_0^* = 2d/3$, and exponents $\chi = 2/3 - 2d/9$, $z = 4/3 + 2d/9$ to first order in d . We have here the possibility of a *controlled* expansion in powers of d . The expressions for exponents agree with the required $\chi/z = 1/2$ at $d = 0$, and in fact match the leading terms of the Kim-Kosterlitz conjecture $\chi = 2/(3 + d)$. This suggests a possible phase diagram sketched in Figure 5.4 in which we see that the “strong coupling” fixed point, not accessible through the conventional $\epsilon = 2 - d$ expansion can now be reached via an expansion around the lower critical dimension $d = 0$. The first-order result has the “strong coupling” fixed point running into the unstable fixed point at $d = 2.4$. It is not known whether the merger of the two

fixed points survives when higher order terms are included. If it does, then we can expect the disappearance of “strong coupling” at higher dimensions. Of course, at this point the expansion about $d = 0$ is only a possible (but tempting) scenario. To say anything more definitive we must analyze the perturbation series in the spirit of section 2.2. In particular we need to learn to calculate higher order loop diagrams in the limit $d \rightarrow \infty$. It should be remarked however, that the small d -expansion is not anymore ad-hoc then the ϵ -expansion since the validity of the latter has not been proven for non-equilibrium systems either.

5.3 Spatial Correlations

We now consider the behavior of Eqs. (5.1) and (5.2) with the noise spectrum given by

$$D(k, \omega) = D_0 + D_\rho k^{-2\rho}. \quad (5.15)$$

As discussed in the appendix, the nonlinearity coefficient λ is not renormalized even in the presence of spatial correlations due to Galilean invariance. Hence we still have the exponent identity and

$$\frac{d\tilde{\lambda}^R}{dl} = \tilde{\lambda}^R [\chi + z - 2]. \quad (5.16)$$

The renormalization of surface tension is calculated just as before but with $D(k, \omega)$ given by (5.15), with the result

$$\nu_R(k) = \nu \left[1 + K_d \frac{\lambda^2 D_0}{\nu^3} \frac{2-d}{4d} \frac{k^{d-2}}{2-d} + K_d \frac{\lambda^2 D_\rho}{\nu^3} \frac{2-d+2\rho}{4d} \frac{k^{d-2-2\rho}}{2-d+2\rho} \right].$$

Defining the dimensionless coupling constants $\tilde{u}_0 = K_d (ae^l)^{2-d} \lambda^2 D_0 / \nu^3$, $\tilde{u}_\rho = K_d (ae^l)^{2-d+2\rho} \lambda^2 D_\rho / \nu^3$ and replacing \tilde{u}_0 , \tilde{u}_ρ , ν by their renormalized counterparts as explained before, we get the recursion relation for $\tilde{\nu}^R(l) = \nu^R(k = ae^l) \cdot (ae^l)^{z-2}$

$$\frac{d\tilde{\nu}^R}{dl} = \tilde{\nu}^R \left[z - 2 + \frac{2-d}{4d} \tilde{u}_0^R + \frac{2-d+2\rho}{4d} \tilde{u}_\rho^R \right]. \quad (5.17)$$

The renormalization for $D(k, \omega)$ is more complicated. Diagrams of the form in Figure 5.2b do not give rise to $k^{-2\rho}$ behavior as $k \rightarrow 0$ for any $D(k)$; such diagram

only renormalize D_0 . D_ρ is in fact not renormalized in the hydrodynamic limit. The recursion relations we obtain after evaluating (5.11) using (5.15) are

$$\frac{d\tilde{D}_\rho^R}{dl} = \tilde{D}_\rho^R [z - 2\chi - d + 2\rho], \quad (5.18)$$

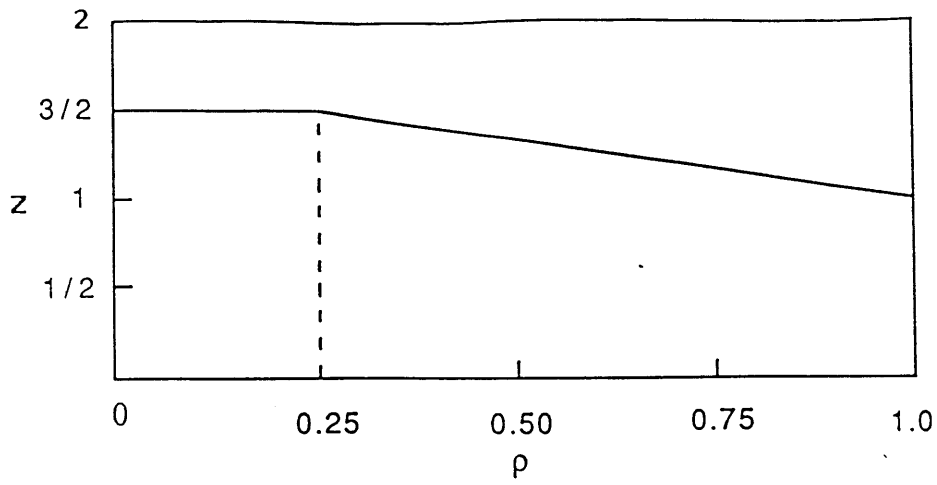
$$\frac{d\tilde{D}_0^R}{dl} = \tilde{D}_0^R [z - 2\chi - d] + \frac{1}{4} (\tilde{u}_0^R \tilde{D}_0^R + \tilde{u}_\rho^R \tilde{D}_\rho^R). \quad (5.19)$$

where $\tilde{D}_\rho^R = D_\rho^R (ae^l)^{2\rho-d-2\chi+z}$ is again a dimensionless variable. Note in (5.19) that white noise D_0^R will be generated by D_ρ even if it is not initially present.

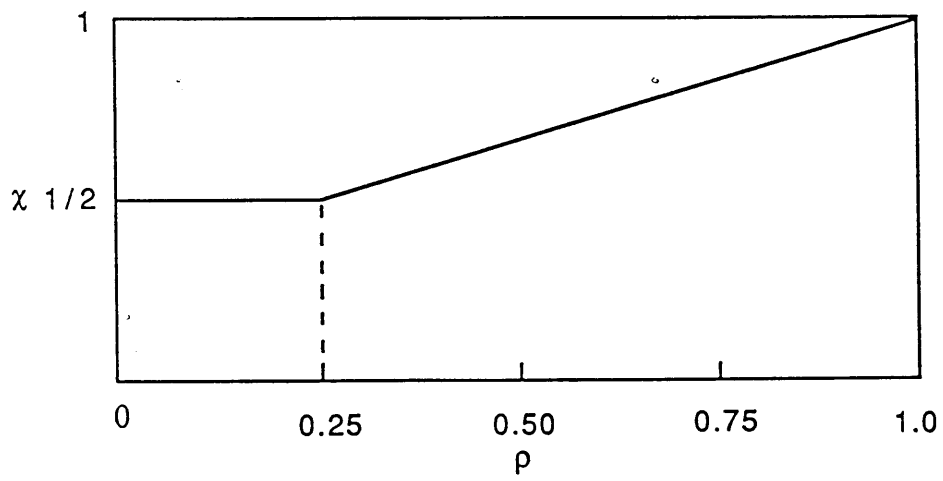
The flow equations (5.16)–(5.19) seem very complicated; but they can be solved exactly if the white noise limit values of χ_w and z_w are known exactly. In $d = 1$ with $z_w = 3/2, \chi_w = 1/2$, (5.18) becomes

$$\frac{d\tilde{D}_\rho}{dl} = \tilde{D}_\rho \left[-\frac{1}{2} + 2\rho \right].$$

Hence, D_ρ is irrelevant for $\rho < 1/4$ and the exponents are those with white noise present only. However for $\rho > 1/4$ (5.18) requires that $z - d - 2\chi + 2\rho = 0$ to have \tilde{D}_ρ^R fixed. This coupled with the identity $\chi + z = 2$ immediately allows us to solve for the exponents exactly: $\chi(\rho) = 1 + 2\rho/3$ and $z(\rho) = 5 - 2\rho/3$ for $\rho > 1/4$ in $d = 1$. The behavior of the exponents as a function of ρ is plotted in Figure 5.5. Recently, the predicted exponent values $\chi(\rho)$ and $z(\rho)$ have also been tested and confirmed through numerical simulations of Meakin and Jullien[56]. In fact the interfaces shown in Figure 4.16a and Figure 4.16b are results of such simulations with



(a)



(b)

Figure 5.5: (a) Dynamic exponent z and (b) roughening exponent χ as a function of the exponent ρ for decay of spatial correlations in $d = 1$.

$\rho = 0$ and $\rho = 1$ respectively. It is clear that the surface growth under correlated noise (Figure 4.16b) is much rougher than the one with uncorrelated noise; the dependence is given by $\chi(\rho)$ in Figure 5.5b.

Finally, we repeat the above exercise with $\chi_w = 2/3 - 2d/9$ and $z_w = 4/3 + 2d/9$, the results of the small d -expansion. In such a case, \tilde{D}_ρ^R is irrelevant for $\rho < \rho_c = d/6$. Beyond that, $\chi(\rho, d) = 2 - d - 2\rho/3$ and $z(\rho, d) = 4 + d - 2\rho/3$. The result that $\rho_c \rightarrow 0$ as $d \rightarrow 0$ contradicts a recent conjecture of Zhang[76] (based on replica arguments) that $\rho_c = 1/4$ for all dimensions d . A number of other consequences of the small d -expansion remain to be worked out.

5.4 Temporal Correlations

We next turn our attention to the case of noise with temporal correlations, i.e.,

$$D(\vec{k}, \omega) = D_0 + D_\theta \omega^{-2\theta} \quad (5.20)$$

Temporal correlations can arise in a number of situations: One possibility is relatively immobile impurities in the path of the interface that get trapped and impede further growth. Another possible case is when there are charged ions that become part of the interface and effect further growth via the long range Coulomb interaction.

In normal (equilibrium) field theories (and also in the case of spatial correlation encountered in the last section), it is often the leading order term (in $k, \omega \rightarrow 0$) that determines the scaling behaviors in the hydrodynamic regime. We will see in this section that the subleading terms (e.g. the D_0 term in (5.20)) can also influence the scaling behavior. In fact, the entire fixed function $D^*(\omega)$ must be determined in order to obtain the scaling properties of the surface in the presence of temporal correlations. Also, in the extreme limit of $\theta = 1/2$, Eqn. (4.19) tells us that the noise becomes permanently correlated, i.e., $\langle \eta(x, t) \eta(x', t') \rangle \sim \delta^d(x - x')$, an example of quenched randomness which appears in a wide variety of localization problems. Systems with quenched disorder are difficult to study, here we show that they can be accessed as the limit of temporally correlated stochastic noise.

Using (5.20) for $D(\vec{k}, \omega)$, we obtain the recursion relations:

$$\frac{d\tilde{\nu}^R}{dl} = \tilde{\nu}^R \left[z - 2 + \tilde{u}_0^R \frac{2-d}{4d} + \tilde{u}_\theta^R \frac{2-d}{4d} (1+2\theta) \sec(\pi\theta) \right], \quad (5.21)$$

$$\frac{d\tilde{\lambda}^R}{dl} = \tilde{\lambda}^R \left[\chi + z - 2 - \tilde{u}_\theta^R \frac{\theta}{d} (1+2\theta) \sec(\pi\theta) \right], \quad (5.22)$$

$$\frac{d\tilde{u}_\theta^R}{dl} = \tilde{u}_\theta^R [z(1+2\theta) - 2\chi - d], \quad (5.23)$$

$$\begin{aligned} \frac{d\tilde{u}_0^R}{dl} = & \tilde{u}_0^R [z - 2\chi - d] + \frac{1}{4}(\tilde{u}_0^R)^2 + \frac{1}{2}\tilde{u}_0^R \tilde{u}_\theta^R (1+2\theta) \sec(\pi\theta) \\ & + \frac{1}{4}(\tilde{u}_\theta^R)^2 (1+4\theta) \sec(2\pi\theta), \end{aligned} \quad (5.24)$$

valid for $\theta < 1/4$. Note that in the absence of temporal correlations, i.e. $\theta = 0$, the correction term to the vertex in Eq. (5.22) vanishes as required by Galilean invariance.

As in the case of spatially correlated noise, \tilde{u}_θ^R does not get renormalized because diagrams such as Figure 5.2b do not generate a $\omega^{-2\theta}$ term in $\omega \rightarrow 0$ limit. Using $z_w = 3/2$ and $\chi_w = 1/2$ for $d = 1$ in (5.23), we find that \tilde{u}_θ is irrelevant for $\theta < \theta_c = 1/6$. Hence we recover the white noise behavior for weakly correlated temporal noise, just like the case with weakly correlated spatial noise. Using $\chi_w = 2/3 - 2d/9$ and $z_w = 4/3 + 2d/9$ from the small d -expansion, we get $\theta_c = d/8$. For $\theta > \theta_c$, the behavior of the system is dominated by the temporally correlated noise, and Eqn. (5.23) gives the exponent identity $z(1+2\theta) - 2\chi - d = 0$ at the fixed point of RG flow. However temporal correlation destroys the Galilean invariance (see the appendix) and we *no longer* have $\chi + z = 2$ as evidenced in the recursion relation (5.22) for $\tilde{u}_\theta^R \neq 0$. Some work is then required to extract the exponents $z(\theta)$ and $\chi(\theta)$ out of the recursion

relations. Eqs. (5.21)–(5.24) can be solved systematically for small d . However, to see the generic structure of the solution and to gain some insight into the role of temporal correlations, we shall study the one-loop recursion relation evaluated at $d = 1$ in some detail.

After eliminating z and χ with the fixed point conditions $d\tilde{\lambda}^R/dl = 0$ and $d\tilde{\nu}^R/dl = 0$, we have

$$\begin{aligned}\frac{d\tilde{u}_\theta^R}{dl} &= \tilde{u}_\theta^R \left[(1 + 4\theta) - \frac{3 + 2\theta}{4} \tilde{u}_0^R - \tilde{u}_\theta^R \sec(\pi\theta)(1 + 2\theta) \frac{3 + 10\theta}{4} \right], \\ \frac{d\tilde{u}_0^R}{dl} &= \tilde{u}_0^R - \frac{1}{2}(\tilde{u}_0^R)^2 - \tilde{u}_0^R \tilde{u}_\theta^R \sec(\pi\theta)(1 + 2\theta) \frac{1 + 8\theta}{4} - \frac{1}{2}(\tilde{u}_0^R)^2 + (\tilde{u}_\theta^R)^2 \sec(2\pi\theta) \frac{1 + 4\theta}{4}.\end{aligned}$$

A stable fixed point in the physical region (i.e. $\tilde{u}_0^R \geq 0$, $\tilde{u}_\theta^R \geq 0$) is found for $0 \leq \theta < 1/4$; the resulting exponents $z(\theta)$ and $\chi(\theta)$ are plotted. As shown in Figure 5.6, the exponents increase for a range of $\theta > \theta_c(d = 1) = 1/6$; but then they turn around and nose-dives as $\theta \rightarrow 1/4$. Beyond $\theta = 1/4$, no stable point in the physical region is found in $(\tilde{u}_0^R, \tilde{u}_\theta^R)$ space.

The behavior close to $\theta = 1/4$ is very suspicious, as physically there should be nothing special at $\theta = 1/4$. The source of such peculiarity is the infrared divergence of the integral (5.11) as $\theta \rightarrow 1/4$. In fact, the renormalized noise spectrum $D^R(\omega)$ has a component $\omega^{1-4\theta}$ which becomes “non-ignorable” as $\theta \rightarrow 1/4$. The renormalized spectrum is of the form $D^R(\omega) = D_0 + D_1\omega^{-2\theta_1} + D_2\omega^{-2\theta_2}$ where $\theta_2 = 2\theta_1 - 1/2$. However with this new form, even more components are generated from the contractions $\overline{D_1 D_2}$ and $\overline{D_2 D_2}$. By simple power counting, the contraction between $D_i\omega^{-2\theta_i}$

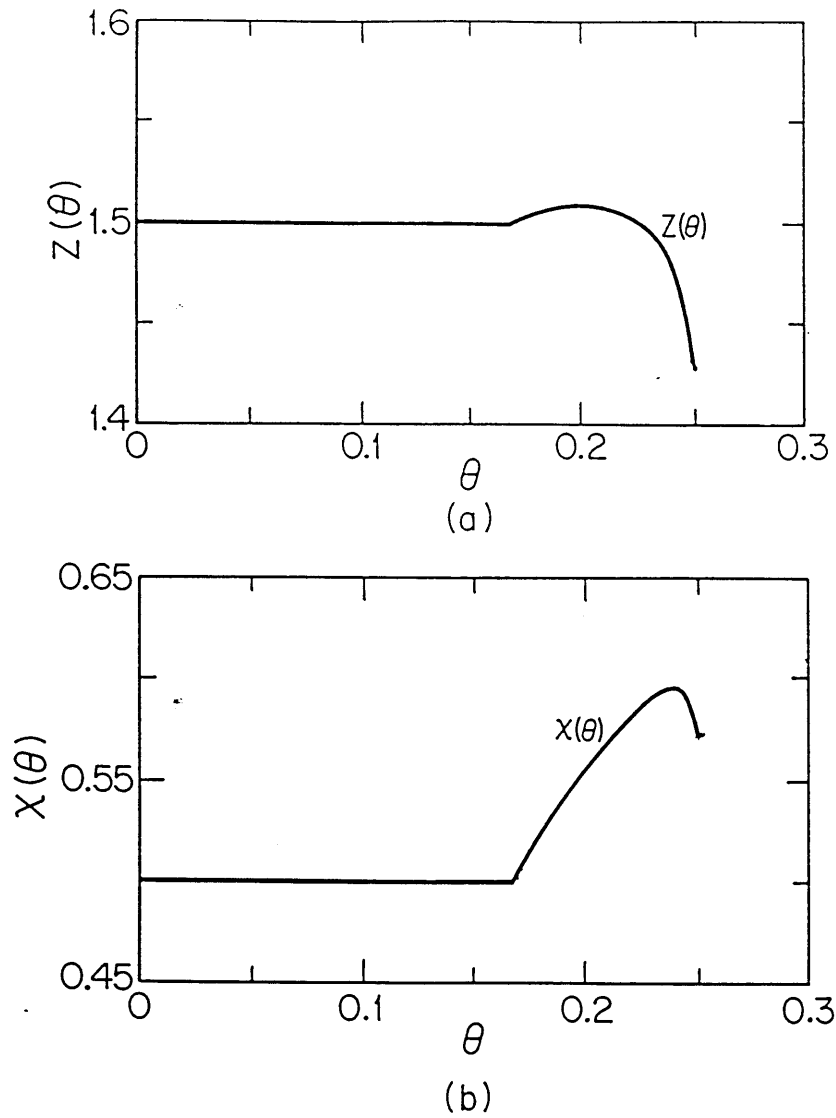


Figure 5.6: (a) Dynamical exponent z and (b) roughening exponent χ as a function of the exponent θ for the decay of temporal correlations in $d=1$. The solution diverges as $\theta \rightarrow 1/4$.

and $D_j \omega^{-2\theta_j}$ terms is

$$\overline{D_i(\omega)D_j(\omega)} = A(i, j)D_i D_j \omega^{1-2\theta_i-2\theta_j} + B(i, j)D_i D_j, \quad (5.25)$$

where $A(i, j)$ and $B(i, j)$ are integration constants. We can denote the new power generated in the same form, $\omega^{-2\theta_{i+j}}$, with $\theta_{i+j} = \theta_i + \theta_j - 1/2$. If the most divergent part of $D(\omega \rightarrow 0)$ is characterized by $\omega^{-2\theta}$, then terms generated by RG are $\omega^{-2\theta_n}$ with $\theta_n = n\theta - \frac{n-1}{2}$, and the fixed function is of the form $D^R(\omega) = D_0^R + \sum D_n^R \omega^{-2\theta_n}$. The number of divergent terms, $M(\theta)$ in the sum is the largest n for which $\theta_n > 0$, i.e.,

$$M(\theta) = \text{Int} \left(\frac{1}{1-2\theta} \right). \quad (5.26)$$

As θ increases from 0 to 1/2, a new divergent term is added to the renormalized noise spectrum whenever $\theta_n(\theta^*) = 0$, where the special values θ^* 's are

$$\theta^* = \frac{n-1}{2n} = 0, \frac{1}{4}, \frac{2}{6}, \frac{3}{8}, \frac{4}{10}, \dots$$

So the unphysical behavior obtained close to $\theta = 1/4$ is a reflection of the emergence of the next divergent term in the fixed function $D^R(\omega)$.

Obviously, the RG flow space must be expanded for an improved treatment. The relevant integral for the noise contraction (5.11) has been computed in reference [18];

the coefficients $A(i, j)$ and $B(i, j)$ in (5.25) are found to be

$$A(i, j) = \frac{4 \sin(\pi\theta_i) \sin(\pi\theta_j) \Gamma(1 - 2\theta_i) \Gamma(1 - 2\theta_j)}{\pi \sin(\pi\theta_{i+j}) \Gamma(1 - 2\theta_{i+j})}$$

$$B(i, j) = (1 + 2\theta_i + 2\theta_j) \sec \pi(\theta_i + \theta_j)$$

for $\theta_{i+j} \neq 0$. The two terms conspire to give $\log(\omega)$ when $\theta_{i+j} = 0$.

Incorporating these results, we try a fixed function of the form

$$D_\theta(\omega) = D_0 + \sum_{n=1}^{N_{max}} \pi D_n \frac{(\omega/\omega_0)^{-2\theta_n} - (1 + 2\theta_n) \sec(\pi\theta_n)}{\Gamma(1 - 2\theta_n) \sin(\pi\theta_n)},$$

with $\theta_n = n\theta - (n - 1)/2$ and the value of the cutoff, N_{max} , will be discussed later.

(Note that this form has the desired logarithms built in when $\theta_n = 0$.) The recursion relations become

$$\frac{d\tilde{\nu}^R}{dl} = \tilde{\nu}^R \left\{ z - 2 + \frac{2-d}{4d} \tilde{u}_0^R \right\},$$

$$\frac{d\tilde{\lambda}^R}{dl} = \tilde{\lambda}^R \left\{ \chi + z - 2 - \frac{1}{d} \left[\sum_{n=1}^{N_{max}} \tilde{u}_n^R \Gamma(2 + 2\theta_n) \right] \right\},$$

$$\frac{d\tilde{u}_1^R}{dl} = \tilde{u}_1^R [z(1 + 2\theta) - 2\chi - d],$$

$$\frac{d\tilde{u}_n^R}{dl} = \tilde{u}_n^R [z(1 + 2\theta_n) - 2\chi - d] + \sum_{\substack{i,j=1 \\ (i+j=n)}}^{N_{max}} \tilde{u}_i^R \tilde{u}_j^R,$$

$$\frac{d\tilde{u}_0^R}{dl} = \tilde{u}_0^R (z - 2\chi - d) + \frac{(\tilde{u}_0^R)^2}{4} + 4z\theta \sum_{n=1}^{N_{max}} \tilde{u}_n^R (1 + 2\theta_n) \Gamma(2\theta_n)$$

$$+ 2[z(1 + 2\theta) - 2\chi - d] \sum_{n=1}^{N_{max}} \tilde{u}_n^R (n - 1)(1 + 2\theta_n) \Gamma(2\theta_n)$$

$$+ \sum_{i,j=1}^{Nmax} \tilde{u}_i^R \tilde{u}_j^R \Gamma(2\theta_i) \Gamma(2\theta_j) \left\{ (1 + 2\theta_i + 2\theta_j) \frac{\cos(\pi\theta_i) \cos(\pi\theta_j)}{\cos(\pi(\theta_i + \theta_j))} - (1 + 2\theta_i)(1 + 2\theta_j) \right\},$$

where the identity $\Gamma(z)\Gamma(1-z) = \pi / \sin(\pi z)$ is used, and $\tilde{u}_i^R \equiv [(\tilde{\lambda}^R)^2 \tilde{D}_i^R / (\tilde{\nu}^R)^3] K_d(ae^l)^{2-d+2z\theta}$ as before.

The condition $d\tilde{u}_1^R/dl = 0$ implies $2\chi + d = z(1 + 2\theta)$ for $\theta > \theta_c$. So

$$\begin{aligned} \frac{d\tilde{u}_n^R}{dl} &= \tilde{u}_n^R z(2\theta_n - 2\theta) + \sum_{i+j=n} \tilde{u}_i^R \tilde{u}_j^R \\ &= \tilde{u}_n^R z(2\theta - 1)(n - 1) + \sum_{i+j=n} \tilde{u}_i^R \tilde{u}_j^R. \end{aligned}$$

By setting $d\tilde{u}_n^R/dl = 0$, it is easy to verify that

$$\tilde{u}_n^R = [z(1 - 2\theta)]^{-n+1} (\tilde{u}_1^R)^n.$$

Hence we can describe the fixed function $D^R(\omega)$ by two parameters, D_0^R and D_θ^R , as:

$$D_\theta^R(\omega) = D_0^R + \sum_{n=1}^{Nmax} \frac{\pi (D_\theta^R)^n}{[z(1 - 2\theta)]^{n-1}} \left[\frac{(\omega/\omega_0)^{-2\theta_n} - (1 + 2\theta_n) \sec(\pi\theta_n)}{\Gamma(1 - 2\theta_n) \sin(\pi\theta_n)} \right].$$

The exponents χ and z are calculated from

$$z = 2 - \frac{2-d}{4d} \tilde{u}_0^*, \quad (5.27)$$

$$\chi = \frac{2-d}{4d} \tilde{u}_0^* + \frac{1}{d} \sum_{n=1}^{Nmax} \tilde{u}_n^* \Gamma(2 + 2\theta_n), \quad (5.28)$$

with

$$\tilde{u}_n^* = \frac{(\tilde{u}_\theta^*)^n}{[z(1-2\theta)]^{n-1}}, \quad \text{and} \quad 2\theta_n = 1 - n(1-2\theta), \quad (5.29)$$

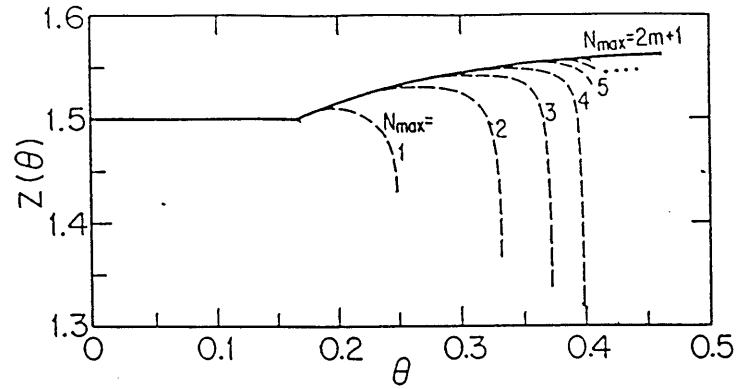
where the fixed points \tilde{u}_0^* and \tilde{u}_θ^* are found from the flow equations:

$$\begin{aligned} \frac{d\tilde{u}_\theta^R}{dl} &= \tilde{u}_\theta^R [z(1+2\theta) - 2\chi - d], \quad (5.30) \\ \frac{d\tilde{u}_0^R}{dl} &= \tilde{u}_0^R (z - 2\chi - d) + \frac{(\tilde{u}_0^R)^2}{4} + 4z\theta \sum_{n=1}^{N_{max}} \tilde{u}_n^R (1+2\theta_n) \Gamma(2\theta_n) \\ &\quad + 2[z(1+2\theta) - 2\chi - d] \sum_{n=1}^{N_{max}} \tilde{u}_n^R (n-1)(1+2\theta_n) \Gamma(2\theta_n) \quad (5.31) \\ &\quad + \sum_{i,j=1}^{N_{max}} \tilde{u}_i^R \tilde{u}_j^R \Gamma(2\theta_i) \Gamma(2\theta_j) \left\{ (1+2\theta_i + 2\theta_j) \frac{\cos(\pi\theta_i) \cos(\pi\theta_j)}{\cos(\pi(\theta_i + \theta_j))} - (1+2\theta_i)(1+2\theta_j) \right\}. \end{aligned}$$

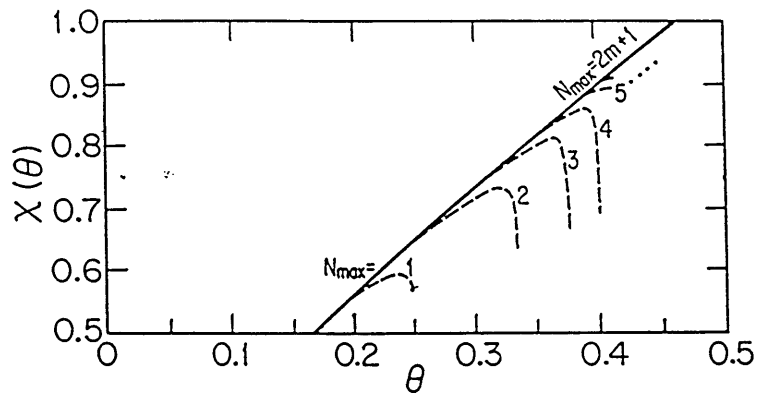
The terms that seem to diverge as $\theta_n \rightarrow 0$ in the last equation cancel each other; and Eqs. (5.27) - (5.31) can be solved numerically in the range $0 \leq \theta < 1/2$ once N_{max} is defined, and the resulting exponents $z(\theta)$ and $\chi(\theta)$ for various N_{max} are shown in Figure 5.7a and Figure 5.7b. We observe that in the region with $M(\theta)$ divergent terms as given by Eq. 5.26, at least $M(\theta)$ terms are necessary to find fixed points and exponents at all; beyond that the convergence of the series is rather fast.

The calculation becomes increasingly difficult to carry out as $\theta \rightarrow 1/2$ because $M(\theta) \sim (1-2\theta)^{-1} \rightarrow \infty$. However the results obtained for $d = 1$ have χ exceeding 1 at $\theta = 0.46$; so the theory is not valid for θ close to $1/2$, since $\chi > 1$ would invalidate the ∇h expansion as explained in Chapter 4.

As mentioned at the begining of this section, $\theta = 1/2$ corresponds to the interesting limit of quenched impurities. It so happens that χ exceeds 1 before θ reaches $1/2$ for



(a)



(b)

Figure 5.7: Same exponents as in Figure 5.6, but including more and more powers θ_n , generated by renormalization of the noise spectrum $D^R(\omega)$. The exponents are found to converge rapidly upon including more powers.

the case of $d = 1$. In higher dimension ($d > 2$), χ will be significantly reduced, and the analysis sketched in this section may provide a controlled way of accessing the quenched randomness limit.

A very important lesson we learned by going through this tedious exercise is that the sub-leading terms in $D(k, \omega)$, which are normally not relevant in determining the asymptotic scaling behaviors in the hydrodynamic limit, must nevertheless be treated systematically. A priori, one does not know whether the subleading terms (in the hydrodynamic limit) may contribute to the leading scaling behavior. In the spatial correlation case, such terms make no difference, because they do not enter the equations determining the exponents; there they only change the position of the fixed points. Similarly, such subleading terms do not affect the leading scaling behavior in simple field theories such as the ϕ^4 -theory. However, we see that they do make a difference in the case of strong temporal correlations. Here the knowledge of the entire fixed function $D^*(\omega)$ is needed in order for the RG procedure to be consistent. This makes the calculations (recursion relations) much more complicated, though the principle is simple as before. Two straight forward predictions are (1) breaking of the Galilean invariance ($\chi + z = 2$) and (2) the exponent identity $z(1 + 2\theta) - 2\chi = d$. It would be interesting to test these numerically.

Appendix: Galilean Invariance

The Burgers' equation (5.4) has a Galilean invariance associated with looking at the fluid in a moving frame. Hence the transformation[59]

$$\vec{v}(\vec{x}, t) \rightarrow \vec{v}_0 + \vec{v}'(\vec{x} - \vec{v}_0 t, t),$$

is an exact symmetry of the equation (with $\lambda = 1$). For the KPZ equation (5.1), this symmetry corresponds to the infinitesimal reparametrization

$$h' = h + \vec{\epsilon} \cdot \vec{x}, \quad \vec{x} = \vec{x}' + \lambda \vec{\epsilon} t', \quad t = t', \quad (5.32)$$

which describes the tilting of the interface by a small angle $\vec{\epsilon}$. The tilted surface to $O(\epsilon)$ satisfies the equation

$$\frac{\partial h'}{\partial t'} = \nu \nabla'^2 h' + \frac{\lambda}{2} (\nabla' h')^2 + \eta(\vec{x}' + \lambda \vec{\epsilon} t', t').$$

Clearly the deterministic equation is invariant under this transformation, while the stochastic equation is subject to a noise $\eta'(\vec{x}', t') = \eta(\vec{x}' + \lambda \vec{\epsilon} t', t')$. Let us examine the correlations in the noise η' :

$$\begin{aligned} \langle \eta'(\vec{x}_1, t_1) \eta'(\vec{x}_2, t_2) \rangle &= \langle \eta(\vec{x}_1 + \lambda \vec{\epsilon} t_1, t_1) \eta(\vec{x}_2 + \lambda \vec{\epsilon} t_2, t_2) \rangle \\ &= F(\vec{x}_1 - \vec{x}_2 + \lambda \vec{\epsilon}(t_1 - t_2), t_1 - t_2). \end{aligned} \quad (5.33)$$

Here F measures the noise correlations, in the original equation. In the absence of temporal correlations $F(\vec{x}, t) = \delta(t)F(\vec{x})$ and from Eqn. (5.33), we observe that the correlations for the new noise η' are identical to that in the original equation; i.e.

$$F'(\vec{x}, t) = F(\vec{x} + \lambda\vec{\epsilon}t, t) = \delta(t)F(\vec{x} + \lambda\vec{\epsilon}t) = \delta(t)F(\vec{x}).$$

This invariance is no longer true if $F(\vec{x}, t)$ is not proportional to $\delta(t)$. Therefore the stochastic equations is invariant under Galilean transformations, only if the noise has no temporal correlations.

Note that the parameter λ appears both as the coefficient of the nonlinearity in Eqn. (5.25); and as an inherent factor relating to \vec{x} and t reparametrizations in Eqn. (5.32). Hence any renormalization of the KPZ equation that preserves Galilean invariance must leave the coefficient λ unchanged. Due to the absence of corrections, Eqn. (5.13) is exact, leading to the exponent identity

$$\chi + z = 2$$

in the absence of temporal correlations.

Chapter 6

Self-Organized Critical

Phenomena

6.1 Introduction

The interface profiles obtained from growth (Figure 4.16) are reminiscent of landscapes seen in nature. In fact, the world we live in is full of complex spatial structures such as mountain ranges, river networks, coastlines, and clouds[12]. Because these objects do not lend themselves readily to “clean” geometrical descriptions, they have eluded the pursuit of analytically minded scientists for centuries. On the other hand, low frequency noise (known as $1/f$ noise) appears in resistance fluctuations[13][77], sand flow in hourglasses[78], and even in traffic and stock market movements[79]. The ubiquity of such broad-band noise have also puzzled the scientific community for a long time.

During the past 10-20 years, we learned to characterize the geometrical aspects of fuzzy and ragged natural landscapes using the concept of fractals, largely through the work of Mandelbrot[12]. There has since been an explosion of “fractal”-motivated studies. Literally speaking, everywhere we look, we find fractals:[5] the structures of colloidal aggregates, patterns of fracture/dielectric breakdown, porosity of soil, and branching of roots, to name a few. Fractal concepts have since been extended to describe a wide variety of other systems in physics: Chaotic dynamics in meteorology[80], star-flicker in astronomy[81], hadron-production in particle physics[82], etc.

It should be noted however, that the studies of fractals have been done mostly at the level of *characterization*: Results of experiments and simulations on these systems are plotted on a log-log scale. If a straight line is obtained, then the slope is related to

some fractal dimension of the system. The answers to general questions of how fractal structures arise and what various fractal dimensions should be, have been lacking. In this chapter, we attempt a systematic investigation of such questions by studying a specific model.

It is well known that many functional dependences look like straight lines when variables are plotted on a log-log scale. The lone, obvious class of exceptions being the exponential functions, or functions with an unambiguous scale. So fractal systems are those that lack natural scales; and the question “why such an abundance of fractal systems?” is to first approximation, “why so many systems behave as if they do not have natural time and/or length scales?”

Systems without natural scales are also known as scale-invariant or self-similar. The analytical tools for dealing with simple scale-invariant systems have been developed from the studies of critical phenomena, and have already been extensively used in the previous chapters. However, in conventional critical phenomena, scale-invariance/self-similarities are only exhibited at a few isolated points (critical points) in the parameter space of the system under study[1]. In contrast systems in nature can exhibit self-similarity without any tuning of parameters. For this reason, this type of phenomena has been given the name “Self-Organized Critical Phenomena” (SOC)[14].

Previous experience strongly suggests that whenever there is an invariance law, there is usually some general principle behind it. For example, in classical mechanics,

the invariance of the total momentum of a closed system is attributed to the translational symmetry in space. Here, we naturally suspect that scale invariances seen in SOC systems also come from certain underlying principles.

Of course, SOC is not an exotic or mystical class of phenomena, though specific SOC models may possess one or more unique features. To take the most trivial case, the stochastic dynamics of a free surface described in section 4.2 is scale-invariant both in space and time (i.e. it is critical); furthermore, criticality for the free surface is obtained without tuning of any parameters, therefore this system may be called SOC.

For a less trivial example of SOC, let us reconsider the growth process described in Chapter 5. As is evident from Fig. 4.16, the surfaces grown exhibit self-similarity without tuning of any parameters. Analytically, the growth process is described by the KPZ equation[10],

$$\frac{\partial h}{\partial t} = \nu \nabla^2 h + \frac{\lambda}{2} (\nabla h)^2 + \eta(\vec{x}, t),$$

which is explicitly scale invariant as manifested by the absence of a $-h/\tau$ term. As carefully explained in the derivation of the KPZ equation in Chapter 4, the $-h/\tau$ term is excluded from the equation of motion because it is incompatible with the translational symmetry, $h \rightarrow h + \text{constant}$, present in the process. We therefore identify the translational symmetry of the surface along the growth direction as the principle responsible for the scale-invariance of the height profile. Once criticality of the

theory is established, we can calculate the scaling exponents (χ, z) for the dynamical field as shown in Chapter 5. With the knowledge of the basic exponents χ and z , we can proceed to calculate other interesting scaling properties. For example, if we are interested in the spatial organization, we can “flood” the 2+1 dimensional landscape with water and look for the fractal dimension of resulting islands; there we find the fractal dimension of the coastlines (of the islands) to be $D_f = 2 - \chi$ [12]. Using the result of small d -expansion for χ , we get an estimate of $D_f = 1.78$ in $d = 2$. Results of latest simulations ($\chi=0.4$) would give a coastline dimension of 1.6.

The growth problem is especially suitable for the visualization of spatial, fractal structures, but it is not a natural system to study if one is interested in $1/f$ noise.¹ Since these low frequency fluctuations often make their appearance in transport processes, we hope to gain insight by studying such phenomena. In section 6.2, we investigate dissipative transport and avalanches using a sandpile automaton. We show that the behavior of the automaton is qualitatively similar to that of the real sand[83], and point out that the scaling regime relevant to $1/f$ noise is the hydrodynamic region. In section 6.3, we analyze the transport properties in this region using the method of dynamical renormalization group.

¹By $1/f$ noise, we mean noise with any power-spectra $S(f) \sim 1/f^\phi$ where $0 < \phi < 2$.

6.2 The Sandpile Model

An interesting model of dissipative transport is the sandpile automata recently proposed by Bak, Tang, and Wiesenfeld (BTW)[14]. The study reported here was inspired by the BTW model. We start with a brief description of the model and present simulation results for a 1D system. Analysis of the automaton model and its outputs reveals various scaling regions : there is a short time region in which temporal fluctuations are dominated by single avalanche events. At a longer time scale, we observe interactions among the avalanches. At yet longer time scales, these interactions are wiped out by system-size discharges (great events). However, due to a memory effect attributed to the threshold nature of the model, even the great events are non-trivially correlated (they are anti-correlated). It is only on time scales exceeding the “memory capacity” of the system that the activities finally become uncorrelated.

The single avalanche region is related to a directed percolation problem, and has been studied by a number of authors[84][85][86]. Interaction among avalanches provides rich, temporal structures, and leads to $1/f$ -type noise. There are similarities to aftershocks in earthquakes, and shock waves in fluid mechanics. The behavior in this region is treated in detail in section 6.3. We show that scaling in the hydrodynamic region is a consequence of conservation laws in the transport dynamics. The existence of a great event region is an unique feature of highly dissipative systems (such as the sandpile automaton) with many metastable states. Similar great events have been

observed in recent studies of models of earthquakes[87] and charge-density waves[88]. These events are found to be temporally anti-correlated due to the threshold nature of the dynamics. We will provide a simple scaling description from which we can understand the underlying mechanism of their generation. Similar behaviors are found in preliminary simulations of 2D automata. We show that the generic behavior found in simulation is similar to those found in experiments of real sand[83], thus dispelling the notion that the sandpile automata do not describe real sand.

6.2.1 The Automaton

Recent interest in the phenomena of SOC springs from a series of very interesting numerical studies on a sandpile cellular automaton invented by BTW[14]. The model leads to some very important issues in dissipative transport in open environments, and is very much worthy of investigation. In the following, we describe the results of simulations of two generalized versions of the BTW sandpile with open boundaries. The discussion is mostly limited to the 1D case, though the argument is general and valid in higher dimensions.

We consider a sandpile defined on a 1-dimensional lattice of length L . Associated with each lattice site n is a variable $H(n, t)$ representing the height of the local sand column, (see Figure 6.1). $H(n, t)$ is an integer in the discrete model of section 6.2.2, but is a real variable for the continuum model of section 6.2.3. Following the generalization of the BTW rule to 1D by Kadanoff *et al*[89] we adopt the following

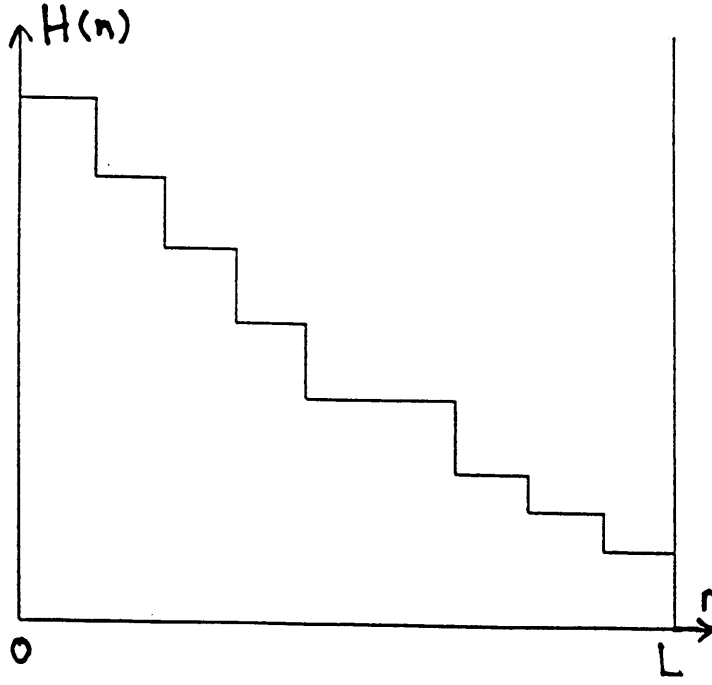


Figure 6.1: A 1 + 1-dimensional sandpile automaton.

evolution rule:

$$\begin{aligned}
 H(n, t + 1) &= H(n, t) - N_f \\
 H(n + 1, t + 1) &= H(n + 1, t) + N_f \\
 &\text{iff } H(n, t) - H(n + 1, t) > \delta H_c.
 \end{aligned}
 \tag{6.1}$$

As reported in reference [89], the scaling behaviour of the system is independent of the values of N_f and δH_c as long as $N_f \geq 2$ and $\delta H_c \geq 2N_f$. In our study, we use $N_f = 2, \delta H_c = 8$ without loss of generality. The boundary at $n = 0$ is kept closed, while the boundary at $n = L$ is open, i.e. $H(0) = H(1)$, and $H(L + 1) = 0$.

The transport process is initiated by depositing sand grains into the system at a rate J_{in} . The activity of the system is monitored by recording the output current $J(t)$ (the number of sand grains leaving the system) and the instantaneous energy

dissipation rate $E(t)$ (the total number of transport activities at each time step). But before describing our simulation result in detail, we first briefly summarize known results. BTW and a number of other authors[89][90][91][92][93][94] have studied the sandpile model in the limit of zero deposition rate, i.e. $J_{\text{in}} \rightarrow 0^+$. In this limit, the response to a single addition of a sand grain can be characterized by identifying the size ($s = \int E(t)dt$) and duration (T) of the “avalanche” resulting from a single addition. In steady-state, these authors observed the signatures of criticality: power law scaling of the distribution function, i.e.

$$D(T) = T^{-\alpha} F(T/L^\sigma), \quad (6.2)$$

$$D(s) = s^{1-\tau} G(s/L^{D_f}). \quad (6.3)$$

Finite-size scaling then yields the dynamical exponent σ , and the “fractal dimension” of avalanches D_f . In fact, the distribution functions may well be more complicated (i.e. multifractal) as indicated in reference [89]. But these simple scaling laws work well for $s \ll L$. (The multifractal aspect will be discussed later.)

Tang and Bak (TB)[90] suggested that the scaling behaviour observed can be thought of as critical phenomena with the average output current $\langle J_{\text{out}} \rangle$ being an order parameter. The sandpile model adjusts itself (self-organizes) to a critical slope at which $\langle J_{\text{out}} \rangle \rightarrow 0^+$. TB also pointed out that if $\langle J_{\text{in}} \rangle$ (and therefore $\langle J_{\text{out}} \rangle$) is finite, then the avalanche clusters will overlap (much like a percolating system beyond the percolation threshold), resulting in a length scale $\xi \sim J^{-\nu/\beta}$ and associated with it

a time scale $\sim \xi^\sigma$. TB claimed that the existence of such scales would then destroy scale-invariance and criticality.

One of the major criticisms of the BTW study is their limitation to the special limit $J_{\text{in}} \rightarrow 0^+$: Indeed, by the definition of steady-state $\langle J_{\text{out}} \rangle = \langle J_{\text{in}} \rangle$, the order-parameter $\langle J_{\text{out}} \rangle$ is indirectly *tuned* by $\langle J_{\text{in}} \rangle$. If the existence of criticality does depend so sensitively on a very small input rate (driving force), then it becomes very puzzling to confront many systems in nature (e.g. water flow in rivers[80] and electron flow in resistors[77]) that do exhibit $1/f$ noise in the presence of obvious driving forces. It is the purpose of our numerical study to demonstrate the fact that critical scaling is *not* destroyed by a finite driving force; rather, we show that interesting temporal fluctuations such as $1/f$ noise only appear in the presence of a finite external driving force J_{in} .

Let us first quantify how small J_{in} must be for avalanche clusters not to overlap each other: An avalanche in the one-dimensional model can be represented as a parallelogram in space-time as shown in Figure 6.2. The width at each time cross-section (t) is the number of active sites $E(t)$ (flame front, or instantaneous energy dissipation). The length is the avalanche duration (T), and the total shaded area is the total size of the avalanche cluster s . Two clusters can be distinguished as long as their *active* zone sites never overlap. If the probability of initiating an avalanche is p per site, then clusters do not overlap if $\bar{s} \cdot p < 1$, where \bar{s} is the average size of clusters. For a system of size L , $\bar{s} = L^{D_f(3-\tau)}$ from the distribution function (6.3). It

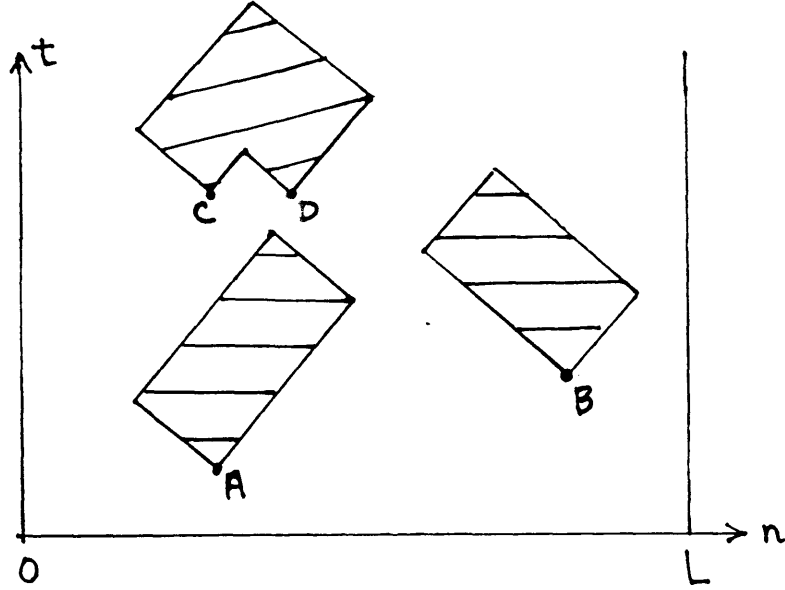


Figure 6.2: One-dimensional avalanche processes represented in space-time diagram. The two avalanches initiated at points A and B are considered independent because they do not overlap in space-time. The two initiated at points C and D however are overlapped.

is found in reference [89] that $\tau \approx 2$ and $D_f \approx 1$ for the 1D sandpile, giving $\bar{s} \sim L$ and the overlap limit

$$p < L^{-1}. \quad (6.4)$$

In the following, we report studies below and above the limit (6.4). In section 6.2.2, we describe a “discrete” model in which sand grains are deposited with probability $p = J_{\text{in}}/L$ per site, and the total input current J_{in} is fixed for different system sizes. (We are forced to using a system-size dependent local input rate because the sandpile model (6.1) has a limited maximum output capacity of N_f grains per time step for any system sizes.) By changing the magnitude of the driving force J_{in} , we can probe both below and above the avalanche-overlap limit (6.4). It is shown that interesting temporal fluctuations (i.e. $1/f$ noise) appear only for driving forces *exceeding* the

limit (6.4).

The discrete model is somewhat artificial due to the dependence of the local deposition rate on the system size L . To circumvent this problem, we introduce a modified “continuum” model in section 6.2.3. We find qualitatively similar behaviors for the continuum and the discrete model. The continuum model does not have the extra L dependence and lends itself better to the analytic treatment of section 6.3.

6.2.2 The Discrete Model

In this model, discrete “sand grains” are randomly deposited to the system. Time is defined by an external clock. At each time step, there is a small probability p of depositing a particle to each site, i.e. $H(n, t + 1) = H(n, t) + 1$ with probability p . As a result, there is an average deposition rate $J_{\text{in}} = p \cdot L$ for a system of size L . Due to the output limitation of the discrete model, we fix the input rate at $J_{\text{in}} < N_f$ independent of system size.

We let the system evolve for a long time until the steady-state is reached, i.e. $\langle J_{\text{in}} \rangle = \langle J_{\text{out}} \rangle$. In steady-state, we record the time series for the output current $J(t)$ and the instantaneous energy dissipation $E(t)$ as previously defined. We then take the power spectra $S(\omega)$ for the output series, where

$$S_X(\omega) = \int dt \int d\tau e^{-i\omega\tau} X(t)X(t + \tau), \quad X \in J, E.$$

If the avalanches do not overlap, then according to BTW, the resulting time series

of output current $J(t)$ and energy dissipation $E(t)$ should be equivalent to the random superposition of single avalanches according to the respective distribution functions $D_J(T)$ and $D_E(T)$. In particular, the power spectrum of the time series is predicted to have the form $S(\omega) \sim \omega^{-\beta} F(\omega L^\sigma)$ where the exponents β can be related to the exponents of the distribution functions and $F(x)$ is a cut-off function due to finite size. Thus, $1/f$ -type noise *may* arise (if $0 < \beta < 2$) as a consequence of random superposition of individual avalanches that are power-law distributed. However there should be no correlation beyond a time scale set by the longest avalanche, i.e. $S(\omega) = \text{constant}$ for $\omega < L^\sigma$.

This is indeed the case when we directly analyze the output time series for systems subject to very small driving forces: Figure 6.3 shows the resulting power-spectra for a system of 100 lattice sites with $J_{\text{in}} = 0.002$, i.e. an average of two (N_f) sand grains deposited to the system every 1000 time steps. From the form of the power spectra, we obtain the exponents $\beta_E \approx 4$ and $\beta_J \approx 2$. Clearly, the power-spectra do not exhibit $1/f$ -type broad-band noise. The lack of $1/f$ -noise in the sandpile model has been noticed recently by several groups[95][96]. This finding amounts to another major short-coming of the sandpile model since the model was originally invented to study the $1/f$ noise in transport.

As many transport systems in nature do have non-negligible driving forces, we next investigate the robustness of the scaling behaviors found above by exciting the avalanches more frequently. According to TB, all that will happen at higher driving

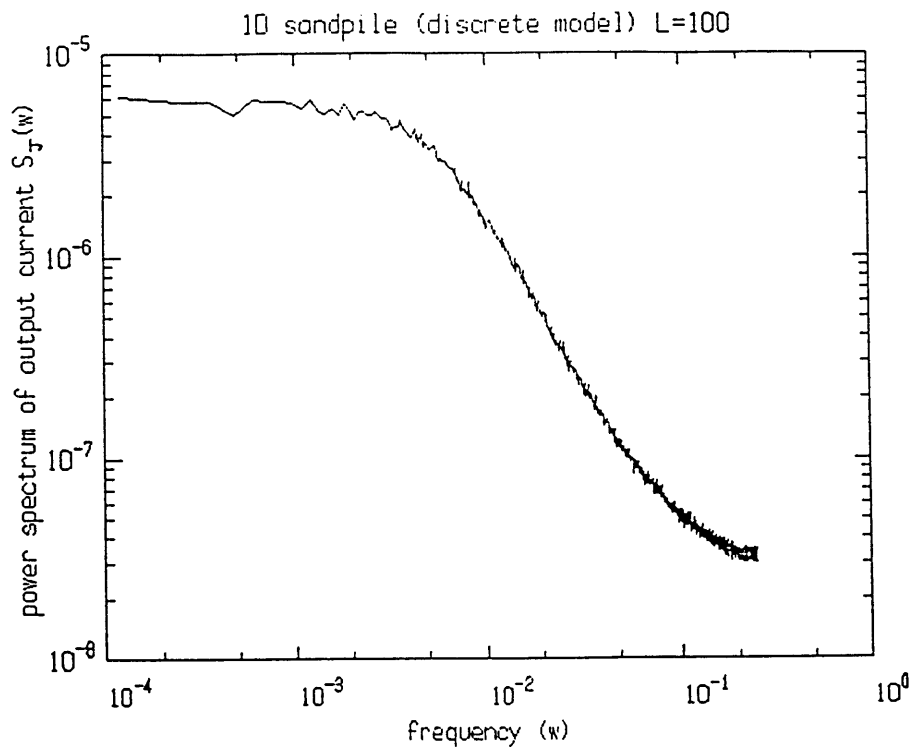
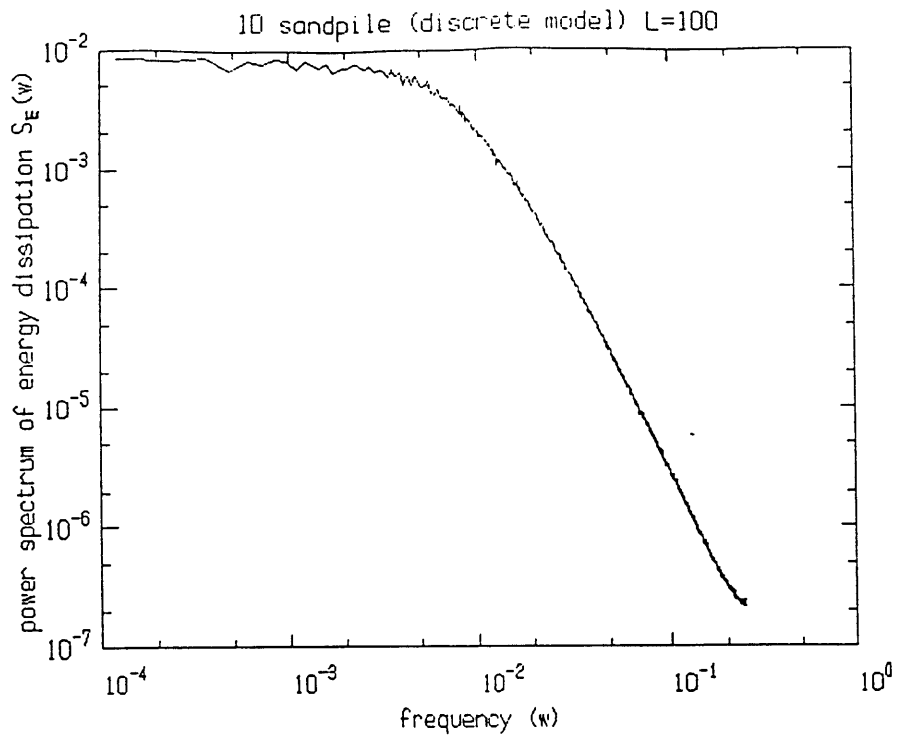


Figure 6.3: Power spectra for energy dissipation and output current of a 100-site system, with $J_{in} = 0.001$.

forces is that the cutoffs to the scaling regions in Figure 6.3 will move to higher frequencies (or shorter times); so that in the large input rate limit, the scaling region will be drastically reduced and one loses criticality in the macroscopic limit. However, when we repeat the simulation at higher input rate ($J_{\text{in}} = 0.02$ and $J_{\text{in}} = 0.2$), we obtain the interesting series of power-spectra shown in Figure 6.4. While the cutoff times do get reduced due to more frequent avalanche overlaps at higher input rate, new scaling regions with $S(\omega) \sim \omega^{-1}$ seem to emerge at a time scale beyond the cutoff.

We have performed a systematic study of the behavior of the sandpile in the overlapping avalanche limit. Using $J_{\text{in}} = 0.2$, the resulting power-spectra for systems of sizes ranging from 25 to 800 are shown in Figure 6.5. The power spectra exhibit a variety of different behaviors depending on the time scale. They are qualitatively divided into three non-trivial regions as sketched in Figure 6.6. We now describe each region in detail.

(I) Single Avalanche Region:

In this region, the observation time is of the order of the avalanche duration. Power spectra can be described by the scaling form, $S_E(\omega, L) = \omega^{-\beta_E} F(\omega L^{\sigma'})$ and $S_J(\omega, L) = \omega^{-\beta_J} L^{-0.5} F(\omega L^{\sigma'})$ where $\beta_E \approx 4$, $\beta_J \approx 2$, and $\sigma' \approx 0.5$.² Note that

²The exponent σ' associated with the finite size scaling of the power-spectra should not be interpreted as the dynamic exponent σ because the cutoff time (T_A of Figure 6.6) is due to the overlap of avalanches, which in turn depends on the input rate J_{in} . We expect T_A to have different L dependences for input rates of different L dependences. The dynamic exponent σ can be easily obtained from the finite-size scaling of the power-spectra in the non-overlapping limit. This however has not been pursued here since our interest lies within the overlapping avalanche limit.

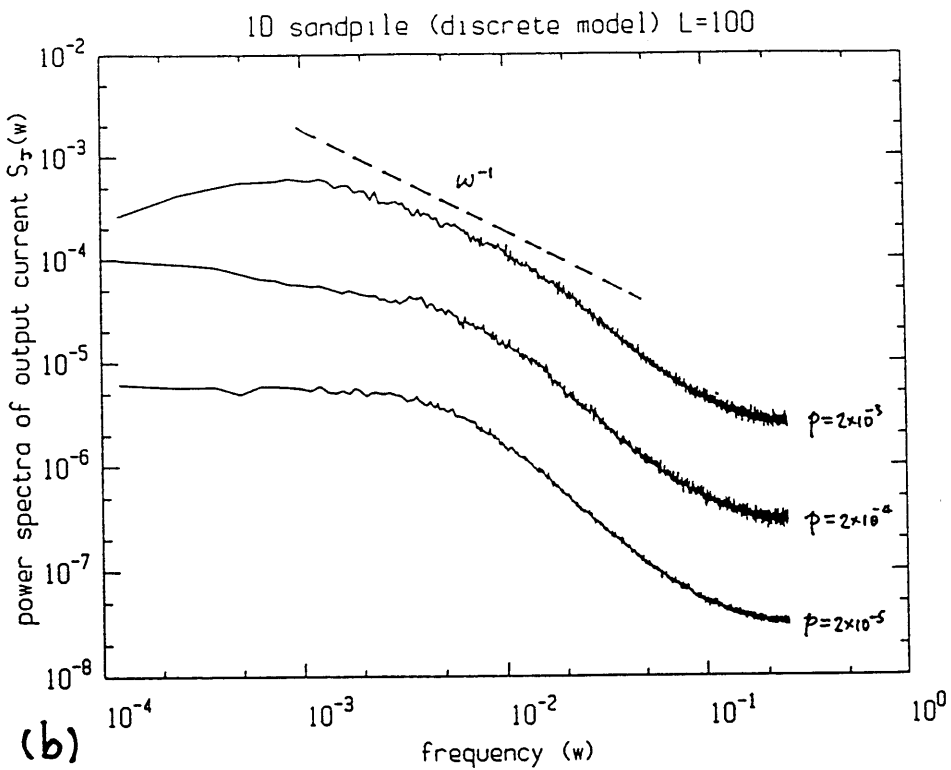
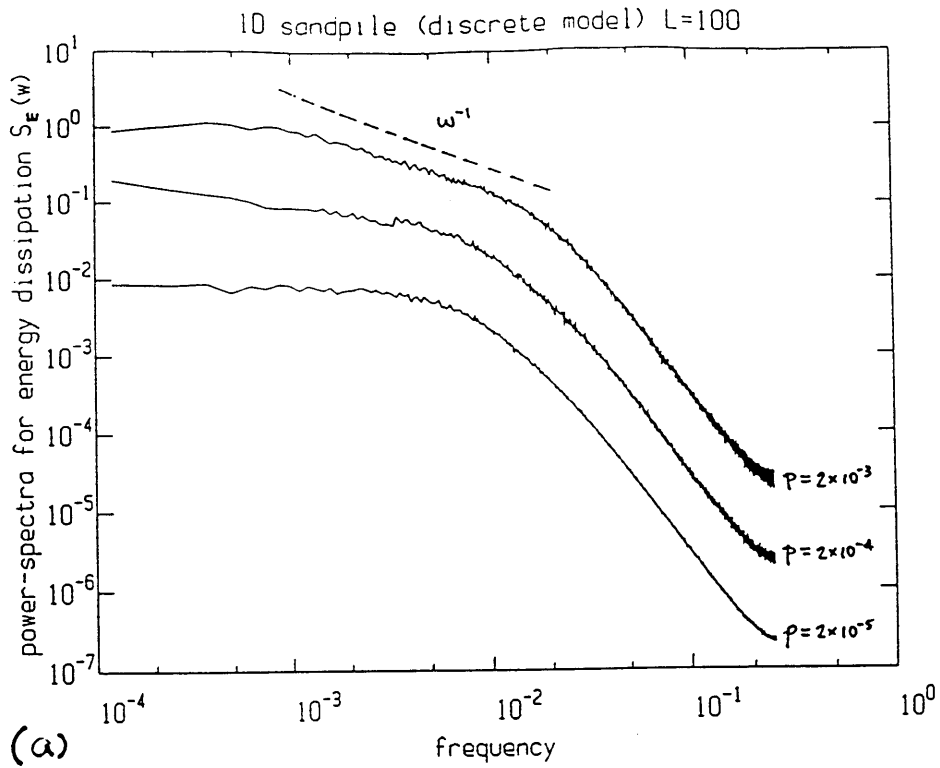


Figure 6.4: Power spectra of (a) the energy dissipation and (b) the output current for a one dimensional sandpile ($L = 100$) with deposition rates $p = 2 \times 10^{-3}$, 2×10^{-4} , and 2×10^{-5} per site. Notice that a new scaling region with $S(\omega) \sim \omega^{-1}$ emerges as we increase the input rate.

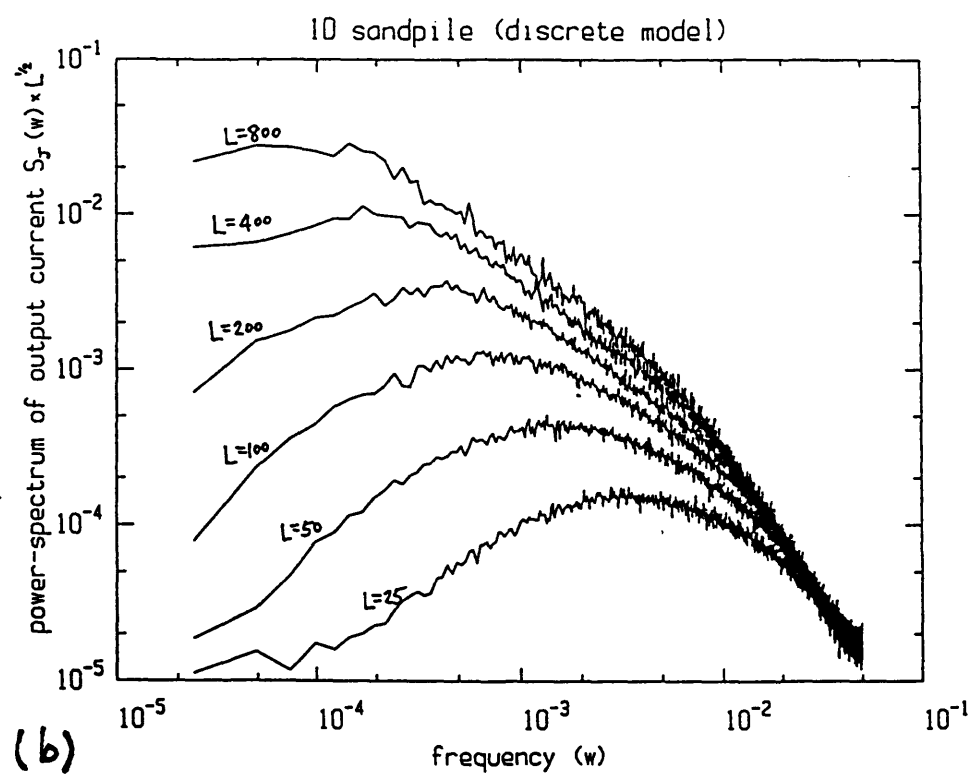
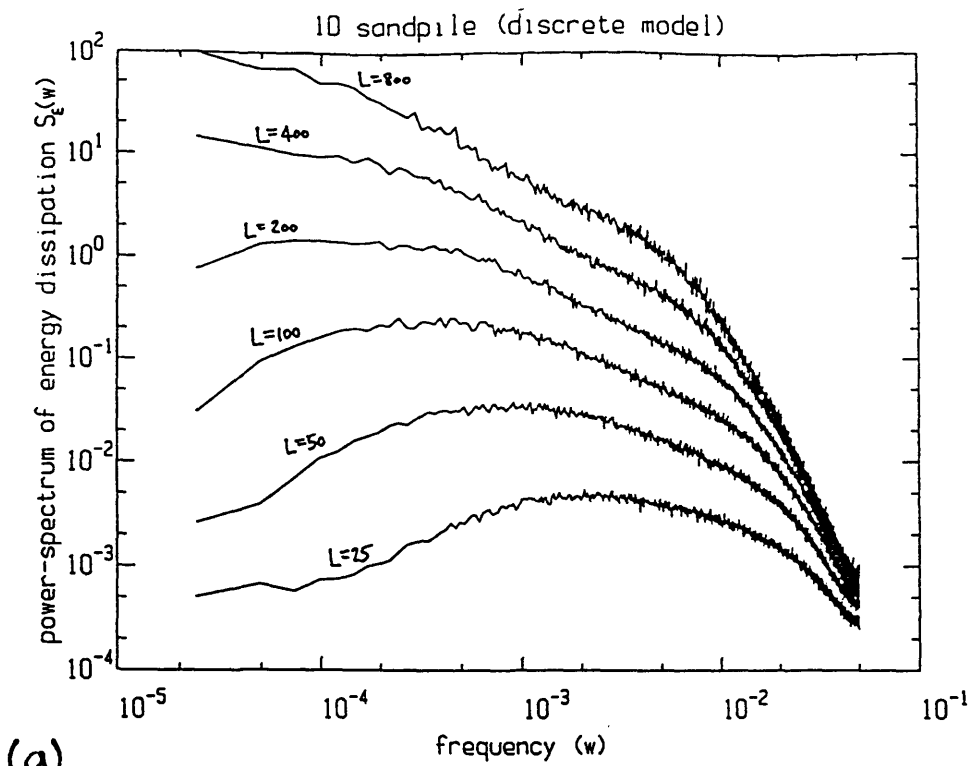


Figure 6.5: Power spectra of the one dimensional sandpile (6.1) for (a) the energy dissipation $E(t)$, and (b) the output current $J(t)$. Note that the vertical axis of (b) is scaled by $L^{0.5}$.

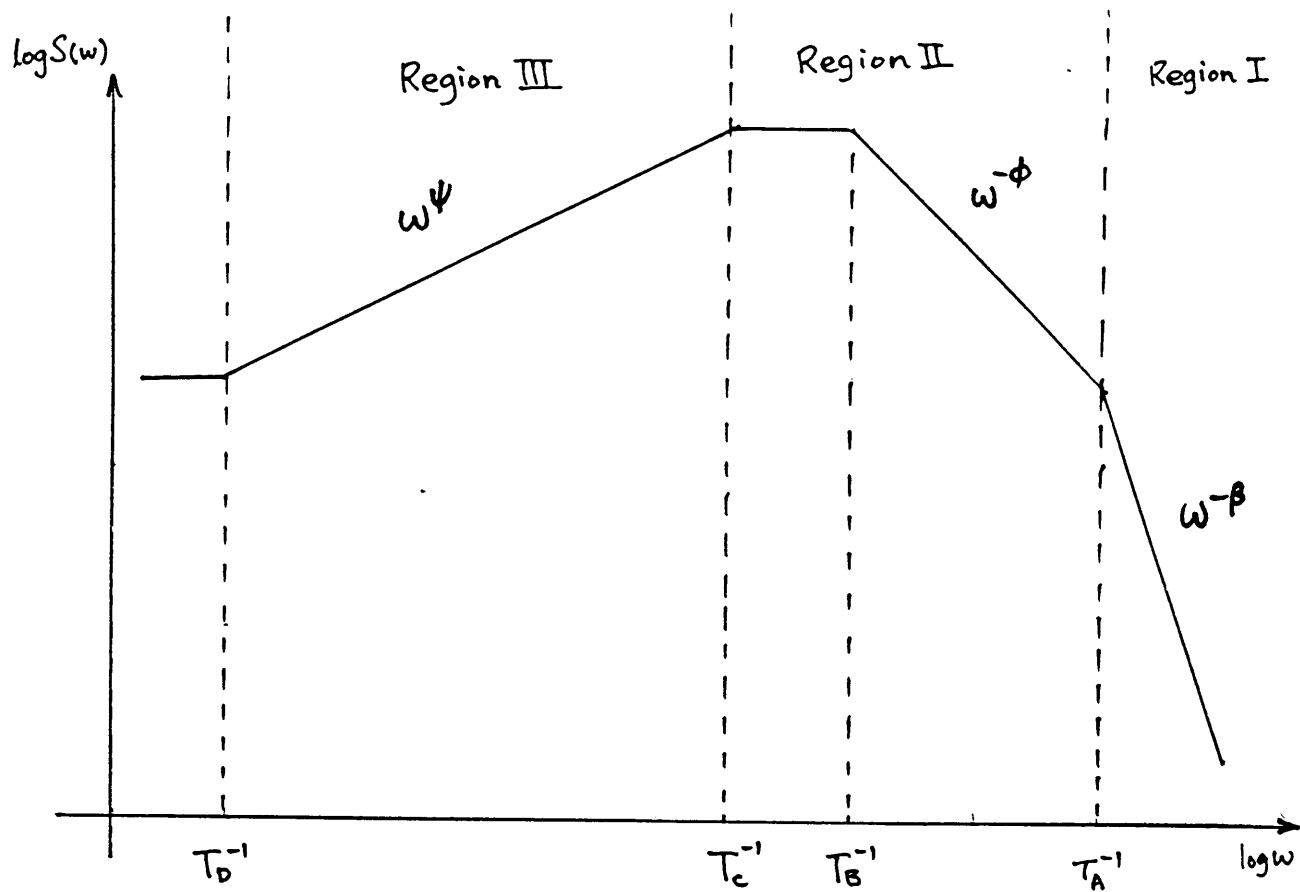


Figure 6.6: Qualitative behavior of power spectra shown in Figure 6.5.

S_J decreases with the system size L . (Note that the vertical axis of Figure 6.5(b) is scaled by $L^{0.5}$.) To understand the scaling region, we first directly examine the time series. Figure 6.7 shows sections of the typical time series of the instantaneous energy dissipation $E(t)$ at the time scale of region (I) for $L = 25$ and $L = 800$ systems. We recognize the activities shown to be the superposition of individual avalanche processes. The smoothness of the time series is a direct result of the addition of random signals; this is reflected in the large value of the exponent β_E . It can also be seen from Figure 6.4 that the scaling behaviors in the high frequency region are the same above and below the overlapping avalanche limit. We are therefore convinced that region (I) does correspond to the random superposition of *independent* avalanches. As already mentioned, the largeness of the exponents ($\beta_E \approx 4$ and $\beta_J \approx 2$) indicates the lack of $1/f$ noise in this region. The frequency dependences of the power spectra are in principle attainable from an analysis of distribution functions as have been done by previous studies[95][96].

The upper cut-off time T_A for region (I) is not very long even in the non-overlapping case; it has an upper bound of the maximum life time of one avalanche, i.e. $T_A \leq L^\sigma$, where the dynamic exponent σ is typically less than unity for a decelerating process. To put it in perspective of a real avalanche process such as an earthquake, T_A can be only of the order of seconds to minutes (if we take our system to be a 100-mile segment of the San Andreas fault between Santa Cruz and Berkeley in California). While the way energy is released during one quake is certainly worthy of study, for

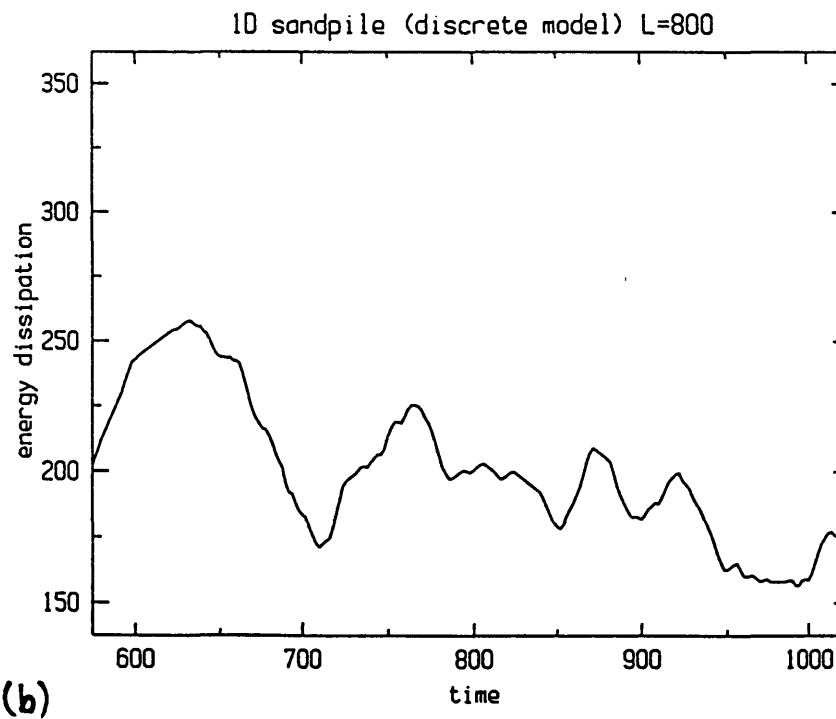
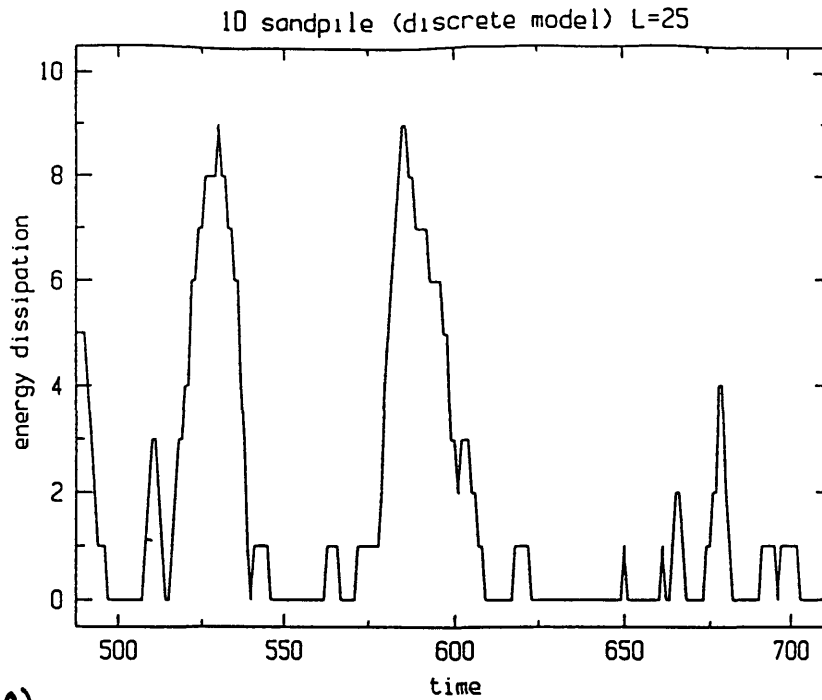


Figure 6.7: Time series for instantaneous energy dissipation $E(t)$ of the 1 dimensional sandpile with (a) $L = 25$, and (b) $L = 800$. Individual avalanche events can be identified at this time resolution.

purposes of investigating long-time fluctuations such as $1/f$ noise observed in river flow, resistors, and in aftershocks after major earthquakes, we need to look at longer time scales.

(II) Interacting Avalanche Region

We now come to a major result of this numerical study. Far from being uncorrelated as implied by BTW, we find $1/f$ noise when looking at time scales beyond the maximum duration of individual avalanches. In this region, the power spectra can be fitted to a power-law of the form $S_X(\omega) = \omega^{-\phi_X}$. The exponents are determined to be $\phi_E \approx 1.0$, and $\phi_J \approx 1.0$ (using the results of $L = 400, 800$ systems in Figure 6.5). The cut-off time T_B for region (II) (see Figure 6.6) is expected to be related to the system size L through another dynamical exponent, z .³ This exponent cannot be determined adequately from the existing data, but can be obtained from the analytical treatment of section 6.3.

A more intuitive feel for this region is obtained by examining the time series coarse-grained to the relevant scale. In Figure 6.8, we illustrate a time-series taken from the $L = 800$ system. It is clear that these time-series are characteristically different from that of Figure 6.7, as the fluctuations here are more erratic (less smooth), but not random—a signature of $1/f$ noise. Since the time scale of these fluctuations are long compared to the maximum lifetime of single avalanches, we conclude that the correlation in this part of the spectrum must arise out of interactions among the

³Note that z is the dynamic exponent for the *interacting* avalanches, different from σ which is the dynamic exponent for a *single* avalanche.

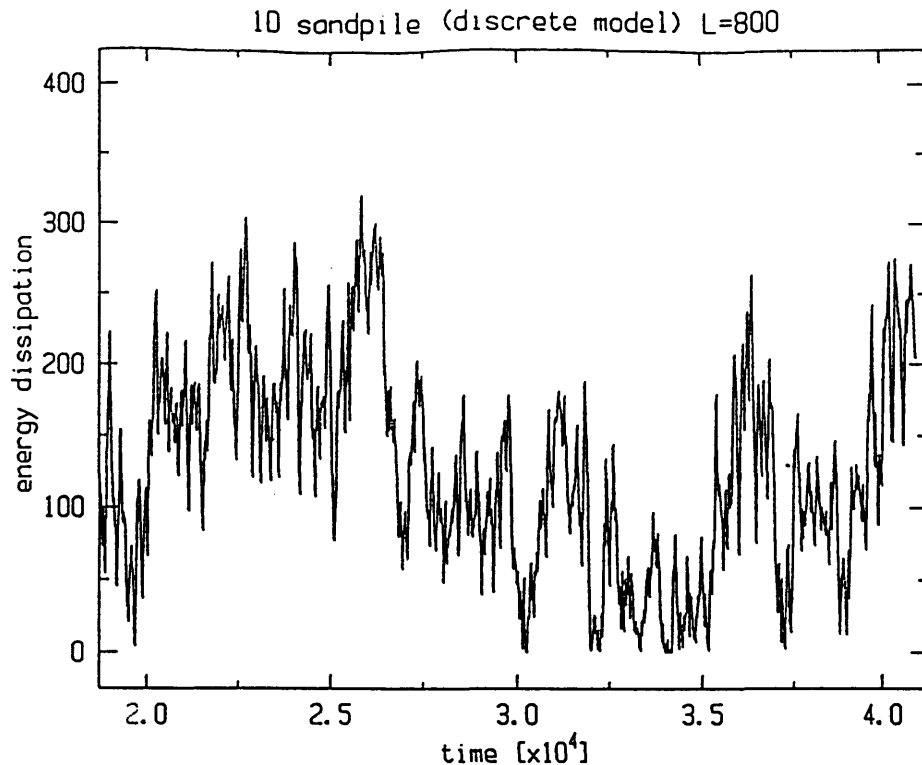


Figure 6.8: Time series for instantaneous energy dissipation $E(t)$ of the one dimensional sandpile with $L = 800$. At this time resolution, correlation among avalanches can be seen.

avalanches. In this way, this region is reminiscent of aftershocks in earthquakes and shock waves in hydrodynamics. The hydrodynamic region gives the asymptotic behaviour of the model in the long-time limit, and is the relevant region for studies of $1/f$ noise. It is natural to resort to means of continuum field theory for a possible description of the behaviours here. A detailed analysis of this region will be the subject of section 6.3. It will be shown that the existence of power-law scaling in the hydrodynamic region is a consequence of the conservative dynamics present in the model. Again, we put these time scales in perspective by making analogies with earthquakes: aftershocks and correlation of quakes along a faultline can exist at time scales ranging from minutes to hundreds of years.

(III) Great Events Region

When we look at even longer time scales, we encounter avalanches whose active

zones are of the order of the system size. These great events sweep through the entire system and effectively reset the slope of the sandpile. They can be thought of as system-wide discharge processes.

The origin of great events has been studied by Carlson and Langer in a different (but possibly related) model[87], and has been alluded to in reference [89]. It can be traced back to a conservation law which we illustrate in the context of this model. For a sandpile of size L , the average input rate is fixed (i.e. $\langle J_{\text{in}} \rangle \sim 1$) while the scaling of output current can be determined from Figure 6.5 to be $J_{\text{out}} \sim L^{-0.25}$. The sandpile is therefore accumulating particles at a constant rate. This process becomes unignorable when the number of particles accumulated reaches the order L^2 (at which point the macroscopic slope of the sandpile is changed). Thus beyond a time scale of $T_C \sim L^2$ (see Figure 6.6), a system-wide discharge process is bound to take place.⁴ It is important to recognize that the accumulation of particles is possible in the sandpile model due to the threshold nature of the dynamics which provides a multitude of metastable states. Other systems exhibiting great events (e.g. in simple models of earthquakes[87] and charge-density waves[88]) all share the feature of metastability. These behaviors should be contrasted with more conventional viscous fluid flows which do not exhibit the discharge activities observed here.

The effect of large scale discharges can also be detected if one only looks at the avalanche distribution function $D(s)$. Because the large s part of the distribution is

⁴Since $T_B \sim L^2$, there may be an uncorrelated interval between T_B and T_C for $z < 2$. See Figure 6.6.

now subject to a different process and weighted more, we do not expect $D(s)$ to obey simple, homogeneous scaling of the form (6.3). As it turns out, the large avalanche end of the distribution is also scale invariant. Furthermore, the small and large size ends of the distribution $D(s)$ must be related. It is found numerically in [89] that the entire distribution function fits well to a multi-fractal scaling form, though the implication of multi-scaling is not understood.

Let us return to the power spectrum shown in Figure 6.5. It can be seen from the low frequency behaviour of the small systems that temporal fluctuations in the great events region is not trivial. The power spectra can be described by $S_X(\omega) \sim \omega^{\psi_X}$ where $\psi_E \approx \psi_J \approx 1$. The positive exponent indicates the existence of anti-correlation. We find such anti-correlations persisting for a long time. For instance, anti-correlation is present for the $L = 25$ system up to a time $T \sim 10^4$. A simple treatment of the scaling behavior of this region will be given in section 6.2.3 in the context of a continuum model.

Although the description of various scaling regions given above are based on results of the 1D sandpile, its generality goes beyond 1D systems. We have also performed the generalization of (6.1) to a 2-dimensional lattice shown in Figure 6.9, with the power spectra of energy dissipation shown in Figure 6.10. We see that the qualitative behavior is the same as those described for the 1-D system (Figure 6.5). The scaling exponents in region I and III are determined to be $\beta_E \approx 2.8$ and $\psi_E \approx 1.3$, though we do not have enough computing power to go to large enough system sizes to see

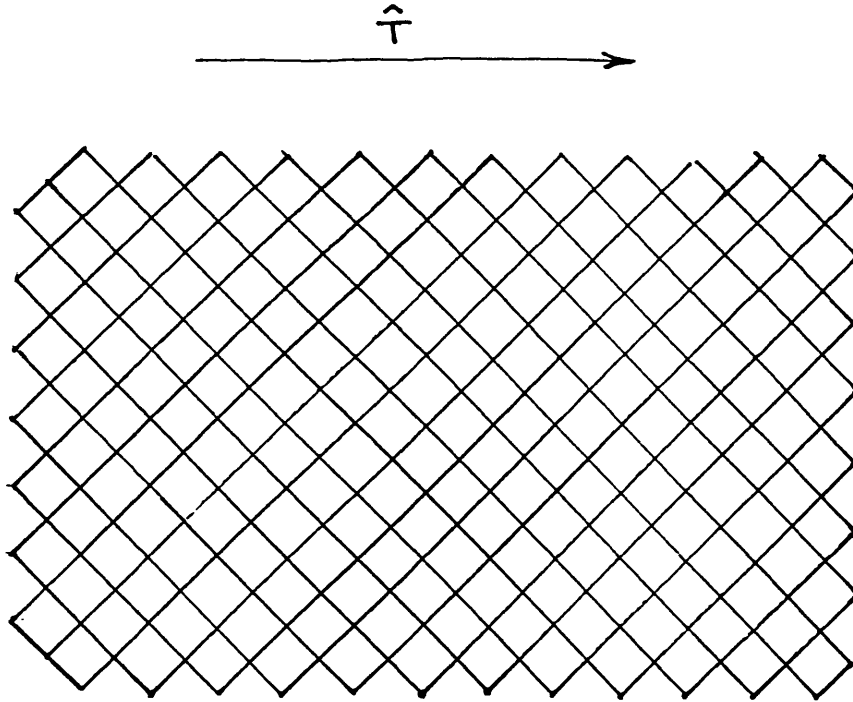


Figure 6.9: A checker-board 2-dimensional lattice. A sandpile is defined on this lattice by an interger height function $H(m, n, t)$. Due to the anisotropic nature of the 2D sandpile (see section 6.3), we need to look at narrow strips of lattices such as the one shown here.

the scaling in the intermediate hydrodynamic region.

The above findings can also be related to recent experiments on real sandpiles. The spectrum shown in Figure 6.10 is qualitatively very similar to the one obtained from recent experiments[83], reproduced here in Figure 6.11. As in Figure 6.10, the power spectrum from experiments has a high frequency part $S(\omega) \sim \omega^{-3}$ which is related to the fluctuation of individual avalanche events. Also, there is an anti-correlating low-frequency part $S(\omega) \sim \omega^{1.5}$ which the authors have identified with the changing angle of inclination. (As we will see in the analysis of the great events region in section 6.2.3, the anti-correlation in the automaton is also related to the changing angle of inclination.) The correspondence between experiment and simulation seem to be very good indeed; but the authors of reference [83] prematurely concluded that the

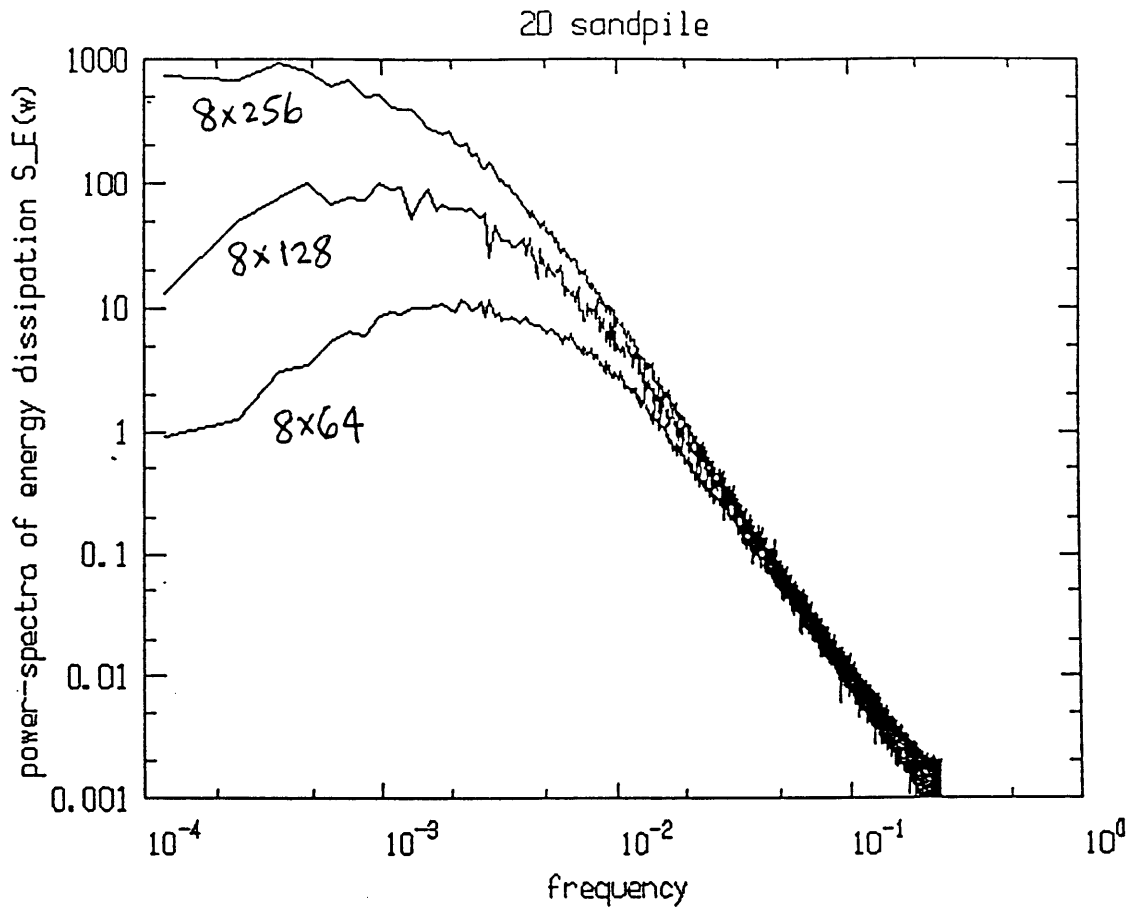


Figure 6.10: Power spectrum for the energy dissipation $E(t)$ of several two-dimensional lattices. The qualitative behavior observed here is similar to that of the one-dimensional lattice shown in Figure 6.5.

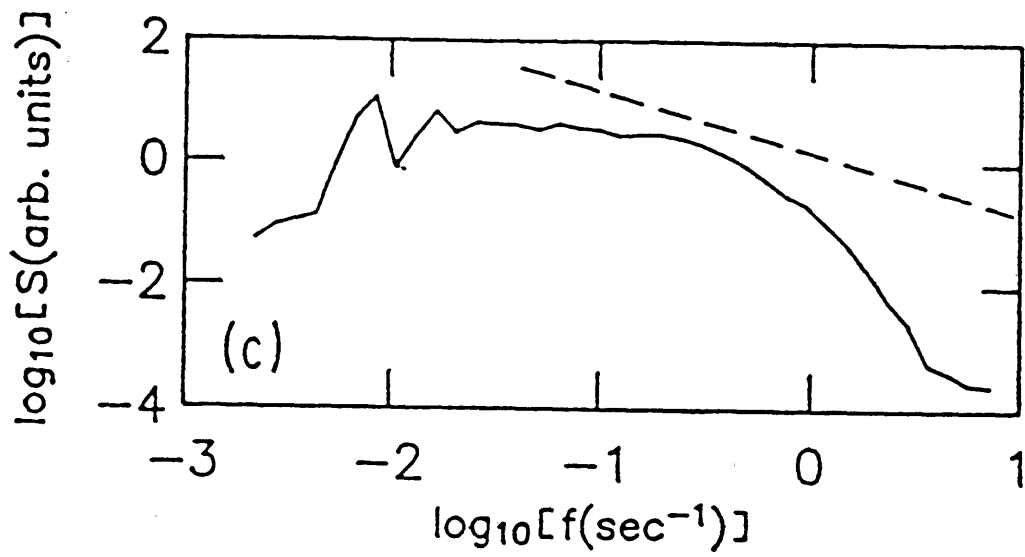


Figure 6.11: Power spectrum for the time series of “total activity” of a 2-dimensional sandpile in a rotating cylinder. Reproduced from reference [83].

sandpile model does not describe real sand based on the lack of $1/f$ -type fluctuations in their sandpile. With the analysis in this section, we now understand that $1/f$ noise should occur in the intermediate frequency range, which never really had a chance to develop in the experiments performed (judging from Figure 6.11). It is possible that interesting temporal structure could be detected as one goes to experiments of larger scales and with larger driving forces.

6.2.3 The Continuum Model

The discrete sandpile investigated in section 6.2.3 suffers a defect in that the local deposition rate p depends on the overall size of the system L . As mentioned previously, we were forced to using such an L dependent deposition rate due to the limited output capacity of the model (6.1). However, this choice of deposition rate makes the problem somewhat artificial. Moreover, the L dependent deposition rate needlessly complicates the finite-size scaling properties of the power-spectra and the cutoff time T_A . To circumvent these difficulties, we introduce a modified version of the sandpile model. This new model will actually make a better connection with the field theory description to be presented in section 6.3.

We again consider a 1-D sandpile of L sites as described by (6.1). But now we generalize the height variable $H(n, t)$ to a real number, and we modify the way the system is driven. Instead of depositing integer particles with probability $p = J_{\text{in}}/L$, we move the net input to the left edge, i.e. $H(1, t + 1) = H(1, t) + J_{\text{in}}$ where $J_{\text{in}} = 0.2$

as before. We mimic the effect of random deposition by associating a random walker of step size P to each lattice site, i.e. $H(n, t+1) = H(n, t) + P \times r(t)$, where $r(t) = \pm 1$ with equal probability. Lumping of input to the left end is done to circumvent the limited-output deficiency of the sandpile model, and the introduction of the random walker can be thought of as a result of coarse-graining of random input. This model can also be thought of as a model for traffic along a busy highway, where cars are constantly fed in from one end, with some cars leaving or entering the highway along the way.

Why might we expect this model to bear any resemblance to the discrete model discussed in section 6.2.2? The reason is two-fold: We learned from simulations that the scaling properties are independent of the parameter N_f . We can imagine a discrete system with N_f being a very large integer; then the local fluctuation is only $1/N_f$ per time step. This can be thought of as a continuous random walker after coarse-graining. Also, scaling properties are insensitive to the average input as long as it is small compared to the maximum output N_f . As is true in the discrete model, what gives rise to interesting dynamics is the fluctuation in input, not the dc-input itself.

The advantage of the continuum model is that the fluctuation in input can be tuned independently of its dc value. For a random walker of step size P , it takes a time of $1/P^2$ to accumulate to a height increment of one grain, at which point it can initiate or stop an avalanche. Hence the probability (per site) of generating an

avalanche is $p \sim P^2$ for the continuum model. Since P is now independent of system size L , we see that the non-overlapping condition (6.4) cannot be satisfied in the thermodynamic limit ($L \rightarrow \infty$) for any finite P . As mentioned earlier, the overlap of avalanches corresponds to a percolating network above the percolation threshold. One can define a L -independent correlation length for the sandpile in the spirit of percolation theory. However, this scale as we will see shortly, is the *lower* cutoff for the hydrodynamic region, as was the case for the discrete model. The important scaling properties of the sandpile in the hydrodynamic region are not changed.

The continuum model is simulated on a computer, and the resulting power spectra are found to be independent of the input parameter J_{in} as long as $J_{\text{in}} < 1$. They are shown in Figure 6.12 for $J_{\text{in}} = 0.2$ for system sizes ranging from 32 to 1024. The power spectra in Figure 6.12 are qualitatively similar to those of the discrete model in Figure 6.5. The most obvious difference between these two sets of power spectra lies in their different L dependence. This is expected as the key modification in the continuum model is precisely the L dependence of the deposition rate p . The spectra for the continuum model reveal a system-size-independent high-frequency cutoff (T_A of Figure 6.6) for $L \geq 256$. As explained in section 6.1, avalanches of size s overlap when $s \cdot p > 1$. Since $p \sim P^2$ is L independent in the continuum model, the upper cutoff size (and similarly the upper cutoff duration T_A) of the non-interacting avalanches should be L independent as observed. To check this interpretation, we have also directly varied the noise level P for a fixed system size ($L = 64$). As seen in

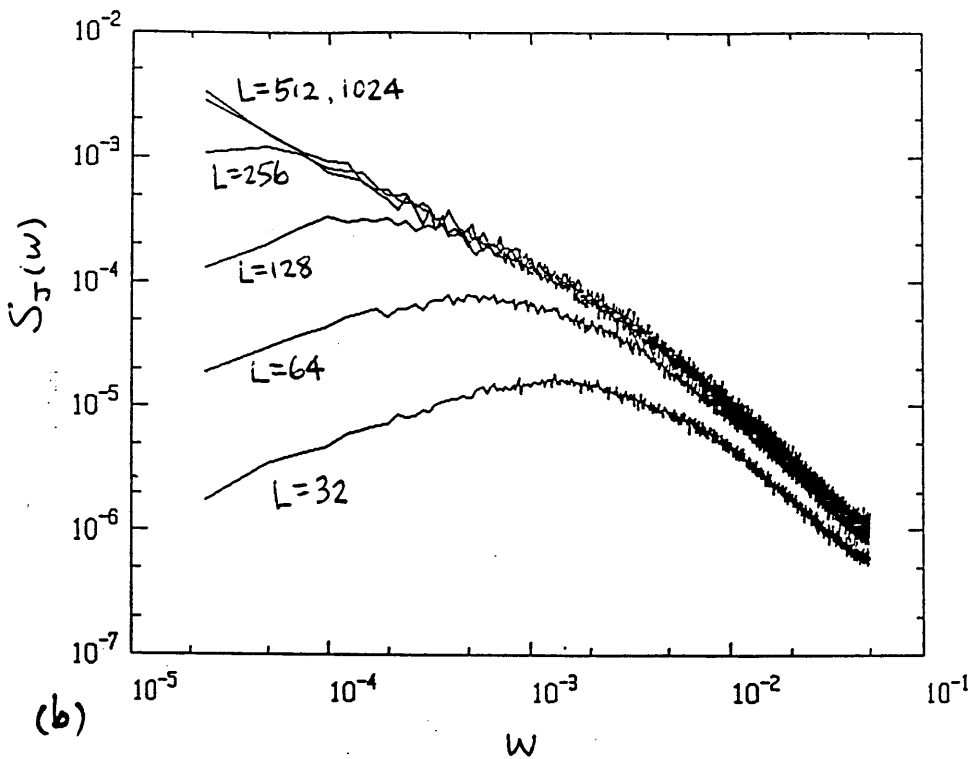
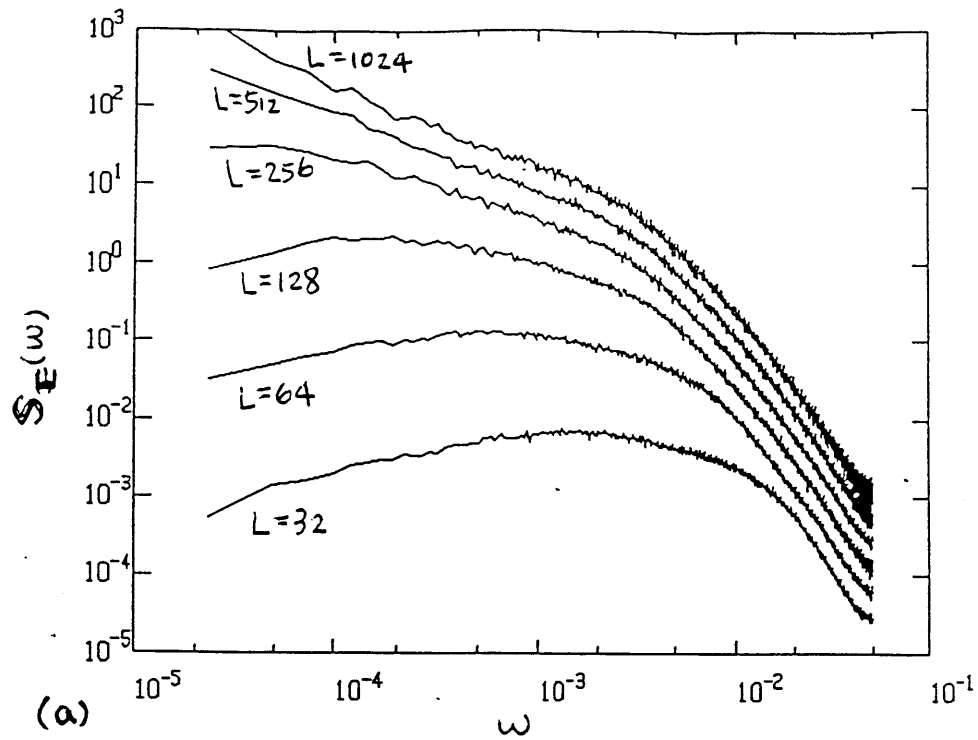


Figure 6.12: Power spectra of the one dimensional sandpile (continuum model) for (a) the energy dissipation $E(t)$, and (b) the output current $J(t)$.

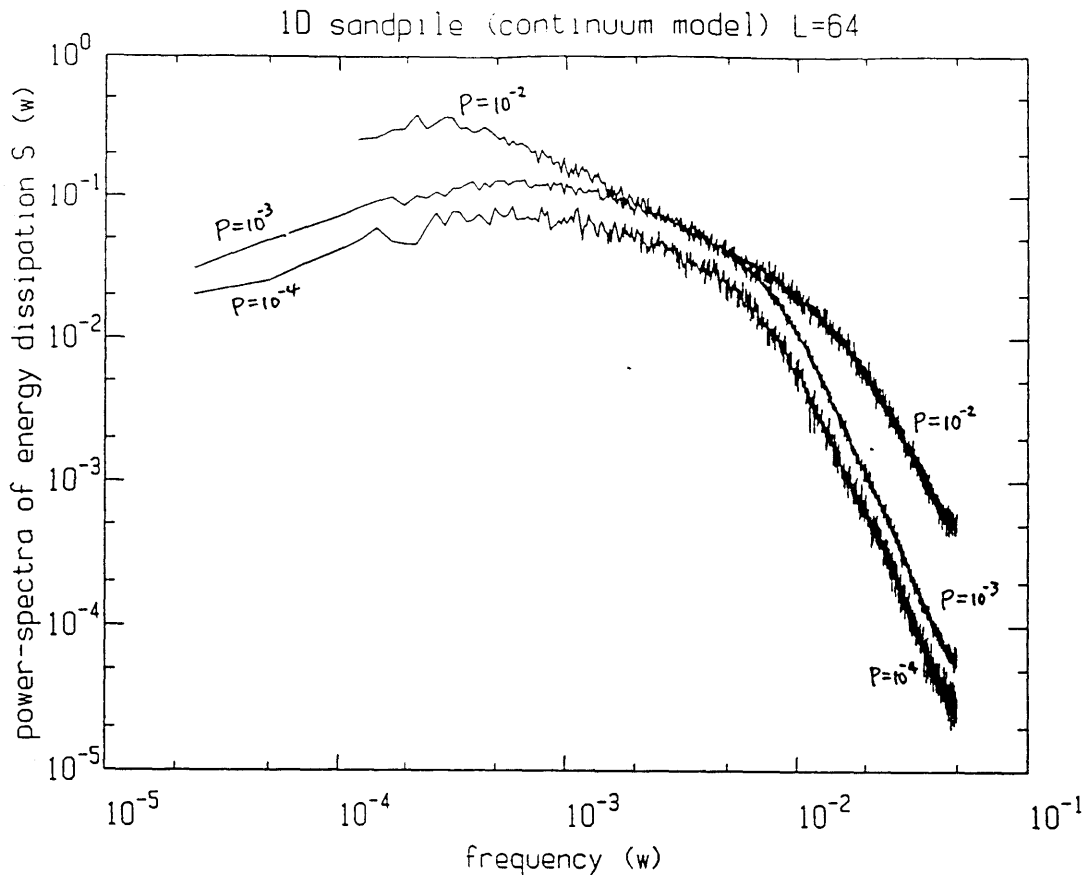


Figure 6.13: Power spectrum for energy dissipation of the continuum version of a one dimensional sandpile. Three different noise levels are shown for a $L = 64$ system.

Figure 6.13, the onset time (T_A) for the hydrodynamic region becomes shorter as we increase P . For $\omega \sim T_A^{-1}$, we again enter the region of overlapping avalanches. There, individual avalanches are stopped or extended due to interference from neighboring avalanches.

Various scaling exponents describing the frequency dependences of the power spectra are listed in Table 6.1, along with those of the discrete model for ease of comparison. Evidently the exponents for the two models are rather close in region I (single avalanche region) and region II (hydrodynamic region). More significant differences are found for region III (great event region), though the statistics in region III is not

| | Region III | Region II | Region I |
|-----------------|----------------|----------------|-----------------|
| Continuum model | $\psi_J = 0.5$ | $\phi_J = 0.8$ | $\beta_J = 1.5$ |
| discrete model | $\psi_J = 1.0$ | $\phi_J = 1.0$ | $\beta_J = 2.0$ |
| Continuum model | $\psi_E = 0.5$ | $\phi_E = 1.0$ | $\beta_E = 3.5$ |
| discrete model | $\psi_E = 1.0$ | $\phi_E = 1.0$ | $\beta_E = 4.0$ |

Table 6.1: The scaling exponents in various regions for the discrete and the continuum model. The exponents are defined in Figure 6.6.

very good for the discrete model.⁵

If we follow the great event region of the continuum model, we see that it dominates the power-spectra of the small systems. In fact, if we run the same simulation (continuum model) for a one-lattice system, we obtain over two decades of anti-correlation in the power spectrum (see Figure 6.14). Anti-correlation is present in the one-lattice system up to a time of $T \sim 10^4$. Where might such a long-term correlation (memory effect) come from?

To understand the origin of the anti-correlated region, let us examine the one-lattice system more closely. If we ignore stochasticity, there will simply be an output pulse of 2 grains every 10 time steps for $J_{in} = 0.2$ and $N_f = 2$. The inclusion of a small

⁵If we compare region III in Figure 6.5 and Figure 6.12, we find the former has barely one decade while the latter has almost two decades. This difference can again be attributed to the different L dependences of the input rate p for the two models.

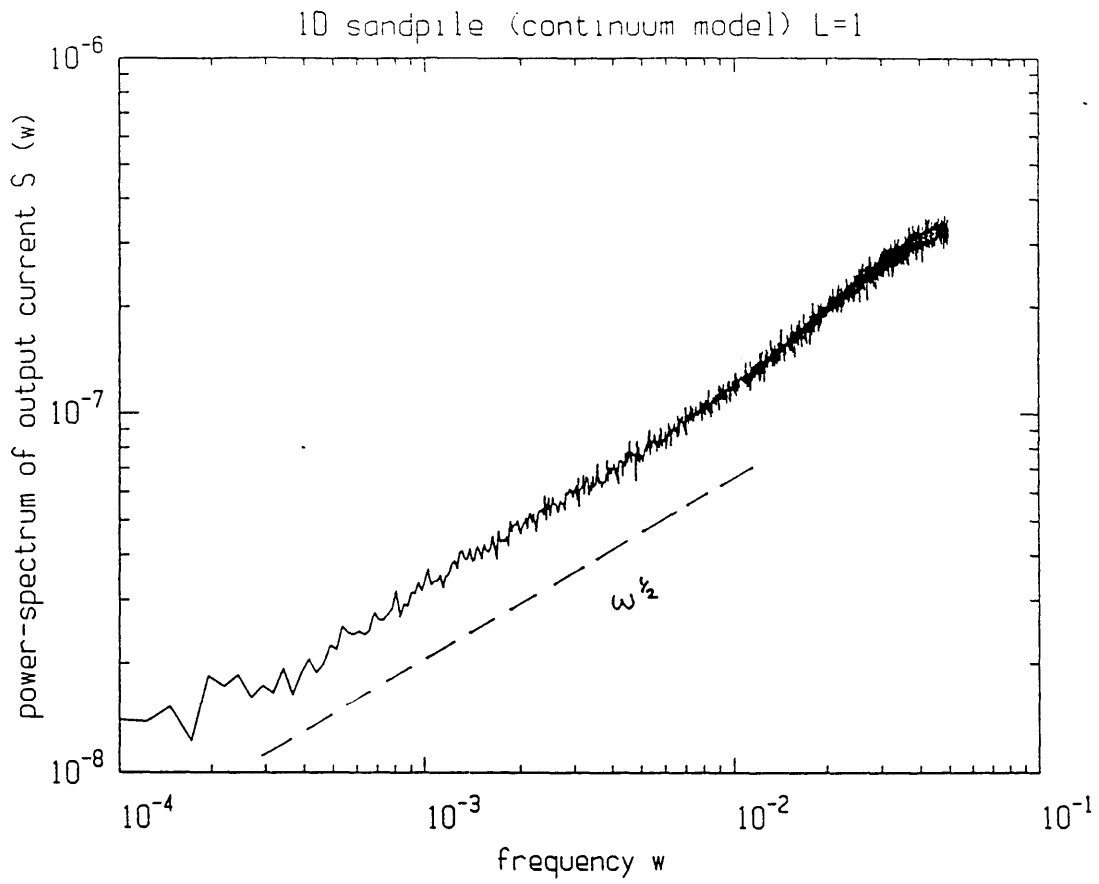


Figure 6.14: The output power spectrum of a one-lattice system with $J_{in} = 0.2$ and $P = 0.01$.

noise $r(t)$ in the input can shift the output series: Suppose the height of the one-lattice system is $\epsilon = 0^+$ right after an output pulse, then we expect another output pulse in 10 time steps; however if the magnitude of the accumulated noise within this time period is $-\delta$ where $\delta > \epsilon$, then the height of the system will be slightly smaller than $N_f = 2$ after 10 time steps, and therefore there will not be an output pulse until the 11th step. Similarly, if the height of an output pulse is $1 - \epsilon$, and the accumulated noise is $\delta > \epsilon$, then the output pulse will be advanced by one time step. The modulation of the output sequence by a small noise is illustrated in Figure 6.15. The output is delayed or advanced by one time step if the accumulated noise (a random walker for simple white noise) is on different sides of the origin between two output pulses. A simple, coarse graining procedure transforms the actual output profile $J(t)$ to $\tilde{J}(t)$ as shown in Figure 6.15b. The function $\tilde{J}(t)$ more clearly represents the relation between the output sequence and zero-crossings of the random walker: $\tilde{J}(t) = +1$ for upward crossings, and $\tilde{J}(t) = -1$ for downward crossing. It is apparent from Figure 6.15 that the output sequence for this simple one-lattice model is anti-correlated: Every positive pulse is followed by a negative pulse. We can quantify this anti-correlation by calculating the correlation function $\langle \tilde{J}(0)\tilde{J}(t) \rangle$. Without loss of generality, we assume that $\tilde{J}(0) = +1$. The correlation function may be calculated by noting that the time series $\tilde{J}(t)$ can be written as $\tilde{J}(t) = dJ'(t)/dt$ (see Figure 6.15) where

$$J'(t) = +1 \quad \text{if} \quad \int_0^t r(t')dt' > 0$$

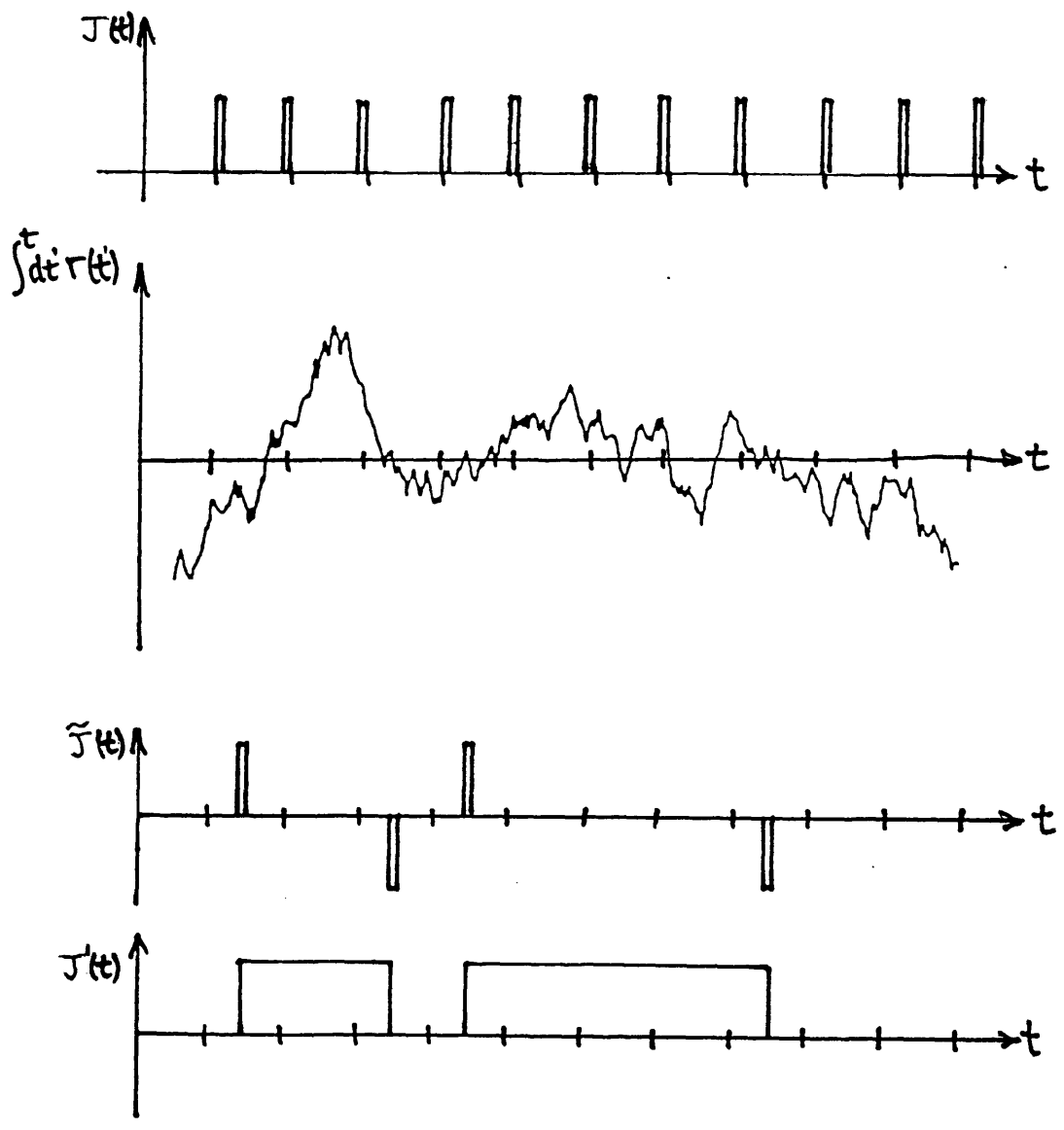


Figure 6.15: The output sequence $J(t)$ of the one-lattice system due to a random noise shown below. The coarse-grained output series is obtained from $\tilde{J}(t) = \sum_{i=1}^{\tau} J(t+i)/\tau - J_{in}$, where $\tau = 10$ is the average number of time steps between two output pulses and $J_{in} = 0.2$. $\tilde{J}(t)$ can also be thought of as the time derivative of the function $J'(t)$ shown at the bottom.

$$J'(t) = 0 \quad \text{if} \quad \int_0^t r(t') dt' < 0$$

and $r(0) = 0, r'(0) > 0$ by the choice of $\bar{J}(0)$. So $\langle \bar{J}(0)\bar{J}(t) \rangle = \frac{d}{dt} \langle J'(t) \rangle$ where $\langle J'(t) \rangle$ is simply the probability of a random walker's return to the origin after a long time ($\tau = 10$), which is well known ($\sim 1/\sqrt{t}$). Thus the correlation function is $\langle J(0)J(t) \rangle \sim t^{-3/2}$, yielding a power spectrum of $S(\omega) \sim \omega^{1/2}$ in agreement with Figure 6.14.

But of course the anti-correlating region cannot persist forever (after all, we started with an uncorrelated noise). After a sufficiently long time T'_D , the random walker would have wandered to a value of ± 1 . At a time scale greater than T'_D , the system behaves as if it has an input which is 0 or 2 with equal probability. And $J_{\text{out}} = J_{\text{in}}$ becomes uncorrelated. The upper cut-off time can easily be estimated: the distance traveled in time t for the random walk released at the origin is $P\sqrt{t}$. Setting this distance to unity yields $T'_D \sim P^{-2}$.

We now relate this one-site problem to a large system (continuum model) of size L in the great events region. During each great event, the number of sand grains discharged is of the order L^2 as required by conservation law described in section 6.2.2. Since this is a non-negligible portion of the total number of sand grains in the system, passage of great events must change the macroscopic slope of the sandpile. For simplicity, if we assume a discharge of fixed size to occur when the slope of the sandpile reaches a threshold θ_{max} , then at an observation time greater than T_C (of

Figure 6.6), the sandpile simply executes the oscillation between a gradual building up to θ_{\max} , followed by sudden discharges, similar to the behavior of the single-site system.

To complete our analysis, we estimate the upper cutoff time (T_D of Figure 6.6) for the anti-correlating great event region. In the simple one-site model, $T'_D \sim P^{-2}$ where P is the size of the noise for the lattice site. Extending this argument to the L -site continuum model, the effective noise amplitude for the system is $\sqrt{L}P$. Since each great event discharges a volume $\sim L^2$, correlation exists until $(\sqrt{L}P)\sqrt{t} \sim L^2$, yielding an upper cutoff time $T_D \sim P^{-2}L^3$. The P dependence has been verified in simulations, but we do not have enough computing capacity to determine the L dependence quantitatively.

Finally we observe that the mechanism for the generation of great events described above appears to be very similar to what was observed in a recent sandpile experiment[83]. There the slope of the sandpile was also found to oscillate between two angles. An elaborate mechanism has been proposed[97] to explain the observed bistable discharge behavior of the sandpile. In light of the present analysis, we see that this behavior is contained within the simple threshold rule of the sandpile automaton. Our result suggests that the occurrence of great events should be common to a wide variety of driven systems that possess metastable states. Uncorrelated noise coupled to a reasonably sharp threshold function may produce long-time anti-correlations in these systems.

6.3 Field Theory of Dissipative Transport

6.3.1 The Driven Diffusion Equation

We will consider the continuum sandpile model of section 6.2.3 and investigate its behavior in the interacting avalanche region (II). To study this region we first coarse-grain the system both in space and time to remove the lower-cutoffs and obtain a coarse-grained landscape $\tilde{H}(\vec{x}, t)$. The coarse-grained unit cell length l_0 and unit time t_0 must be large compared to the length scale at which deceleration of individual avalanches takes place. For the continuum model, the cutoff of the single avalanche region is L -independent. (For the discrete sandpile model, we would have $l_0 \sim t_0 > T_A \sim L^{1/2}$.) Since discharge processes do not occur until a time scale $t > T_C \sim L^2$, the slope of the coarse-grained sandpile may be considered stationary. Furthermore, we assume the landscape of the sandpile to be flat on average, i.e. the average slope is uniform. (The assumption of uniformity and stationarity of the slope will be checked later for self-consistency of the theory). We may now consider the avalanche dynamics from the point of view of fluctuations of the sandpile surface.

We define a dynamical field $h(\vec{x}, t)$ which is the difference between the coarse-grained landscape $\tilde{H}(\vec{x}, t)$ and the flat average profile $H_0(x) = \lambda_0(L - x)$, as shown in Figure 6.16. Let us closely examine the presence/absence of various symmetries from which we construct the equation of motion for h . The component of gravity parallel to the surface picks out a direction of transport \hat{T} . Let $\vec{x}_{\parallel} = (\hat{T} \cdot \vec{x})\hat{T}$ and

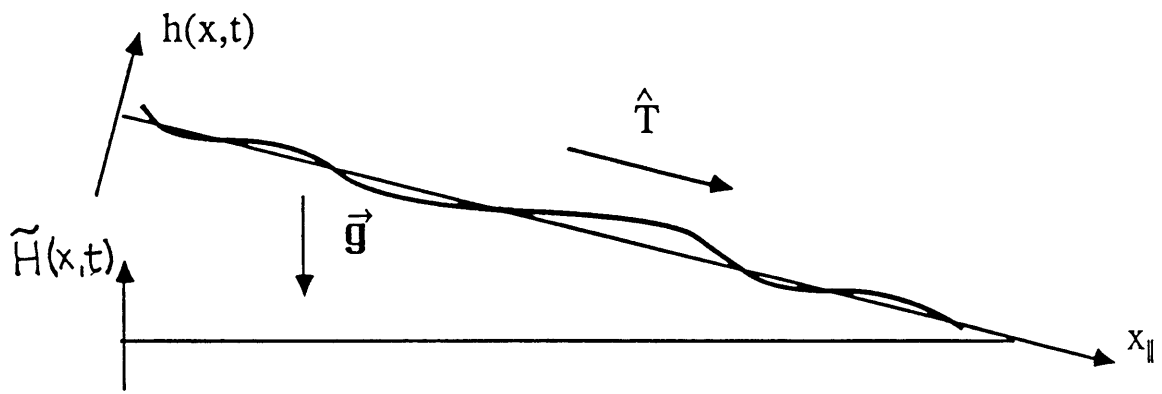


Figure 6.16: The height function $h(\vec{x}, t)$ is defined as a deviation from the flat steady-state sand profile. Gravity drives sand along the transport direction \hat{T} .

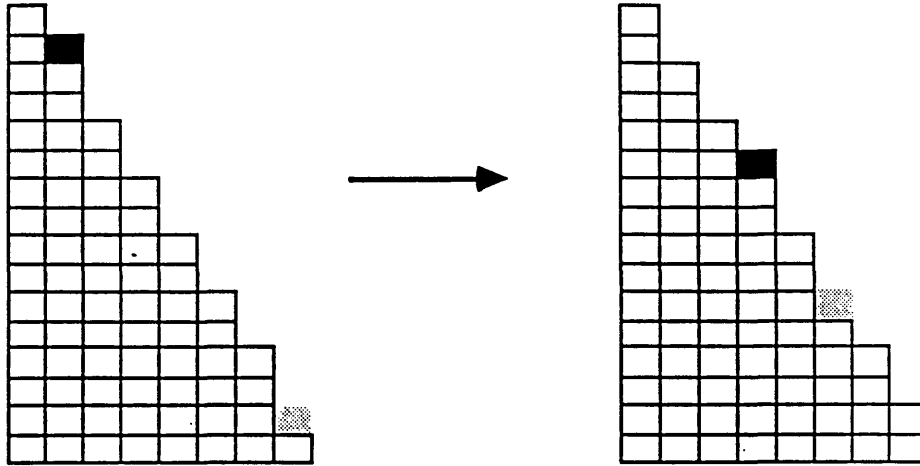


Figure 6.17: The joint inversion symmetry $h \rightarrow -h$ and $x_{\parallel} \rightarrow -x_{\parallel}$: $+h$ (filled block) moves down the slope while $-h$ (void, shaded block) moves uphill.

$\vec{x}_{\perp} \equiv \vec{x} - \vec{x}_{\parallel}$, then (1) the system has rotational invariance in \vec{x}_{\perp} and translational invariance in $\vec{x}_{\perp}, \vec{x}_{\parallel}$; but (2) it lacks reflection symmetry in x_{\parallel} and in h because of the presence of a preferred direction \hat{T} . However, with respect to the average flat surface, “bumps” will move downhill while “voids” will move uphill as illustrated in Figure 6.17. We therefore have (3) the joint inversion symmetry $h \rightarrow -h$ and $x_{\parallel} \rightarrow -x_{\parallel}$. (4) The system lacks translational symmetry in h because of the presence of gravity. (h measures the deviation from the average slope which is fixed once the input rate and the box size are specified). We also take note of (5) an important conservation law that the relaxation dynamics during an avalanche does not change the number of particles, except (6) for the particles added randomly from outside.

We now construct the equation of motion based solely on factors (1) to (6) listed above. From the conservative nature of the transport dynamics (5), the equation of

motion is required to take on the form

$$\frac{\partial h}{\partial t} + \vec{\nabla} \cdot \vec{j}(h) = \eta(\vec{x}, t), \quad (6.5)$$

with the stochasticity η being the only sink/source from condition (6). There has to be a transport current $\vec{j}(h)$. The current can depend directly on h as there is no translational symmetry in h by (4). We use the other symmetry factors to specify the form of $\vec{j}(h)$. Since the current is a vector, it must be constructed from $\vec{\nabla}$ and \hat{T} , the only vectors in the problem. In general, the current has the form

$$\begin{aligned} \vec{j}(h) \equiv & -a_1 \vec{\nabla} h - a_2 \vec{\nabla}(h^2) - \dots - b_n \vec{\nabla}(\vec{\nabla} h)^{2n} - c_n \vec{\nabla}(\nabla^2 h)^n + \dots \\ & + \lambda_1 h \hat{T} + \lambda_2 h^2 \hat{T} + \dots + \lambda_n (h^n) \hat{T} + v_n (\nabla h)^{2n} \hat{T} + w_n (\nabla^2 h)^n \hat{T} + \dots \end{aligned}$$

We are interested in the large-distance ($k \rightarrow 0$) properties of the system. In this limit, the term a_2 can be neglected compared to the λ_2 term because it involves a spatial derivative. Similarly, the terms b_n and c_n are ignored when compared to v_n and w_n respectively, and the v_n and w_n are themselves small compared to the λ_n terms. As to the remaining terms $\lambda_n h^n \hat{T}$, we expect the fluctuation of h to be small if the surface is flat as initially assumed. (The self consistency of this assumption will be checked when the scaling behavior of h is calculated). Therefore higher order

h terms are also ignored, and we have

$$\vec{j}(h) = -a_1 \vec{\nabla} h + \lambda_1 h \hat{T} + \lambda_2 h^2 \hat{T}, \quad (6.6)$$

to leading order. Of course the a_1 and λ_2 terms are also small compared to the λ_1 term, except that the λ_1 term is forbidden by the joint inversion symmetry (3). In fact, even without (3), the λ_1 term corresponds to a simple streaming motion and can be transformed away by going to a moving frame $x_{\parallel} = x_{\parallel} - \lambda_1 t$. Of the two remaining terms, $\lambda_2 \equiv \lambda/2$ is the driving force proportional to the slope of the average flat surface; this term originates from local transport dynamics such as the nonlinear friction or the threshold dynamics. The $\vec{\nabla} h$ term is the linear current present in any diffusive process; a_1 can be interpreted as the surface tension for the sandpile. However, for the anisotropic problem (2) at hand, the surface tension is in general a tensor $\vec{\nu}$, with components ν_{\parallel} and ν_{\perp} in directions parallel and perpendicular to transport \hat{T} respectively. We thus arrive at

$$\vec{j} = -\nu_{\perp} \vec{\nabla}_{\perp} h - \nu_{\parallel} \partial_{\parallel} h \vec{T} + \frac{\lambda}{2} h^2 \hat{T}, \quad (6.7)$$

and the equation of motion (6.5) becomes

$$\partial_t h(\vec{x}, t) = \nu_{\parallel} \partial_{\parallel}^2 h + \nu_{\perp} \nabla_{\perp}^2 h - \frac{\lambda}{2} \partial_{\parallel} (h^2) + \eta(\vec{x}, t). \quad (6.8)$$

Before we present a detailed analysis of (6.8), we emphasize that the most important feature of this equation is that it has no mass term ($-h/\tau$) which would destroy criticality. In Chapter 5, we saw that translational symmetry along the surface normal can remove the mass term and “produce” criticality. Here translational symmetry is explicitly absent by (4). It is the conservative nature (5) of the deterministic part of the dynamics that rules out the mass term in the equation of motion (6.8).

Equation (6.8) describes driven-diffusion and has been studied[98] in the context of a conservative noise $\langle \eta(\vec{x}, t) \eta(\vec{0}, 0) \rangle = 2D \nabla^2 \delta^2(\vec{x}) \delta(t)$. In the present case, the addition of sand particles from the outside destroys the local conservation rule. Although in steady-state the balance of drainage from the boundaries and the flux of the added particles implies $\langle \eta(\vec{x}, t) \rangle = 0$, the random-walkers associated to each site give a leading moment of noise

$$\langle \eta(\vec{x}, t) \eta(\vec{x}', t') \rangle = 2D \delta^d(\vec{x} - \vec{x}') \delta(t - t'), \quad (6.9)$$

in the hydrodynamic limit. Here D is a measure of the strength of the noise; it is related to the step size P of the random-walkers by $D \sim P^2$. Note that for the discrete model, D would be system size dependent due to the size dependences of the local deposition rate p and the coarse-grained unit cell size l_0 and t_0 . This ultimately results in the different L dependences of the power spectra between the discrete and the continuum model (see Figure 6.5 and Figure 6.12).

6.3.2 Dynamical Renormalization Group Analysis

To study the scaling of fluctuations in the hydrodynamic region, we do a dynamical renormalization group calculation. We calculate the two-point correlation function $\langle h(\vec{x}, t)h(\vec{x}', t') \rangle \equiv C(\vec{x} - \vec{x}', t - t')$. In the absence of nonlinearity, (6.8) is simply a diffusion equation (with anisotropy). Its solution is

$$C(\vec{x}, t) = \frac{D}{\nu_{\parallel}} x_{\parallel}^{2-d} G\left(\frac{\nu_{\parallel} t}{x_{\parallel}^2}, \sqrt{\frac{\nu_{\parallel}}{\nu_{\perp}}} \frac{x_{\perp}}{x_{\parallel}}\right). \quad (6.10)$$

Nonlinearity can be included perturbatively, the net effect is the modification (i.e., renormalization) of the parameters $D, \nu_{\parallel}, \nu_{\perp}$. In general we have

$$D^R = D \left[1 + a_1(\lambda x_{\parallel}^{\epsilon}) + a_2(\lambda x_{\parallel}^{\epsilon})^2 + \dots \right], \quad (6.11)$$

with similar expansions for ν_{\parallel}^R and ν_{\perp}^R . Here x_{\parallel}^{ϵ} is the length dimension of the nonlinearity λ . For renormalizable theories, series such as (6.11) can be summed to yield scaling forms, i.e.

$$\begin{aligned} D^R &= D(1 + \alpha_1(\lambda x_{\parallel}^{\epsilon}))^{\beta_1} \\ \nu_{\parallel}^R &= \nu_{\parallel}(1 + \alpha_2(\lambda x_{\parallel}^{\epsilon}))^{\beta_2} \\ \nu_{\perp}^R &= \nu_{\perp}(1 + \alpha_3(\lambda x_{\parallel}^{\epsilon}))^{\beta_3}. \end{aligned}$$

Inserting the above into (6.10), we find that in the hydrodynamic limit the correlation function has the simple form

$$C(\vec{x}, t) = x_{\parallel}^{2\chi} F\left(\frac{t}{x_{\parallel}^z}, \frac{x_{\perp}}{x_{\parallel}^{\zeta}}\right) \quad (6.12)$$

where the exponents χ , z and ζ are the roughness, dynamic and anisotropy exponents respectively. In the absence of nonlinearity, we have the free exponent values $\chi_0 = (2-d)/2$, $z_0 = 2$, and $\zeta_0 = 1$ by comparing (6.10) and (6.12). Finding the exponents in the presence of nonlinearities requires in general the knowledge of the entire perturbation series such as (6.11). The method of renormalization group short cuts this process. We make a hypothesis that $C(\vec{x}, t)$ scales as (6.12).⁶ We then perform the series of operations outlined at the end of Chapter 2 to obtain the exponents χ , z , and ζ .

(i) Naive dimensions:

A change of scale $x_{\parallel} \rightarrow bx_{\parallel}$ is accompanied by $t \rightarrow b^z t$, $\vec{x}_{\perp} \rightarrow b^{\zeta} \vec{x}_{\perp}$ and $h \rightarrow b^{\chi} h$.

After this rescaling, Eqn. (6.8) transforms to

$$b^{x-z} \frac{\partial h}{\partial t} = \nu_{\parallel} b^{x-2} \partial_{\parallel}^2 h + \nu_{\perp} b^{x-2\zeta} \partial_{\perp}^2 h - \frac{\lambda}{2} b^{2x-1} \partial_{\parallel} h^2 + b^{-z/2-(d-1)\zeta/2-1/2} \eta,$$

where Eqn. (6.9) has been used to determine the scaling of η . Thus we identify the

⁶This is in essence the hypothesis of the summability of (6.11), and is otherwise known as the renormalizability hypothesis.

naive scaling for these parameters:

$$\begin{aligned}
\nu_{\parallel} &\rightarrow b^{z-2}\nu_{\parallel}, \\
\nu_{\perp} &\rightarrow b^{z-2\zeta}\nu_{\perp}, \\
\lambda &\rightarrow b^{\chi+z-1}\lambda, \\
D &\rightarrow D^{z-2\chi-\zeta(d-1)-1}.
\end{aligned} \tag{6.13}$$

(ii) Perturbative Calculation

We next calculate the correction to the parameters due to nonlinearity. Here we will carry out the calculation to the leading order. We go to Fourier space, where

$$h(\vec{x}, t) = \int \int \frac{d\omega}{2\pi} \frac{d^d k}{(2\pi)^d} h(\vec{k}, \omega) e^{i(\vec{k}\cdot\vec{x} - \omega t)}.$$

Eqn. (6.8) becomes

$$h(\vec{k}, \omega) = G_0(\vec{k}, \omega)\eta(\vec{k}, \omega) - \frac{\lambda}{2} G_0(\vec{k}, \omega)(ik_{\parallel}) \int \int \frac{d^d q}{(2\pi)^2} \frac{d\mu}{2\pi} h(\vec{q}, \mu) h(\vec{k} - \vec{q}, \omega - \mu). \tag{6.14}$$

Here

$$G_0(\vec{k}, \omega) = \frac{1}{\nu_{\parallel} k_{\parallel}^2 + \nu_{\perp} k_{\perp}^2 - i\omega}$$

is the bare propagator, and the Fourier transformed noise spectrum is

$$\langle \eta(\vec{k}, \omega) \eta(\vec{k}', \omega') \rangle = 2D \delta^d(\vec{k} + \vec{k}') \delta(\omega + \omega'). \tag{6.15}$$

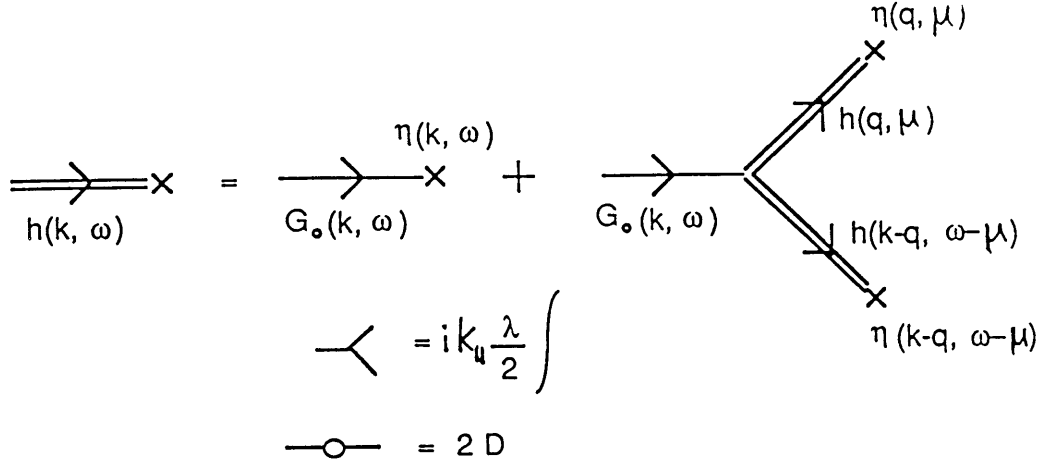


Figure 6.18: Diagrammatic representation of the nonlinear integral equation (6.14) , and the perturbation series that results from it.

Eqn. (6.14) is a convenient starting point for a perturbative calculation of $h(\vec{k}, \omega)$ in powers of λ as indicated diagrammatically in Figure 6.18. The graphic expansion is quite standard[59] with \longrightarrow indicating the propagator G_0 , and \times depicting the noise $\eta(\vec{k}, \omega)$. The averaging over stochastic noise is performed using Eqn. (6.15), and the renormalized response function $G(\vec{k}, \omega)$ [defined by $h(\vec{k}, \omega) \equiv G^R(\vec{k}, \omega)\eta(\vec{k}, \omega)$] is given perturbatively in Figure 6.19a. The lowest order (one loop) correction is

$$G^R(\vec{k}, \omega) = G_0(\vec{k}, \omega) + 4 \left(\frac{\lambda}{2}\right)^2 2D G_0^2(\vec{k}, \omega) \int \frac{d\mu}{2\pi} \frac{d^d q}{(2\pi)^d} i k_{||} i \left(\frac{k_{||}}{2} - q_{||}\right) G_0\left(\frac{\vec{k}}{2} - \vec{q}, \frac{\omega}{2} - \mu\right) G_0\left(\frac{\vec{k}}{2} + \vec{q}, \frac{\omega}{2} + \mu\right) G_0\left(-\frac{\vec{k}}{2} - \vec{q}, -\frac{\omega}{2} - \mu\right) + O(\lambda^4),$$

where the combinatorial factor of four represents possible noise contractions leading to Figure 6.19a.

Clearly, the correction to the propagator above is proportional to k_{\parallel} . For symmetry reasons odd powers of k_{\parallel} and k_{\perp} cannot survive after performing the spherical average $\int d^d q$. The leading k dependences are therefore of the form $k_{\parallel}^2, k_{\parallel}^4, k_{\parallel}^2 k_{\perp}^2$ of which only the k_{\parallel}^2 term is kept, since we are interested in the hydrodynamical limit of $k \rightarrow 0$. After performing the integrals (see the Appendix), we have to $O(k^2)$,

$$G_0^R(\vec{k}, 0) = G_0(\vec{k}, 0) + G_0^2(\vec{k}, 0) \left[-\frac{3\pi}{32} \nu_{\parallel} k_{\parallel}^2 \left(u \frac{k_{\parallel}^{-\epsilon}}{\epsilon} \right) \right], \quad (6.16)$$

where $\epsilon = 4 - d$ and we have defined an effective coupling constant

$$u \equiv \frac{\lambda^2 D}{\nu_{\parallel}^{3/2} \nu_{\perp}^{3/2}} \frac{2S_{d-1}}{(2\pi)^d}.$$

The propagator can now be written as

$$G^R(\vec{k}, 0) = \frac{1}{\nu_{\parallel}^R k_{\parallel}^2 + \nu_{\perp}^R k_{\perp}^2 - i\omega},$$

with the effective surface tension

$$\nu_{\parallel}^R = \nu_{\parallel} \left[1 + \frac{3\pi}{32} \left(u \frac{k_{\parallel}^{-\epsilon}}{\epsilon} \right) + O(u^2) \right] \quad (6.17)$$

and $\nu_{\perp}^R = \nu_{\perp}$. Note that there is no correction to ν_{\perp} to leading order because the

nonlinearly is proportional to k_{\parallel} . In fact ν_{\perp} is not renormalized to any order of the perturbation expansion because the correction propagator is always proportional to k_{\parallel} as shown in Figure 6.19a.

A renormalized noise spectrum $D^R(\vec{k}, \omega)$ can be defined from

$$\langle h^*(\vec{k}, \omega)h(\vec{k}, \omega) \rangle = 2G^R(\vec{k}, \omega)G^R(-\vec{k}, -\omega)D^R(\vec{k}, \omega). \quad (6.18)$$

Again, because the vertex is proportional to k_{\parallel} , the leading order graph (Figure 6.19b) is of order k_{\parallel}^2 which can be neglected in the hydrodynamical limit and the coefficient D is not renormalized to all orders in the perturbation series, i.e. $D^R = D$.

The last parameter to consider is the nonlinearity parameter λ which has a contribution from the graphs in Figure 6.19c. A one-loop calculation gives a null result. In fact this is also true to all orders of the perturbation series. The nonrenormalizability of λ is due to a Galilean invariance in the equation of motion. (See Appendix to Chapter 5 for a detailed discussion.) Eqn. (6.8) is invariant under an infinitesimal reparameterization $x_{\parallel} \rightarrow x_{\parallel} - \delta\lambda t, t \rightarrow t$ if $h \rightarrow h + \delta$. Note that the parameter λ appears both as the coefficient of the nonlinearity in Eqn. (6.8) and as an invariant factor relating to x_{\parallel} and t reparametrizations. Hence any renormalization of the driven-diffusion equation that preserves Galilean invariance must leave the coefficient λ unchanged, i.e. $\lambda^R = \lambda$ to all orders.

(iii) Recursion Relations

Let us find the rescaling behavior of the surface tension ν_{\parallel} . Define an observation

length scale $k_{\parallel}^{-1} = b \cdot a_0$ where a_0 is a microscopic cutoff length, then the dimensionless renormalized surface tension is

$$\tilde{\nu}_{\parallel}^R(b) \equiv \nu_{\parallel}^R(ba_0)^{z-2} = \nu_{\parallel}(ba_0)^{z-2} \left[1 + \frac{3\pi}{32} u \frac{(ba_0)^\epsilon}{\epsilon} + O(u^2) \right].$$

We apply the rescaling operator and obtain

$$b \frac{\partial}{\partial b} \tilde{\nu}_{\parallel}^R(b) = \nu_{\parallel}(ba_0)^{z-2} \left[z - 2 + \frac{3\pi}{32} u (ba_0)^\epsilon \right]$$

We assume the renormalizability of the theory (see section 2.4) and replace ν_{\parallel} by ν_{\parallel}^R .

Then $\nu_{\parallel}(ba_0)^{z-2} = \tilde{\nu}_{\parallel}^R(b)$, and

$$u(ba_0)^\epsilon = \frac{(\lambda^R)^2 D^R}{(\nu_{\parallel}^R)^{3/2} (\nu_{\perp}^R)^{3/2}} \frac{2S_{d-1}}{(2\pi)^d} (ba_0)^{2-d} \equiv \tilde{u}^R(b)$$

(since we already have $\lambda^R = \lambda$, $D^R = D$, $\nu_{\perp}^R = \nu_{\perp}$). Expressing in terms of $l = \log b$, we arrive at the recursion relation

$$\frac{d}{dl} \tilde{\nu}_{\parallel}^R = \tilde{\nu}_{\parallel}^R \left[z - 2 + \frac{3\pi}{32} \tilde{u}^R \right] \quad (6.19)$$

and similarly

$$\frac{d}{dl} \tilde{\nu}_{\perp}^R = \tilde{\nu}_{\perp}^R [z - 2\zeta], \quad (6.20)$$

$$\frac{d}{dl} \tilde{\lambda}^R = \tilde{\lambda}^R [\chi + z - 1], \quad (6.21)$$

$$\frac{d}{dl}\tilde{D}^R = \tilde{D}^R[z - 2\chi - (d-1)\zeta - 1]. \quad (6.22)$$

(iv) RG Flows, Fixed Points and Exponents:

In the hydrodynamic limit ($b \rightarrow \infty$, or $l \rightarrow \infty$), we expect the scaling behavior to be described by (6.10). If this expectation is true, then the parameters $\tilde{\nu}^R$, etc. should be dimensionless in the hydrodynamic limit. This necessarily implies $\frac{d}{dl}\tilde{\nu}_{\parallel}^R = 0$ as $l \rightarrow \infty$ for instance. The exponents may then be solved at the infra-red fixed point ($l \rightarrow \infty$) of the flow equations (6.19) through (6.22).

Since (6.20), (6.21), and (6.22) are exact as explained, we immediately obtain from them the exponents exactly,

$$\chi = \frac{1-d}{7-d}, \quad z = \frac{6}{7-d}, \quad \zeta = \frac{3}{7-d}. \quad (6.23)$$

Using the value of the exponents (6.23) and the recursion relation (6.19), we may obtain the flow equation for the effective interaction parameter

$$\frac{d}{dl}\tilde{u}^R = \tilde{u}^R \left[(4-d) - \frac{9\pi}{64}\tilde{u}^R \right]. \quad (6.24)$$

Above the upper critical dimension of $d_c = 4$, the nonlinearity is irrelevant, and we recover the ideal scaling $z_0 = 2$, $\chi_0 = (2-d)/2$, $\zeta_0 = 1$. Below $d = 4$, there is a stable fixed point at $\tilde{u}^* \equiv \tilde{u}^R(l \rightarrow \infty) = (64/9\pi)\epsilon$ to first order in $\epsilon = 4-d$. At the fixed point \tilde{u}^* , the scaling behavior of the surface is described by the set of exponents

found in (6.23).

It is important to realize that though the fixed point \tilde{u}^* is known only perturbatively to $O(\epsilon)$, the scaling exponents (6.23) are exact. The exactness of these exponents is a result of the non-renormalizability conditions on ν_\perp , λ and D which remove anomalous dimensions to all loop orders. This point can probably be best represented by direct examination of the correlation function $C(\vec{x}, t)$. We have already shown the parameters D, λ, ν_\perp are not changed by the inclusion of nonlinearity. The form of ν_\parallel^R can be obtained from integration of the flow equation. From (6.24) we obtain the renormalized coupling constant:

$$\tilde{u}^R(x_\parallel) = \frac{ux_\parallel^\epsilon}{1 + \frac{9\pi u}{64\epsilon}x_\parallel^\epsilon}, \quad \text{with } x_\parallel = a_0 e^l$$

to leading order in ϵ . The renormalized surface tension can now be obtained by integrating (6.19), giving

$$\tilde{\nu}_\parallel^R(x_\parallel) = \nu_\parallel^R x_\parallel^{z-2} = \nu_\parallel x_\parallel^{z-2} \left(1 + \frac{9\pi u}{64\epsilon}x_\parallel^\epsilon\right)^{1/3}.$$

Inserting $\nu_\parallel^R(x_\parallel)$ and $D^R = D$, $\lambda^R = \lambda$, $\nu_\perp^R = \nu_\perp$ into (6.10) we obtain the renormalized correlation function

$$C^R(\vec{x}, t) = \frac{D}{\nu_\parallel} \left(1 + \frac{9\pi u}{64\epsilon}x_\parallel^\epsilon\right)^{-1/3} x_\parallel^{2-d} G \left(\frac{\nu_\parallel t}{x_\parallel^2} \left(1 + \frac{9\pi u}{64\epsilon}x_\parallel^\epsilon\right)^{1/3}, \sqrt{\frac{\nu_\parallel}{\nu_\perp}} \frac{x_\perp}{x_\parallel} \left(1 + \frac{9\pi u}{64\epsilon}x_\parallel^\epsilon\right)^{1/6} \right). \quad (6.25)$$

Comparing the above with (6.12), we can immediately read off the exponents (6.23) in the hydrodynamic limit $x_{\parallel} \rightarrow \infty$. It is now apparent how the exponents will not be affected by higher-order loop corrections because they only change the coefficient in front of x_{\parallel}^{ξ} (i.e. the fixed point position) but not the exponent $1/3$. It is also worth noting that the diagrams which contribute to order $k_{\parallel}^2 k_{\perp}^2$ in the propagator $G^R(\vec{k}, \omega)$ and to k_{\parallel}^2 in the noise spectrum $D^R(\vec{k}, \omega)$ also amount to a correction to the coefficient of x_{\parallel}^{ξ} . They do not modify the leading scaling behaviors (6.23).

Finally we point out that the roughening exponent χ as given by (6.23) is negative for $d > 1$. Since the width of the interface (see section 4.2 for a detail discussion) is characterized by $w \sim L_{\parallel}^{\chi}$, then $\chi < 0$ implies that the surface is asymptotically flat for $d > 1$. Also the exponent $z \leq 2$ for all dimensions. This gives an upper cutoff time $T_B \sim L^z$ that is small compared to the onset of sandpile's discharge region. ($T_C \sim L^2$, see Figure 6.6). Hence the slope does not change appreciably in the hydrodynamic region (II). These results provide a self-consistent check of the “flat and stationary surface” assumption made at the outset of the analysis. The assumption is no longer valid below $1 + 1$ dimensions.

6.3.3 Spatial and Temporal Fluctuations

The exponents χ , z , and ζ are the fundamental scaling dimensions of the system; other quantities can in principle be calculated from them. In particular, we are interested in the spatial and temporal correlations of observables such as the transport current and

the energy dissipation. Although the spatial part of the fluctuations is easily defined in a formal sense, it is not easily visualizable. As mentioned in the beginning of this chapter, fractal structures are more easily seen in the growth model of chapter 5, while temporal fluctuations can be naturally probed in transport systems such as the one studied in this chapter. In the following, we show how the spatial and temporal fluctuations can be related to the fundamental dynamical field h .

(i) Spatial Structures

To probe the spatial structure of our fluctuating surface, we need to calculate the response of the surface to an infinitesimal perturbation. This response function can be defined in the following way. We start with some initial height configuration $h_0(\vec{x})$ and deposit particles randomly as described by $\eta(\vec{x}, t)$ and obtain a series of height profiles $h(\vec{x}, t)$. This is followed by another run starting from the same configuration $h_0(\vec{x})$, and depositing particles with the same randomness $\eta(\vec{x}, t)$ except for a small difference $\delta\eta(\vec{x}, t)$. The surface profile obtained the second time is $h'(\vec{x}, t)$ and is different from the first by an amount $\delta h(\vec{x}, t) = h(\vec{x}, t) - h'(\vec{x}, t)$. The response function is then $R(\vec{x}, \vec{x}', t, t') = \delta h(\vec{x}, t) \cdot \delta\eta^{-1}(\vec{x}', t')$. Mathematically, we can obtain this response function by substituting $h + \delta h$ for h and $\eta + \delta\eta$ for η in Eqn. (6.8), and

$$\frac{\partial}{\partial t}(\delta h) = \nu_{\parallel} \partial_{\parallel}^2(\delta h) + \nu_{\perp} \nabla_{\perp}^2(\delta h) - \frac{\lambda}{2} \partial_{\parallel}(h \cdot \delta h) - \frac{\lambda}{2} \partial_{\parallel}(\delta h)^2 + \delta\eta.$$

To linear order, the response function is represented by the following shorthand

$$R(\vec{x}, t) = \left[\frac{\partial}{\partial t} - \nu_{\parallel} \partial^2 - \nu_{\perp} \nabla_{\perp}^2 + \frac{\lambda}{2} \partial_{\parallel} h + \frac{\lambda}{2} h \partial_{\parallel} \right]^{-1}. \quad (6.26)$$

In Fourier space the linear response function is the free propagator $R_0(\vec{k}, \omega) = 1/[-i\omega + \nu_{\parallel} k_{\parallel}^2 + \nu_{\perp} k_{\perp}^2]$. With the nonlinearity $\partial_{\parallel} h \sim x_{\parallel}^{z-1} = x_{\parallel}^{-z}$. Since $z < 2$ as found in the previous section, the $\partial_{\parallel} h$ term in (6.26) dominates ∂_{\parallel}^2 in the hydrodynamic limit. The large distance scaling properties are therefore governed by the response

$$R(\vec{k}, \omega) = \frac{1}{\omega} f\left(\frac{\omega}{k_{\perp}^2}, \frac{\omega}{k_{\parallel}^z}\right).$$

For a point perturbation $\delta\eta(\vec{x}, t) = \delta(t)\delta^d(\vec{x})$, the response is

$$\delta h(\vec{x}, t) = t^{-d/z} f\left(\frac{t}{x_{\perp}^2}, \frac{t}{x_{\parallel}^z}\right). \quad (6.27)$$

Not surprisingly, we see that the influence of the perturbation spreads as $t^{1/2}$ perpendicular to the driving direction and as $t^{1/z} > t^{1/2}$ in the downhill direction. In $2 + 1$ dimensions, $1/z = 5/6$ and the effect of anisotropy is quite dominating. From (6.27), we can also calculate other useful quantities such as the size distribution of the sites influenced, and the fractal dimension of the influenced region, etc. However, the relation of these quantities to the fundamental dynamical field h are model dependent and will not be pursued here.

(ii) Temporal Fluctuations

A direct comparison with simulation results of the previous section can be made by computing the power-spectra for the output current $J(t)$ and the energy dissipation $E(t)$. The output current measured in section 6.2 is the local current $j(\vec{x}, t)$ at the boundary $x_{\parallel} = L_{\parallel}$, and for a general $d + 1$ dimensional system it is $J(t) = \int d^{d-1} x_{\perp} \vec{j}(k_{\parallel}, \vec{x}_{\perp}, t) \cdot \hat{T}$. Using (6.6) for \vec{j} and noting that in $d < 4$ scaling is dominated by the h^2 part of the current, we obtain

$$\begin{aligned} \langle J(t)J(0) \rangle_c &= \int d^{d-1} x_{\perp} d^{d-1} x'_{\perp} \langle h^2(\vec{x}, t) h^2(\vec{x}', 0) \rangle_c \\ &\sim L_{\perp}^{d-1} t^{[4x+(d-1)\zeta]/z}, \end{aligned}$$

where we used $\langle h^2(\vec{x}, t) h^2(\vec{0}, 0) \rangle_c \sim \langle h(\vec{x}, t) h(\vec{0}, 0) \rangle_c^2$. The Fourier transform of the correlation function yields the power spectrum $S_J(\omega) \sim \omega^{-\phi_J}$ with $\phi_J = 1/z$.

A similar calculation can be carried out for the energy dissipation $E(t)$. Here we start from the total “potential energy” of the system $U(t) = \frac{1}{2} \int d^d x [\tilde{H}(\vec{x}, t)]^2$ where $\tilde{H}(\vec{x}, t) = H_0(\vec{x}) + h(\vec{x}, t)$ is the time-dependent coarse-grained landscape of the sandpile. The energy dissipated is simply the loss of potential energy, i.e.

$$E(t) = -\frac{dU}{dt} = -\int d^d x H_0(\vec{x}) \frac{\partial h}{\partial t}$$

(only the leading order term in $h(\vec{x}, t)$ is kept). Using the equation of motion (6.8),

| d | ≥ 4 | 3 | 2 | 1 |
|----------|-----------|-------|-------|-----|
| z | 2 | 1.50 | 1.20 | 1 |
| χ | $(2-d)/2$ | -0.50 | -0.20 | 0 |
| ζ | 1 | 0.75 | 0.60 | ... |
| ϕ_J | 0.5 | 0.67 | 0.83 | 1 |
| ϕ_E | 1 | 1.33 | 1.67 | 2 |

Table 6.2: Numerical values for some of the exponents defined in the text.

and by partial integration we obtain

$$E(t) = \int d^d x \hat{T} \cdot \vec{J}(\vec{x}, t) = \int d^d x h^2(\vec{x}, t).$$

We see that the total energy dissipated at each time is just the sum of local transport activities, precisely the quantity monitored in the simulation. The energy correlation function can again be calculated using the basic correlation function $\langle hh \rangle$, giving

$$\begin{aligned} \langle E(t)E(0) \rangle_c &= \int d^d x d^d x' \langle h^2(\vec{x}, t) h^2(\vec{x}', 0) \rangle_c \\ &\sim L^{d_t [4\chi + (d-1)\zeta + 1]/z}. \end{aligned}$$

Fourier transform of the above then gives us the energy dissipation power spectrum $S_E(\omega) \sim L^d \omega^{-\phi_E}$, with $\phi_E = 2/z$. The numerical values of various exponents are listed in Table 6.2.

Comparing the exponent values for $d = 1$ to the simulation result of section 6.2, we see that while the L dependences of the power spectra is the same as those derived above, the frequency dependences of the observed spectra ($\phi_J \approx 0.8$ and $\phi_E \approx 1.0$

for the continuum model) do not agree with the above results. This discrepancy is attributed to the over-simplification of the noise-spectrum (6.9). The coarse grained unit cell of the sandpile has a length l_0 which is system size independent. View this unit cell as an isolated system: According to the analysis of section 6.2, there is a time scale $T_C \sim l_0^2$ above which this unit cell is in the discharge mode, effectively generating a temporally anti-correlated noise. A large system in the interaction region is then actually subject to an anti-correlated noise with spectrum

$$\langle \eta(\vec{x}, \omega) \eta(\vec{x}', -\omega) \rangle \sim \delta^d(\vec{x} - \vec{x}') \omega^{1/2}$$

in one dimension.⁷ We therefore expect the scaling behaviour for the continuum model to be modified.

In the case of correlated noise, we can no longer evaluate the exponents exactly because Galilean invariance is no longer valid (see chapter 5). Nevertheless, let us ignore the contribution of vertex renormalization in the spirit of Flory. We simply balance the exponents using naive dimensional counting, and find that the result $\phi_J = 1/z$ and $\phi_E = 2/z$ is not altered, but with $z = 6/5$ in 1-D. This gives $S_J(\omega) \sim \omega^{-0.83}$, $S_E(\omega) \sim L\omega^{-1.67}$, which is an improvement in the right direction. Systematic calculation including the renormalization of λ can be carried out using the method described in chapter 5.

⁷This situation does not happen to the discrete model because $l_0 \sim L^{1/2}$. The anti-correlating part is not seen until a time scale $T_C > l_0^2 \sim L$. But that is already the upper cutoff for the driven diffusion equation since $z = 1$ for the 1-D sandpile.

6.3.4 Universality Classes and Other Models

As stated in section 6.3.1, the analytical model described in this section applies to transport processes that (a) are locally conservative, (b) have an unique transport direction, (c) have non-conservative uncorrelated noise throughout the system, and (d) have an uniform and stationary gradient set up by the material transported (e.g. flat average surfaces). Given the above conditions, the large distance, long time scaling behaviour found in section 6.3.2 is universal, i.e., the “hydrodynamic” properties should not depend on the microscopic details of the system. However, alterations in any of the above conditions can lead to different scaling behaviours; indeed it can even destroy criticality.

Of the four conditions listed above, (d) is by far the most model dependent one in that its existence is based on simulation results. We have constructed a self-consistent theory based on this assumption. We will focus our discussion on conditions (a)-(c) assuming that (d) is somehow given by the process. In other words, we will only look at processes that exhibit (d).

(i) Role of Conservation Laws:

Conservation laws are generally satisfied by most transport systems and can lead to criticality as seen in section 6.3.2 . However, it is worth pointing out that conservation laws are not necessary for the occurrence of SOC. As we have seen in chapter 5, a translational symmetry in the dynamic field (h) can also bring the system to criticality. There can be still other mechanisms. Also, conservation laws themselves

are not sufficient to guarantee the existence of criticality. With a conserved transport quantity (h), we will have an equation of motion

$$\frac{\partial h}{\partial t} + \vec{\nabla} \cdot \vec{j}(h) = \eta(\vec{x}, t), \quad (6.28)$$

in which the criticality breaking term h/τ is excluded. But there are still other mechanisms preventing criticality.

One such possibility is pointed out by Grinstein, Lee and Sachdev[99]; it can easily be appreciated in the following simple example. Consider an ideal diffusion equation

$$\frac{\partial h}{\partial t} = \nu \nabla^2 h + \eta(\vec{x}, t),$$

which does not have any time or length scales. If the noise is conservative, i.e., $\langle \eta(\vec{x}, t) \eta(\vec{0}, 0) \rangle = 2D \nabla^2 \delta^d(\vec{x}) \delta(t)$, then the solution is $\langle h(\vec{x}, t) h(\vec{0}, 0) \rangle = t^{-d/2} e^{-x^2/\nu t}$. Although the correlation function has a long time tail $t^{-d/2}$, the equal time spatial correlation function is delta correlated, i.e. $\langle h(\vec{x}, 0) h(\vec{0}, 0) \rangle = \delta^d(\vec{x})$. There is no long-range spatial correlation and hence no criticality. For a given theory, it is important to check whether the correlation function is long-ranged. It is however believed that the nonlinearity will enhance spatial correlation and that the above scenario is not a problem in low dimensions where nonlinearities are relevant.

Barring a few problematic cases, conservation laws seem to give rise to criticality in a wide variety of situations. Next, we point out a number of possible universality

classes for critical systems with conservative dynamics.

(ii) Role of Stochasticity and Randomness

We first restrict ourselves to anisotropic transport processes and explore the effect of the noise term. As derived in section 6.3.2, the simplest nontrivial equation of motion is

$$\frac{\partial h}{\partial t} = \nu \nabla^2 h - \frac{\lambda}{2} \partial_x (h^2) + \eta(\vec{x}, t). \quad (6.29)$$

If the noise is conservative, i.e.

$$\langle \eta(\vec{x}, t) \eta(\vec{0}, 0) \rangle = 2D \nabla^2 \delta^d(\vec{x}) \delta(t), \quad (6.30)$$

then a change in scale $x \rightarrow bx$ (accompanied by $t \rightarrow b^z t$, $h \rightarrow b^\chi h$) leads to transformation of the parameters

$$\nu \rightarrow b^{z-2} \nu, \quad D \rightarrow b^{z-2\chi-d-2} D, \quad \lambda \rightarrow b^{\chi+z-1} \lambda.$$

In the absence of nonlinearity (i.e., $\lambda = 0$), the equation is made scale-invariant upon the choice of $z_0 = 2$ and $\chi_0 = -d/2$. A nonlinearity added to this scale invariant equation has a dimension $y_\lambda^0 = \chi_0 + z_0 - 1 = 1 - d/2$. For $d > 2$, a small nonlinearity is irrelevant, while for $d < 2$, the nonlinearity is relevant and grows under rescaling. The upper critical dimension for the problem with conservative noise is $d_c = 2$. This is actually the problem of forced particle diffusion studied by Schmittmann and Janssen[98]. The exponents found are similar to those in (6.23) but with d replaced

by $d - 2$.

There is another class of driven transport systems where the input is not from the “top” of the box, but from the end opposite to the open (exit) end. One example is the transport of vortices through a piece of type II superconductor[100]. There have also been some recent simulation of such processes[101]. In the simplest scenario, such a process may be described by (6.29), with the noise term

$$\langle \eta(\vec{x}, t) \eta(\vec{x}', t') \rangle = 2D \delta(x_{\parallel}) \delta(x'_{\parallel}) \delta^{d-1}(\vec{x}_{\perp} - \vec{x}'_{\perp}) \delta(t - t'),$$

where the delta functions $\delta(x_{\parallel}) \delta(x'_{\parallel})$ force the noise to be at the input edge. We again do the naive scaling analysis and find the parameters to transform as

$$\nu \rightarrow b^{z-2} \nu, \quad D \rightarrow b^{z-2\chi-d-1} D, \quad \lambda \rightarrow b^{\chi+z-1} \lambda.$$

The free exponents (for $\lambda = 0$) are in this case $z_0 = 2$, $\chi_0 = 1 - d/2$, giving the nonlinearity a dimension $y_{\lambda}^0 = \chi_0 + z_0 - 1 = (3 - d)/2$, and hence an upper critical dimension $d_c = 3$. This agrees with the upper critical dimension of a similar problem found by Dhar et al.

Another recurring situation is that the medium through which a transport process takes place has quenched randomness. Such a scenario may be described by a “noise” of the form

$$\langle \eta(\vec{x}, t) \eta(\vec{x}', t') \rangle = 2D \delta^d(\vec{x} - \vec{x}'),$$

which is explicitly time independent. Similiar scaling analysis yields $y_\lambda^0 = (6 - d)/2$ giving an upper critical dimension $d_c = 6$ for this process. In general, for spatially and temporally correlated noise of the form

$$\langle \eta(\vec{x}, t) \eta(\vec{0}, 0) \rangle \sim |\vec{x}|^{2\rho-d} |t|^{2\theta-1},$$

the upper critical dimension for the nonlinearity in Eqn. (6.29) is $d_c = 4 + 2\rho + 4\theta$.

(iii) Effect of Isotropy

Transport systems do not always have to be driven in one specific direction. As an example, we can consider the traffic problem in a big city: We assume that the total number of cars on the road is on average constant, but there are random local sources and sinks (i.e. parking lots) so the equation of motion is again Eqn. (6.28) where h is now the density of cars and η describes the randomness. What is the form of \vec{j} if the cars in our system are simply wandering aimlessly? Since this problem is now isotropic, the current operator \vec{j} can only be constructed from combinations of $\vec{\nabla}$ and h 's. Leading terms are $\vec{j} = -\nu \vec{\nabla} h + (\lambda/2) \vec{\nabla}(h^2)$. The first term represents random wanderings of cars (diffusive term). The second term mimicks a cooperative crowding effect. If we write the current above as

$$\vec{j} = -\nu \left(1 - \frac{\lambda}{\nu} h \right) \vec{\nabla} h$$

then it becomes apparent that the second term slows down the wandering of cars if

local car density becomes high, i.e., it is more difficult for cars in traffic jams to get out. Inserting the current operator into the conservation law (6.28), we obtain the following equation of motion

$$\frac{\partial h}{\partial t} = \nu \nabla^2 h - \frac{\lambda}{2} \nabla^2 (h^2) + \eta(\vec{x}, t). \quad (6.31)$$

This is yet another version of the nonlinear diffusion equation. It looks somewhat like the KPZ equation (5.1) but is in fact quite different because it does not have the symmetry $h \rightarrow h + \text{constant}$. Naive dimensional analysis gives an upper critical dimension of 2 above which small nonlinearity is irrelevant. If we transform equation (6.31) into Fourier space, we find that the vertex of the nonlinear term is proportional to k^2 . Following the analysis of section 6.3.2, we immediately see that the loop correction to the noise spectrum is of $O(k^4)$. Therefore for non-conservative noise η the noise spectrum $\langle \eta(\vec{x}, t) \eta(\vec{0}, 0) \rangle = 2D \delta^d(\vec{x}) \delta(t)$ is not changed to any loop order. The nonrenormalization of D immediately gives us an exponent identity $z - 2\chi = d$. However, the parameters ν and λ do get renormalized; they can be calculated in the usual way (as described in section 6.3.2).

Of course, equation (6.31) can be coupled to different types of noise spectra giving rise to different universality classes. We will not try to repeat the enumeration as it is very similar to the one already presented for the anisotropic case.

6.4 Conclusion

In this chapter, we studied the sandpile problem as a model for dissipative transport, both numerically and analytically. We found a number of scaling regions for the sandpile automaton, much like what was found in experiments on real sand. The hydrodynamic region can be studied using the methods of continuum field theory, and the anomalous scaling properties of the long-time tail can be obtained using dynamic renormalization-group. We demonstrated that the hydrodynamic region is the interesting region which exhibits broad band, $1/f$ type, noise spectrum, and the scaling behavior in this region is not cut-off by applying an external driving force as previously believed. These results are illustrated both by numerical simulations, and by deriving the relevant equations of motion using symmetry and conservation laws.

Other new and interesting features of the sandpile automaton are the non-trivial short-time and long-time scaling regions. We have analyzed the long-time region and demonstrated the origin of the great events and their anti-correlation. The power-spectrum for the anti-correlating output current is derived for the one-dimensional system. We expect such long-term memory effects to be present in other processes which have threshold dynamics and metastability; these may include charge-density waves, earth-quakes, and neural activities. What remains to be understood are the relations (if any) among the various scaling regions, the interpretation of multi-fractality, and the role of the boundary conditions in determining the macroscopic scaling properties.

Appendix: Propagator Renormalization

The first order correction to $G^R(\vec{k}, \omega)$ is $G_0^2(\vec{k}, \omega)\Sigma(\vec{k}, \omega)$ where Σ is calculated from the diagram in Figure 6.19a.

$$\begin{aligned} \Sigma(\vec{k}, \omega) &= 4 \left(\frac{\lambda}{2}\right)^2 2D \int \frac{d^d q}{(2\pi)^d} \frac{d\mu}{2\pi} \frac{ik_{\parallel} i \left(\frac{k_{\parallel}}{2} - q_{\parallel}\right)}{\nu_{\parallel} \left(\frac{k_{\parallel}}{2} - q_{\parallel}\right)^2 + \nu_{\perp} \left(\frac{k_{\perp}}{2} - q_{\perp}\right)^2 - i \left(\frac{\omega}{2} - \mu\right)} \\ &\quad \times \frac{1}{\left(\frac{\omega}{2} + \mu\right)^2 + \left[\nu \left(\frac{k_{\parallel}}{2} + q_{\parallel}\right)^2 + \nu_{\perp} \left(\frac{k_{\perp}}{2} + q_{\perp}\right)^2\right]^2}. \end{aligned}$$

The $\omega \rightarrow 0$ and $k_{\perp} \rightarrow 0$ limits can be taken right away. After integration over the internal frequency μ , we have to leading order in k_{\parallel}^2

$$\begin{aligned} \Sigma(k_{\parallel}) &= \left(-\frac{\lambda^2 D}{4}\right) \int \frac{d^d q}{(2\pi)^d} \frac{k_{\parallel}^2 - 2k_{\parallel}q_{\parallel}}{(\nu_{\parallel}q_{\parallel}^2 + \nu_{\perp}q_{\perp}^2) \cdot (\nu_{\parallel}q_{\parallel}^2 + \nu_{\perp}q_{\perp}^2 + \nu_{\parallel}k_{\parallel}q_{\parallel})} \\ &= -\frac{\nu_{\parallel}k_{\parallel}^2}{4} \left(\frac{\lambda^2 D}{\nu_{\parallel}^3}\right) \left(\frac{\nu_{\parallel}}{\nu_{\perp}}\right)^{\frac{d-1}{2}} \frac{2S_{d-1}}{(2\pi)^d} \int_{k_{\parallel}}^{\infty} dq_{\parallel} q_{\parallel}^{d-5} \cdot \int_0^{\infty} dy y^{d-2} \left[(1+y^2)^{-2} + 2(1+y^2)^{-3}\right]. \end{aligned}$$

Note that the above integral is infrared divergent for $d < 4$. This apparent divergence signals the relevance of nonlinearity below 4 dimensions; it is this type of divergences the renormalization procedure is designed to handle. For now we give the diverging integral an infrared cutoff, $k_{\parallel} \rightarrow 0$. It will be made clear in the text that it is only necessary to evaluate the expression for $\Sigma(k_{\parallel})$ to leading order in $\epsilon = 4 - d$,

giving the result

$$\Sigma(k, \omega) = -\frac{\nu_{\parallel} k_{\parallel}^2}{4} \left(\frac{\lambda^2 D}{\nu_{\parallel}^{3/2} \nu_{\perp}^{3/2}} \right) \frac{2S_{d-1}}{(2\pi)^d} \left(\frac{k_{\parallel}^{-\epsilon}}{\epsilon} \right) \frac{3\pi}{8},$$

which leads to (6.16).

Chapter 7

Conclusions and Future Outlooks

In this thesis, I have presented a number of studies of current topics in statistical mechanics and non-equilibrium dynamics, in the context of surfaces and membranes. Some of these studies are refinements of existing knowledge, while others are adventures into the unknown. These works have generated a certain amount of interest and are worthy of further pursuit. In the following, I will give an overall summary of the status of each project and my own view of future developments in these and related fields.

In the theoretical investigation of the macroscopic conformations of the self-avoiding tethered membranes in d -dimensional embedding space, I demonstrated, through direct summations of the perturbation series, the emergence of the anomalous scaling of the two-point correlation function and a finite second virial-coefficient, in a generalized ϵ -expansion scheme. I presented the Renormalization-Group (RG) formalism which can be used to short-cut the direct summation procedure. By deriving the RG recursion relations to second-order in ϵ , I explicitly showed how the results of the direct summations (also known as the one-loop renormalizability) are required to validate the ϵ -expansion. The calculations of the RG fixed points and the exponent values to higher orders in ϵ are traditionally done by performing a series of formal, field theoretical manipulations[102]. The RG procedure outlined in this work represents an alternative way of doing the systematic calculations but using the more intuitive recursion relations.

I have also presented an interpretation of the generalized ϵ -expansion, and illus-

trated how universal quantities such as the fixed points and the exponent values may be extracted to order ϵ . However, the ϵ -expansion does not have any power in predicting the macroscopic membrane conformations because the expansion parameter ϵ is 8 for membranes in 3-dimensions. The ϵ -expansion was also carried out near the “stretched-membrane” limit and revealed that the lower-critical dimension for the existence of membrane’s “crumpled” phase may not be the lower bound $d = 2$ previously thought. This finding allows the possibility that membranes in 3-dimension may be always “flat” as suggested by recent simulations[8][33].

Among the unfinished businesses in this study are (a) a proof of the “dimensional regularization” procedure which can be achieved by a direct summation of the full partition function, and (b) a demonstration that the ϵ -expansion may be carried out to higher orders. The former subject can probably be done without too much difficulty and will be discussed in a forth coming article. The latter is much more formidable as it is marred by algebraic complexities of various multi-handle diagrams required by the RG procedure. Here one faces the reality that the RG procedure is at the present time still very primitive and inefficient. (It involves the calculations of many redundant terms which eventually cancel each other.) In conventional field theories and polymer theories, one can cope with the inefficiencies and the redundancies because all of the calculations involved are in principle simple, and one has a systematic way of doing them (the Feynman integral tricks). In the membrane case, the difficulties lie within the calculations of the redundant terms; they are the boundary dependent terms. I

believe that the minimal calculations needed for the final answers to physical questions (such as the scaling properties of the radius of gyration) are still simple. However, a better understanding of RG is needed to identify the relevant contributions. With a better understanding of RG, we can also pursue the behavior of the membrane at its θ -point, as well as calculating the dynamical behaviors of a suspension of membranes.

The light scattering study of GO suspension reported in this thesis is the first direct experimental study of the tethered membranes. Measurements of the static structure factor indicate that the conformation of membranes in good suspension is *crumpled* rather than *flat*, in contradiction with recent simulation results[8][33]. The experimental results yield a fractal dimension of 2.4 and a radius-of-gyration exponent of 0.83 for the GO membranes; these values are close to that of Flory's mean-field estimate. A number of future experiments are being planned: By adjusting the pH values of the GO suspension, one can probe the θ -point transition of the membranes. A possible crumpling transition can be searched by varying the ambient temperatures and the solvent qualities. Also the light scattering set-ups are being modified to allow a detailed study of dynamical properties of the membranes. Through the proposed theoretical and experimental studies, one can obtain more "practical" knowledge of the graphite membranes, which can lead to further theoretical inquiries as well as novel technological applications.

The study of pattern formation on swelling gels is a good example of a problem where the macroscopic patterns are directly derived from a reasonable microscopic

model. In this study, we see explicitly the diffusive growth of the gel network, the amplification of modes through linear instabilities, and the taming of instabilities by nonlinearities and cusp formations. The complete growth process including nonlinearities are followed on a computer, and the patterns obtained are in qualitative agreements with all observed phenomena. By including a density-dependent frictional coefficient, one may be able to extend this model to describe the patterns obtained from the reverse (shrinking) process.

The ideas of obtaining Langevin equations from considerations of symmetries and conservation laws, and then using them to describe non-equilibrium dynamics, have proven successful as reported in the study of surface growth[10][18]. Scale-invariant surface morphology observed in the growth problem is guaranteed by a translational symmetry. Critical exponents can then be obtained in principle through Dynamical Renormalization-Group (DRG) calculations. The DRG method gives the exact exponents for the $1 + 1$ dimensional surface growth problem, even in the presence of strong spatially-correlated noises. The problem involving temporally correlated noise is much more difficult to treat. In the study, I showed that the full noise spectrum was needed in a self-consistent RG treatment. I also showed that the RG procedure failed to yield a systematic ϵ -expansion (about the upper critical dimension $d_u = 2$) for the growth of a general d -dimensional surface. I proposed an alternative expansion about a lower critical dimension $d_l = 0$. The first-order result of various scaling exponents in the small d -expansion scheme matched the exact result at $d = 0$ as well as the

leading terms of the Kim-Kosterlitz exponent conjecture[68] which had been found to be consistent with results of all recent large scale numerical simulations. However, a stronger theoretical basis needs to be established for the small d -expansion.

One interesting area of investigation associated with the growth problem is the limit of very strongly correlated temporal noise, i.e. noise with a power-spectrum $\langle \eta(k, \omega) \eta(k', \omega') \rangle = 2D \delta^d(k + k') |\omega + \omega'|^{-2\theta}$, where $\theta \geq 1/2$. Traditional RG methods are not enough to tame the infra-red divergences in this problem because it involves *two* independent diverging scales, the system size L and the duration of the process T . Extensions of the existing RG formalisms are needed to treat this problem properly. The existence of two independent length scales is intimately related to the occurrence of multi-fractal scaling[103] which has been observed in a number of growth related problems[5]. New RG formalism may therefore shed some light into the nature of multi-fractal scaling which has been mysterious since its discovery. Numerical simulations with noise in the $\theta \geq 1/2$ limit can provide evidences for or against any direct connections between the large θ limit and the appearance of multi-fractal scaling.

A topic of more fundamental importance is the origin of the correlated noise. It is numerically known[63] that deterministic nonlinear equations such as the Sivashinski flame-front propagation equation can generate an effective stochasticity just by starting from a random initial condition. An analytical understanding of this process can lend insight into the origin of stochasticity.

Finally, I investigated the phenomena of dissipative transport and avalanches by

studying in detail variations of a simple “sandpile” automaton invented by Bak, Tang and Wiesenfeld[14]. Numerical simulations were first carried out using a 1-dimensional “running” sandpile. Various scaling regimes consisting of random superposition of single avalanches at small time scales, interacting avalanches at intermediate time scales, and system-wide great events at large times scales were identified and scaling exponents estimated. Qualitatively similar behaviors were observed in preliminary simulations of 2-dimensional systems as well as in recent experiments of real sand[83].

To understand the long-time behavior of the model transport system, I focused the study on the intermediate and large time-scale regions. First of all, I found that $1/f$ -type broad-band noises in the transport current only appeared in the presence of a finite driving force, contrary to the general belief which was based on an erroneous argument by Tang and Bak[90]. Interesting broad-band noise occurs in the intermediate scaling region which is studied using the methods of continuum field theories. Scale invariance observed in this region is shown to be a consequence of a conservation law (in the number of sand grains transported). Symmetry principles are then used to construct the simplest equation of motion. The scaling exponents in this region can be obtained exactly using the method of dynamical RG as in the surface growth problem.

The great events observed in the long-time limit is an unique feature of driven transport systems that possess a large number of metastable states. In the case

of the sandpile automaton, metastabilities are provided by the threshold nature of the dynamics. Other systems (such as simple models of earthquakes[87] and charge-density-waves[88]) sharing the properties of metastability and threshold dynamics also exhibit great events in the long-time region. The great events of the sandpile model are found to be anti-correlated. I provided a simple analysis of a one-site system, and demonstrated the underlying mechanism of anti-correlation. It is believed that the anti-correlation of the great events is also a consequence of threshold dynamics and can occur in a wide variety of systems.

A number of questions concerning the sandpile problem remain to be resolved. Among them, an important question is the role of the boundary condition in determining the scaling behaviors. Also, the connections among various scaling regions need to be understood, as this is related to the multifractal scaling observed in the distribution functions of the 1-dimensional sandpiles[89]. From the sandpile model, one can proceed to study more complicated transport problems by allowing additional fields to move on top of the sandpile. For example, if we randomly deposit “water” to the sandpile and allow the water to flow on the landscape, then we have a simple system of river network. By introducing nonlinear couplings between the sand and the water flows, we can have the landscape channeling the flow of water and water flow re-shaping the structure of the landscape.

The subject matter studied in this thesis, conformations of membranes, surface patterns of gels, surface morphology of deposits, and flow patterns of sandpiles, are

all properties of “down-to-the-earth” objects we frequently encounter in nature. The choice of these topics reflects my preference to stay close to the everyday life. I believe that much meaningful physics can be learned from the most ordinary of objects if we will only pay attention to them. I also believe that nature will reveal her secrets to those who keep in close touch with her. The work reported in this thesis is the beginning of a “romantic” journey in appreciating the beauty of nature.

Bibliography

- [1] H. E. Stanley, *Introduction to Phase Transitions and Critical Phenomena*, (Oxford University Press, Oxford, 1971), chapter 1.
- [2] See e.g., M. E. Fisher, "The Theory of Equilibrium Critical Phenomena", *Reports on Progress in Physics*, Vol. XXX, 615 (1967). See also L. P. Kadanoff et al, *Rev. Mod. Phys.* **39**, 395 (1967).
- [3] The development of the field can be found through many of the fine articles collected in the famous series *Phase Transitions and Critical Phenomena*, ed. C. Domb and M. S. Green, (Academic Press, London).
- [4] A good review of current topics in the field of surfaces can be found in *Statistical Mechanics of Membranes and Surfaces*, ed. D. Nelson, T. Piran and S. Weinberg, (World Scientific, Singapore, 1989).
- [5] See e.g., *Random Fluctuations and Pattern Growth: Experiments and Models*, ed. H. E. Stanley and N. Ostrowsky, (Kluwer Academic Publishers, Dordrecht, 1988).
- [6] M. Mezard, G. Parisi, M. A. Virasoro, *Spin Glass Theory and Beyond*, (World Scientific, Singapore, 1987).
- [7] M. Kardar and D. R. Nelson, *Phys. Rev. A* **38**, 966 (1988).
- [8] M. Plischke and D. H. Boal, *Phys. Rev. A* **38**, 4943 (1988); F. F. Abraham, W. E. Rudge, and M. Plischke, *Phys. Rev. Lett.* **62**, 1757 (1989); J. -S. Ho and A. Baumgartner, *Phys. Rev. Lett.* **63**, 1324 (1989).
- [9] T. Tanaka, S. -T. Sun, Y. Hirokawa, S. Katayama, J. Kucera, Y. Hirose, and T. Amiya, *Nature (London)*, **325**, 796 (1987).
- [10] M. Kardar, G. Parisi and Y.-C. Zhang, *Phys. Rev. Lett.* **56**, 889 (1986).

- [11] S.-k. Ma *Modern Theory of Critical Phenomena*, (Benjamin-Cummings, Reading, 1976).
- [12] B. Mandelbrot, *The Fractal Geometry of Nature*, (Freeman, San Francisco, 1982).
- [13] See e.g., P. Dutta and P. M. Horn, *Rev. Mod. Phys.* **53**, 497 (1981).
- [14] P. Bak, C. Tang, and K. Wiesenfeld, *Phys. Rev. Lett.* **59**, 381 (1987); *Phys. Rev. A* **38**, 364 (1988).
- [15] B. Duplantier, T. Hwa and M. Kardar, *Phys. Rev. Lett.* **64**, 2022 (1990).
- [16] T. Hwa, *Phys. Rev. A* **41**, 1751 (1990).
- [17] T. Hwa and M. Kardar, *Phys. Rev. Lett.* **61**, 106 (1988).
- [18] E. Medina, T. Hwa, M. Kardar, and Y.-C. Zhang, *Phys. Rev. A* **39**, 3053 (1989).
- [19] T. Hwa and M. Kardar, *Phys. Rev. Lett.* **62**, 1813 (1989).
- [20] M. Mutz, W. Helfrich, *Phys. Rev. Lett.* **62**, 2881 (1989).
- [21] A.M. Polyakov, *Gauge Fields and Strings*, (Harwood-Academic, Chur, 1987).
- [22] Y. Kantor, M. Kardar, and D.R. Nelson, *Phys. Rev. A* **35**, 3056 (1987).
- [23] J.A. Aronowitz and T.C. Lubensky, *Europhys. Lett.* **4**, 395 (1987).
- [24] B. Duplantier, *Phys. Rev. Lett.* **58**, 2733 (1987); and contribution to [4].
- [25] P.G. de Gennes, *Scaling Concepts in Polymer Physics*, (Cornell University Press, Ithaca, New York, 1979), chapter 1.
- [26] S.F. Edwards, *Proc. Phys. Soc. London* **85**, 613 (1965).
- [27] See Y. Kantor's contribution to [4].
- [28] P. G. deGennes, *Phys. Rev. A* **38**, 339, (1972).
- [29] M. Benhamou and G. Mahoux, *J. Phys. (Paris)* **47**, 559 (1986); B. Duplantier, *ibid.* 569; L. Schäfer and T.A. Witten, *J. Phys. (Paris)* **41**, 459 (1980).
- [30] B. Duplantier, *Phys. Rev. Lett.* **62**, 2337 (1989).
- [31] J. des Cloizeaux, *J. Phys. (Paris)* **42**, 635 (1981).
- [32] M. Paczuski, M. Kardar and D. R. Nelson, *Phys. Rev. Lett.* **60**, 2638 (1988); M. Paczuski and M. Kardar, *Phys. Rev. A* **39**, 6086 (1989).

- [33] D. R. Nelson and F. F. Abraham, (submitted to Nature, 1990).
- [34] D. R. Nelson and R. Meyer, private communication; see also a brief description in D. R. Nelson's contribution in [4].
- [35] C. Schmit, private communication.
- [36] B. Brodie, Phil. Trans. **140**, 249 (1859).
- [37] L. Staudenmaier, Ber. deut. chem. Ges. **31**, 1481 (1898).
- [38] W. S. Hummers and R. E. Offeman, J. Amer. Chem. Soc. **80**, 1339 (1958).
- [39] H. P. Boehm, A. Clauss, G. Fischer and U. Hofmann, Z. Naturforschg. **17b**, 150 (1962); *Proc. Fifth Carbon Conf.* 73, Pergamon Press, (1962).
- [40] B. J. Berne and R. Pecora, *Dynamic Light Scattering*, (John Wiley & Sons, New York, 1976).
- [41] G. Swislow, MIT Ph.D. Thesis (1984).
- [42] M. A. F. Gomes and G. L. Vasconcelos, Phys. Rev. Lett. **60**, 237 (1988); and Y. Kantor, M. Kardar, and D. R. Nelson, Phys. Rev. Lett. **60**, 238 (1988).
- [43] R. C. Ball, private communication.
- [44] T. Tanaka, Physica (Amsterdam) **140A**, 261 (1986).
- [45] A. Onuki, J. Phys. Soc. Jpn. **3**, 703 (1988).
- [46] K. Sekimoto and K. Kawasaki, J. Phys. Soc. Jpn. **9**, 2997 (1987).
- [47] T. Tanaka, Sci. Am. **244**(1), 124 (1981), and references therein.
- [48] I. Ohmine, and T. Tanaka, J. Chem. Phys. **11**, 5725 (1982).
- [49] M. Ilavsky, Macromolec. **15**, 782 (1982).
- [50] T. Tanaka, D. J. Fillmore, S.-T. Sun, I. Nishio, G. Swislow and A. Shah, Phys. Rev. Lett. **45**, 1636 (1980).
- [51] Y. Hirokawa, T. Tanaka, and S. Katayama, in *Microbial Adhesion and Aggregation*, ed. K. C. Marshal, (Springer-Verlag, 1984).
- [52] T. Tanaka and D. J. Fillmore, J. Chem. Phys. **70**, 1214 (1979).
- [53] L. D. Landau and E. M. Lifschitz, *Teoria Uprogosti*, (Nauka, Moscow, 1986).
- [54] M. Kardar, in Proceedings of 1989 Cargese meeting on "Disorder and Fracture".

- [55] T. Hwa, M. Paczuski and M. Kardar, manuscript in preparation.
- [56] P. Meakin and R. Jullien, *Europhys. Lett.* **9**, 71 (1989).
- [57] S. F. Edwards and D. R. Wilkinson, *Proc. R. Soc. Lond. A* **381**, 17 (1982).
- [58] J. M. Burgers, *The Nonlinear Diffusion Equation*, (Reidel, Boston, 1974).
- [59] D. Forster, D. R. Nelson and M. J. Stephen, *Phys. Rev. A* **16**, 732 (1977).
- [60] M. Kardar and Y. -C. Zhang, *Phys. Rev. Lett.* **58**, 2087 (1987).
- [61] D. A. Huse, C. L. Henley, and D. S. Fisher, *Phys. Rev. Lett.* **55**, 2924 (1985); and references therein.
- [62] H. van Beijeren, R. Kutner, and H. Spohn, *Phys. Rev. Lett.* **54**, 2026 (1985).
- [63] S. Zalesky, *Physica D* **34**, 427 (1989); G.I. Sivashinski, *Acta Astronautica* **6**, 569 (1979); and references therein.
- [64] J. G. Zabolitzky and D. Stauffer, *Phys. Rev. A* **34**, 1523 (1986); and *Phys. Rev. Lett.* **57**, 1809 (1986).
- [65] P. Meakin, P. Ramanlal, L. M. Sander and R. C. Ball, *Phys. Rev. A* **34**, 5091 (1986).
- [66] M. Plischke, Z. Racz and D. Liu, *Phys. Rev. B* **35**, 3485 (1987).
- [67] D. E. Wolf and J. Kertesz, *J. Phys. A* **20**, L257 (1987); and references therein.
- [68] J. M. Kim and J. M. Kosterlitz, *Phys. Rev. Lett.* **62**, 2289 (1989).
- [69] J. G. Amar and F. Family, *Phys. Rev. Lett.* **64**, 543 (1990).
- [70] J. G. Amar and F. Family, *Phys. Rev. B*, 1990 (in press).
- [71] H. Yan, D. Kessler, and L. M. Sander, *Phys. Rev. Lett.* **64**, 926 (1990).
- [72] H. Guo, B. Grossmann, and M. Grant, *Phys. Rev. Lett.* **64**, 1262 (1990).
- [73] J. Derrida and S. Golinelli, (preprint 1989).
- [74] L.-H. Liu and B. M. Forrest, *Phys. Rev. Lett.* **64**, 1405 (1990).
- [75] Y. P. Pellegrini and R. Jullien, *Phys. Rev. Lett.* **64** 1745 (1990).
- [76] Y. C. Zhang, preprint (1990).
- [77] J. J. Brophy, *J. Appl. Phys.* **40**, 3551 (1969).

- [78] K. L. Schick and A. A. Vereen, *Nature (London)* **251**, 599 (1974).
- [79] B. B. Mandelbrot and J. W. Van Ness, *SIAM Review* **10**, 422 (1968).
- [80] B. B. Mandelbrot and J. R. Wallis, *Water resources Res.* **5**, 321 (1969).
- [81] W. H. Press, *Comments Mod. Phys. Part C7*, 103 (1978).
- [82] For reviews, see W. Kittel and R. Peschanski, in *Proc of 1989 EPS Conference, Madrid*; B. Buschbeck and P. Lipa, *Mod. Phys. Lett. A* **4**, 1871 (1989).
- [83] H. M. Jaeger, C.-h. Liu, and S. R. Nagel, *Phys. Rev. Lett.* **62**, 40 (1989).
- [84] S. P. Obukhov, in [5].
- [85] D. Dhar and R. Ramaswamy, *Phys. Rev. Lett.* **63**, 1659 (1989).
- [86] D. Dhar, *Phys. Rev. Lett.* **64**, 1613 (1990).
- [87] J. M. Carlson and J. S. Langer, *Phys. Rev. Lett.* **62**, 2632 (1989); *Phys. Rev. A* **40**, 6470 (1989).
- [88] S. N. Coppersmith, preprint (1990).
- [89] L. P. Kadanoff, S. R. Nagel, L. Wu and S. M. Zhou, *Phys. Rev. A* **39**, 6524 (1989).
- [90] C. Tang and P. Bak, *Phys. Rev. Lett.* **60**, 2347 (1988).
- [91] B. Grossmann, H. Guo, and M. Grant, preprint (1990).
- [92] S. S. Manna, *Hochleistungsrechenzentrum Jülich report*, 1989 (to be published).
- [93] P. Grassberger and S. S. Manna, *Wuppertal report*, 1990 (to be published).
- [94] J. M. Carlson, J. T. Chayes, E. R. Grannan, and G. H. Swindle, preprint (1990).
- [95] H. J. Jensen, K. Christensen, and H. C. Fogedby, *Phys. Rev. B* **40**, 7425 (1989).
- [96] J. Kertesz and L. B. Kiss, preprint (1990).
- [97] H. M. Jaeger, C.-h. Liu, S. R. Nagel, and T. A. Witten, preprint (1990).
- [98] H. K. Janssen and B. Schmittmann, *Z. Phys. B* **63**, 517 (1986).
- [99] G. Grinstein, S. Sachdev, and D. H. Lee, *Phys. Rev. Lett.* **64**, 1927 (1990).
- [100] W. J. Yeh and Y. H. Kao, *Phys. Rev. Lett.* **53**, 1590 (1984).

- [101] H. J. Jensen, Nordita preprint (1989).
- [102] See e.g., D. J. Amit, *Field Theory, the Renormalization Group, and Critical Phenomena*, (World Scientific, Singapore, 1984).
- [103] See e.g., B. B. Mandelbrot in [5]; also see M. H. Morgen in [5].

About the Author

Terence Hwa was born on May 30, 1964 in Shanghai, China, where he attended Dong-Hu Elementary School and Shanghai No. 51 Middle School. He moved to the United States at the age of 15, attended South Eugene High School in Eugene, Oregon and then Homestead High School in Cupertino, California. He entered Stanford University in 1982, and received the degree of Bachelor of Science in Physics, Biology and Electrical Engineering with distinction and honors in 1986. His physics honors thesis "Proposals to Determine the Muon's $g - 2$ Anomaly" won the 1986 Apker Award.

The author continued his graduate study in statistical physics at the Massachusetts Institute of Technology. There he pursued a number of theoretical studies under the supervision of Professor Mehran Kardar and experimental studies under Professor Toyochi Tanaka. For the next year or two, the author will be a postdoctoral research associate with the physics department at Harvard University.